Publication 1

R. Konefał, J. Spěváček, P. Černoch

Thermoresponsive poly(2-oxazoline) homopolymers and copolymers in aqueous solutions studied by NMR spectroscopy and dynamic light scattering

European Polymer Journal 2018, in production

Thermoresponsive poly(2-oxazoline) homopolymers and copolymers in aqueous solutions studied by NMR spectroscopy and dynamic light scattering

Rafał Konefał, Jiří Spěváček,* Peter Černoch

Institute of Macromolecular Chemistry, Academy of Sciences of the Czech Republic, Heyrovsky Sq. 2 162 06, Prague, 6, Czech Republic

ABSTRACT
Structural changes during temperature-induced phase transition in D_2O solutions of poly(2-ethyl-2-oxazoline) (PEOx) and P(EOx-*grad*-2-methyl-2-oxazoline (MOx)) copolymers were investigated by ^{1}H NMR methods in combination with dynamic light scattering. NMR spectra showed that in PEOx solutions on molecular level structures formed during gradual heating are preserved during subsequent cooling. Phase transition in solutions of P(EOx-*grad*-MOx) copolymers as revealed by NMR exists irrespective the solution is turbid or nonturbid at higher temperatures. In contrast to PEOx homopolymers it is very broad, virtually independent of the copolymer composition and molecular weight, and reversible with some hysteresis. Reduced intensities of cross-peaks in NOESY spectra of copolymer solutions at elevated temperatures are mainly due to the changed mobility of copolymer segments. In all investigated solutions two types of water, „free“ and „bound“ with long and very short spin-spin relaxation times T_2, respectively, were detected in the transition region and above the transition. The existence of two T_2 components shows that exchange between „bound“ and „free“ water is slow regarding T_2 values.

Keywords:
Thermoresponsive polymer; poly(2-ethyl-2-oxazoline); poly(2-ethyl-oxazoline-*grad*-2-methyl-2-oxazoline) copolymer; aqueous solution; NMR; dynamic light scattering

1. Introduction

In recent years, smart polymers are one of the most exciting and intensively studied class of materials. They are able to change their properties by response to external stimuli such as changes in temperature, pH, ionic strength and light irradiation [1–4]. From this group, systems based on thermoresponsive polymers are widely investigated due to variety of prospective applications such as drug delivery, tissue engineering, bioseparation, thermoresponsive films, oil-gas industry and nanoreactors [5–11]. Most of the studies focus on polymers that show phase separation in water above the lower critical solution temperature (LCST). The best known and most widely studied polymer from this group is poly(*N*-isopropylacrylamide) (PNIPAm) with LCST around 305 K [12,13]. However, nowadays due to their biocompatibility and possible applications, poly(*2*-oxazoline)s (POx)s are receiving considerable attention [14,15]. Side chain of POx controls hydrophilicity of the polymer: poly(2-methyl-2-oxazoline) (PMOx) is hydrophilic and thus well soluble in water, poly(2-ethyl-2-oxazoline) (PEOx) and poly(2-propyl-2-oxazoline)s exhibit thermoresponsive LCST behavior in aqueous solutions where the respective LCST depends on molecular weight of polymer chains, while polymers with longer side chains are insoluble in water [16–23].

In comparison with methods which are often used in studies of the LCST-type phase transition (cloud point measurement, infrared (IR) spectroscopy, light scattering, small angle X-ray scattering, calorimetry etc.) [20,22,24–26], NMR spectroscopy can provide quantitative information on the LCST phase separation behavior [27]. Relaxation time measurements and diffusion experiments can show changes in molecular motions of polymer and water in solution. In last two decades ^{1}H NMR spectroscopy and NMR relaxation times techniques were successfully applied to study various single- and multi-component thermoresponsive polymer systems in aqueous solutions [27–34].

In the present work we applied ^{1}H NMR spectroscopy, ^{1}H spin-spin relaxation times (temperature and time dependences) and 2D nuclear Overhauser effect spectroscopy (NOESY) at various temperatures (applied only to copolymers) to study temperature-induced phase separation in aqueous solutions of PEOx homopolymers (with different molecular weights) and copolymers of EOx and MOx (with different composition and molecular weight). Due to the fact that both PMOx and PEOx are biocompatible and do not accumulate in the tissues, in principle these systems can be applied in biomedicine, drug and gene delivery systems as well as in electronic industry [35–42].

2. Experimental

2.1. Chemicals

2-methyl-2-oxazoline (MOx), 2-ethyl-2-oxazoline (EOx), methyl p-tosylate (MeTos), calcium hydride (CaH_2) and acetonitrile (AN) were received from Sigma-Aldrich. Sodium hydroxide (NaOH) was obtained from LachNer. MOx, EOx, MeTos and AN were distilled over CaH_2.

2.2. Synthesis and Characterization

POx homopolymers and copolymers with variable ratio of monomer units were prepared by cationic ring-opening polymerization of EOx and MOx in AN, initiated by MeTos [43]. Molecular weight of the samples was controlled by the monomer/initiator molar ratio. Briefly, e.g., in synthesis of equimolar P(EOx-*grad*-MOx) copolymers 10 mL of AN, 2.32 g (27.24 mmol, 100 eq) of MOx, 2.7 g (27.24 mmol, 100 eq) of EOx and 51 mg (0.27 mmol, 1 eq) of MeTos were added into Schlenk tube with magnetic stirrer. The mixture was degassed with argon and placed into oil bath preheated to 343 K. The polymerization was carried for 5 days. After that, the reaction was terminated with 1 mL of 1M-NaOH (4 fold excess related to initiator) and stirred at 343 K for 6 hrs. After removal of the solvent under reduced pressure, the solid material was dissolved in 40 mL of water and dialyzed against water (MWCO 2000) for 5 days. The product was isolated with lyophilisation. Hoogenboom et al. [44] determined reactivity ratios for cationic ring-opening copolymerizations of EOx and MOx and concluded that the copolymerizations resulted in the formation of gradient copolymers. We presume that this holds also for our copolymers.

All samples were characterized by ^{1}H NMR spectroscopy and size-exclusion chromatography (SEC). Values of the molar ratio of EOx and MOx units in copolymers were determined from integrated intensities of NMR signals of respective methyl protons. Molecular weights (M_w and M_n) and molecular-weight dispersities *MWD* were determined by SEC measurements (*N, N*-dimethylacetamide as the eluent, 0.7 mL/min, 303 K, RI detector, calibration on polystyrene standards). All these values are shown in Table 1.

Table 1
Molecular characteristics of POx homopolymers and copolymers

Sample*	EOx/MOx (eq)**	EOx/MOx NMR***	M_w	M_n	*MWD*
PEOx-H	100/0	100/0	24600	17200	1.43
PEOx-L	100/0	100/0	7400	5900	1.25
P(EOx/MOx)(75/25)-H	75/25	75/25	24900	15100	1.65
P(EOx/MOx)(53/47)-H	50/50	53/47	14700	10200	1.44
P(EOx/MOx)(75/25)-L	75/25	75/25	8200	6300	1.29
P(EOx/MOx)(52/48)-L	50/50	52/48	9600	7300	1.32

*Suffixes H and L denote higher and lower molecular weight, respectively; **monomer ratio in the synthesis; *** molar ratio in the copolymer determined by ^{1}H NMR spectra

2.3.NMR measurements

Temperature dependences of ^{1}H NMR spectra were acquired with Bruker Avance III 600 spectrometer operating at 600.2 MHz. The width of 90° pulse was 10 μs, relaxation delay 10 s, acquisition time 2.18 s, 16 scans. Each sample was kept for 15 min at the desired temperature before measurement. The integrated intensities were determined with spectrometer integration software with an accuracy of ±1%. 2D ^{1}H–^{1}H NOESY NMR spectra were recorded on the same spectrometer with 4098 Hz spectral window in f_1 and f_2 frequency axes, and mixing times 100 ms, 200 ms and 600 ms. A total of 16 scans was accumulated over 512 t_1 (evolution time) increments with a relaxation delay of 10 s. The temperature and time dependences of ^{1}H spin-spin relaxation times T_2 of HDO were measured using the CPMG pulse sequence $90°_x$-(t_d-$180°_y$-t_d)$_n$-acquisition [45]. The relaxation delay between scans was 100 s, acquisition time 2.84 s with 2 scans. The relative error for T_2 values did not exceed ±5%.Spin-lattice relaxation times T_1 of copolymer protons were measured using an inversion recovery pulse sequence 180°-t_d-90° with 32 t_d values and 1 scan; relaxation delay was 50 s. In all measurements temperature was maintained constant within ±0.2 K in the range 295-360 K using a BVT 3000 temperature unit. Temperature was calibrated using a standard 80% ethylene glycol (DMSO-d_6) sample. All samples in D_2O (Sigma, 99.9% of deuterium) solutions (polymer concentrations c = 0.5, 5 and 20 wt%) were filled into 5-mm NMR tubes, which were degassed and sealed under nitrogen.

2.4. Dynamic Light Scattering (DLS) Measurements

Individual samples were investigated using ALV-6010 correlator equipped with an ALV/CGS-8F goniometer, a 22 mW He-Ne laser (wavelength λ = 632.8 nm) and pair of avalanche photodiodes operated in a pseudo-cross-correlation mode. All measurements were made at a 90° angle. The measured intensity correlation function $g^2(t)$ was analyzed using the algorithm REPES [46] performing the inverse Laplace transformation according to

$$g^2(t)=1+\beta\left[\int A(t)\exp(-t/\tau)\,d\tau\right]^2=1+\beta\left[\sum_{i=1}^{n}A_i\exp(-t/\tau_i)\right]^2$$

where t is the delay time of the correlation function and β an instrumental parameter, and yielding distribution A(τ) of relaxation times τ. The relaxation time τ is related to the diffusion coefficient D and relaxation (decay) rate Γ by the relation:

$$\Gamma = \frac{1}{\tau} = Dq^2$$

where q is the scattering vector defined as $q = (4\pi n/\lambda)\sin(\theta/2)$ where n is the refractive index of the solvent and θ is the scattering angle. The hydrodynamic radius R_h of the particles can be calculated from the diffusion coefficient using the Stokes-Einstein equation:

$$D = k_B T/6\pi\eta R_h$$

where T is absolute temperature, η the viscosity of the solvent and k_B the Boltzmann constant. The studied solutions were prepared in D_2O (c = 5 wt%, i.e., the same as in most of NMR measurements), filtered into clean glass tubes, flame-sealed to prevent evaporation of the solvent and stabilized for 24 hrs at ambient temperature.

2.5. DSC measurements

DSC measurements on the D_2O solutions (c = 20 wt%) of the PEOx homopolymers were carried out using a Perkin-Elmer 8500 differential scanning calorimeter with a heating rate 1 K/min or 5 K/min in the temperature range from 303 K to 364 K.

3. Results and discussion

3.1. DLS

We investigated temperature behavior of D_2O solutions (c = 5 wt%) of the investigated PEOx homopolymers and P(EOx-*grad*-MOx) copolymers by using DLS in temperature range 298 – 358 K with 2 K steps. Fig. 1 shows temperature dependences of normalized intensity of scattered light for these solutions. Increase of the intensity as observed for both PEOx homopolymers and P(EOx/MOx) (75/25)-H copolymer reflects an increased turbidity of the respective solutions. For PEOx homopolymers these results are consistent with former transmittance measurements on aqueous solutions of lower polymer concentration (c = 0.5 wt%) [21]. From Fig. 1 it follows that with exception of the P(EOX/MOx) (75/25)-H copolymer with larger EOx content and higher molecular weight, turbidity was not detected in solutions of other three copolymer samples in accord with visual observations.

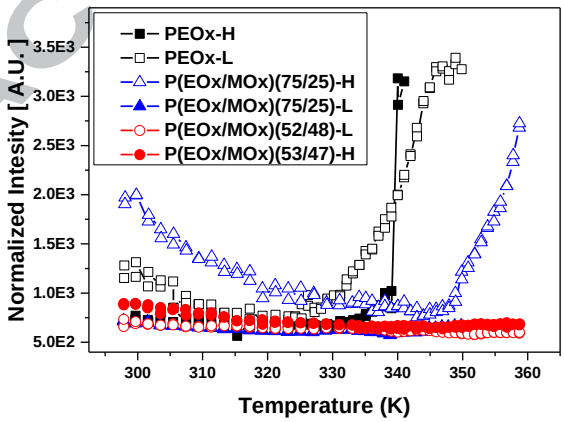

Fig. 1. Temperature dependences of intensity of scattered light in D_2O solutions (c = 5 wt%) of PEOx homopolymers and P(EOx-*grad*-MOx) copolymers during gradual heating.

DLS was mainly used to obtain information on particle sizes in investigated solutions. Fig. 2 shows for illustration intensity-based distributions of the hydrodynamic radius R_h for D_2O solutions of the PEOx-H and PEOx-L homopolymers and P(EOx/MOx)(53/47)-H copolymer at 298 K, 338 K and 351 or 355 K. Results obtained by DLS for solutions of other investigated copolymers were very similar to behavior of the P(EOx/MOx)(53/47)-H sample (Fig. 2c). In all cases two diffusional modes have been observed which is in accord with recent study of other authors [47]. At 298 K a mode No. 1 corresponded to molecularly dissolved polymer molecules with hydrodynamic radii $R_h \cong$ 3-5 nm and a mode No. 2 to bigger molecular clusters characterized by hydrodynamic radii $R_h \cong$ 320-610 nm. It is well-known that in DLS larger particles are favoured in intensity-based distribution. Largest R_h values of the big clusters (mode No. 2) were found for PEO_x-H homopolymer and P(EOx/MOx) (75/25)-H copolymer. While for PEOx-H homopolymer and temperatures below the critical point where intensity of scattered light starts to increase the R_h values of the big clusters are virtually constant, for P(EOx/MOx) (75/25)-H copolymer in the same region they somewhat decrease with increasing temperature. This fact therefore can explain why for P(EOx/MOx) (75/25)-H copolymer in the range 298 – 345 K the intensity of scattered light decreases.

Transformation to volume or number based distributions is laden with undefined errors, nevertheless, it is acceptable for comparison of proportions in the studied systems. We have used the approximation where the ratio of amplitudes of the intensity- and volume-based distributions is proportional to R_h^3. The volume-based distributions of the R_h as derived from the respective intensity-based distributions are shown for solutions of the PEOx-H and PEOx-L homopolymers and P(EOx/MOx)(53/47)-H copolymer in Fig. 3. It is clearly visible that for PEOx-L and P(EOx/MOx)(53/47)-H the peak related to the big aggregates disappeared as their total amount (volume) is extremely small; the same result was obtained also for all other investigated copolymers. Therefore the contribution of big aggregates can be neglected for all samples with one exception: for D_2O solution of the PEOx-H homopolymer at 351 K the peak corresponding to large aggregates predominated in the volume-based distribution (cf. Fig. 3a).

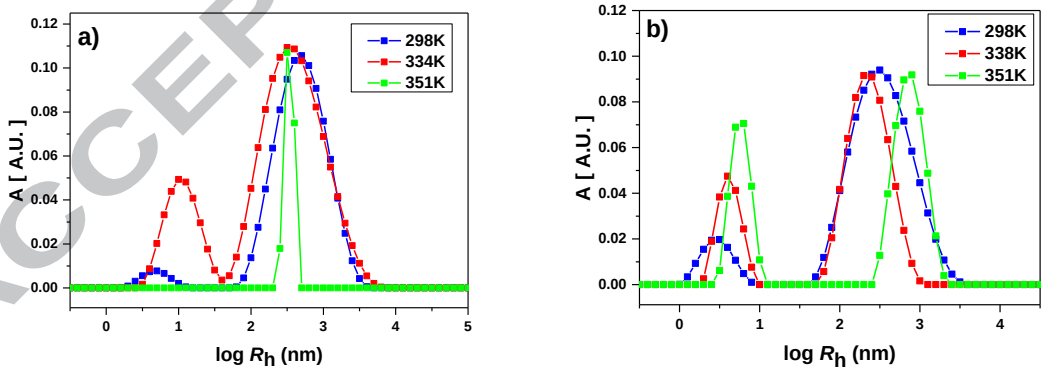

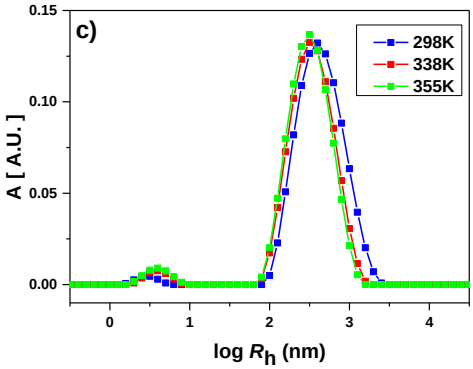

Fig. 2. Intensity-based distributions of the hydrodynamic radius R_h for D_2O solutions (c = 5 wt%) of the PEOx-H homopolymer (a), PEOx-L homopolymer (b) and P(EOx/MOx)(53/47)-H copolymer (c) at 298 K, 338 K and 351 or 355 K.

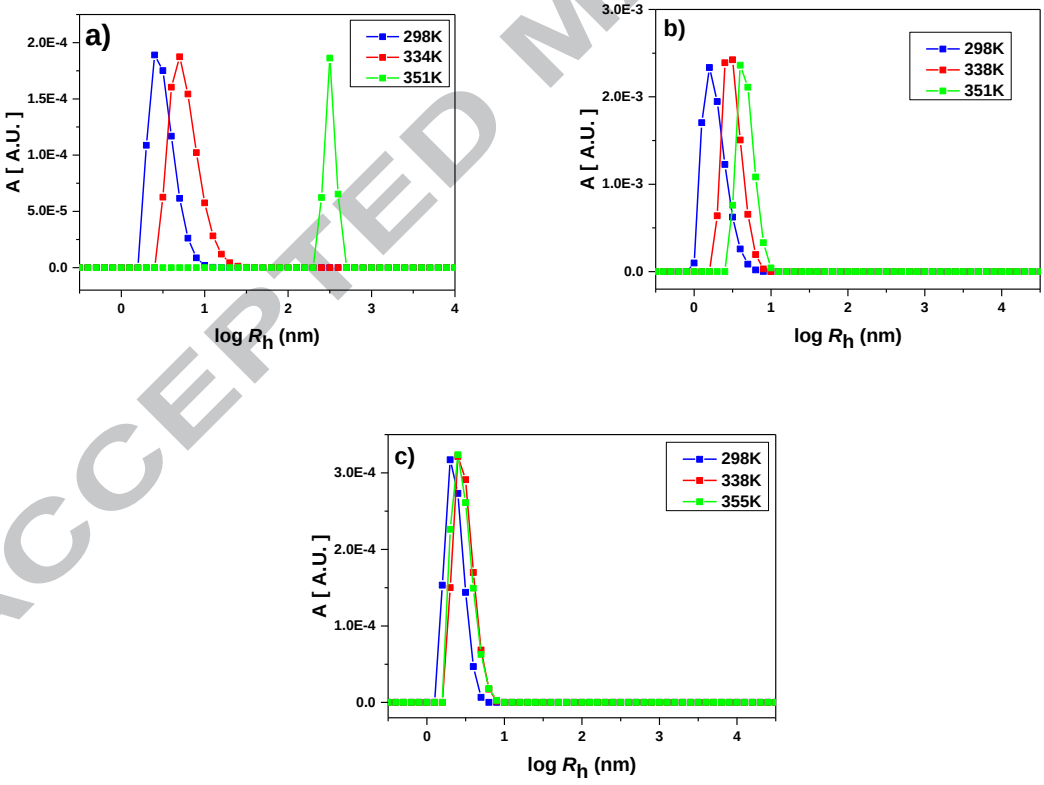

Fig. 3. Volume-based distributions of the hydrodynamic radius R_h for D_2O solutions (c = 5 wt%) of the PEOx-H homopolymer (a), PEOx-L homopolymer (b) and P(EOx/MOx)(53/47)-H copolymer (c) at 298 K, 338 K and 351 or 355 K.

Temperature dependences of hydrodynamic radius R_h for predominating mode No. 1 are shown in Fig. 4. For PEOx homopolymers an increase in R_h values can be observed at

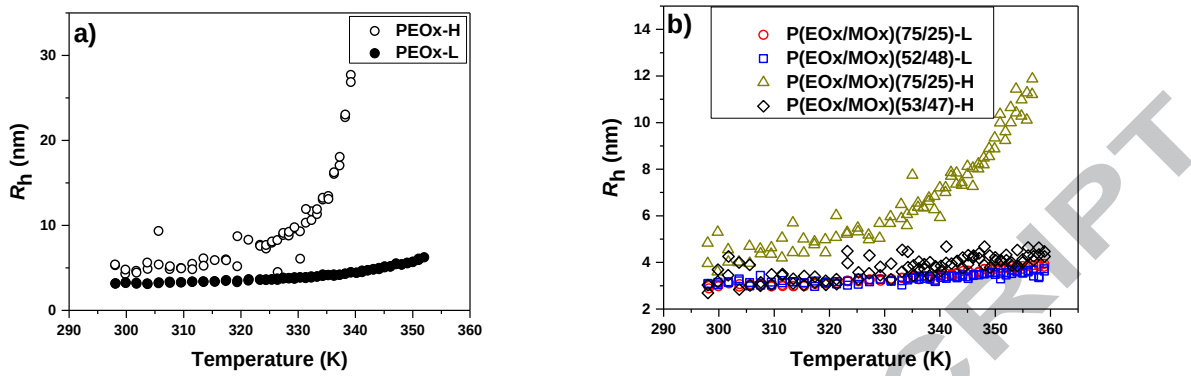

Fig. 4. Temperature dependences of the hydrodynamic radius R_h (mode No. 1) in D_2O solutions (c = 5 wt%) of PEOx homopolymers (a) and P(EOx-*grad*-MOx) copolymers (b).

temperatures above 325 K. At the same time this increase is more pronounced for PEOx-H of higher molecular weight (R_h = 28 nm at 338 K) in comparison with PEOx-L (R_h = 6 nm at 353 K). The temperature dependence of R_h values shown for D_2O solution of PEOx-H in Fig. 4 suggests that at 351 K these values will reach several hundreds nm so explaining why for this sample the peak corresponding to large aggregates predominated in the volume-based distribution (cf. Fig 3a). For solutions of P(EOx-*grad*-MOx) copolymers a significant increase in R_h values at higher temperatures was observed only for P(EOx/MOx)(75/25)-H copolymer, i.e., the sample where both the EOx content and molecular weight are relatively large; for this sample R_h = 12 nm at 356 K. For other investigated copolymers the increase in R_h values at 356 K in comparison with 298 K does not exceed 1 nm, i.e., the R_h values are almost constant in the whole temperature range (cf. also Fig. 1).

3.2. ^{1}H NMR spectra and fraction p of units with significantly reduced mobility

Fig. 5 shows high-resolution ^{1}H NMR spectra of a D_2O solution (c=5 wt%) of the PEOx-H homopolymer measured under the same instrumental conditions at three temperatures. The assignment of resonances to various proton types is shown directly in the spectrum measured at 360 K and chemical structure of homopolymer is shown at the figure. The signal "a" is related to methylene protons NCH_2 from the main chain of PEOx, while PEOx side chain groups $COCH_2$ and CH_3 correspond to peaks "b" and "c", respectively. ^{1}H NMR spectra presented in Fig. 5 were measured at temperatures below the LCST (295 K), in the middle of the transition (338 K) and above the LCST (360 K) of PEOx. We assume that splitting of the signal of ethyl CH_2 protons, which exists at 295 K and disappears at 360 K, can be in connection with hindered rotation around the N-CO bond at lower temperatures. In this section we shall concentrate on changes in integrated intensities of polymer signals. The most significant effect observed in the spectra is a visible reduction in integral intensities of all signals of PEOx units although even at 360 K the integral intensities still remain relatively large. This result is evidently related to the fact that with increasing temperature, the mobility of the part of polymer segments which form globular-like structures (mesoglobules) decreases to such an extent that they escape detection in high-resolution NMR spectra. Similar behavior was previously observed also for other thermoresponsive polymer systems [27-29].

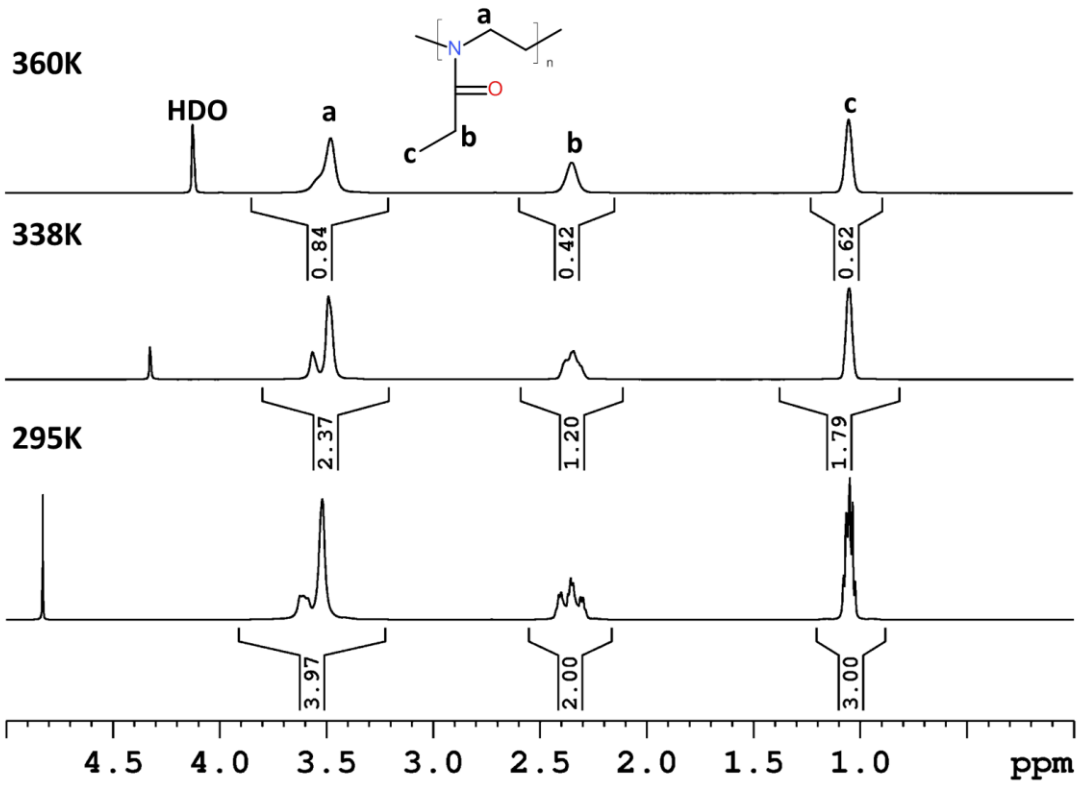

Fig. 5. 600.2 MHz ^{1}H NMR spectra of PEOx-H homopolymer in D_2O solution (c=5 wt%) measured at 295, 338 and 360 K under the same instrumental conditions.

High-resolution ^{1}H NMR spectra of the D_2O solution (c=5 wt%) of the copolymer P(EOx/MOx)(53/47)-H recorded at three temperatures 295 K, 337 K and 360 K under the same instrumental conditions are presented in Fig. 6. Similarly as in Fig. 5 peaks assignments of the various proton types are shown in the spectrum measured at 360 K. Signals of EOx units (a, b, c) are at the same positions as in the spectra of PEOx homopolymer (cf. Fig. 5). Additionally peak "d" of methyl protons from MOx units is detected. Similarly as described above for the PEOx homopolymer, a hindered rotation around N-CO bond can result in splitting of signals of CH_2 protons of EOx units and CH_3 protons of MOx units at lower temperatures. The spectra at 337 K and 360 K show similar effect as observed for homopolymer, i.e., a decreasing integral intensity of all copolymer signals with increasing temperature. Nevertheless, in comparison with PEOx homopolymers (cf. Fig. 5) this effect is much weaker.

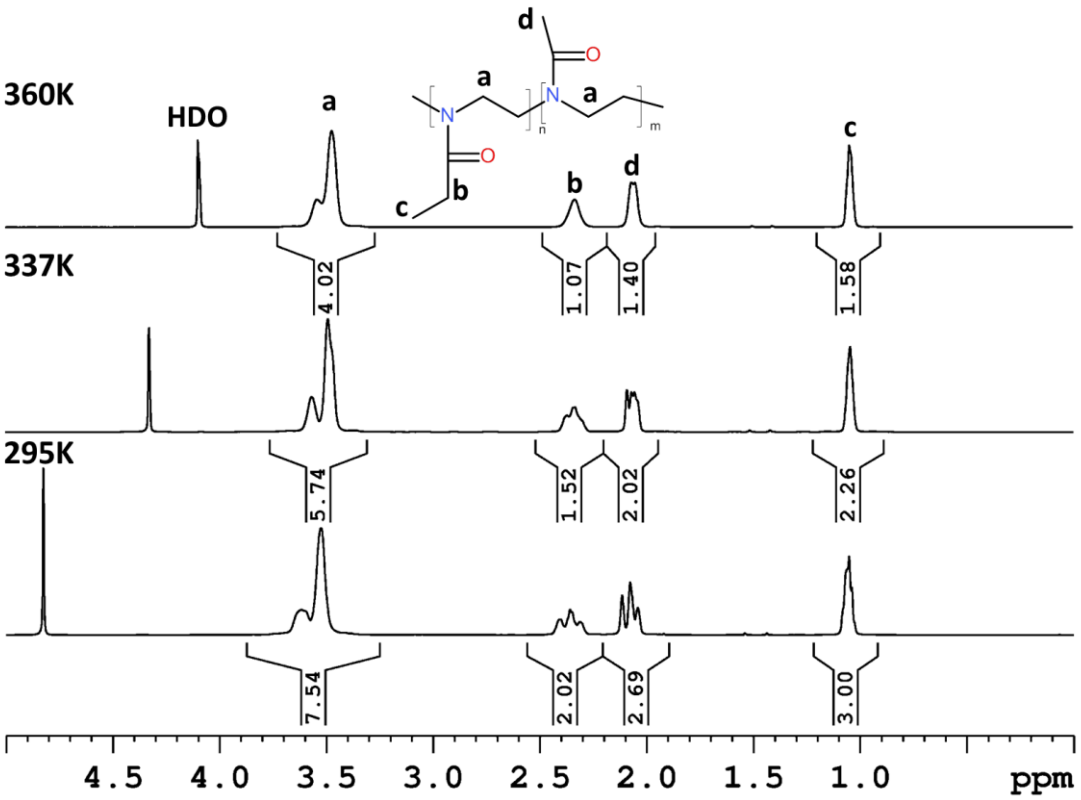

Fig. 6. 600.2 MHz ^{1}H NMR spectra of P(EOx/MOx) (53/47)-H copolymer in D_2O solution (c=5 wt%) measured at 295, 337 and 360 K under the same instrumental conditions.

From temperature dependent integrated intensities of NMR signals it is possible to quantitatively characterize changes occurring during the heating and cooling processes. For this purpose the values of the fraction *p* of units with significantly reduced mobility were obtained using the relation [27,29,34]:

$$p = 1 - \frac{I(T)}{I(T_0) \times \frac{T_0}{T}} \qquad (1)$$

where $I(T)$ is the integrated intensity of given polymer signal in the spectrum at given absolute temperature T and $I(T_0)$ is the integrated intensity of this signal when no phase transition or other reason for the reduced mobility of polymer segments occurs. For T_0 we chose the temperature where the integrated intensity of the given signal was the highest and therefore $p(T_0) = 0$. Additionally, in denominator of the Eq. (1) we took into account the fact that the integrated intensities should decrease with temperature as $1/T$ (Curie law holds also for nuclear magnetization). As shown in Figs. 7 and 8 and in the Fig. S1 in the Supplementary material for investigated solutions of PEOx homopolymers and P(EOx-*grad*-MOx) copolymers the temperature T_0 where the integrated intensity of the given signal was highest (i.e., $p(T_0) = 0$) was in the range 305-315 K while $p \cong 0.04$ at 295 K. Small *p*-value at 295 K indicates that 5 wt% solutions of investigated systems are probably not true solutions on molecular level at room temperature.

Fig. S1 in the Supplementary material shows that temperature dependences of the fraction *p* determined from integrated intensities of various PEOx signals *a*, *b*, *c* are the same so confirming that *p*-fraction relates to PEOx units as a whole. From Figs. 7 and 8 it follows

that this holds also for P(EOx-*grad*-MOx) copolymers where temperature dependence of the fraction *p* determined for the signal *d* of methyl protons of hydrophilic MOx units is the same as dependences determined from integrated intensities of signals *b*, *c* of EOx units. In this respect behavior of P(EOx-*grad* -MOx) copolymers markedly differs from the behavior of random copolymers poly(*N*-isopropylmethacrylamide-*co*-acrylamide) (P(NIPMAm-*co*-AAm)) where virtually all hydrophilic AAm units were directly detected in high-resolution NMR spectra even at temperatures above the LCST transition [48]. Compared to P(NIPMAm-*co*-AAm) copolymers where in mesoglobules AAm sequences and surrounding IPMAm sequences are hydrated and mobile while most of IPMAm sequences are dehydrated and their mobility is strongly reduced, in P(EOx-*grad*-MOx) copolymers both EOx units and hydrophilic MOx units show the same temperature behavior. Though there are some indications that P(NIPMAm-*co*-AAm) copolymers need not be ideal random copolymers [48], the different behavior of the P(EOx-*grad*-MOx) and P(NIPMAm-*co*-AAm) copolymers might be in connection with somewhat distinct distribution of monomer units in the respective polymer chain.

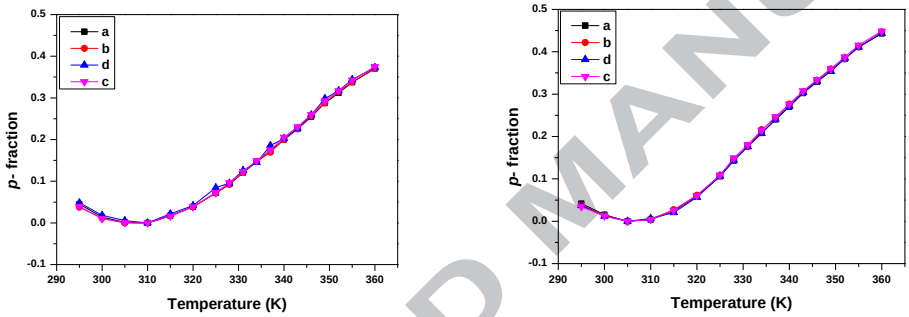

(a) (b)

Fig. 7. Temperature dependences of the fraction *p* (relative error ±2%) as determined for four signals of various proton types in D_2O solutions (*c* = 5 wt%) of copolymers P(EOx/MOx)(75/25)-H (a) and P(EOx/MOx)(53/47)-H (b) during gradual heating.

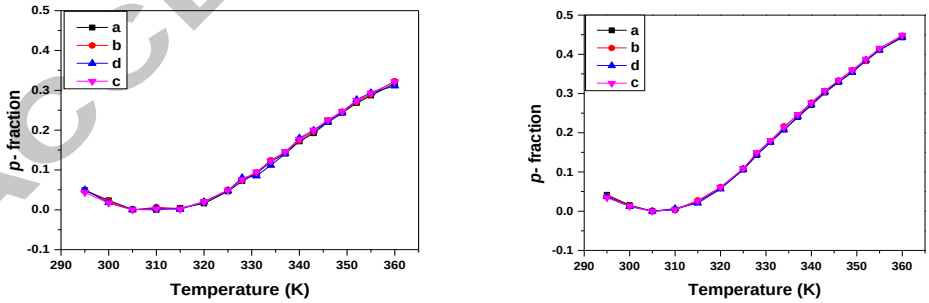

Fig. 8. Temperature dependences of the fraction *p* (relative error ±2 %) as determined in D_2O solutions (*c* = 5 wt%) during gradual heating for four copolymer signals of copolymers (P(EOx/MOx)(75/25)-L (a) and P(EOx/MOx)(52/48)-L (b).

Temperature dependences of the fraction *p* of D_2O solutions (c=5 wt %) of all investigated homopolymers and copolymers are shown in Fig. 9. For comparison, Fig. 9 also shows temperature dependence of the *p*-fraction for PNIPAm (M_n = 35480; *MWD* = 1.6) in

D_2O solution (c=5 wt %) (dashed line in Fig. 9) which is taken from ref. [49]. From Fig. 9 it follows that in comparison with PNIPAm where the phase transition is rather sharp (transition width 2 K) and complete (maximum value of the *p*-fraction, $p_{max} = 1$), for PEOx homopolymers the transition is broader (transition width approx. 8 K) and $p_{max} \approx 0.8$, i.e., around 20% of PEOx units retain high mobility and do not participate in the phase transition. Taking into account cooperative nature of the phase transition we assume that a part of these units corresponds to PEOx chains (oligomers) which are too short to exhibit the phase transition [27]. In addition, the LCST (defined as the temperature at $p_{max}/2$) of the PEOx-H with higher molecular weight (≈ 338 K) is substantially lower than for PEOx-L (≈ 352 K), i.e., in accord with what was reported in the literature that LCST of PEOx is related to the molecular weight [14,21]. Moreover, for PEOx-H the temperature where the phase transition starts (335 K) is in good correlation with temperature where the sharp increase of the size of particles (mode No.1) begins (cf. Fig. 4). Therefore both values of the *p*-fraction and DLS results indicate that PEOx homopolymers exhibit typical LCST type phase separation by formation of hydrophobic aggregates at temperatures above the critical temperature.

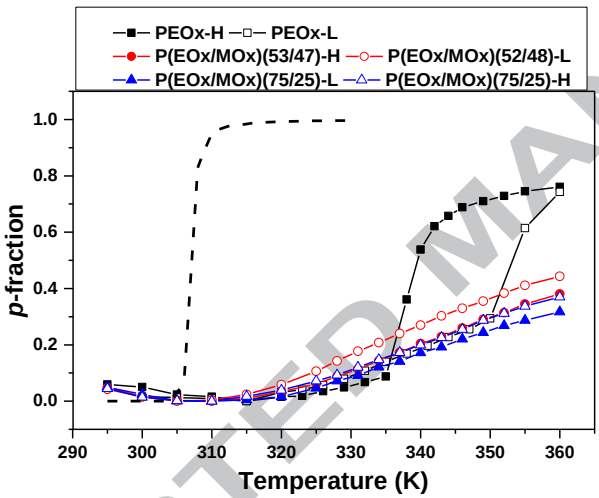

Fig. 9. Temperature dependences of the fraction *p* (relative error ±2%) of units with significantly reduced mobility in D_2O solutions (*c* = 5 wt%) of PEOx homopolymers and P(EOx-*grad*-MOx) copolymers during gradual heating. Dashed line shows temperature dependence of the *p*-fraction for D_2O solution (*c* = 5 wt%) of PNIPAm for comparison [49].

In contrast to PEOx homopolymers, the phase transition in D_2O solutions of P(EOx-*grad*-MOx) copolymers is very broad, *p*-values gradually increase from 315 K without any noticeable jump (transition width at least ≈ 45 K). In addition, values of p_{max} are rather low; they are in the range $p_{max} = 0.32 – 0.44$. At the same time temperature dependences of the *p*-fraction are almost independent of copolymer composition what is in contrast to D_2O solutions of P(NIPMAm-*co*-AAm) copolymers [48]. Very similar temperature dependences of the *p*-fraction were found for the solution of the P(EOx/MOx)(75/25)-H copolymer which is turbid at high temperatures and for solutions of other copolymers which do not show any turbidity (cf. Fig. 1). As shown in Fig. 9 temperature dependences of the *p*-fraction are for samples of larger molecular weight (P(EOx/MOx)(75/25)-H and P(EOx/MOx)(53/47)-H) just the same while pronounced differences exist in temperature dependences of hydrodynamic radius R_h for these two samples (cf. Fig. 4b). For samples of the lower molecular weight *p*-values are even somewhat larger for P(EOx/MOx)(52/48)-L in comparison with P(EOx/MOx)(75/25)-L while concerning temperature dependences of R_h values the situation is rather opposite (cf. Fig. 4b). Somewhat larger *p*-values found for P(EOx/MOx)(52/48)-L in

comparison with P(EOx/MOx)(75/25)-L can be partly in connection with the fact that the molecular weight of P(EOx/MOx)(52/48)-L sample is slightly higher (cf. Table 1). Our results indicate that there is no direct correlation between R_h values determined by DLS and values of the *p*-fraction determined from NMR spectra. NMR results show that copolymer segments with substantially reduced mobility exist also in copolymer solutions which are not cloudy at higher temperatures. Interestingly enough, a similar very broad transition and low p_{max}-values as shown for copolymer samples in Fig. 9 were recently reported for PEOx blocks in block terpolymers containing poly(ethylene oxide) (PEO), PEOx and poly(ε-caprolactone) (PCL) blocks [34].

Characterization of the reversibility of the phase transition after heating process was obtained directly by similar measurements during subsequent gradual cooling. Similarly to heating, behavior of all proton groups of the main chain and side chain is the same during cooling in all cases for respective homopolymer or copolymer sample as illustrated in Figs. S2 and S3 in the Supplementary material; for copolymers this holds also for MOx units (signal "d"). Fig. 10 shows temperature dependences of the fraction *p* in D_2O solutions (c=5 wt%) of the homopolymer PEOx-H (a) and copolymer P(EOx/MOx)(53/47)-H (b) during gradual heating and subsequent gradual cooling. Similar dependences as shown in Fig. 10a were obtained also for PEOx-L homopolymer, similar dependences as shown in Fig. 10b were obtained for other investigated copolymers. As we can see in the case of the PEOx homopolymer (Fig. 10a) the values of the *p*-fraction remain unchanged during gradual cooling in the whole range of temperatures of measurements which means that on local level the structures formed during heating are preserved during cooling. In other words, on molecular level the phase transition of PEOx homopolymer is irreversible, which is in contrast with the fact that the sample of PEOx-H in D_2O was transparent after pulling out from the magnet at 295 K. This is also at variance with macroscopic cloud point measurements on 0.5 wt% solutions [21]. NMR spectra show that reaching of the initial state after preceding heating and subsequent cooling is a very slow process (approx.1 month) but the initial state can be reached promptly by ultrasonic treatment for 15 min. On the other hand in copolymer samples changes in *p*-fraction, which are connected with phase separation, are reversible as illustrated on example of P(EOx/MOx)(53/47)-H in Fig. 10b. Here gradual cooling after previous heating results in a continuous decrease of the *p*-fraction with some hysteresis which was reported also for PNIPAm and other thermoresponsive polymer systems [50-53]. For

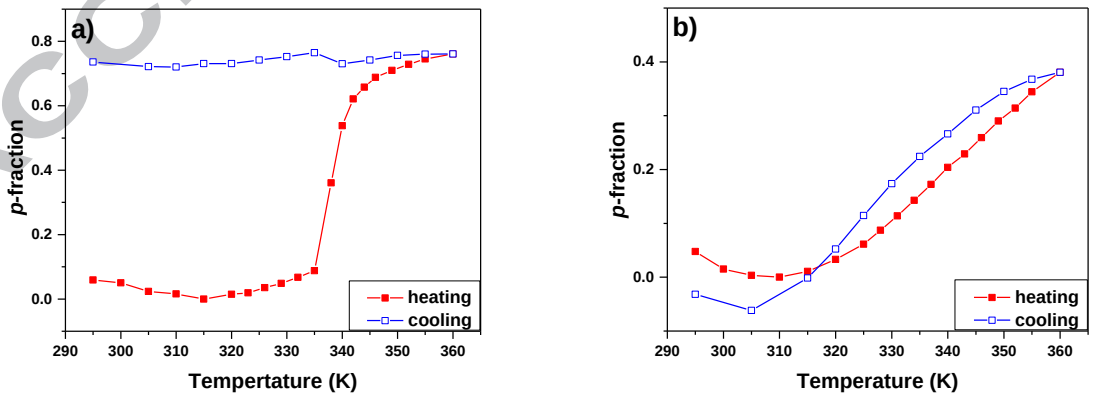

Fig. 10. Temperature dependences of the fraction *p* (relative error ±2%) of units with significantly reduced mobility in D_2O solutions (*c* = 5 wt%) of PEOx-H homopolymer (a) and P(EOx/MOx)(53/47)-H copolymer (b) during gradual heating and subsequent gradual cooling.

PNIPAm aqueous solutions the hysteresis was attributed to polymer-polymer hydrogen bonding in the globular-like structures. However, POx cannot form polymer-polymer hydrogen bonds due to the absence of hydrogen in the amide group. We assume that in this case water molecules ("bound" water), hydrogen bonded to carbonyl groups, can act as intermediaries of interactions between polymer segments in similar way as suggested for poly(*N*-vinylcaprolactam) (PVCL) solutions [52].

From studies based on cloud point measurements it follows that LCST of PEOx homopolymers and P(EOx-*co*-2-*n*-propyl-2-oxazoline) copolymers in aqueous solutions depends on polymer concentration [21]. For this reason we studied solutions of the PEOx-H homopolymer and P(EOx/MOx)(53/47)-H copolymer with three different polymer concentrations c = 0.5, 5 and 20 wt%. Similarly to samples with 5 wt% concentration also in samples with 0.5 and 20 wt% concentrations all polymer proton types show virtually the same temperature dependences of the p-fraction (cf. Figs. S4 and S5 in the Supplementary material). Fig. 11 shows temperature dependences of the fraction p of units with significantly reduced mobility in D_2O solutions with polymer concentrations c = 0.5, 5 and 20 wt% for the homopolymer PEOx-H (a) and copolymer P(EOx/MOx)(53/47)-H (b) recorded during gradual heating . From Fig. 11a we clearly see that for the PEOx-H homopolymer the character of these dependences for c = 0.5 wt% and c = 5 wt% is very similar but for 0.5 wt% concentration the LCST (≈ 344 K at $p_{max}/2$) is approx. 5 K higher and p_{max} = 0.7 is slightly lower. Similar behavior was previously observed for PVCL [52] which is another thermoresponsive polymer of type I where the LCST decreases with increasing molecular weight [4]. In contrast, the solution with c = 20 wt% concentration shows completely different character of the transition (cf. Fig. 11a). Starting value of the p-fraction at 295 K (0.28) is much higher than p-values obtained for lower concentrations (≈ 0.07) and from 310 K p-fraction is gradually increasing to 0.35 at 335 K; next it notably decreases to reach the minimum (p = 0) at 345 K and then again rises to p = 0.4. Decreasing values of the p-fraction in the temperature range 335-345 K show increasing mobility of polymer segments at these temperatures. PEOx-H solution with concentration c = 20 wt% is very viscous (jelly-like) at room temperature. We assume that at temperatures 335-345 the respective physical network structure is breaking and reorganizing, and this process is confirmed by broad and relatively strong endotherm detected around ≈ 348 K in DSC measurements (Fig. S6 in the Supplementary material). Similar behavior of 20 wt% solution was also obtained for second homopolymer PEOx-L where minimum of the p-fraction as well as endotherm in DSC measurements appear at 355 K, i.e., at somewhat higher temperature (cf. Figs. S7 and S8 in the Supplementary material). Temperature dependences of the p-fraction during gradual heating of the P(EOx/MOx)(53/47)-H copolymer in D_2O solutions with polymer concentrations 0.5, 5 and 20 wt% are presented in Fig. 11b. From this figure it follows that these dependences are very similar in all cases. Nevertheless, some small differences are also visible: minimum of the p-fraction appears at 315 K, 310 K and 305 K for 0.5, 5 and 20 wt% concentration, respectively; p_{max} values slightly increase with concentration (0.35 for 0.5 wt%; 0.38 for 5 wt% and 0.39 for 20 wt%) and finally established LCST values (temperatures at $p_{max}/2$ which are ≈ 340 K, 337 K and 335 K for c = 0.5 wt%, 5 wt% and 20 wt%, respectively), somewhat decrease with increasing concentration.

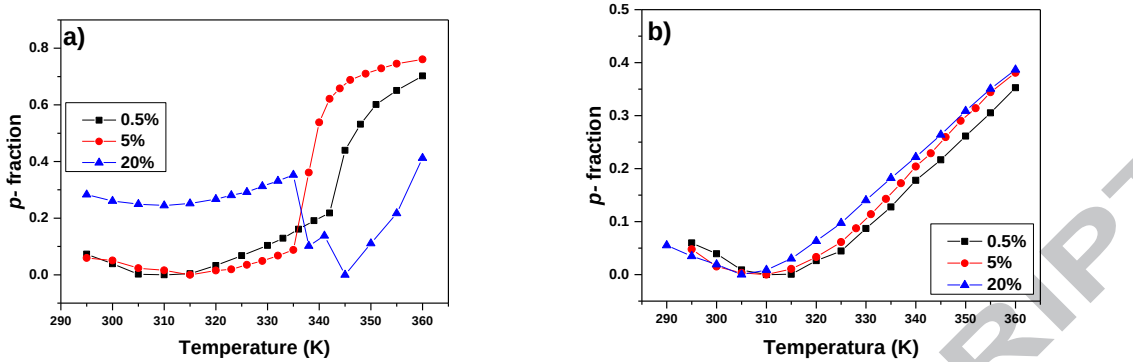

Fig. 11. Temperature dependences of the fraction *p* (relative error ±2%) of PEOx-H homopolymer (a) and P(EOx/MOx)(53/47)-H copolymer (b) in D_2O solutions with three polymer concentrations (*c* = 0.5; 5; 20 wt%) during gradual heating.

3.3. 2D ^{1}H-^{1}H NOESY NMR spectra

To obtain information on spatial proximity between proton groups of EOx and MOx units, on D_2O solutions (*c* = 5 wt%) of P(EOx/MOx)(75/25)-L and P(EOx/MOx)(53/47)-H copolymers we measured also 2D ^{1}H-^{1}H NOESY NMR spectra at three temperatures: at 295 K (below the transition), 340 K (in the middle of the transition) and 360 K (above the transition) (cf. Fig. 9). We assumed to use the fact that for these copolymers even at 360 K the values of the *p*-fraction are relatively low (p_{max} = 0.32 and 0.37, respectively) and therefore a major part of these copolymers is directly detected in high-resolution NMR spectra at this temperature. NOESY spectra of the P(EOx/MOx)(75/25)-L sample are shown in Fig. 12. In NOESY spectrum measured at 295 K (Fig. 12a) we detected not only cross-peaks between various proton groups of EOx or MOx units, but also weaker cross-peaks between side chain CH_3 or CH_2 protons of EOx units (signals at 1.05 ppm and 2.35 ppm, respectively) and CH_3 protons of MOx units (signal at 2.1 ppm). At 295 K in the range of mixing times 100-600 ms intensities of all these cross-peaks roughly linearly increased with the mixing time. In Fig. 12a the cross-peaks between EOx and MOx protons are encircled. The presence of all these cross-peaks implies that distances between respective protons are smaller than 0.5 nm. EOx and MOx units which are in close proximity can be both from the same chain of the copolymer, assuming random-coil conformation of copolymer chains at room temperature, and from different copolymer chains. At 340 K the cross-peaks between EOx and MOx protons disappeared and cross-peaks between various proton groups of EOx or MOx units are weaker (Fig. 12b). In the NOESY spectrum measured at 360 K (Fig. 12c) all cross-peaks disappeared (only the residual cross-peak between side chain CH_3 and CH_2 protons of EOx units remained) in spite of the fact that at this temperature 68% of copolymer segments (cf. Fig. 9) are directly detected in NMR spectra.

For the quantitative characterization of the intensities of the cross-peaks we used integrated intensities of signals of EOx and MOx proton groups in 1D slices extracted from the signal of CH_3 protons of EOx units at 1.05 ppm of the NOESY spectra. These 1D slices are shown in the right part of the Fig. 12 together with slices extracted from the signal of NCH_2 protons of both EOx and MOx units. Temperature dependences of the absolute integrated intensities in slices extracted from the signal of CH_3 protons of EOx units measured with mixing time 600 ms for D_2O solution (*c* = 5 wt%) of the P(EOx/MOx)(75/25)-L copolymer are shown in Fig. 13. Very similar dependences were obtained for the respective integrated intensities in 1D slices extracted from NOESY spectra of this sample measured

with mixing time 100 ms and 200 ms, as well as for D_2O solution (c = 5 wt%) of the copolymer P(EOx/MOx)(53/47)-H measured with mixing time 200 ms. Intensity of these cross-peaks in the middle of the transition region (at 340 K) drastically decreases and at higher temperature (360 K) virtually no cross-peaks were detected. At the same time it follows from Fig. 13 that at 340 K and 360 K also intensity of the cross-peak between ethyl CH_3 and CH_2 protons of EOx units is markedly reduced. The distance between these protons in the ethyl group cannot change with temperature and therefore there must be another source of this reduction which is not determined by proton distances. It is well known that magnitude of the NOE depends also on the motional correlation time τ_c and that NOE = 0 when $\omega_0\tau_c \approx 1$ where ω_0 is the resonance frequency [54]. It is also well known that spin-lattice relaxation time T_1 as a function of correlation time τ_c shows a minimum when $\omega_0\tau_c \approx 1$. In this connection we measured ^{1}H spin-lattice relaxation times of polymer protons in D_2O solution (c = 5 wt%) of the P(EOx/MOx)(75/25)-L copolymer at several temperatures; in all cases the relaxation curves were monoexponential (Table 2). From Table 2 it follows that with exception of ethyl CH_3 protons of EOx units, for all other proton groups (NCH_2, ethyl CH_2 of EOx units, CH_3 of MOx units) in the transition region T_1 values decrease with increasing temperature (for CH_3 and CH_2 protons of EOx units a further small reduction in T_1 values was observed when the sample was kept for 14 hrs at 360 K). These results imply that in the transition region with increasing temperature we move towards T_1 minimum where NOESY is ineffective. This is combined with the fact that in about one third of polymer segments their mobility is reduced to such an extent that they escape detection in high-resolution NMR spectra. We assume that similarly to P(NIPMAm-*co*-AAm) random copolymers [48], there is dynamic heterogeneity of polymer chains in structures formed by P(EOx-*grad* -MOx) copolymers. These chains probably contain both parts where copolymer segments are hydrated and relatively mobile, and parts where polymer segments are dehydrated and their mobility is strongly reduced.

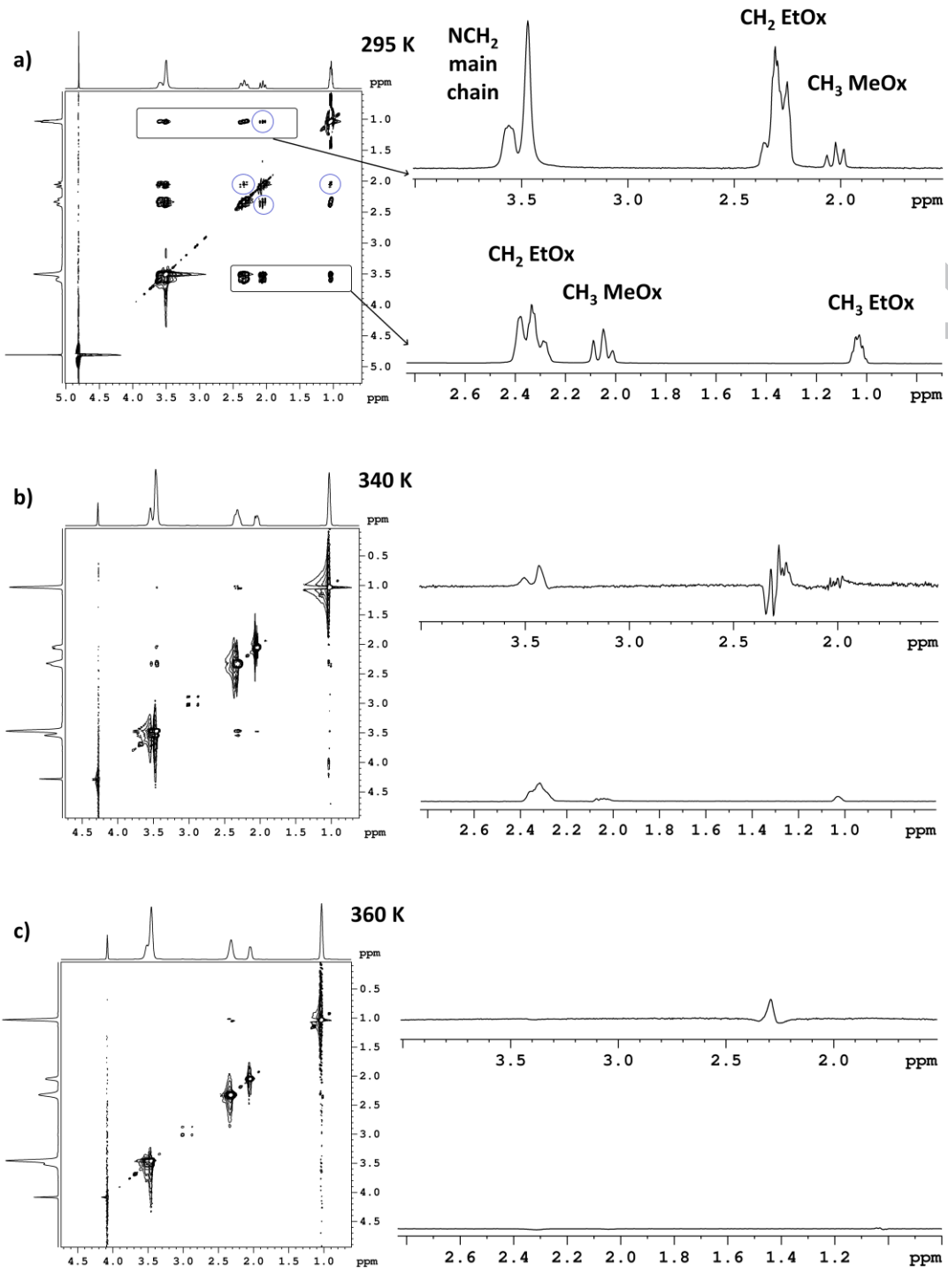

Fig. 12. 2D NOESY spectra of the P(EOx/MOx)(75/25)-L copolymer in D_2O solution (*c* = 5wt%) measured at three temperatures with mixing time 600 ms. On the right there are 1D slice spectra extracted from the signal at 1.05 ppm of CH_3 protons of EOx units (in Fig.6 signal „c“) (at the top) and from the signal at 3.55 ppm of NCH_2 protons of both EOx and MOx units (in Fig. 6 signal „a“) (below).

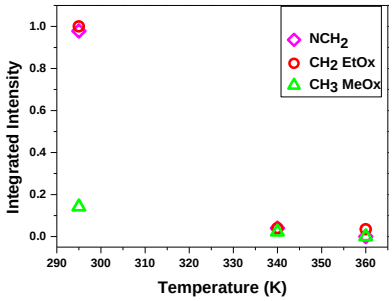

Fig. 13. Temperature dependences of integrated intensities (estimated relative error ± 3%) of various signals in 1D slices extracted from the signal of CH_3 protons of EOx units (at 1.05 ppm) of the NOESY NMR spectra of D_2O solution (c = 5wt%) of P(EOx/MOx)(75/25)-L copolymer.

Table 2
^{1}H spin-lattice relaxation times T_1 of proton groups of the P(EOx/MOx) (75/25)-L copolymer in D_2O solution (c = 5 wt%) at several temperatures.

Temperature (K)	T_1 (s)[a]			
	NCH_2 (EOx + MOx)	CH_2 (EOx)	CH_3 (MOx)	CH_3 (EOx)
295	0.86	1.37	1.93	2.11
340	0.54	1.30	1.18	2.77
360	0.49	1.26	1.13	2.76
360 (14h)[b]	0.47	1.17	1.12	2.42

[a]The relative error ±5%.
[b]The sample kept for 14 hrs at 360 K.

3.4. Spin-spin relaxation times T_2 of water (HDO) molecules

Studies on aqueous solutions of various thermoresponsive homopolymers and copolymers have shown that valuable information on behavior of water during LCST type phase transition can be obtained from measurements of spin-spin relaxation times T_2 of water (HDO protons or D_2O deuterons) [27,30,34,48,49,52]. Fig. 14a shows temperature dependence of ^{1}H spin-spin relaxation time T_2 of HDO in D_2O solution (c = 5 wt%) of the PEOx-L homopolymer. Measurements were done at temperatures based on the temperature dependence of the p-fraction (cf. Fig. 9). At all temperatures there was a single line of HDO in ^{1}H NMR spectrum and this holds for all investigated samples. As shown for PEOx-L solution in Fig. S9 in the Supplementary material while at room temperature and other temperatures T < 335 K the T_2 relaxation curves were monoexponential, at $T \geq$ 335 K, i.e., in the transition region and above the transition, the relaxation curves were non-exponential and two T_2 components were necessary to fit well experimental relaxation curves. These results show the existence of two type of water at temperatures ≥ 335 K. First type is "free water" with longer relaxation times, which are similar to T_2 values at lower temperatures (T_2 = 3-4 s), which corresponds to HDO molecules in solution. Second type is "bound" water, with T_2 values which are 2 orders of magnitude shorter (T_2 = 42 ms at 335 K, T_2 = 21 ms at 360 K), which corresponds to HDO molecules bound (confined) inside the collapsed globular

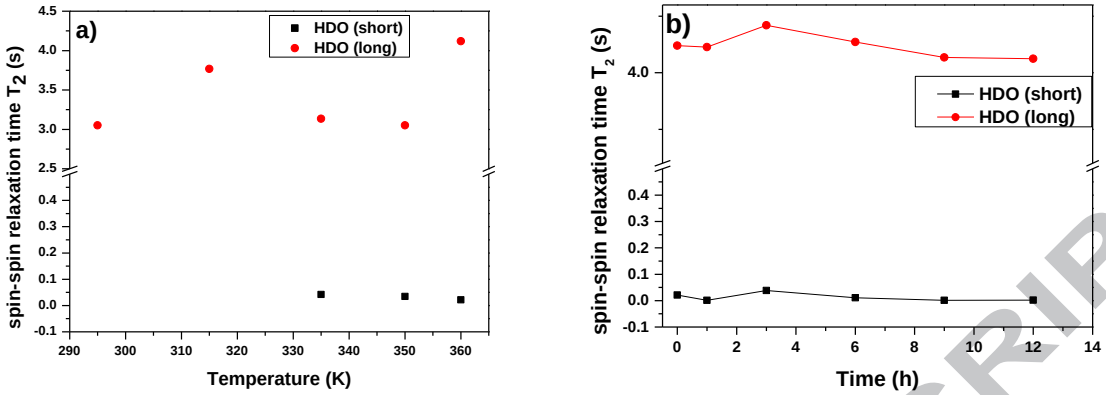

Fig. 14. Temperature dependence (a) and time dependence at 360 K (b) of ^{1}H spin-spin relaxation times T_2 (relative error ± 5%) of HDO in D_2O solution (c = 5 wt%) of the PEOx-L homopolymer.

structures. From intensities of the two T_2 components it follows that at 360 K the content of the "bound" water is around 10%. Fig. 14b shows time dependences of two T_2 components measured in the D_2O solution of the PEOx-L at 360 K. From Fig. 14b it follows that T_2 values are virtually constant for both types of water molecules showing that arrangement with "free" and "bound" water is stable at least for 12 hrs. Similar behavior as shown in Fig. 14 was observed also with PEOx-H homopolymer and P(EOx-*grad* -MOx) copolymers; results are depicted in Figures S10-S13 in the Supplementary material. Also in D_2O solutions of P(EOx-*grad*-MOx) copolymers T_2 measurements revealed existence of two types of water, "free" and "bound", at temperatures 340 K and 360 K, i.e., in the transition region. Similarly to PEOx homopolymers, the amount of the "bound"water in solutions of P(EOx-*grad*-MOx) copolymers at 360 K was ~10% and two types of water were stable for at least 12-17 hrs. Temperature and time dependences of T_2 relaxation times, as well as T_2 values at 360 K, were very similar for solution of the P(EOx/MOx)(75/25)-H copolymer where at 360 K the hydrodynamic radius of the particles is 12 nm and solutions of other copolymers where the hydrodynamic radius of the particles is 3-4 nm (cf. Fig. 4). Similar behavior as shown in Fig. 14 and Figs. S10-S13 in the Supplementary material was recently found also for aqueous solutions of block terpolymers containing PEO, PEOx and PCL blocks [34]. In all these systems containing thermoresponsive PEOx segments the existence of two T_2 components shows that the exchange between „bound" and „free" water molecules must be slow regarding T_2 values. In another words the residence time of the „bound" HDO must be longer than 0.1 s. The existence of the „bound" water above the LCST phase transition was evidenced also for other thermoresponsive homopolymers and copolymers (PNIPAm, PNIPMAm, PVME, PVCL, P(NIPMAm-*co*-AAm), PEO-*b*-PNIPAm, PEO-*b*-$(PNIPAm)_2$) [27,48,49,52]. However, for these systems T_2 relaxation curves were monoexponential even above the transition region and for concentrations $c \approx 5$ wt% and temperatures above the transition the „bound" water was demonstrated by reduced T_2 values of HDO. Therefore in these systems there is a fast exchange between „bound" and „free" sites and the measured relaxation rates T_2^{-1} are then given as a weighted average of the relaxation rates of bound and free HDO [55,56]. It was shown for PVME, PNIPMAm and PVCL solutions that a residence time of the bound HDO is ~1 ms [27,52]. Reason for two orders of magnitude difference in residence time of the „bound" water in solutions of PEOx homopolymers and copolymers on the one hand and for other thermoresponsive polymers on the other hand remains unclear so far.

4. Conclusions

In the present study we report on temperature behavior of thermoresponsive PEOx homopolymers and P(EOx-*grad*-MOx) copolymers in D_2O solutions as investigated by ^1H NMR methods which were combined with DLS and in some cases with DSC measurements. Measurements of ^1H NMR spectra, 2D ^1H-^1H NOESY spectra and ^1H spin-spin relaxation time T_2 were used for the characterization of structural changes on molecular level and behavior of water molecules during the temperature-induced phase transition. In comparison with other thermoresponsive polymers (PNIPAm, PNIPMAm, PVME, PVCL) some important differences were revealed for PEOx homopolymers and copolymers.

Two PEOx homopolymers with different molecular weight and four P(EOx-*grad* -MOx) copolymers (with two molar ratios of EOx and MOx units, 3/1 and 1/1, and different molecular weight within each pair) were studied. Though in the transition region we observed at similar temperatures an increase of both intensity of scattered light and hydrodynamic radius of respective particles, as determined by DLS, and fraction *p* of units with significantly reduced mobility, as determined from NMR spectra, there is no correlation between particle size and values of the *p*-fraction. Temperature dependences of the *p*-fraction show that for D_2O solutions of PEOx homopolymers the phase transition is relatively sharp and transition temperatures substantially depend on molecular weight and concentration of the solution. An anomalous dependence of the *p*-fraction observed for PEOx solution of highest concentration (c = 20 wt%) is presumably in connection with existence of the physical network at room temperature; the network is disrupted around 350 K as evidenced by NMR and DSC measurements. From temperature dependences of the *p*-fraction measured during gradual cooling after preceding gradual heating it follows that for PEOx homopolymers local structures formed during heating are preserved during cooling. This means that on the molecular level the phase transition of PEOx homopolymers is irreversible and reaching of the initial state is a very slow process. Phase transition in solutions of P(EOx-*grad*-MOx) copolymers as revealed by NMR exists irrespective the solution is turbid or nonturbid at higher temperatures and the temperature dependences of the *p*-fraction are the same for EOx and hydrophilic MOx units. In contrast to PEOx homopolymers, phase transition in solutions of P(EOx-co-MOx) copolymers is very broad (~45 K) so that the term “transition” even seems to be somewhat inappropriate. Temperature dependences of the *p*-fraction are for P(EOx-*grad* -MOx) copolymers almost independent of the content of MOx units and molecular weight, and only slightly dependent on concentration of the solution. At the same time the maximum values of the *p*-fraction are for copolymers (p_{max} = 0.32-0.44) significantly lower in comparison with PEOx homopolymers ($p_{max} \approx 0.8$). For P(EOx-*grad* -MOx) copolymers the phase transition process is reversible and only some hysteresis was observed during gradual cooling after previous gradual heating.

2D ^1H-^1H NOESY NMR spectra show that in D_2O solutions (c = 5 wt%) of P(EOx-*grad* -MOx) random copolymers some EOx and MOx units are in close contact at room temperature. With increasing temperature the respective cross-peaks in NOESY spectra disappear though at 360 K there are still ~60-68% of copolymer segments that are directly detected in 1D ^1H NMR spectra. From the fact that at 340 and 360 K also intensity of the cross-peak between ethyl CH_3 and CH_2 protons of EOx units is markedly reduced and from measurements of spin-lattice relaxation times T_1 of copolymer protons it follows that reduced intensities of cross-peaks in NOESY spectra at elevated temperatures are mainly due to the changed mobility of copolymer segments including those which remain hydrated and therefore are directly detected in NMR spectra.

From measurements of ^1H spin-spin relaxation times T_2 of HDO, a very similar behavior of the water molecules in homopolymer and copolymer solutions was observed. In

all investigated solutions two types of water, „free“ and „bound“ with long and very short T_2 values, respectively, were detected at temperatures in the transition region and above the transition. The content of the “bound” water is around 10% at 360 K. The two types of water remain stable for at least 12 hrs at 360 K and no release of the “bound” water was observed during this time. The existence of two T_2 components shows that the exchange between „bound“ and „free“ water molecules must be slow regarding T_2 values (residence time of the „bound“ HDO $\geq$ 0.1 s). This behavior is in contrast to behavior of other thermoresponsive homopolymers and copolymers where the exchange between „bound“ and „free“ water is fast (residence time of the bound HDO is ~1 ms).

Acknowledgment

Support by the Czech Science Foundation (Project 15-13853S) is gratefully acknowledged. R.K. acknowledges the Charles University, Faculty of Science for providing the opportunity to pursue his PhD studies. Authors thank J. Kovářová for DSC measurements.

Appendix A. Supplementary material

Supplementary data associated with this article can be found, in the online version, at

References

[1] F. Liu, M.W. Urban, Recent advances and challenges in designing stimuli-responsive polymers, Prog. Polym. Sci. 35 (2010) 3-23.
[2] S. Petrova, E. Jäger, R. Konefał, A. Jäger, C.G. Venturini, J. Spěváček, E. Pavlova, P. Štěpánek, Novel poly(ethylene oxide monomethyl ether)-b-poly(ε-caprolactone) diblock copolymers containing a pH-acid labile ketal group as a block linkage, Polym. Chem. 5 (2014) 3884-3893.
[3] X. Han, X. Zhang, H. Zhu, Q. Yin, H. Liu, Y. Hu, Effect of composition of PDMAEMA b-PAA block copolymers on their pH- and temperature-responsive behaviors, Langmuir 29 (2013) 1024-1034.
[4] V.O. Aseyev, H. Tenhu, F.M. Winnik, Temperature dependence of the colloidal stability of neutral amphiphilic polymers in water, Adv. Polym. Sci. 196 (2006) 1-85.
[5] M.A. Ward, T.K. Georgiou, Thermoresponsive polymers for biomedical applications, Polymers 3 (2011) 1215-1242.
[6] N. Rapoport, Physical stimuli-responsive polymeric micelles for anti-cancer drug delivery, Prog. Polym. Sci. 32 (2007) 962-990.
[7] M.C. Branco, J.P. Schneider, Self-assembling materials for therapeutic delivery, Acta Biomater. 5 (2009) 817-831.
[8] A. Harada, K. Kataoka, Novel polyion complex micelles entrapping enzyme molecules in the core: Preparation of narrowly-distributed micelles from lysozyme and poly(ethylene glycol)-poly(aspartic acid) block copolymer in aqueous medium, Macromolecules 31 (1998) 288-294.
[9] P.-F. Cao, J.D. Mangadlao, R.C. Advincula, Stimuli-responsive polymers and their potential applications in oil-gas industry, Polym. Rev. 55 (2015) 706-733.
[10] K. Sakai, E.G. Smith, G.B. Webber, M. Baker, E.J. Wanless, V. Bütün, S.P. Armes, S. Biggs, Characterizing the pH-responsive behavior of thin films of diblock copolymer micelles

at the silica/aqueous solution interface, Langmuir 22 (2006) 8435-8442.
[11] K. Nagase, T. Okano, Thermoresponsive-polymer-based materials for temperature-modulated bioanalysis and bioseparations, J. Mater. Chem. B. 4 (2016) 6381-6397.
[12] S. Fujishige, K. Kubota, I. Ando, Phase transition of aqueous solutions of poly(N-isopropylacrylamide) and poly(N-isopropylmethacrylamide), J. Phys. Chem. 93 (1989) 3311-3313.
[13] A. Halperin, M. Kroeger, F.M. Winnik, Poly(N-isopropylacrylamide) phase diagrams: fifty years of research, Angew. Chem. - Int. Ed. 54 (2015) 15342-15367.
[14] C. Weber, R. Hoogenboom, U.S. Schubert, Temperature responsive bio-compatible polymers based on poly(ethylene oxide) and poly(2-oxazoline)s, Prog. Polym. Sci. 37 (2012) 686-714.
[15] V.R. De La Rosa, Poly(2-oxazoline)s as materials for biomedical applications, J. Mater. Sci. Mater. Med. 25 (2014) 1211-1225.
[16] O. Sedlacek, B.D. Monnery, S.K. Filippov, R. Hoogenboom, M. Hruby, Poly(2-oxazoline)s - Are they more advantageous for biomedical applications than other polymers?, Macromol. Rapid Commun. 33 (2012) 1648-1662.
[17] T.T. Chiu, B.P. Thill, W.J. Fairchok, Poly(2-ethyl-2-oxazoline): a new water- and organic-soluble adhesive, Adv. Chem. 213 (1986) 425-433.
[18] P. Lin, C. Clash, E.M. Pearce, T.K. Kwei, M.A. Aponte, Solubility and miscibility of poly(ethyl oxazoline), J. Polym. Sci. Part B Polym. Phys. 26 (1988) 603-619.
[19] D. Christova, R. Velichkova, W. Loos, E.J. Goethals, F. Du Prez, New thermo-responsive polymer materials based on poly(2-ethyl-2-oxazoline) segments, Polymer 44 (2003) 2255-2261.
[20] A. Dworak, B. Trzebicka, A. Kowalczuk, C. Tsvetanov, S. Rangelov, Polyoxazolines — mechanism of synthesis and solution properties, Polimery 59 (2014) 88-94.
[21] R. Hoogenboom, H.M.L. Thijs, M.J.H.C. Jochems, B.M. van Lankvelt, M.W.M. Fijten, U.S. Schubert, Tuning the LCST of poly(2-oxazoline)s by varying composition and molecular weight: alternatives to poly(N-isopropylacrylamide)?, Chem. Commun. (2008) 5758-5760.
[22] C. Diab, Y. Akiyama, K. Kataoka, F.M. Winnik, Microcalorimetric study of the temperature-induced phase separation in aqueous solutions of poly(2-isopropyl-2-oxazolines), Macromolecules 37 (2004) 2556-2562.
[23] M.M. Bloksma, C. Weber, I.Y. Perevyazko, A. Kuse, A. Baumgärtel, A. Vollrath, R. Hoogenboom, U.S. Schubert, Poly(2-cyclopropyl-2-oxazoline): from rate acceleration by cyclopropyl to thermoresponsive properties, Macromolecules. 44 (2011) 4057-4064.
[24] A. Bogomolova, S.K. Filippov, L. Starovoytova, B. Angelov, P. Konarev, O. Sedlacek, M. Hruby, P. Stepanek, Study of complex thermosensitive amphiphilic polyoxazolines and their interaction with ionic surfactants. Are hydrophobic, thermosensitive, and hydrophilic moieties equally important?, J. Phys. Chem. B. 118 (2014) 4940-4950.
[25] M. Hruby, S.K. Filippov, J. Panek, M. Novakova, H. Mackova, J. Kucka, D. Vetvicka, K. Ulbrich, Polyoxazoline thermoresponsive micelles as radionuclide delivery systems, Macromol. Biosci. 10 (2010) 916-924.
[26] P. Tatar Güner, A.L. Demirel, Effect of anions on the cloud point temperature of aqueous poly(2-ethyl-2-oxazoline) solutions, J. Phys. Chem. B. 116 (2012) 14510-14514.
[27] J. Spěváček, NMR investigations of phase transition in aqueous polymer solutions and gels. Curr. Opin. Colloid Interface Sci. 14 (2009) 184-191.
[28] F. Zeng, Z. Tong, H. Feng, N.m.r.investigation of phase separation in poly(N-isopropyl acrylamide)/water solutions, Polymer 38 (1997) 5539-5544.
[29] J. Spěváček, L. Hanyková, M. Ilavský, Phase separation in poly(N,N-diethylacrylamide)/D_2O solutions and physical gels as studied by ^1H NMR spectroscopy, Macromol. Chem. Phys. 202 (2001) 1122-1129.

[30] M. Rusu, S. Wohlrab, D. Kuckling, H. Möhwald, M. Schönhoff, Coil-to-globule transition of PNIPAM graft copolymers with charged side chains: a 1H and 2H NMR and spin relaxation study, Macromolecules. 39 (2006) 7358-7363.
[31] R. Plummer, D.J.T. Hill, A.K. Whittaker, Solution properties of star and linear poly(*N*-isopropylacrylamide), Macromolecules 39 (2006) 8379-8388.
[32] P.V. Yushmanov, I. Furó, I. Illiopoulos,Kinetics of demixing and remixing transition in aqueous solutions of poly(*N*-isopropylacrylamide): a temperature- jump ^{1}H NMR study. Macromol. Chem. Phys. 207 (2006) 1972-1979.
[33] W. Hiller, N. Engelhardt, A.L. Kampmann, P. Degen, R. Weberskirch, Micellization and mobility of amphiphilic poly(2-oxazoline) based block copolymers characterized by ^{1}H NMR spectroscopy, Macromolecules 48 (2015) 4032-4045.
[34] R. Konefał, J. Spěváček, E. Jäger, S. Petrova, Thermoresponsive behaviour of terpolymers containing poly(ethylene oxide), poly(2-ethyl-2-oxazoline) and poly(ε-caprolactone) blocks in aqueous solutions: an NMR study, Colloid Polym. Sci. 294 (2016) 1717-1726.
[35] M. Bauer, S. Schroeder, L. Tauhardt, K. Kempe, U.S. Schubert, D. Fischer, In vitro hemocompatibility and cytotoxicity study of poly(2-methyl-2- oxazoline) for biomedical applications, J. Polym. Sci. Part A Polym. Chem. 51 (2013) 1816-1821.
[36] M. Bauer, C. Lautenschlaeger, K. Kempe, L. Tauhardt, U.S. Schubert, D. Fischer, Poly(2-ethyl-2-oxazoline) as alternative for the stealth polymer poly(ethylene glycol): comparison of in vitro cytotoxicity and hemocompatibility, Macromol. Biosci. 12 (2012) 986-998.
[37] W.G. Lee, S.W. Kang, Highly selective polymer electrolyte membranes consisting of poly(2-ethyl-2-oxazoline) and Cu(NO_3)$_2$ for SF_6 separation, Sci. Rep. 6 (2016) 20430.
[38] S. Nam, J. Seo, S. Woo, W.H. Kim, H. Kim, D.D.C. Bradley, Y. Kim, Inverted polymer fullerene solar cells exceeding 10% efficiency with poly(2-ethyl-2-oxazoline) nanodots on electron-collecting buffer layers, Nat. Commun. 6 (2015) 1-9.
[39] R. Hoogenboom, H. Schlaad, Bioinspired poly(2-oxazoline)s, Polymers 3 (2011) 467-488.
[40] W. Chen, Y. Zhu, Y. Yu, L. Xu, G. Zhang, Z. He, Low cost and solution processed interfacial layer based on poly(2-ethyl-2-oxazoline) nanodots for inverted perovskite solar cells, Chem. Mater. 28 (2016) 4879-4883.
[41] R. Hoogenboom, Poly(2-oxazoline)s: a polymer class with numerous potential applications, Angew. Chem. - Int. Ed. 48 (2009) 7978-7994.
[42] R. Luxenhofer, Y. Han, A. Schulz, J. Tong, Z. He, A.V Kabanov, R. Jordan, Poly(2-oxazoline)s as polymer therapeutics, Macromol. Rapid Commun. 33 (2012) 1613–1631.
[43] C. Diehl, H. Schlaad, Polyoxazoline-based crystalline microspheres for carbohydrate-protein recognition. *Chem. Eur. J.* **2009**, *15*, 11469-11472.
[44] R. Hoogenboom, M.W.M. Fijten, S. Wijnans, A.M.J. van den Berg, H.M.L. Thijs, U.S. Schubert, High-throughput synthesis and screening of a library of random and gradient copoly(2-oxazoline)s, J. Comb. Chem. 8 (2006) 145-148.
[45] T.C. Farrar, E.D. Becker, Pulse and Fourier Transform NMR, Academic Press, New York, 1971, pp. 27-29.
[46] J. Jakeš, Regularized positive exponential sum (REPES) program - a way of inverting Laplace transform data obtained by dynamic light scattering, Collect. Czech. Chem. Commun. 60 (1995), 1781-1797.
[47] X. Ye, J. Yang, J. Ambreen, Scaling laws between the hydrodynamic parameters and molecular weight of linear poly(2-ethyl-2-oxazoline), RSC Adv. 3 (2013) 15108-15113.
[48] H. Kouřilová, J. Šťastná, L. Hanyková, Z. Sedláková, J. Spěváček, ^{1}H NMR study of temperature-induced phase separation in solutions of poly(*N*-isopropylmethacrylamide-*co*-

acrylamide) copolymers, Eur. Polym. J. 46 (2010) 1299-1306.
[49] J. Spěváček, R. Konefał, J. Dybal, E. Čadová, J. Kovářová, Thermoresponsive behavior of block copolymers of PEO and PNIPAm with different architecture in aqueous solutions: a study by NMR, FTIR, DSC and quantum-chemical calculations, Eur. Polym. J. 94 (2017) 471-483.
[50] Y. Maeda, T. Higuchi, I. Ikeda, Change in hydration state during the coil-globule transition of aqueous solutions of poly(*N*-isopropylacrylamide) as evidenced by FTIR spectroscopy, Langmuir 16 (2000) 7503-7509.
[51] H. Cheng, L. Shen, C. Wu, LLS and FTIR studies on the hysteresis in association and dissociation of poly(*N*-isopropylacrylamide) chains in water, Macromolecules 39 (2006) 2325-2329.
[52] J. Spěváček, J. Dybal, L. Starovoytova, A. Zhigunov, Z. Sedláková, Temperature-induced phase separation and hydration in poly(*N*-vinylcaprolactam) aqueous solutions: a study by NMR and IR spectroscopy, SAXS, and quantum-chemical calculations, Soft Matter 8 (2012) 6110-6119.
[53] A. Saeed, D.M.R. Georget, A.G. Mayes, Solution thermal properties of a family of thermo-responsive *N*-isopropyl acrylamide-*co*-*N*-hydroxymethyl acrylamide copolymers – aspects intrinsic to the polymers, React. Funct. Polym. 72 (2012) 77-82.
[54] D. Neuhaus, M.P. Williamson, The Nuclear Overhauser Effect in Structural and Conformational Analysis, VCH Publishers, Inc., New York, 1989, Ch. 2 and 3.
[55] J. Spěváček, L. Hanyková, ^{1}H NMR study on the hydration during temperature-induced phase separation in concentrated poly(vinyl methyl ether)/D_2O solutions, Macromolecules 38 (2005) 9187-9191.
[56] B. Sierra-Martín, M.S. Romero-Cano, T. Cosgrove, B. Vincent, A. Fernández-Barbero, Solvent relaxation of swelling PNIPAM microgels by NMR, Collloids Surf. A 270-271(2005) 296-300.

Supplementary material

Thermoresponsive poly(2-oxazoline) homopolymers and copolymers in aqueous solutions studied by NMR spectroscopy and dynamic light scattering

Rafał Konefał, Jiří Spěváček,* Peter Černoch

Institute of Macromolecular Chemistry, Academy of Sciences of the Czech Republic, Heyrovsky Sq. 2 162 06, Prague, 6, Czech Republic
E-mail: spevacek@imc.cas.cz

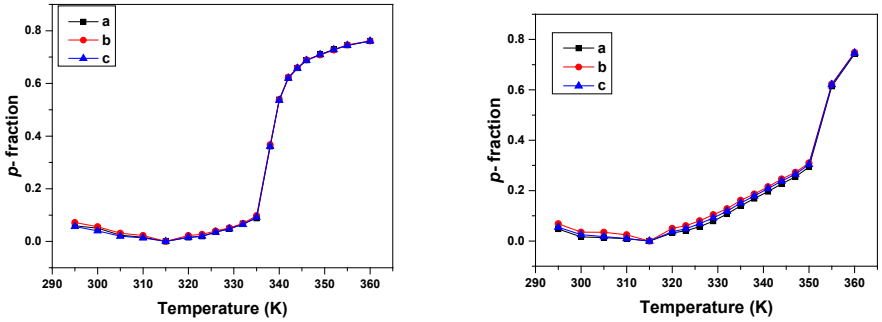

(a) (b)

Fig. S1. Temperature dependences of the fraction p (relative error ±2 %) as determined in D_2O solutions (c = 5 wt%) during gradual heating for three polymer signals of homopolymers PEOx-H (a) and PEOx-L (b).

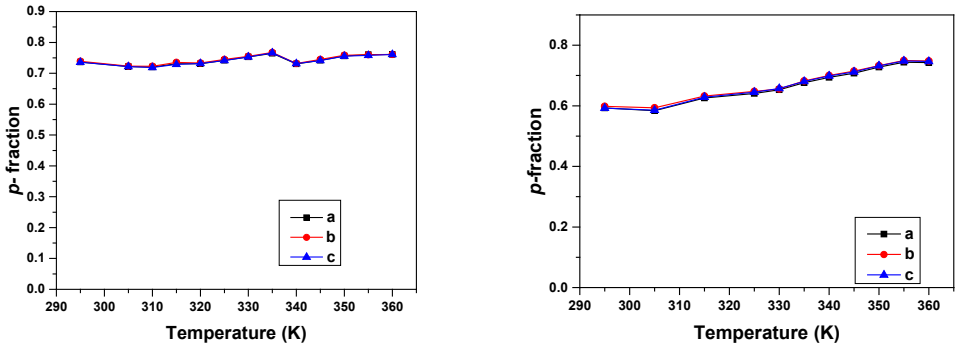

(a) **(b)**

Fig. S2. Temperature dependences of the fraction p (relative error ±2 %) as determined for three signals of various proton types in D_2O solutions (c = 5 wt%) of homopolymers PEOx-H (a) and PEOx-L (b) during gradual cooling.

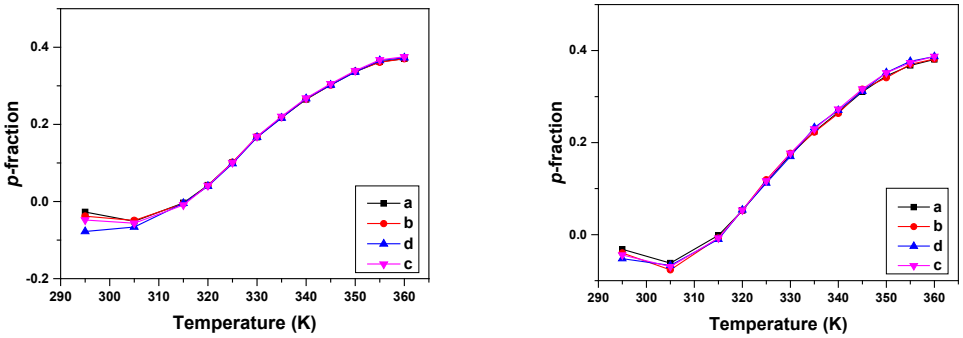

(a) **(b)**

Fig. S3. Temperature dependences of the fraction *p* (relative error ±2 %) as determined for four signals of various proton types in D_2O solutions (*c* = 5 wt%) of copolymers P(EOx/MOx)(75/25)-H (a) and P(EOx/MOx)(53/47)-H (b) during gradual cooling.

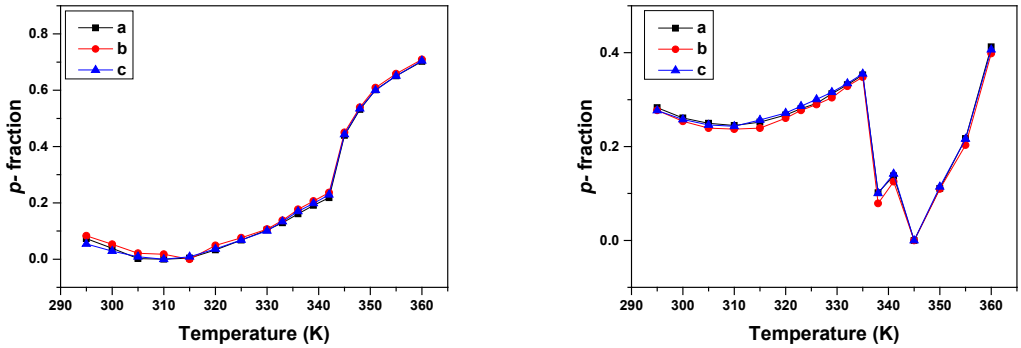

(a) **(b)**

Fig. S4. Temperature dependences of the fraction *p* (relative error ±2 %) as determined for three signals of various proton types in D_2O solutions of polymer concentration *c* = 0.5 wt% (a) and *c* = 20 wt% (b) of the PEOx-H homopolymer during gradual heating.

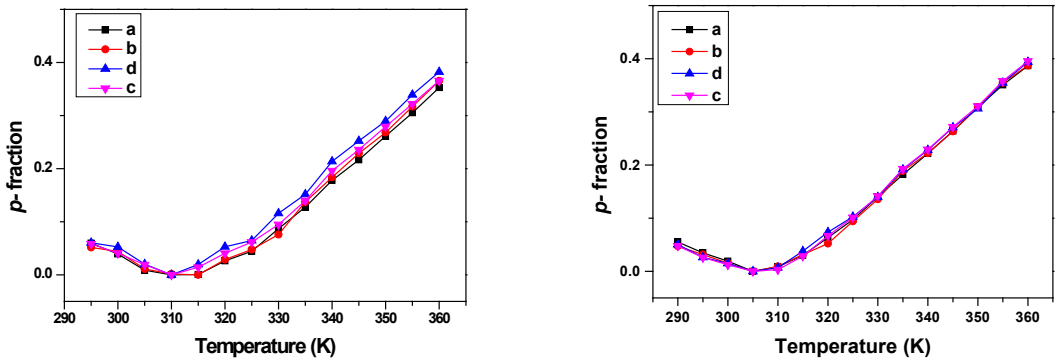

(a) **(b)**

Fig. S5. Temperature dependences of the fraction *p* as determined for four signals of various proton types in D_2O solutions of polymer concentration *c* = 0.5 wt% (a) and *c* = 20 wt% (b) of the P(EOx/MOx)(53/47)-H copolymer during gradual heating.

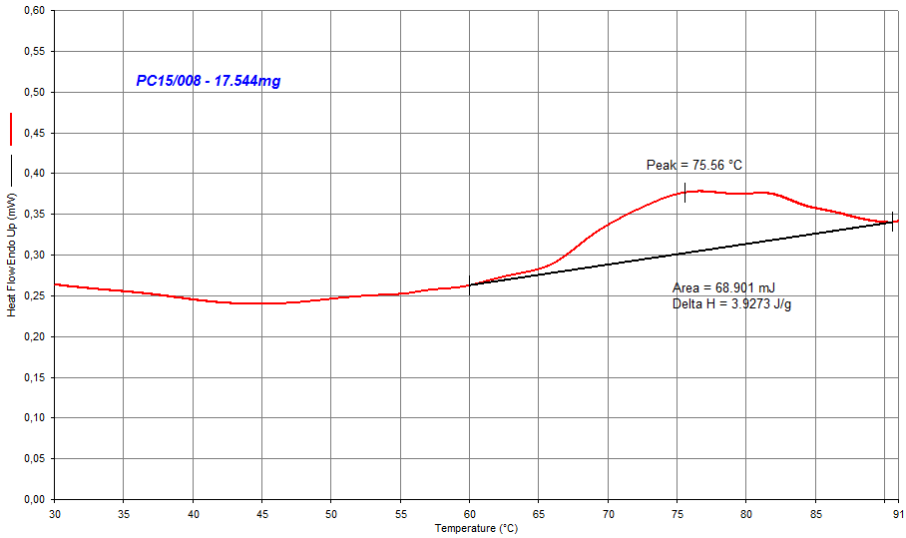

Fig. S6. DSC thermogram of D_2O solution (c = 20 wt%) of PEOx-H homopolymer measured with a heating rate 1K/min.

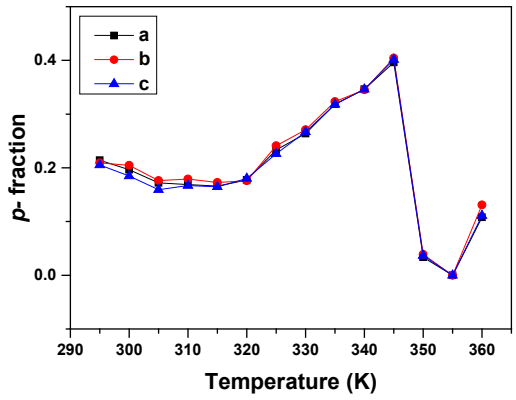

Fig. S7. Temperature dependences of the fraction p (relative error ±2 %) as determined for three signals of various proton types of PEOx-L homopolymer in D_2O solution of polymer concentration c = 20 wt% during gradual heating.

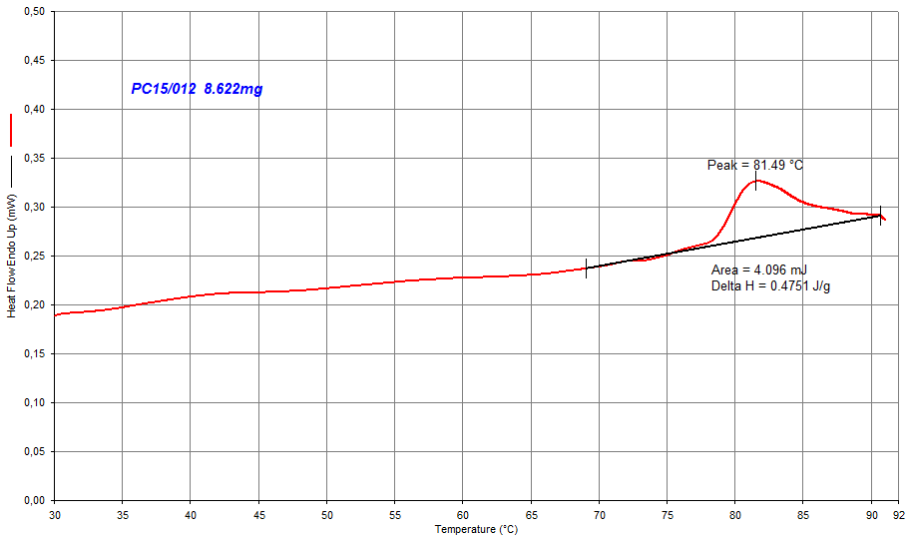

Fig. S8. DSC thermogram of D_2O solution (c = 20 wt%) of PEOx-L homopolymer measured with a heating rate 5 K/min.

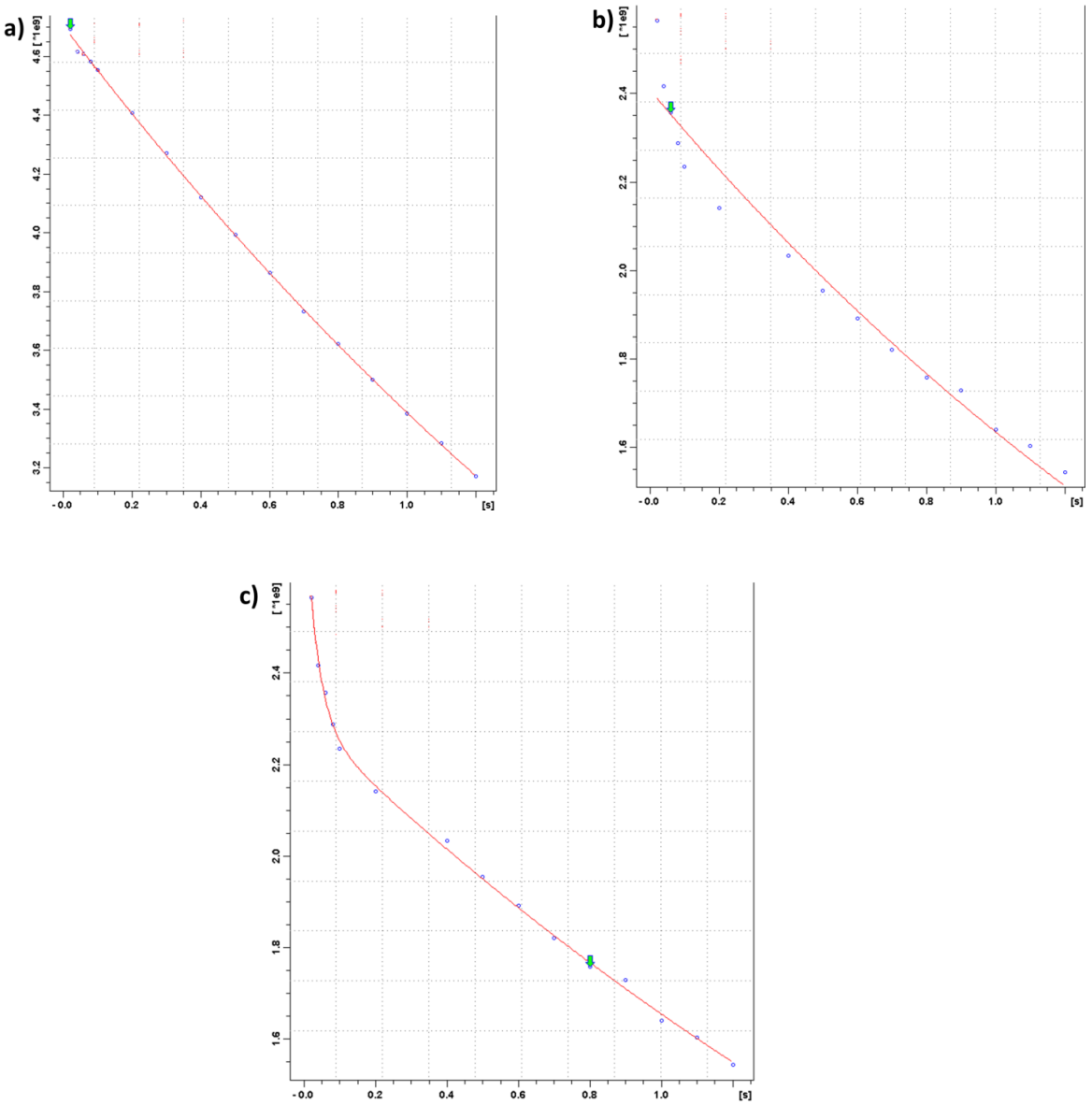

Fig. S9. CPMG T_2 relaxation curves of HDO in D_2O solution (c = 5 wt%) of the PEOx-L homopolymer showing monoexponential fit at 295 K (a), monoexponential fit at 350 K (b) and biexponential fit at 350 K (c).

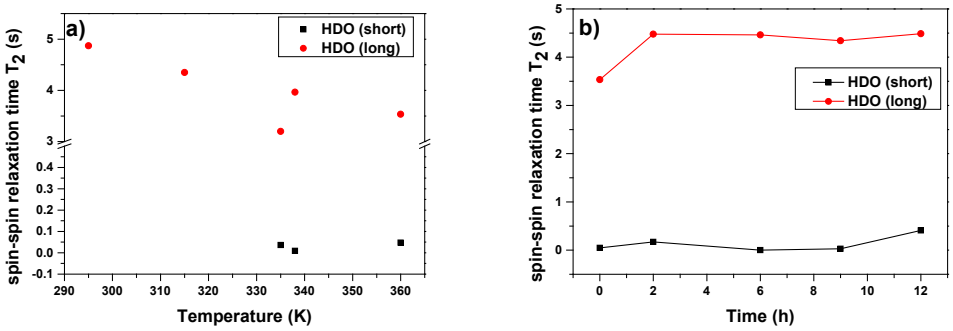

Fig. S10. Temperature dependence (a) and time dependence at 360 K (b) of ^{1}H spin-spin relaxation times T_2 (relative error ± 5%) of HDO in D_2O solution (c = 5 wt%) of the PEOx-H homopolymer.

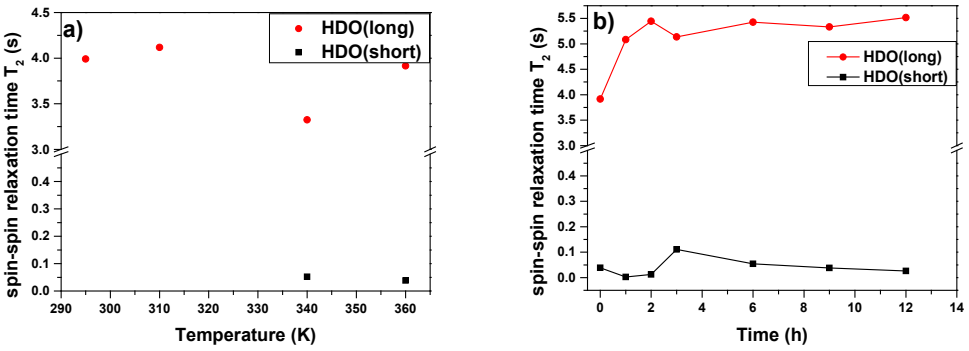

Fig. S11. Temperature dependence (a) and time dependence at 360 K (b) of ^{1}H spin-spin relaxation times T_2 (relative error ± 5%) of HDO in D_2O solution (c = 5 wt%) of the P(EOx/MOx)(75/25)-H copolymer.

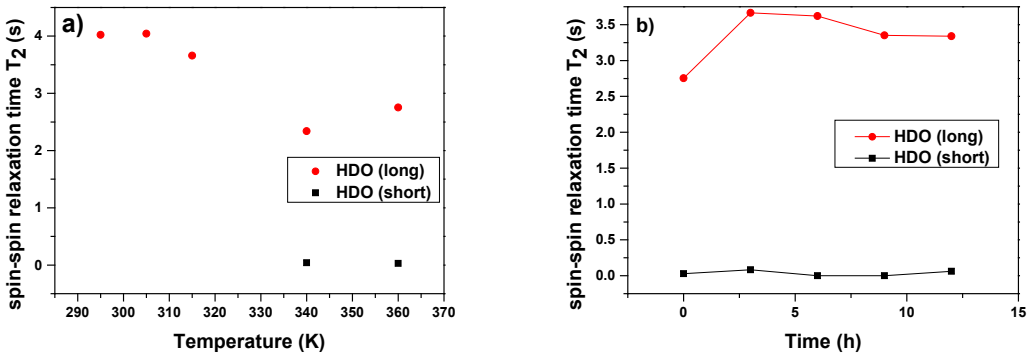

Fig. S12. Temperature dependence (a) and time dependence at 360 K (b) of ^{1}H spin-spin relaxation times T_2 (relative error ± 5%) of HDO in D_2O solution (c = 5 wt%) of the P(EOx/MOx)(75/25)-L copolymer.

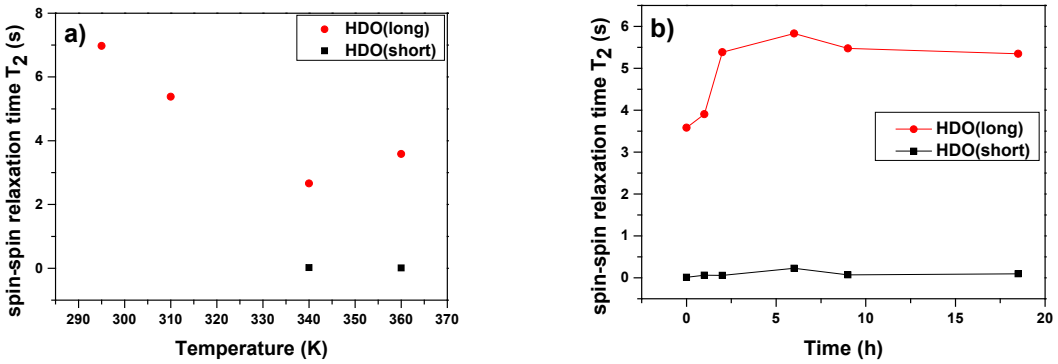

Fig. S13. Temperature dependence (a) and time dependence at 360 K (b) of ^{1}H spin-spin relaxation times T_2 (relative error ± 5%) of HDO in D_2O solution (c = 5 wt%) of the P(EOx/MOx)(53/47)-H copolymer.

Publication 2

R. Konefał, J. Spěváček, E. Jäger, S. Petrova

Thermoresponsive behaviour of terpolymers containing poly(ethylene oxide), poly(2-ethyl-2-oxazoline) and poly(ε-caprolactone) blocks in aqueous solutions: an NMR study.

Colloid and Polymer Science, **2016**, 294, 1717-1726.

Colloid Polym Sci (2016) 294:1717–1726
DOI 10.1007/s00396-016-3930-7

ORIGINAL CONTRIBUTION

Thermoresponsive behaviour of terpolymers containing poly(ethylene oxide), poly(2-ethyl-2-oxazoline) and poly(ε-caprolactone) blocks in aqueous solutions: an NMR study

Rafał Konefał[1] · **Jiří Spěváček**[1] · **Eliezer Jäger**[1] · **Svetlana Petrova**[1]

Received: 15 April 2016 / Revised: 28 July 2016 / Accepted: 30 July 2016 / Published online: 12 August 2016

Abstract ^{1}H NMR spectroscopy was used for the first time to investigate temperature behaviour of aqueous solutions of nanoparticles (NPs) prepared from linear and Y-shape terpolymers containing blocks of poly(ethylene oxide) (PEO), poly(2-ethyl-2-oxazoline) (PEtOx) and one linear or two star poly(ε-caprolactone) (PCL) blocks with different length. Structural changes were characterized separately for all blocks in a temperature range 295–360 K, and a broad transition was observed at temperatures above ~320 K. The temperature behaviour of NPs solutions depends on polymer concentration and especially on terpolymer architecture. At the same time, NMR measurements revealed important role of PCL blocks in this behaviour. The spin-spin relaxation times T_2 of water (HDO) give information on the behaviour of water and on polymer-water interactions within the aforementioned temperature range. In NPs solutions of the linear copolymer, two types of water were detected at higher temperatures: "free" and "bound" water molecules with long and very short T_2 values, respectively. For NPs solution of non-linear terpolymer, two types of water were observed only for the highest used (1.5 wt%) polymer concentration.

Keywords Thermoresponsive polymer · Terpolymer containing poly(ethylene oxide), poly(2-ethyl-2-oxazoline) and poly(ε-caprolactone) blocks · Nanoparticles · Aqueous solution · NMR

Electronic supplementary material The online version of this article (doi:10.1007/s00396-016-3930-7) contains supplementary material, which is available to authorized users.

✉ Jiří Spěváček
spevacek@imc.cas.cz

[1] Institute of Macromolecular Chemistry, Academy of Sciences of the Czech Republic, Heyrovsky Sq. 2, 162 06 Prague 6, Czech Republic

Introduction

Fast development of synthetic chemistry gives rise to novel polymers with various architectures. In the last years, researches have focused on design and synthesis of amphiphilic block copolymers which are based on a combination of hydrophilic and hydrophobic blocks [1, 2]. It is well known that in aqueous media, linear and star-shaped amphiphilic block copolymers undergo self-assembly into micelle-like structures containing hydrophobic core covered by hydrophilic shell [3–5]. A special type of amphiphilic block copolymers composed of two or more water soluble blocks of different chemical nature are the double hydrophilic block copolymers (DHBCs). Generally, in solution, one of the blocks of the DHBCs promotes dissolution while the second can be induced to form micelle structures by external stimuli such as changes in temperature, pH, ionic strength, light irradiation or complexation with appropriate molecules [6–9]. However, there are also DHBCs systems in which self-assembly is driven by configurational entropy of the two blocks or hydrophobic interactions in the absence of external stimulus [10–12]. Due to their special self-assembly properties, the thermoresponsive biocompatible polymer micelles of amphiphilic, double hydrophilic and hydrophobic blocks can be used for a range of applications including drug and gene delivery, nanoreactors, smart surface coatings, bio-separation and in oil-gas industry [13–17]. Among the studies of smart systems, the class of polymers with lower critical solution temperature (LCST) phase behaviour in water predominates. The most common polymers of this class are as follows: poly(*N*-isopropylacrylamide) (PNIPAAm) with LCST around 305 K, poly(*N*,*N*-diethylacrylamide)

(PDEAAm) with an LCST between 298 and 305 K, poly(*N*-vinylcaprolactam) (PVCL) with an LCST over the range 298 to 308 K, poly[*2*-(dimethylamino)ethyl methacrylate] (PDMAEMA) with LCST around 323 K, poly(methyl vinyl ether) (PVME) with LCST range 305 to 313 K and the poly(*2*-oxazoline)s (POx)s with LCST in the range 297 to 338 K according to their type [18–24].

Among the methods used to investigate complex systems on molecular level, NMR spectroscopy plays the key role [25]. NMR spectroscopy can provide more detailed information about the LCST phase separation behaviour and molecular motions of polymer and water in solution. Over the last 25 years, ^{1}H NMR spectroscopy and NMR relaxation times techniques have been used to study single and multicomponent thermoresponsive polymer systems in aqueous solutions. These techniques were applied to study phase transitions in a number of various thermoresponsive and amphiphilic systems [26–30].

Herein, measurements of ^{1}H NMR spectra and spin-spin relaxation times have been employed to investigate the temperature behaviour of poly(ethylene oxide)-*b*-poly(*2*-ethyl-2-oxazoline)-*b*-poly(ε-caprolactone) (PEO_{44}-*b*-$PEtOx_{252}$-*b*-PCL_{35}) triblock and Y-shaped [PEO_{44}-*b*-$PEtOx_{252}$-*b*-$(PCL_{87})_2$], [PEO_{44}-*b*-$PEtOx_{252}$-*b*-$(PCL_{131})_2$] terpolymer nanoparticles (NPs) in aqueous solution. Due to their biocompatibility, this type of copolymers has potential applications as drug nanocarriers in the field of biomedicine. PCL is a hydrophobic, biodegradable and biocompatible non-toxic aliphatic polyester [31] while PEtOx is a thermoresponsive polymer with the LCST around 334–343 K according to molecular weight and polymer concentration [32, 33]. Furthermore, PEtOx has similar biological and chemical properties as PEO; both are non-toxic, water soluble and can be eliminated from the human body when they possess appropriate particle size [34, 35].

Experimental

Synthesis and characterization

The terpolymers with linear and Y-shaped architecture used in this study were synthesized by a three-step pathway using a combination of living cationic and anionic ring-opening polymerization as described recently [36, 37]. Poly(ethylene oxide monomethyl ether) 2000 used in this synthesis was purchased from Fluka. Size exclusion chromatography has shown for all block copolymers a unimodal distribution and polydispersity index (M_w/M_n) in the range 1.3–1.4 [37]. Composition and structure of copolymers was confirmed by ^{1}H NMR spectra which were recorded using a Bruker Avance DPX 300 NMR spectrometer with $CDCl_3$ as the solvent at 295 K. Molar ratios of PEO, PEtOx and PCL units in the block copolymers were determined from integrated intensities of signals of OCH_2 protons in PEO and PCL blocks (signals a and i, respectively; electronic supplementary material (ESM) Figs. S1 and S2) and signal of NCH_2 protons in PEtOx block (signal b; ESM Figs. S1 and S2). Taking into account that the length of PEO block is 44 units, from obtained molar ratios of PEO, PEtOx and PCL units, we were able to obtain lengths of PEtOx and PCL blocks.

Preparation of the nanoparticles (NPs) solutions

NPs solutions were prepared by nanoprecipitation method. Terpolymers were dissolved in acetone at 40 °C, and polymer solution was added drop-wise to D_2O under magnetic stirring. Acetone was further removed by evaporation under reduced pressure. For NMR measurements, samples of NPs in D_2O (concentrations c = 0.5 and 1.5 wt%) were filled into 5-mm NMR tubes, which were degassed and sealed under nitrogen.

Dynamic light scattering (DLS) characterization of the NPs

DLS measurements were performed using an ALV/CGE laser goniometer system consisting of a 22-mW HeNe linearly polarized laser operating at a wavelength of 632.8 nm, an ALV 6010 correlator and a pair of avalanche photodiodes operating in the pseudo cross-correlation mode. The samples were maintained at various temperatures (298–348 K). The data were collected using the ALV Correlator Control software based on ten independent runs of 60 s counting time. The measured intensity correlation functions $g_2(t)$ were analysed using the algorithm REPES (incorporated in the GENDIST program) resulting in the distribution of relaxation times–$A(\tau)$. The hydrodynamic radius R_H of the NPs was calculated from the Stokes-Einstein relation with $D = \tau^{-1}q^{-2}$:

$$R_H = \frac{k_B T q^2}{6\pi\eta}\tau \quad (1)$$

where k_B is the Boltzmann constant, T is the absolute temperature, q is the scattering vector, η is the viscosity of the solvent and τ is the mean relaxation time related to the diffusion of the nanoparticles.

NMR measurements

Temperature dependences of ^{1}H NMR spectra were acquired with Bruker Avance III 600 spectrometer operating at 600.2 MHz. The width of 90° pulse was 10 μs, relaxation delay 20 s, acquisition time 2.18 s, 8 scans. The integrated intensities were determined with spectrometer integration software with an accuracy of ±1 %. Before measurement, the samples were equilibrated at the desired temperature for

at least 10 min. Temperature dependences of ^{1}H spin-spin relaxation times T_2 of HDO were measured on the same spectrometer using the CPMG pulse sequence $90°_x$-(t_d-$180°_y$-t_d)$_n$-acquisition [38]. The relaxation delay between scans was 100 s, acquisition time 2.84 s, 1 scan. The relative error for T_2 values did not exceed ±5 %. Every T_2 experiment was done immediately after recording ^{1}H NMR spectrum at the same temperature and in all measurements the temperature was maintained constant within ±0.2 K in the range 295–360 K using a BVT 3000 temperature unit.

Results and discussion

^{1}H NMR spectra and fraction of units with significantly reduced mobility

Figure 1 shows high-resolution ^{1}H NMR spectra of a D_2O solution (c = 0.5 wt%) of the [PEO_{44}-*b*-$PEtOx_{252}$-*b*-$(PCL_{87})_2$] NPs measured under the same instrumental conditions at three temperatures. The assignment of resonances to various proton types is shown directly in the spectrum measured at 295 K; the chemical structure of terpolymer is shown in Scheme 1. The strong peak at 4.84 ppm corresponds to HDO and the signal "S" is from residual acetone after NPs preparation. At the same time, the amount of acetone is negligible because from integrated intensities of respective signals determined, molar ratio acetone/HDO = 10^{-2} and taking into account the degree of deuteration of the used D_2O (99.9 %), it follows for the molar ratio acetone/D_2O = 10^{-5}. The signal "a" is related to CH_2 groups of PEO while methylene protons of main chain of PEtOx are marked "b". PEtOx side chain groups C(O) CH_2 and CH_3 correspond to peaks "c" and "d", respectively. C(O) CH_2 (e) of PCL is overlapped with the signal from PEtOx (c), and the remaining peaks (f, g, h, i) correspond to further groups of the PCL. Comparison between spectra recorded in a solvent suitable for all blocks (deuterated chloroform, cf. ESM Fig. S1) and D_2O at 295 K shows that the weaker and broader signals of hydrophobic PCL blocks and stronger signals of hydrophilic PEO and thermoresponsive PEtOx blocks are consistent with a core-shell formation in D_2O. On the basis of these results, we assume that the PCL protons are restricted in mobility in the moderately hydrated solid-like core of NPs while PEtOx and PEO blocks create a liquid-like shell [31]. The remaining spectra in Fig. 1 were measured at temperatures of 325 K (below LCST of PEtOx) and 360 K (above LCST of PEtOx). The most important effect observed in the spectra measured at higher temperatures is a visible change in the integrated intensity of all PEtOx, PEO and PCL signals; the PCL peaks almost disappear and the intensity of PEtOx and PEO signals is reduced. This decreasing intensity and broadening of signals is due to the fact that with increasing temperature, the mobility of the part of

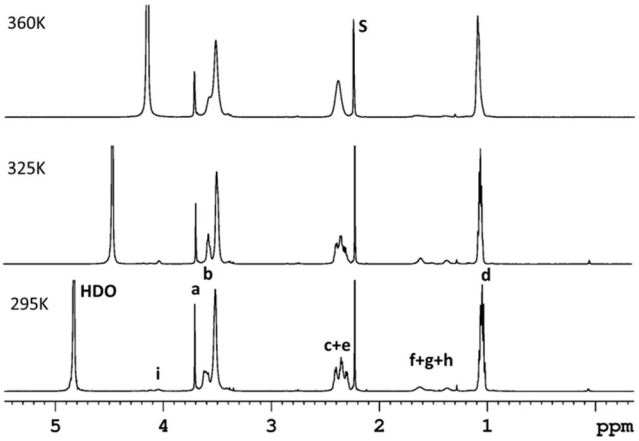

Fig. 1 600.2 MHz ^{1}H NMR spectra of [PEO_{44}-*b*-$PEtOx_{252}$-*b*-$(PCL_{87})_2$] NPs in D_2O solution (c = 0.5 wt%) measured at 295, 325 and 360 K under the same instrumental conditions. Peak assignments are explained in the text

polymer segments decreases to such an extent that they escape detection in high-resolution NMR spectra. Similar behaviour was previously reported for other thermoresponsive polymer systems [26, 28, 30, 39].

High-resolution ^{1}H NMR spectra of the D_2O solution (c = 0.5 wt%) of linear PEO_{44}-*b*-$PEtOx_{252}$-*b*-PCL_{35} NPs recorded at three temperatures under the same instrumental conditions are presented in Fig. 2 (terpolymer spectrum in $CDCl_3$ is shown in ESM Fig. S2). Peak assignments of the various proton types are shown in the spectrum measured at 295 K. Chemical structure of the linear terpolymer is shown in the same figure, above the spectrum recorded at 360 K. All signals are at the same positions as in the spectra of Y-shape block copolymer (Fig. 1). The main difference between these two types of terpolymers is visible in spectra recorded at 325 K. In contrast to the non-linear copolymer, in spectrum of linear terpolymer, integral intensities of PCL signals (f + g + h, i) are significantly increased. The spectrum at 360 K shows similar effects for both types of copolymers: decreasing integral intensity and broadening of all signals related to protons of PEO (a), PEtOx (b, c, d) and PCL (e, f + g + h, i).

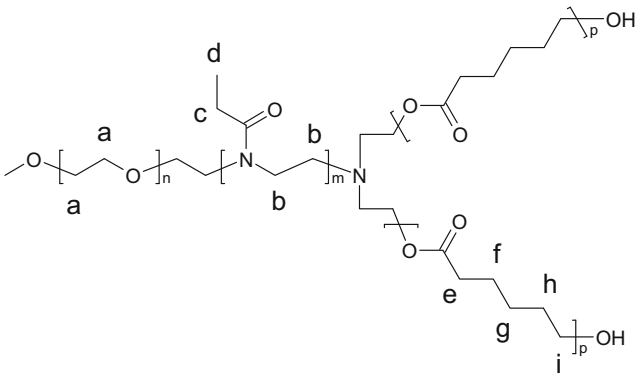

Scheme 1 General structural formula of Y-shaped [PEO-*b*-PEtOx-*b*-$(PCL)_2$] terpolymer

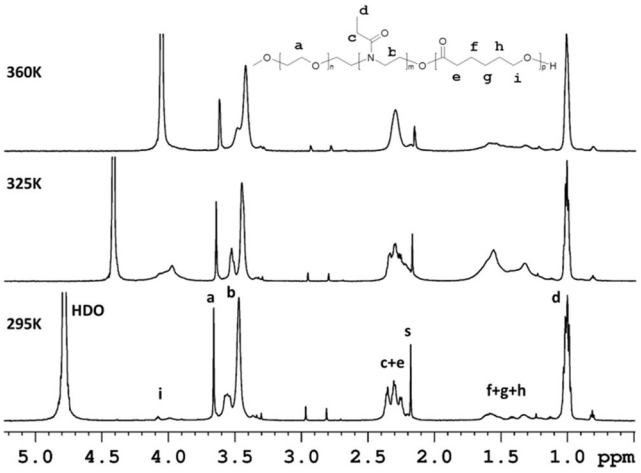

Fig. 2 600.2 MHz ^{1}H NMR spectra of PEO_{44}-*b*-$PEtOx_{252}$-*b*-PCL_{35} NPs in D_2O solution (c = 0.5 wt%) measured at 295, 325 and 360 K under the same instrumental conditions

Temperature changes in chemical shift of the HDO signal are well known and described in literature [40].

To quantitatively characterize changes occurring during the heating process, the values of the fraction p for units with significantly reduced mobility were calculated from integrated intensities in ^{1}H NMR spectra using the relation [26, 30]:

$$p = 1 - \frac{I(T)}{I(T_0) \times \frac{T_0}{T}} \quad (2)$$

where $I(T)$ is the integrated intensity of given polymer signal in the spectrum at temperature T and $I(T_0)$ is the integrated intensity of this signal when no phase separation or other reason for the reduced mobility of polymer segments occurs. Due to the fact that integrated intensities should decrease with reciprocal absolute temperature as $1/T$ (Curie law holds also for nuclear magnetization) i.e., $I_0(T) = I_0(T_0) \times (T_0/T)$, temperature T appears explicitly in the denominator of the second term in Eq. (2). For T_0, we took the temperature where the integrated intensity of the given signal was the highest and therefore $p(T_0) = 0$.

In Fig. 3a, temperature dependences of the p-fraction of various proton types [PEO_{44}-*b*-$PEtOx_{252}$-*b*-$(PCL_{87})_2$] NPs D_2O solution (c = 0.5 wt%) are shown. For all the blocks, p-fraction first slightly decreases and has a shallow minimum at ~315 K. At 310 K, where $p = 0$ for all block types, the ratios of integrated intensities of various PEO, PEtOx and PCL signals are the same as respective ratios in $CDCl_3$ (good solvent for all block types in investigated NPs), so confirming that at this temperature really all PCL units are directly detected in high-resolution spectrum. Above 315 K, the values of the p-fraction are again increasing as terpolymer chains become less hydrated. In the temperature range 330–340 K, a strong jump of p values that correspond to the PCL block (f + g + h, i) occurs and also values related to PEtOx (b, d) and PEO (a) blocks are increasing. Final p values for the PCL blocks (≈0.65) at 360 K are almost twice as high as values for hydrophilic PEO blocks (≈0.39) and also higher than the p values for the thermoresponsive PEtOx blocks (≈0.42). The increase in p values is probably induced by long thermoresponsive PEtOx blocks which changed their hydrophilic properties to hydrophobic ones at the LCST. Phase transition of the main chain (b) and the side chain (d) in PEtOx blocks is the same exhibiting a broad transition width (45 K) and transition temperature ≈338 K (temperature for $p_{max}/2$). At the same time, the transition temperature is virtually the same as obtained using the same NMR approach on D_2O solution (c = 5 wt%) of PEtOx homopolymer (M_n = 17,200 i.e., similar as molecular weight of the PEtOx block in the investigated terpolymer), but transition width (8 K) is for PEtOx homopolymer significantly smaller. Above 320 K, the NPs become more hydrophobic and start to aggregate (increasing p values of PEO blocks); their core becomes more solid-like (increasing p-values of PCL blocks) and they precipitate at high temperatures. The obtained results are in qualitative agreement with a recent study of NPs solutions of PEO-*b*-PEtOx-*b*-$(PCL)_2$ terpolymers by static and dynamic light scattering and cryo-transmission electron microscopy (TEM) [37].

Temperature dependences of the p-fraction for various proton groups in D_2O solution of [PEO_{44}-*b*-$PEtOx_{252}$-*b*-$(PCL_{87})_2$] NPs (c = 1.5 wt%) are shown in ESM Fig. S3. They are very similar to dependences shown in Fig. 3a for solution with c = 0.5 wt%. At the higher concentration, similar effects are observed as in solution with 0.5 wt%, only with larger maximum values p_{max} reached at c = 1.5 wt% where p_{max} = 0.85, 0.58 and 0.55 for PCL, PEtOx and PEO blocks, respectively.

Temperature dependences of the p-fraction for the second Y-shape terpolymer with longer PCL blocks i.e., its NPs water solution (c = 0.5 wt%) are presented in Fig. 3b. Though both the length of PCL blocks and molar fraction of PCL units are in this case larger (1.5 and 1.3 times, respectively) than in the [PEO_{44}-*b*-$PEtOx_{252}$-*b*-$(PCL_{87})_2$] sample, behaviour of both terpolymers is very similar. Also, for [PEO_{44}-*b*-$PEtOx_{252}$-*b*-$(PCL_{131})_2$], the temperature dependences show a shallow minimum at ≈315 K and values of p_{max} are 0.67, 0.45 and 0.36 for PCL (f + g + h, i), PEtOx (b, d) and PEO (a) proton groups, respectively. Similarly, to the [PEO_{44}-*b*-$PEtOx_{252}$-*b*-$(PCL_{87})_2$] terpolymer, NPs of [PEO_{44}-*b*-$PEtOx_{252}$-*b*-$(PCL_{131})_2$] are seen to swell slightly up to 315 K. Above this temperature, the NPs start to collapse, aggregate (increasing p values) and subsequently precipitate.

Figure 4 shows temperature dependences of the p-fraction in the linear PEO_{44}-*b*-$PEtOx_{252}$-*b*-PCL_{35} NPs D_2O solution (c = 0.5 wt%). Similarly, to the Y-shape terpolymers also the linear copolymer shows a similar behaviour for the PEtOx (b, d) and PEO (a) blocks. The values of the p-fraction of these two blocks decrease slightly to a minima at 315 K (PEO) and

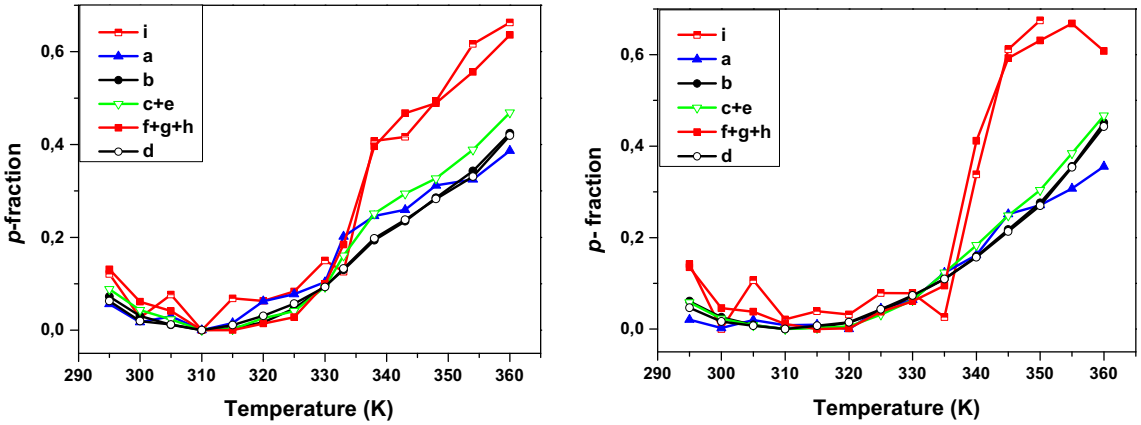

Fig. 3 Temperature dependences of *p*-fraction for various proton groups in NPs D_2O solutions ($c = 0.5$ wt%) of [PEO_{44}-*b*-$PEtOx_{252}$-*b*-$(PCL_{87})_2$] (**a**) and [PEO_{44}-*b*-$PEtOx_{252}$-*b*-$(PCL_{131})_2$] (**b**)

325 K (PEtOx). Above these temperatures, the *p* values start to increase and achieve final values $p_{max} \approx 0.34$ at 360 K. As in systems with the non-linear architecture, also here the transition is the same for the PEtOx main chain (b) and the side chain (d). In contrast to the Y-shape terpolymers in the linear system, we observed a significant difference in the behaviour of the PCL block (signals f + g + h, i) during the heating process. Though the content of PCL units (10.6 mol%) is in the linear terpolymer 3.5 times smaller in comparison with [PEO_{44}-*b*-$PEtOx_{252}$-*b*-$(PCL_{87})_2$] sample, room temperature value of the *p*-fraction is for PCL segments in linear sample five times larger (cf. Figs. 3 and 4, signals i and f + g + h). This fact indicates important role of the terpolymer architecture on PCL behaviour. High values of the *p*-fraction (≈0.8) for the PCL units are virtually constant up to 315 K; next, they steeply decrease to a minimum at 325 K, then return to their initial value at 340–345 K and remaining almost unchanged thereafter. These results show that PCL block plays a crucial role in the temperature behaviour of the linear system studied.

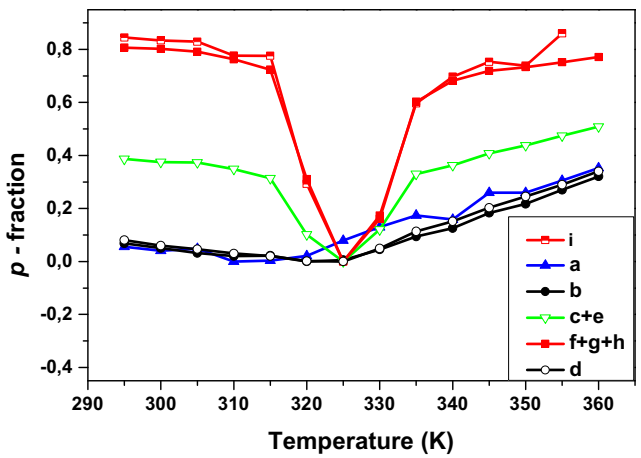

Fig. 4 Temperature dependences of *p*-fraction for various proton groups in PEO_{44}-*b*-$PEtOx_{252}$-*b*-PCL_{35} NPs D_2O solution ($c = 0.5$ wt%)

The steep decrease of the *p*-fraction of the PCL blocks in the temperature range of 315–325 K can be in connection with faster segmental motion in PCL blocks and/or in faster motion of NPs as a whole. We assume that first reason is crucial. The melting point of the PCL homopolymer is reported in the temperature range of 332–337 K [41]; in NPs systems, the "melting" temperature can be somewhat shifted to lower temperatures. Therefore, at 315–325 K the *p* values decrease as the partially hydrated hydrophobic core "melts" and PCL blocks become more mobile (i.e., the respective integrated intensity increases, cf. Fig. 2). Afterwards, with increasing temperature, the NPs reorganize, core collapses and returns back to a solid-like, partially hydrated state. The presented interpretation that a certain disintegration of structures formed by hydrophobic PCL blocks plays a main role in the steep decrease of their *p*-fraction is corroborated by the fact that a weak endotherm was detected in DSC measurements at 313 K i.e., at temperature where the decrease of the *p*-fraction starts, as shown in ESM Fig. S4.

Second possible effect related to the zero value of the *p*-fraction of the PCL blocks at 325 K can be in connection with motion of the NPs as a whole. In the case that motion of the whole NPs is sufficiently fast, subsequent spin-spin relaxation times T_2 of PCL protons can be long enough (and linewidths of PCL signals sufficiently narrow) to be detected in high-resolution spectra measured with a liquid-state NMR spectrometer. Figure 5 shows temperature dependences of the hydrodynamic radius R_H obtained by DLS technique for NPs D_2O solutions ($c = 0.5$ wt%) of PEO_{44}-*b*-$PEtOx_{252}$-*b*-PCL_{35} and [PEO_{44}-*b*-$PEtOx_{252}$-*b*-$(PCL_{87})_2$] terpolymers. The R_H values in Fig. 5 are average values from ten measurements with unimodal distributions as illustrated in ESM Fig. S5. From Fig. 5, it follows that in both cases, NPs sizes decrease with increasing temperature reaching a minimum around 325 K. At the same time, in the temperature range 298–330 K, the R_H values are approximately twice as large for

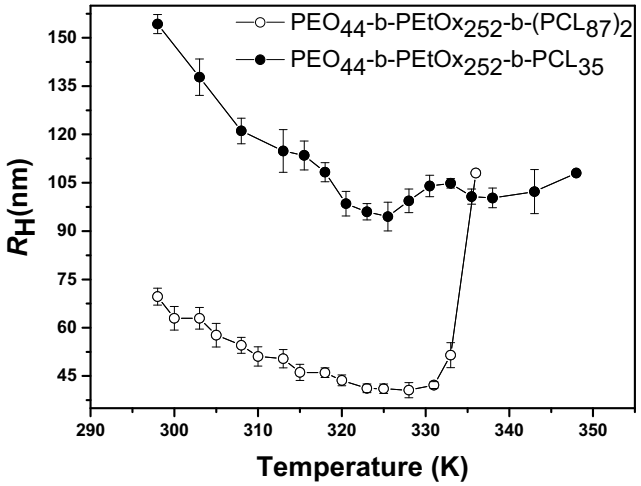

Fig. 5 Temperature dependences of hydrodynamic radius R_H of NPs in D_2O solutions (c = 0.5 wt%) of PEO_{44}-*b*-$PEtOx_{252}$-*b*-PCL_{35} and [PEO_{44}-*b*-$PEtOx_{252}$-*b*-$(PCL_{87})_2$] terpolymers

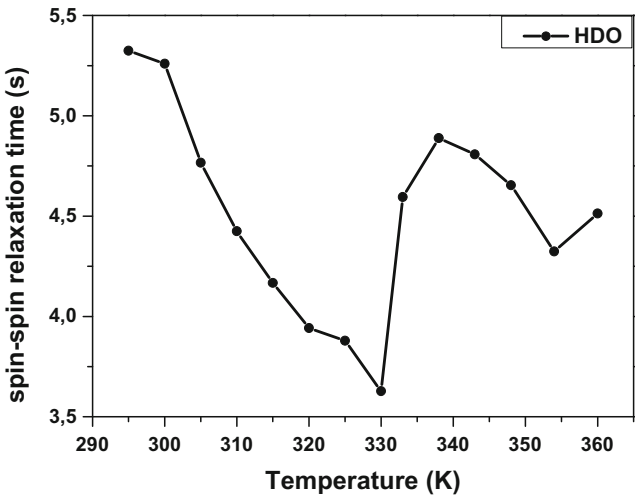

Fig. 6 Temperature dependence of ^{1}H spin-spin relaxation time T_2 of HDO in [PEO_{44}-*b*-$PEtOx_{252}$-*b*-$(PCL_{87})_2$] NPs D_2O solution (c = 0.5 wt%)

NPs of the linear sample in comparison with Y-shape terpolymer which shows that NPs of Y-shape terpolymer are more compact. The fact that NPs of linear terpolymers are always larger in comparison with NPs of Y-shape terpolymers follows also from comparison of R_H values presented in previous studies where a good correlation between DLS and cryo-TEM results was shown [36, 37]; these studies indicated that hydrophilic (PEO-*b*-PEtOx) shell is significantly longer in comparison to the hydrophobic PCL core and therefore a small core can be expected. It was suggested that the temperature-driven PEtOx dehydration can induce the onset of NPs aggregation [36]. With increasing temperature above the LCST of PEtOx (≈330 K), a steep increase in the R_H is really visible for Y-shape terpolymer (followed by precipitation at temperatures above 336 K), while only a mild increase of the NPs size is shown for linear terpolymer. In accord with other studies on similar systems [42, 43], we assume that NPs of linear terpolymer are diffuse core-shell or soft ball particles containing a high amount of water entrapped inside which leads to the increase of the NPs size, while NPs of Y-shape terpolymers are more compact and containing less water inside. Taking into account the NMR results (Fig. 4), the correlation time τ_c of the motion of NPs as a whole is with good approximation given by the relation [44]

$$\tau_c = 4\pi\eta {R_H}^3 \Big/ 3k_B T \qquad (3)$$

A reduction in the R_H values of the linear terpolymer at 325 K to 61 % of the value at 298 K (as shown in Fig. 5) will then result in 4.4 times smaller values of the Brownian tumbling correlation time τ_c for the NPs as a whole. Assuming that linewidths $\Delta\nu$ (with $\Delta\nu \approx {T_2}^{-1}$) are proportional to correlation time τ_c (cf. e.g., ref. [45]), reduction of τ_c values by factor 4.4 is itself probably not sufficient to explain the marked increase in integrated intensity of PCL signals as shown in Fig. 2 and decrease of the respective p-fraction as shown in Fig.4. Nevertheless, in combination with faster segmental motion in PCL blocks, the reduced size of NPs of linear terpolymer at 325 K in comparison with 298 K might contribute to the final effect.

Temperature dependences of p-fraction in PEO_{44}-*b*-$PEtOx_{252}$-*b*-PCL_{35} NPs D_2O solution (c = 1.5 wt%) are shown in ESM Fig. S6. In comparison with the lower concentration (Fig. 4), we observed a few small differences in the behaviour of blocks of terpolymer. The minima of the p-dependences are shifted to lower temperatures, 310 K for PEtOx (b, d) and PEO (a), and 320 K for PCL (f + g + h, i). PEtOx and PEO blocks achieved similar values of p_{max} (≈0.35) as at lower polymer concentration. More pronounced difference is in the behaviour of PCL component where the values of the p-fraction (≈0.4) in the temperature range of 295–315 K are twice smaller than at the lower NPs concentration (≈0.8), and p_{max} values are larger than values of the p-fraction at 295 K. These differences can be connected with the fact that at the higher concentration, there is a larger probability of interactions between NPs themselves affecting hydration of the shell.

Spin-spin relaxation times T_2 of HDO molecules

Information on behaviour of water and polymer-solvent interactions (hydration) during phase transition in aqueous solutions can be provided by NMR relaxation measurements. It was shown that especially spin-spin relaxation times T_2 of water (HDO protons or D_2O deuterons) are useful in this respect [26, 29, 30, 39, 46]. In our investigations of D_2O

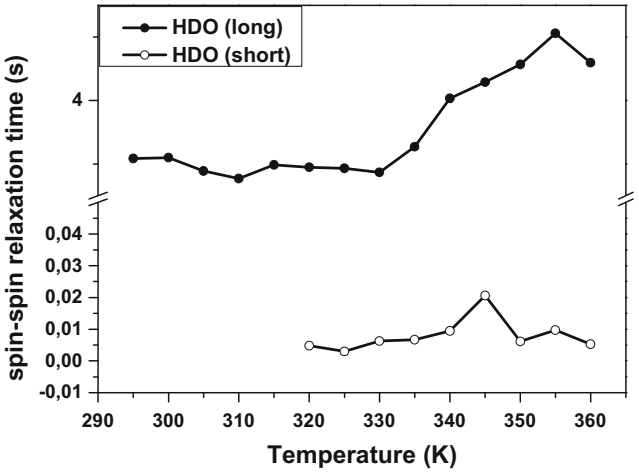

Fig. 7 Temperature dependence of ^{1}H spin-spin relaxation time T_2 of HDO in [PEO_{44}-*b*-$PEtOx_{252}$-*b*-$(PCL_{87})_2$] NPs D_2O solution (c = 1.5 wt%)

solutions of NPs, we provide all T_2 values at the same temperatures as in ^{1}H NMR spectra used to establish the *p*-fraction values. Results for all samples are shown in Figs. 6, 7 and 8; furthermore, detailed values for systems with two types of water together with intensities for both components are shown in ESM Table S1. In Fig. 6, temperature dependence of ^{1}H spin-spin relaxation time T_2 of HDO in [PEO_{44}-*b*-$PEtOx_{252}$-*b*-$(PCL_{87})_2$] NPs D_2O solution (c = 0.5 wt%) is shown. From this figure, it follows that mobility of the HDO molecules decreases with increasing temperature to 330 K; this effect is in connection with swelling of the NPs. Water is hydrating the copolymer chains where newly created hydrogen bonds between carbonyl oxygen and water molecules reduce their mobility. Heating above 330 K results in increasing values of T_2 which is connected with NPs aggregation: hydrophobic forces predominate, polymer-water hydrogen bonds break, water molecules are released and their mobility increases. Very similar dependence is shown in ESM Fig. S7 which depicts temperature dependence of ^{1}H spin-spin relaxation time T_2 of HDO in [PEO_{44}-*b*-$PEtOx_{252}$-*b*-$(PCL_{131})_2$] NPs D_2O solution (c = 0.5 wt%).

Temperature dependence of ^{1}H spin-spin relaxation time T_2 of HDO in [PEO_{44}-*b*-$PEtOx_{252}$-*b*-$(PCL_{87})_2$] NPs D_2O solution (c = 1.5 wt%) is shown in Fig. 7. In comparison with the lower polymer concentration (c = 0.5 wt%), the starting T_2 value at 295 K is smaller, around 3.0 s. This is due to the fact that at higher polymer concentration, more water molecules are involved in the hydration process. During the heating process, T_2 values are virtually constant up to 320 K. At this temperature, NPs start to aggregate, and at higher temperatures, relaxation curves are non-exponential and two T_2 components are necessary to fit the experimental relaxation curves. This analysis therefore shows the existence of two types of water molecules at temperatures above 320 K. First type is "free" water with longer relaxation times (>3 s); HDO molecules in solution. Second type is "bound" water with very short T_2 relaxation times (≈10 ms); HDO molecules bound (confined, entrapped) inside the NPs aggregates. From ESM Table S1, it follows that intensities of both components and therefore also the fractions of both types of water molecules are roughly comparable.

Figure 8a shows temperature dependence of ^{1}H spin-spin relaxation time T_2 of HDO in PEO_{44}-*b*-$PEtOx_{252}$-*b*-PCL_{35} NPs D_2O solution (c = 0.5 wt%). In contrast to the Y-shape terpolymers with c = 0.5 wt% (Fig. 6 and ESM Fig. S7) for solution of linear copolymer, T_2 values of HDO are roughly constant up to 325 K i.e., to temperature of the minimum in dependence of the *p*-fraction of the PCL block (cf. Fig. 4). Further increase of temperature results in splitting of the T_2 values into two components: one with longer and one with much shorter relaxation times. During the reorganization of NPs at 325 K, one part of water molecules (long T_2

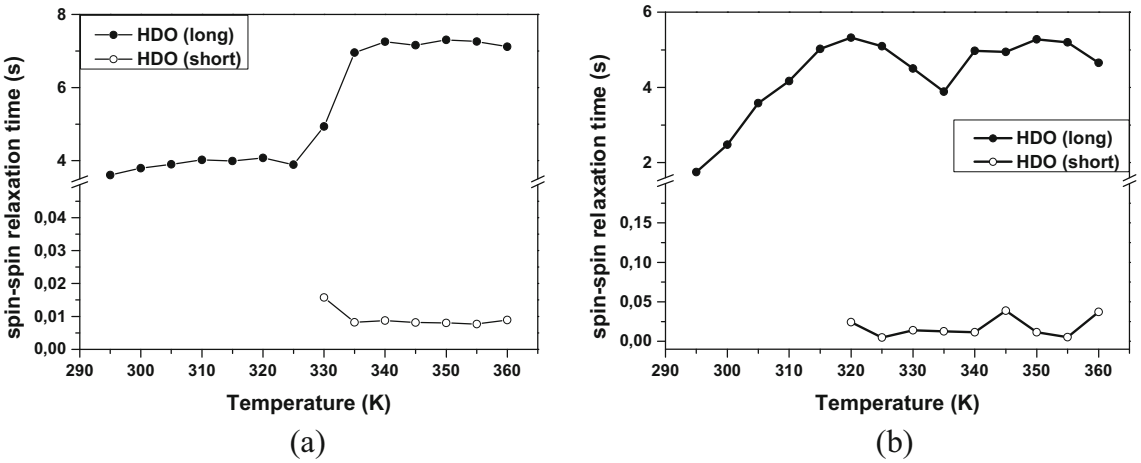

Fig. 8 Temperature dependence of ^{1}H spin-spin relaxation time T_2 of HDO in PEO_{44}-*b*-$PEtOx_{252}$-*b*-PCL_{35} NPs D_2O solutions. c = 0.5 wt% (**a**) and 1.5 wt% (**b**)

component) remains in solution and observed increase of T_2 values with temperature indicates that they are partly released from interactions with the polymer segments. The existence of the second component with very short T_2 values ($T_2 \approx 10$ ms) shows that some water molecules are bound inside the NPs; these molecules are not released up to 360 K, as indicated by constant values for the short component.

Temperature dependence of ^{1}H spin-spin relaxation time T_2 of HDO in PEO_{44}-*b*-$PEtOx_{252}$-*b*-PCL_{35} NPs D_2O solution (c = 1.5 wt%) is shown in Fig. 8b. In contrast to the 0.5 wt% solution, here the T_2 values are initially increasing with temperature in connection with breaking of hydrogen bonds between polymer segments and water resulting in an increase of the p-fraction of the PCL blocks in the temperature range up to 315 K (cf. ESM Fig. S6). At 320 K (temperature of the minimum of the p-fraction of the PCL blocks) and higher temperatures, T_2 relaxation times are divided into two components, long and short, similarly as in the system with polymer concentration of 0.5 wt%. For both concentrations, c = 0.5 wt% and 1.5 wt%, intensities of the long and the short T_2 components are roughly comparable (cf. ESM Table S1).

Existence of water molecules bound in globular structures formed at temperatures above the LCST transition was shown previously by NMR both in aqueous solutions and hydrogels of thermoresponsive polymers. In solutions, the bound water is manifested e.g., by reduced T_2 values; in D_2O solutions, there is usually a single line of HDO in ^{1}H NMR spectra and single-exponential character of T_2 relaxation curves indicates a fast exchange between bound and free sites [26]. On the other hand, two separate signals of water were detected above the LCST in highly concentrated PVME/D_2O [29, 39] and PVME/D_2O/ethanol [47] solutions, as well as in collapsed PVME and PNIPAAm hydrogels [48–51], homo- and copolymer microgels of NIPAAm and NNDEAAm in water/methanol mixtures [52] and hydrogels of interpenetrating networks poly(*N*-isopropylmethacrylamide)/PNIPAAm, PVCL/PNIPAAm and PNIPAAm/polyacrylamide [53, 54]. These two water signals were interpreted as signals of free and bound (confined) water. The shape of the HDO signals in ^{1}H NMR spectra of D_2O solutions of linear and Y-shape triblock copolymers investigated in the present study at temperatures above 335 K also suggests the existence of two partly overlapping components. At the same time, the difference of chemical shifts of these two components is very small, it does not exceed 0.008 ppm. Nevertheless, the existence of two T_2 components shown in Figs. 7 and 8 implies that the exchange between bound and free water molecules in these systems must be slow regarding T_2 values i.e., the residence time of bound HDO molecules has to be ≥0.1 s, similarly as in systems where two separate water signals are clearly resolved.

Conclusions

By means of ^{1}H NMR methods, temperature behaviour of NPs water solutions of terpolymers containing PEO, PEtOx and PCL blocks with linear and non-linear (Y-shape) architectures was studied for the first time. We confirmed that a series of ^{1}H NMR and ^{1}H spin-spin relaxation time T_2 experiments are suitable for investigation of structural changes on molecular level caused by temperature, as well as changes in behaviour of water molecules during the heating process. NPs prepared from two Y-shape terpolymers: [PEO_{44}-*b*-$PEtOx_{252}$-*b*-$(PCL_{87})_2$] (c = 0.5 and 1.5 wt%) and [PEO_{44}-*b*-$PEtOx_{252}$-*b*-$(PCL_{131})_2$] (c = 0.5 wt%), and one linear system: PEO_{44}-*b*-$PEtOx_{252}$-*b*-PCL_{35} (c = 0.5 and 1.5 wt%) were studied. In all investigated samples, a broad transition of PEtOx blocks was observed in a temperature range ~320–360 K with maximum values of the p-fraction (fraction of units with significantly reduced mobility) around $p_{max} \approx 0.4$. The PEO blocks reach similar p_{max} as PEtOx blocks. Furthermore, pronounced differences in the temperature behaviour of linear and non-linear systems were found, especially in connection with behaviour of PCL blocks. Though the content of hydrophobic PCL units is in the linear terpolymer 3.5 times smaller in comparison with [PEO_{44}-*b*-$PEtOx_{252}$-*b*-$(PCL_{87})_2$] Y-shape sample, room temperature value of the p-fraction is for PCL segments in linear sample five times larger. From measurements of spin-spin relaxation times T_2 of HDO, different behaviour of the water molecules in NPs solutions of linear and Y-shape systems was observed. In NPs solutions of the linear copolymer, two types of water ("free" and "bound") were detected at higher temperatures. For NPs solutions of Y-shape terpolymers such two types of water were observed only for the higher (1.5 wt%) polymer concentration.

Acknowledgments Support by the Czech Science Foundation (Project 15-13853S) is gratefully acknowledged. R.K. acknowledges Charles University, Faculty of Science (Prague, CZ) for the opportunity to pursue his PhD studies. S.P. acknowledges support from Norwegian funds no. 7F14009. Authors thank A. Sikora for DSC measurements.

Compliance with ethical standards

Conflict of interest The authors declare that they have no conflict of interest.

References

1. Mai Y, Eisenberg A (2012) Self-assembly of block copolymers. Chem Soc Rev 41:5969–5985
2. Schacher FH, Rupar PA, Manners I (2012) Functional block copolymers: nanostructured materials with emerging applications. Angew Chem Int Ed 51:7898–7921

3. Petrova S, Jäger E, Konefał R, Jäger A, Venturini CG, Spěváček J, Pavlova E, Štěpánek P (2014) Novel poly(ethylene oxide monomethyl ether)-b-poly(ε-caprolactone) diblock copolymers containing a pH-acid labile ketal group as a block linkage. Polym Chem 5:3884–3893
4. Allen C, Maysinger D, Eisenberg A (1999) Nano-engineering block copolymer aggregates for drug delivery. Colloids Surfaces B Biointerfaces 16:3–27
5. Liu H, Xu J, Jiang J, Yin J, Narain R, Cai Y, Liu S (2007) Syntheses and micellar properties of well-defined amphiphilic AB2 and A2B Y-shaped miktoarm star copolymers of e-caprolactone and 2-(dimethylamino)ethyl methacrylate. J Polym Sci Part A-Polymer Chem 45:1446–1462
6. Ge Z, Cai Y, Yin J, Zhu Z, Rao J, Liu S (2007) Synthesis and "schizophrenic" micellization of double hydrophilic AB4 miktoarm star and AB diblock copolymers: structure and kinetics of micellization. Langmuir 23:1114–1122
7. Forder C, Patrickios CS, Armes SP, Billingham NC (1996) Synthesis and aqueous solution characterization of dihydrophilic block copolymers of methyl vinyl ether and methyl triethylene glycol vinyl ether. Macromolecules 29:8160–8169
8. Wang XS, Jackson R, Armes SP (2000) Facile synthesis of acidic copolymers via atom transfer radical polymerization in aqueous media at ambient temperature. Macromolecules 33:255–257
9. Colfen H (2001) Double-hydrophilic block copolymers: synthesis and application as novel surfactants and crystal growth modifiers. Macromol Rapid Commun 22:219–252
10. Blanazs A, Warren NJ, Lewis AL, Armes SP, Ryan AJ (2011) Self-assembly of double hydrophilic block copolymers in concentrated aqueous solution. Soft Matter 7:6399–6403
11. Casse O, Shkilnyy A, Linders J, Mayer C, Haussinger D, Volkel A, Thunemann AF, Dimova R, Colfen H, Meier W, Schlaad H, Taubert A (2012) Solution behavior of double-hydrophilic block copolymers in dilute aqueous solution. Macromolecules 45:4772–4777
12. Brosnan SM, Schlaad H, Antonietti M (2015) Aqueous self-assembly of purely hydrophilic block copolymers into giant vesicles. Angew Chem Int Ed 54:975–978
13. Rapoport N (2007) Physical stimuli-responsive polymeric micelles for anti-cancer drug delivery. Prog Polym Sci 32:962–990
14. Branco MC, Schneider JP (2009) Self-assembling materials for therapeutic delivery. Acta Biomater 5:817–831
15. Harada A, Kataoka K (1998) Novel polyion complex micelles entrapping enzyme molecules in the core: preparation of narrowly-distributed micelles from lysozyme and poly(ethylene glycol)-poly(aspartic acid) block copolymer in aqueous medium. Macromolecules 31:288–294
16. Sakai K, Smith EG, Webber GB, Baker M, Wanless EJ, Bütün V, Armes SP, Biggs S (2006) Characterizing the pH-responsive behavior of thin films of diblock copolymer micelles at the silica/aqueous solution interface. Langmuir 22:8435–8442
17. Cao PF, Mangadlao JD, Advincula RC (2015) Stimuli-responsive polymers and their potential applications in oil-gas industry. Polym Rev 55:706–733
18. Fujishige S, Kubota K, Ando I (1989) Phase transition of aqueous solutions of poly(N-isopropylacrylamide) and poly(N-isopropylmethacrylamide). J Phys Chem 93:3311–3313
19. Idziak I, Avoce D, Lessard D, Gravel D, Zhu XX (1999) Thermosensitivity of aqueous solutions of poly(N,N -diethylacrylamide). Macromolecules 32: 1260–1263
20. Maeda Y, Nakamura T, Ikeda I (2002) Hydration and phase behavior of poly(N-vinylcaprolactam) and poly(N-vinylpyrrolidone) in water. Macromolecules 32:217–222
21. Han X, Zhang X, Zhu H, Yin Q, Liu HL, Hu Y (2013) Effect of composition of PDMAEMA-b-PAA block copolymers on their pH- and temperature-responsive behaviours. Langmuir 29:1024–1034
22. Thavenesan T, Herbert C, Plamper FA (2014) Insight in the phase separation peculiarities of poly(dialkylaminoethyl methacrylate)s. Langmuir 30:5609–5619
23. Aseyev VO, Tenhu H, Winnik FM (2006) Temperature dependence of the colloidal stability of neutral amphiphilic polymers in water. Adv Polym Sci 196:1–85
24. Hoogenboom R, Thijs HML, Jochems MJHC, van Lankvelt BM, Fijten MVM, Schubert US (2008) Tuning the LCST of poly(2-oxazoline)s by varying composition and molecular weight: alternatives to poly(N-isopropylacrylamide)? Chem Commun:5758–5760
25. Monduzzi M, Lampis S, Murgia S, Salis A (2014) From self-assembly fundamental knowledge to nanomedicine developments. Adv Colloid Interf Sci 205:48–67
26. Spěváček J (2009) NMR investigations of phase transition in aqueous polymer solutions and gels. Curr Opin Colloid Interface Sci 14: 184–191 and references therein
27. Yoo MK, Jang MK, Nah JW, Park MR, Cho CS (2006) Effect of temperature on the mobility of core-shell-type nanoparticles composed of poly(γ-benzyl-L-glutamate) and poly(N-isopropylacrylamide). Macromol Chem Phys 207:528–535
28. Hiller W, Engelhardt N, Kampmann AL, Degen P, Weberskirch R (2015) Micellization and mobility of amphiphilic poly(2-oxazoline) based block copolymers characterized by ^{1}H NMR spectroscopy. Macromolecules 48:4032–4045
29. Spěváček J, Hanyková L, Labuta J (2011) Behavior of water during temperature-induced phase separation in poly(vinyl methyl ether) aqueous solutions. NMR and optical microscopy study. Macromolecules 44:2149–2153
30. Spěváček J, Dybal J, Starovoytova L, Zhigunov A, Sedláková Z (2012) Temperature-induced phase separation and hydration in poly(N-vinylcaprolactam) aqueous solutions: a study by NMR and IR spectroscopy, SAXS, and quantum-chemical calculations. Soft Matter 8:6110–6119
31. Ryu JG, Jeong YI, Kim IS, Lee JH, Nah JW, Kim SH (2000) Clonazepam release from core-shell type nanoparticles of poly(epsilon-caprolactone)/poly(ethylene glycol)/poly(epsilon-caprolactone) triblock copolymers. Int J Pharm 200:231–242
32. Lin P, Clash C, Pearce EM, Kwei TK, Aponte MA (1988) Solubility and miscibility of poly(ethyl oxazoline). J Polym Sci Part B Polym Phys 26:603–619
33. Christova D, Velichkova R, Loos W, Goethals EJ, Du Prez F (2003) New thermo-responsive polymer materials based on poly(2-ethyl-2-oxazoline) segments. Polymer 44:2255–2261
34. Bauer M, Lautenschlaeger C, Kempe K, Tauhardt L, Schubert US, Fischer D (2012) Poly(2-ethyl-2-oxazoline) as alternative for the stealth polymer poly(ethylene glycol): comparison of in vitro cytotoxicity and hemocompatibility. Macromol Biosci 12:986–998
35. Velander WH, Madurawe RD, Subramanian A, Kumar G, Sinai-Zingde G, Riffle JS, Orthner CL (1992) Polyoxazoline-peptide adducts that retain antibody avidity. Biotechnol Bioeng 39:1024–1030
36. Petrova S, Venturini CG, Jäger A, Jäger E, Černoch P, Kereïche S, Kováčik L, Raška I, Štěpánek P (2015) Novel thermo-responsive double-hydrophilic and hydrophobic MPEO-b-PEtOx-b-PCL triblock terpolymers: synthesis, characterization and self-assembly studies. Polymer 59:215–225
37. Petrova S, Venturini CG, Jäger A, Jäger E, Hrubý M, Pavlova E, Štěpánek P (2015) Supramolecular self-assembly of novel thermo-responsive double-hydrophilic and hydrophobic Y-shaped [MPEO-b-PEtOx-b-$(PCL)_2$] terpolymers. RSC Adv 5:62844–62854
38. Farrar TC, Becker ED (1971) Pulse and Fourier transform NMR. Academic Press pp:27–29
39. Spěváček J, Hanyková L (2005) ^{1}H NMR study on the hydration during temperature-induced phase separation in concentrated poly(-vinyl methyl ether)/D_2O solutions. Macromolecules 38:9187–9191

40. Gottlieb HE, Kotlyar V, Nudelman A (1997) NMR chemical shifts of common laboratory solvents as trace impurities. J Org Chem 62: 7512–7515
41. Sinha VR, Bansal K, Kaushik R, Kumria R, Trehan A (2004) Poly-ϵ-caprolactone microspheres and nanospheres: an overview. Int J Pharm 278:1–23
42. Li LY, He WD, Li J, Zhang BY, Pan TT, Sun XL, Ding ZL (2010) Shell-cross-linked micelles from PNIPAM-*b*-$(PLL)_2$ Y-shaped miktoarm star copolymer as drug carriers. Biomacromolecules 11: 1882–1890
43. Yang L, Hu X, Wang W, Liu S, Sun T, Huang Y, Jing X, Xie Z (2014) Y-shaped block copolymer (methoxy-poly(ethylene glycol)$_2$-b-poly(L-glutamic acid): preparation, self-assembly, and use as drug carriers. RSC Adv 4:41588–41596
44. Bovey FA, Mirau PA (1996) NMR of polymers. Academic Press, San Diego, p. 16
45. Bovey FA (1972) High resolution NMR of macromolecules. Academic Press, New York Chapter 1
46. Rusu M, Wohlrab S, Kuckling D, Möhwald H, Schönhoff M (2006) Coil-to-globule transition of PNIPAM graft copolymers with charged side chains: a ^{1}H and ^{2}H NMR and spin-relaxation study. Macromolecules 39:7358–7363
47. Hanyková L, Labuta J, Spěváček J (2006) NMR study of temperature-induced phase separation and polymer-solvent interactions in poly(vinyl methyl ether)/D_2O/ethanol solutions. Polymer 47:6107–6116
48. Hanyková L, Spěváček J, Ilavský M (2001) ^{1}H NMR study of thermotropic phase transition of linear and crosslinked poly(vinyl methyl ether) in D_2O. Polymer 42:8607–8612
49. Díez-Peña E, Quijada-Garrido I, Barrales-Rienda JM, Wilhelm M, Spiess HW (2002) NMR studies of the structure and dynamics of polymers gels based on *N*-isopropylacrylamide (N-iPAAm) and methacrylic acid (MAA). Macromol Chem Phys 203:491–502
50. Wang N, Ru G, Wang L, Feng J (2009) ^{1}H MAS NMR studies of the phase separation of poly(*N*-isopropylacrylamide) gel in binary solvents. Langmuir 25:5898–5902
51. Alam TM, Childress KK, Pastoor K, Rice CV (2014) Characterization of free, restricted and entrapped water environments in poly(*N*-isopropyl acrylamide) hydrogels via ^{1}H HRMAS PFG NMR spectroscopy. J Polym Sci B Polym Phys 52:1521–1527
52. Hofmann CH, Plamper FA, Scherzinger C, Hietala S, Richtering W (2013) Cononsolvency revisited: solvent entrapment by *N*-isopropylacrylamide and *N,N*-diethylacrylamide microgels in different water/methanol mixtures. Macromolecules 46:523–532
53. Hanyková L, Spěváček J, Radecki M, Zhigunov A, Šťastná J, Valentová H, Sedláková Z (2015) Structures and interactions in collapsed hydrogels of thermoresponsive interpenetrating polymer networks. Colloid Polym Sci 293:709–720
54. Radecki M, Spěváček J, Zhigunov A, Sedláková Z, Hanyková L (2015) Temperature-induced phase transition in hydrogels of interpenetrating networks of poly(*N*-isopropylacrylamide) and polyacrylamide. Eur Polym J 68:68–79

Electronic supplementary material (ESM)

Thermoresponsive behavior of terpolymers containing poly(ethylene oxide), poly(2-ethyl-2-oxazoline) and poly(ε-caprolactone) blocks in aqueous solutions: an NMR study

Rafał Konefał • Jiří Spěváček (✉) • Eliezer Jäger • Svetlana Petrova

Institute of Macromolecular Chemistry, Academy of Sciences of the Czech Republic, Heyrovsky Sq. 2, 162 06 Prague 6, Czech Republic
e-mail: spevacek@imc.cas.cz

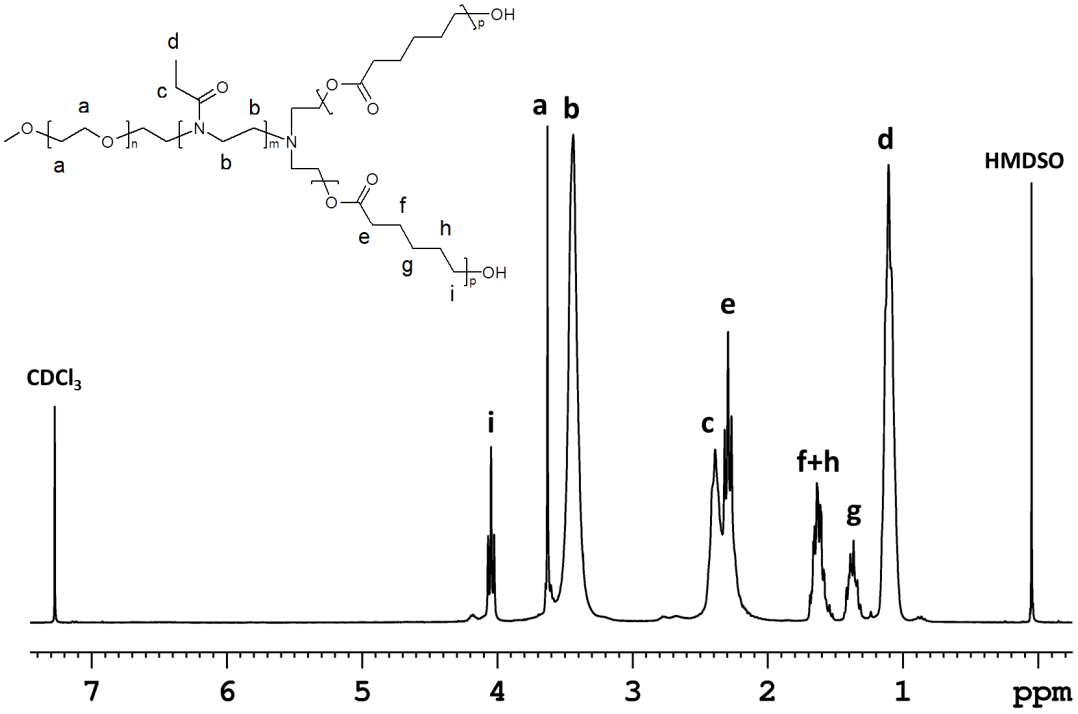

Fig. S1 300.1 MHz ^{1}H NMR spectrum of [PEO_{44}-*b*-$PEtOx_{252}$-*b*-$(PCL_{87})_2$] terpolymer in $CDCl_3$ measured at 295 K.

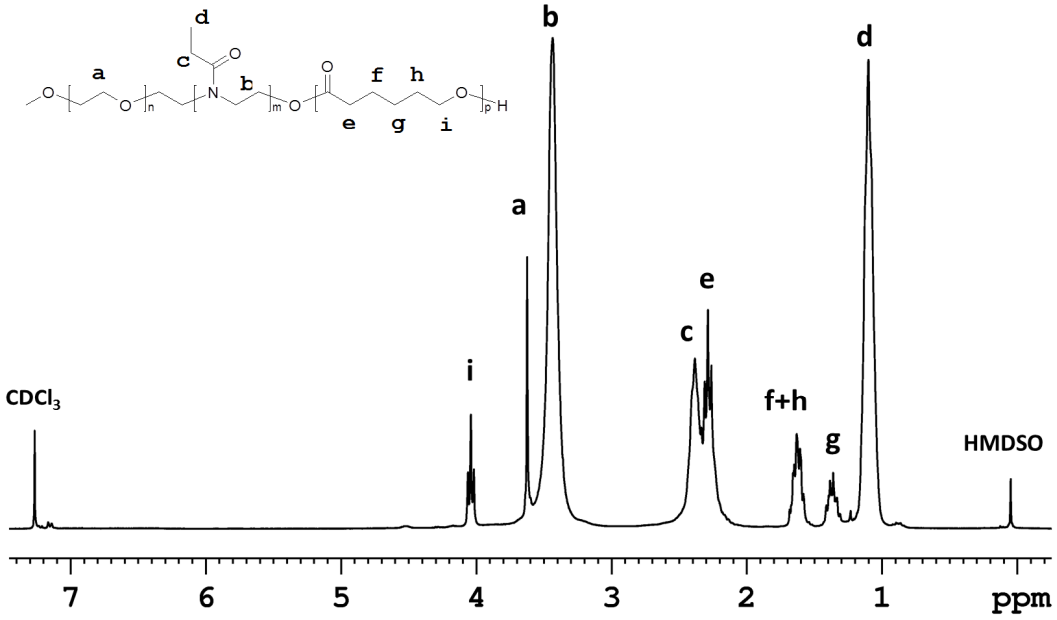

Fig. S2 300.1 MHz ^{1}H NMR spectrum of PEO_{44}-*b*-$PEtOx_{252}$-*b*-PCL_{35} terpolymer in $CDCl_3$ at 295 K.

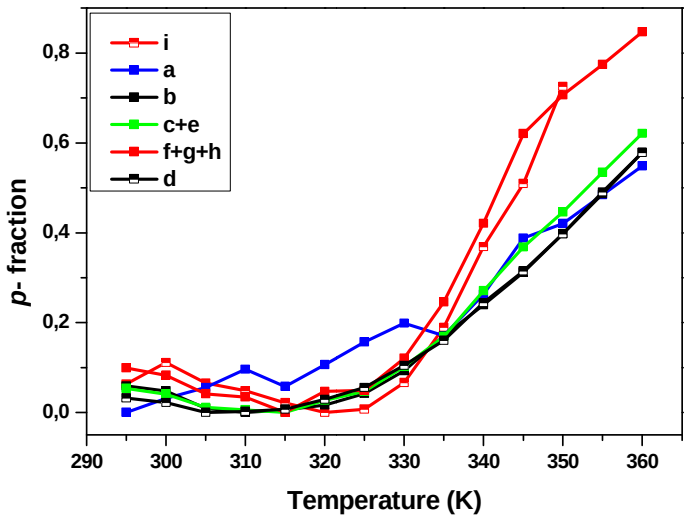

Fig. S3 Temperature dependences of *p*-fraction for various proton groups in [PEO_{44}-*b*-$PEtOx_{252}$-*b*-$(PCL_{87})_2$] NPs D_2O solution (c=1.5 wt%).

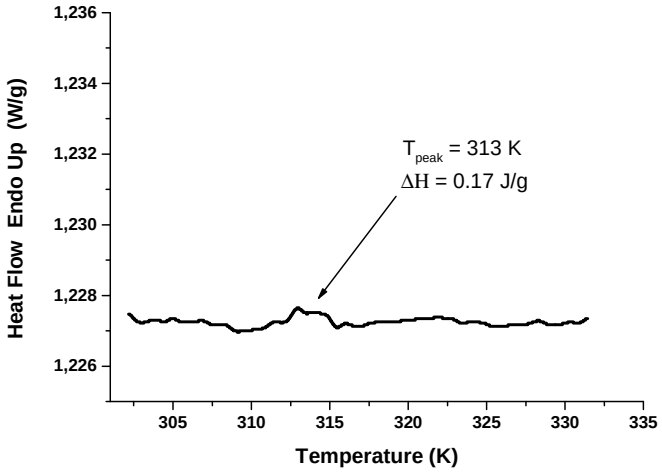

Fig. S4 DSC thermogram (thermodynamic C_p curve) of PEO_{44}-*b*-$PEtOx_{252}$-*b*-PCL_{35} NPs in D_2O solution (c=0.5 wt%) obtained by temperature modulated technique StepScan with Perkin-Elmer Q 8500 instrument (ΔT = 0.5 K, heating rate 5 K/min).

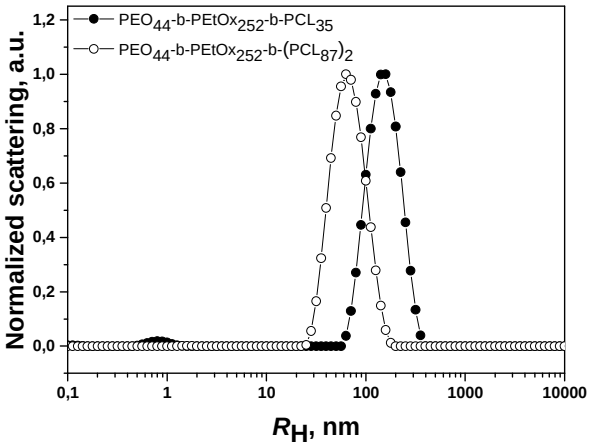

Fig. S5 Normalized intensity versus size distribution of the linear and Y-shape terpolymer NPs in D_2O (c = 0.5 wt%) measured at angle 90° and 303 K.

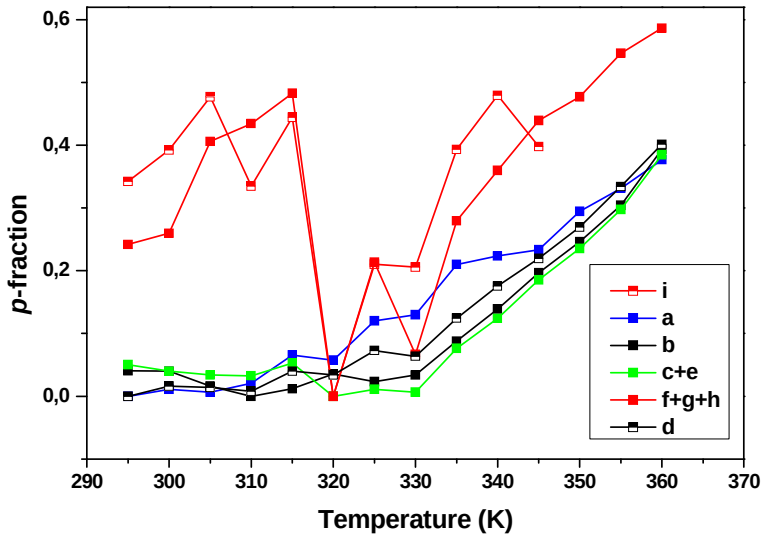

Fig. S6 Temperature dependences of *p*-fraction of various proton groups in PEO_{44}-*b*-$PEtOx_{252}$-*b*-PCL_{35} NPs D_2O solution (c=1.5 wt%).

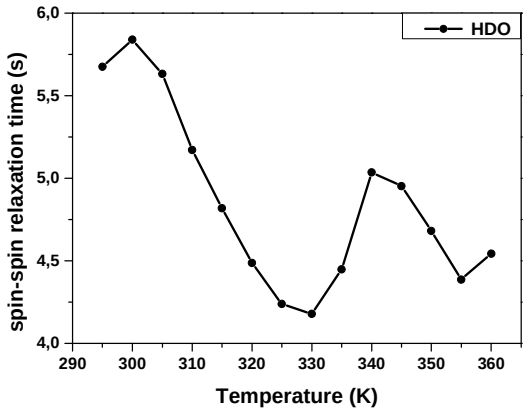

Fig. S7 Temperature dependence of ^1H spin-spin relaxation time T_2 of HDO in [PEO_{44}-*b*-$PEtOx_{252}$-*b*-$(PCL_{131})_2$] NPs D_2O solution (c=0.5 wt%).

Table S1 Spin-spin relaxation time T_2 of HDO in NPs D_2O solutions.

T [K]	T_2 relaxation time of HDO [s]					
	$[PEO_{44}$-*b*-$PEtOx_{252}$-*b*-$(PCL_{87})_2]$ c=1.5 wt%		PEO_{44}-*b*-$PEtOx_{252}$-*b*-PCL_{35} c=0.5 wt%		PEO_{44}-*b*-$PEtOx_{252}$-*b*-PCL_{35} c=1.5 wt%	
295	3.1		3.6		1.7	
300	3.1		3.8		2.5	
305	2.9		3.9		3.6	
310	2.8		4.0		4.2	
315	3.0		4.0		5.0	
320	3.0 73%	0.0048 27%	3.9		5.3 89%	0.0243 11%
325	2.9 36%	0.0030 64%	3.9		5.1 54%	0.0047 46%
330	2.9 76%	0.0063 24%	5.0 12%	0.0172 88%	4.5 78%	0.0140 22%
335	3.3 71%	0.0067 29%	6,9 44%	0.0082 56%	3.9 71%	0.0125 29%
340	4.0 55%	0.0095 44%	7.0 41%	0.0094 59%	5.0 75%	0.0114 25%
345	4.3 72%	0.0206 28%	7.2 50%	0.0084 50%	4.9 89%	0.0387 11%
350	4.6 54%	0.0062 46%	7.4 27%	0.0071 73%	5.3 74%	0.0113 26%
355	5.1 76%	0.0097 24%	7.3 36%	0.0067 64%	5.2 68%	0.0052 32%
360	4.6 41%	0.0052 59%	7.1 45%	0.0089 55%	4.6 81%	0.0371 19%

Publication 3

J. Spěváček, **R. Konefał**, J. Dybal, E. Čadová, J. Kovářová

Thermoresponsive behavior of block copolymers of PEO and PNIPAm with different architecture in aqueous solutions: a study by NMR, FTIR, DSC and quantum-chemical calculations.
European Polymer Journal, **2017**, 94, 471-483.

European Polymer Journal 94 (2017) 471–483

Contents lists available at ScienceDirect

European Polymer Journal

journal homepage: www.elsevier.com/locate/europolj

Thermoresponsive behavior of block copolymers of PEO and PNIPAm with different architecture in aqueous solutions: A study by NMR, FTIR, DSC and quantum-chemical calculations

Jiří Spěváček*, Rafał Konefał, Jiří Dybal, Eva Čadová, Jana Kovářová

Institute of Macromolecular Chemistry, Academy of Sciences of the Czech Republic, Heyrovsky Sq. 2, 162 06 Prague 6, Czech Republic

ARTICLE INFO

Keywords:
Thermoresponsive polymer
Diblock copolymer PEO-*b*-PNIPAm
Y-shape triblock copolymer PEO-*b*-$(PNIPAm)_2$
Aqueous solution
NMR
FTIR

ABSTRACT

Temperature behavior of D_2O solutions of thermoresponsive diblock poly(ethylene oxide) (PEO)-*b*-poly(*N*-isopropylacrylamide) (PNIPAm) copolymers and Y-shape triblock PEO-*b*-$(PNIPAm)_2$ copolymers was investigated and compared with the phase transition of the PNIPAm homopolymer by combination of NMR and ATR FTIR spectroscopy, DSC and model quantum-chemical calculations. It is shown that the phase transition and structures of PNIPAm component (forming micellar cores) are significantly affected not only by the presence of the PEO block but also by copolymer architecture. Both these factors affect energetics of the phase transition, influence of the polymer concentration and behavior of bound water at elevated temperatures. They also affect the degree of dehydration of PNIPAm segments (C═O groups) at temperatures above the phase transition which is higher for block copolymers (especially for the diblock) in comparison with PNIPAm homopolymer. NOESY NMR spectra likewise revealed influence of the architecture of the block copolymer on its conformational behavior in the pretransition region.

1. Introduction

It is well established that poly(*N*-isopropylacrylamide) (PNIPAm) and other acrylamide-based polymers, as well as other polymers with amphiphilic character (e.g., poly(*N*-vinylcaprolactam) (PVCL), poly(vinyl methyl ether)) show in aqueous solutions a lower critical solution temperature (LCST) which, especially at polymer concentrations $c \geq 1$ wt%, makes solutions milk-white turbid above the LCST [1,2]. For dilute solutions of PNIPAm, which is a most often investigated thermoresponsive polymer, a coil-globule transition was revealed by light scattering at the LCST [3,4], while for semidilute and concentrated solutions aggregation results in formation of larger globular-like structures called mesoglobules [2]. The transition is almost certainly connected with a changed balance between hydrophilic interactions (hydrogen bonding between polymer and water) and hydrophobic interactions which are also in connection with changes in local structure of water molecules surrounding polymer hydrophobic groups [5,6]. Their thermosensitivity makes these homopolymers and copolymers attractive for a wide range of biomedical and technological applications, e.g., as drug release polymers [1,2,7]. A similarity to thermal denaturation of proteins in aqueous solution also makes them interesting from an academic point of view.

Block copolymers where only one component is thermoresponsive can form in aqueous solutions various self-assembled structures. Diblock copolymers poly(ethylene oxide) (PEO)-*b*-PNIPAm can form in aqueous solutions at elevated temperatures (above the transition temperature of PNIPAm component) micelles [8–12], vesicles [13,14] or gels [15,16], depending on copolymer

* Corresponding author.
E-mail address: spevacek@imc.cas.cz (J. Spěváček).

http://dx.doi.org/10.1016/j.eurpolymj.2017.07.034
Received 25 May 2017; Received in revised form 12 July 2017; Accepted 24 July 2017
Available online 25 July 2017
0014-3057/

concentration and molecular weight. A rich and complex aggregation and phase behavior of these systems was established [11–18]. Thermoresponsive polymersome assembly of a PEO-*b*-PNIPAm diblock copolymer was reported recently [19]. Formation of micelles [7], flowerlike micelles [20] and nanoparticles [21] has been reported also for PNIPAm-*b*-PEO-*b*-PNIPAm triblock copolymers. Van Durme at al. used DSC to compare copolymers of PNIPAm with either PEO blocks or grafts from the point of view of their thermal response rate [22].

Concerning methods used in studies of diblock and triblock PEO – PNIPAm copolymers, scattering methods, especially light scattering, predominated [9–13,16,19–21]. They have shown that hydrodynamic radius of the micelles (nanoparticles, aggregates) formed at elevated temperatures is in the range 20–180 nm. Though power of NMR and infrared (IR) spectroscopy in investigation of PNIPAm and its copolymers in aqueous media is well established, because they can provide important information on phase-separated globular structures and interactions in these systems [23–33], they were applied to block copolymers of PEO and PNIPAm only in several cases [12,20,21,34,35]. In the present work we used NMR and FTIR spectroscopy combined with DSC and quantum-chemical calculations on model systems to present in-depth investigations on a series of samples of both diblock PEO-*b*-PNIPAm copolymers with various length of the PNIPAm block and Y-shape triblock PEO-*b*-$(PNIPAm)_2$ copolymers with different architecture in D_2O solutions. This enabled us, in comparison with behavior of PNIPAm homopolymer, to characterize the effects of the presence of the PEO block and copolymer architecture on structures of the PNIPAm component and on interactions (especially hydration) in these systems at various temperatures.

2. Experimental

2.1. Samples: synthesis and characterization

Synthetic route is illustrated in Scheme S1 in Supplementary Material. Macroinitiators for the synthesis of the PEO-*b*-PNIPAm diblock and PEO-*b*-$(PNIPAm)_2$ triblock copolymers were prepared by elimination reaction of poly(ethylene glycol) monomethyl ether 5000 (Sigma-Aldrich, M_n = 5000) with chloroacetyl chloride (alternatively 2-bromoisobutyryl bromide or 2-chloropropionyl chloride) or dichloroacetyl chloride, respectively. PEO-*b*-PNIPAm diblock and Y-shape PEO-*b*-$(PNIPAm)_2$ triblock copolymers were synthesized by means of single-electron transfer living radical polymerization method [36]. The polymerization of NIPAm on PEG 5000 macroinitiator was carried out in the mixture DMF/H_2O = 3/1 in presence of tris(2-(dimethylamino)ethyl)amine (Me_6TREN) and CuCl at 313 K for 5.5–19 h; molar ratios of components were PEG macroinitiator/NIPAm/CuCl/Me_6TREN = 1/400/2/4. The products were isolated by repeated precipitation into petrolether and diethylether. Details of the synthesis of PEG macroinitiators and block copolymers of PEO and PNIPAm are described in the Supplementary Material.

To confirm the Y-shape structure of PEO-*b*-$(PNIPAm)_2$ copolymers, ^1H and ^{13}C NMR spectra of the PEO_{114}-*b*-$(PNIPAm_{165})_2$ copolymer in D_2O solution (c = 20% wt) were measured with the aim to detect signals of methine proton and carbon in the (CO)CH$(CH_2)_2$ structure at the branching point. Unfortunately, in 1D spectra the respective signals, which are expected at ≈1 ppm [37] in the ^1H NMR spectrum and at ≈41 ppm [38] in the ^{13}C NMR spectrum, are overlapped by strong peaks from repeating units of the

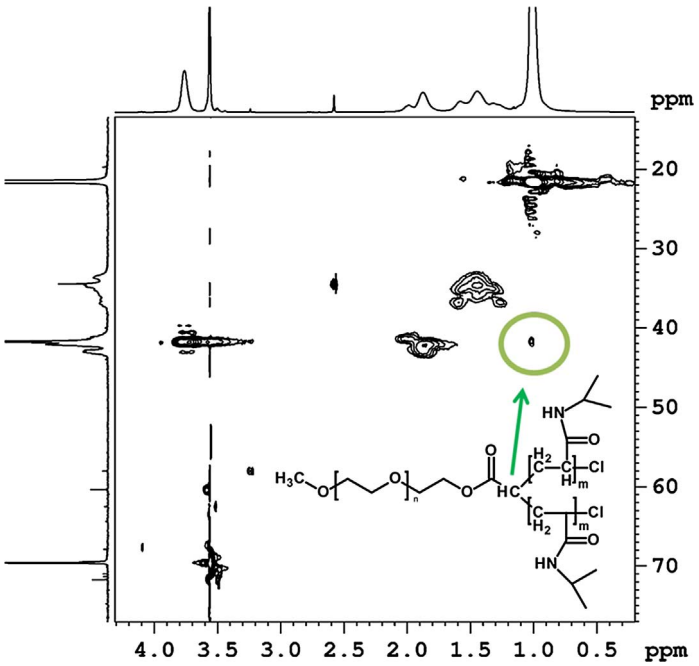

Fig. 1. ^1H-^{13}C HSQC 2D NMR spectrum of the PEO_{114}-*b*-$(PNIPAm_{165})_2$ in D_2O (*c* = 20 wt%).

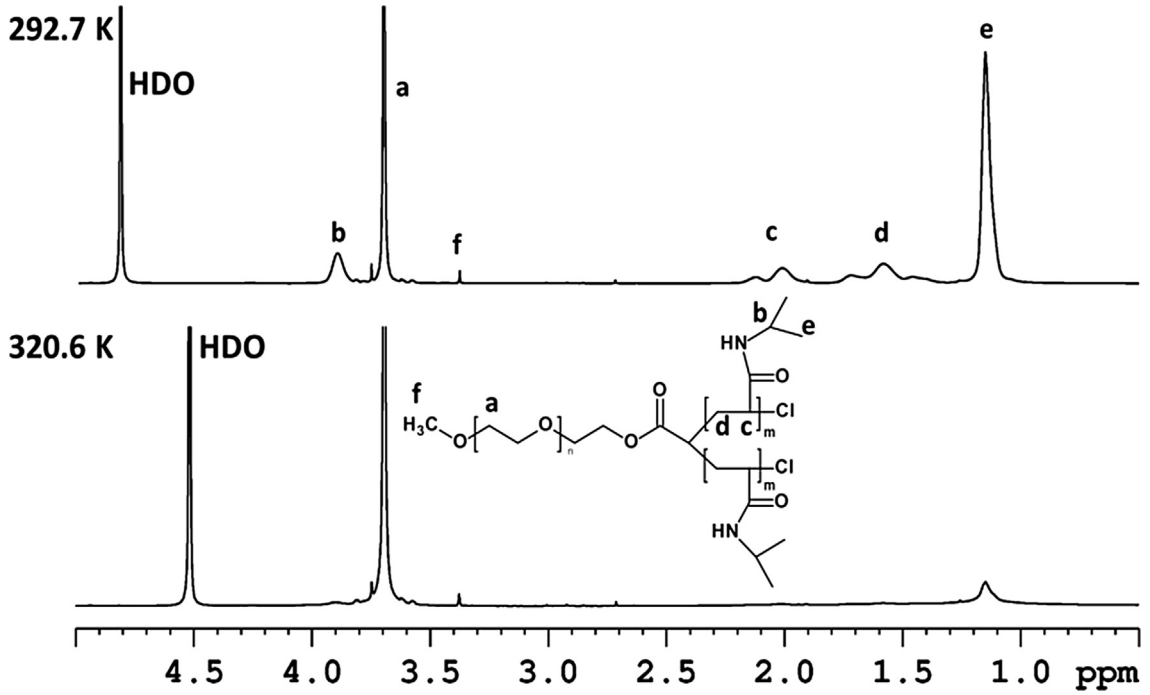

Fig. 2. ^{1}H NMR spectra of PEO_{114}-*b*-$(PNIPAm_{47})_2$ block copolymer in D_2O solution (c = 5 wt%) measured at 292.7 and 320.6 K under the same instrumental conditions.

block copolymer. For this reason, 2D ^{1}H-^{13}C HSQC (hetero single-quantum coherence) NMR spectrum was measured in which cross-peaks show correlation between respective carbon and directly attached protons. In this spectrum, which is shown in Fig. 1, the desired cross-peak (marked by the green circle) was detected, so confirming the Y-shape structure of the PEO-*b*-$(PNIPAm)_2$ copolymers.

All samples were characterized by ^{1}H NMR spectroscopy and size-exclusion chromatography (SEC). From integrated intensities of NMR signals of PEO protons and CH_3 protons of the PEO end-group at 3.38 ppm (cf. Fig. 2) we confirmed that the length of PEO block is 114 units (M_n = 5000). Molar ratio of PEO and PNIPAm units in the resulting block copolymers was determined from ^{1}H NMR spectra recorded at room temperature by using integrated intensities of the signal of PEO protons and signals of isopropyl CH or CH_3 protons of PNIPAm (cf. Fig. 2). For the length of PNIPAm block in three PEO-*b*-PNIPAm copolymers we then obtained values 109, 154 and 249 units. The length of PNIPAm block in two Y-shape PEO-*b*-$(PNIPAm)_2$ copolymers was 47 and 165 units. Similarly as other authors [10,11,13,21,36] dealing with block copolymers of PEO and PNIPAm, for the characterization of the distribution of molecular weights by SEC first we also used tetrahydrofuran (THF) as the mobile phase and polystyrene standards for calibration. These measurements have shown a virtually unimodal distribution with relatively narrow polydispersity (1.1–1.3) but only apparent values of molecular weight M_n were obtained in THF. They were not only significantly smaller in comparison with M_n values calculated from copolymer composition as determined by NMR, but even smaller than M_n of the PEO block, even using a procedure suggested by Ganachaud et al. [39]. We assume that unrealistically small M_n values can be due to the combination of two factors: (*i*) adsorption of copolymer on the column and subsequent elution at longer times; (*ii*) calibration on polystyrene standards where differences in molecular weight can amount up to a factor of three [40]. In connection with these facts we used for determination of the molecular weights of the block copolymers by SEC a methanol and sodium acetate buffer (0.3 M, pH 6.5) mixture (80:20 vol%, flow rate of 0.5 ml/min) as the mobile phase [41]. HPLC Ultimate 3000 system (Dionex, USA) equipped with a GPC column (TSKgel G4000SWxl 300 × 7.8 mm, 8 μm) was used. Three detectors, UV/vis, refractive index (RI) Optilab-rEx, and multiangle light scattering (MALS) DAWN EOS (Wyatt Technology Co., USA) were employed. SEC traces and values of M_n and PDI are shown in Fig. S1 and Table S1, respectively, in the Supplementary Material. Fig. S1 shows in most cases an unimodal distribution with exception of PEO_{114}-*b*-$PNIPAm_{109}$ where a bimodal distribution was detected. Table S1 shows a very good agreement between M_n values obtained by NMR and values determined by SEC for all diblock copolymers but for PEO_{114}-*b*-$PNIPAm_{109}$ sample this holds only for the minor component. The value M_n = 91000 of the major component in this sample is unrealistically high and at variance with the NMR spectrum of this sample in D_2O solution (Fig. S2 in the Supplementary Material) which clearly shows that molar ratio of PEO and PNIPAm units in this copolymer is close to 1:1. The major SEC component in this sample very probably corresponds to aggregates which are formed in the methanol/sodium acetate buffer mixture, possibly because of the so-called cononsolvency effect [42]. The presence of aggregates in this medium was confirmed for PEO_{114}-*b*-$PNIPAm_{109}$ sample by dynamic light scattering (DLS) measurements on ALV-6010 correlator (Fig. S3 in the Supplementary Material). For the Y-shape PEO_{114}-*b*-$(PNIPAm_{165})_2$ copolymer Table S1 shows M_n and PDI values obtained with DMF as the mobile phase and calibration on polystyrene standards because M_n value with methanol/sodium

acetate buffer mixture was unrealistically very high, evidently again due to aggregation. From Table S1 it follows that PDI values were in the range 1.1–1.4.

The PNIPAm homopolymer was prepared by free radical polymerization of NIPAm monomer in ethanol at 343 K for 24 h using 2,2′-azobis(2-methylpropionitrile) (ABIN, Fluka) as initiator. The product was isolated by precipitation into hexane and repeated precipitation into diethylether. ^{1}H NMR spectrum of this homopolymer in solution recorded at room temperature is the same as spectra of PNIPAm blocks in investigated block copolymers showing the same tacticity (atactic chains) in both cases. Molecular weight determined by SEC (with Superose 6 (Amersham Biosciences) on a HPLC Shimadzu system equipped with UV, a Optilab rEX differential refractometer, and MALS DAWN® 8™ (Wyatt Technology, USA) detectors; a 0.3 M acetate buffer (CH_3COONa/CH_3COOH; pH 6.5): M_n = 35,480; M_w/M_n = 1.6. Therefore the number-average degree of polymerization (314) is of the same order as respective values for PNIPAm blocks in most of the investigated block copolymers.

2.2. NMR measurements

1D ^{1}H NMR spectra were recorded with Bruker Avance III 600 spectrometer operating at 600.2 MHz. Typical conditions were as follows: π/2 pulse width 10 μs, relaxation delay 10 s, spectral width 15 kHz, acquisition time 2.18 s, 16 scans. The integrated intensities were determined with spectrometer integration software with an accuracy of ± 1%. 2D ^{1}H-^{1}H nuclear Overhauser effect spectroscopy (NOESY) NMR spectra were recorded on the same spectrometer with 4098 Hz spectral window in f_1 and f_2, and mixing times 100 ms and 400 ms. A total of 16 scans was accumulated over 512 t_1 increments with a relaxation delay of 10 s. 2D ^{1}H-^{13}C HSQC NMR spectrum was recorded with 8012 Hz ^{1}H and 32468 Hz ^{13}C spectral windows. A total of 70 scans were accumulated over 256 t_1 increments with a relaxation delay of 3 s. Temperature dependences of ^{1}H spin-spin relaxation times T_2 of HDO were measured on the same spectrometer using the CPMG pulse sequence 90°_x-(t_d-180°_y-t_d)$_n$-acquisition [43]. The relaxation delay between scans was 100 s, acquisition time 2.84 s, 2 scans. All obtained T_2 relaxation curves had monoexponential character. The relative error for T_2 values did not exceed ± 5%. In all NMR measurements temperature was maintained constant within ± 0.2 K in the range 292–333 K using a BVT-3000 temperature unit. Temperature was calibrated using a standard 80% ethylene glycol (DMSO-d_6) sample. The D_2O (Sigma, 99.9% of deuterium) solutions of the PEO-*b*-PNIPAm and PEO-*b*-(PNIPAm)$_2$ copolymers with polymer concentrations c = 0.2, 5 and 20 wt% were prepared for NMR measurements; D_2O solutions (c = 5 and 20 wt%) of the PNIPAm homopolymer were also studied. The solutions in 5 mm NMR tubes were degassed and sealed under nitrogen.

2.3. FTIR measurements

ATR FTIR spectra of the D_2O solutions (c = 10 wt%) of diblock and Y-shape triblock copolymers, as well as of PNIPAm homopolymer, and neat solid samples were collected on a Nicolet Nexus 870 FTIR spectrometer purged with dry air and equipped with a cooled mercury-cadmium-telluride (MCT) detector. The spectra were measured on a horizontal micro-ATR Golden Gate unit (SPECAC) with a diamond prism and a controlled heated top plate; spectral resolution was 4 cm^{-1}. All spectra were processed by the advanced ATR correction using the OMNIC™ software.

2.4. DSC measurements

DSC measurements on the D_2O solutions (c = 5 wt%) of investigated block copolymers and PNIPAm homopolymer were carried out using a Perkin-Elmer 8500 differential scanning calorimeter. The measurements were done with a heating rate 1 K/min in the temperature range from 283 K to 323 K.

2.5. Quantum-chemical calculations

The model calculations were carried out at the density functional theory (DFT) with the B3LYP functional and the 6-311 + G(d,p) basis set employing the Gaussian 09 program package [44]. In order to verify the reliability of the DFT results, the stable structures were then reoptimized at the Møller-Plesset (MP2) level of theory (MP2/6-31G(d)). Vibrational frequencies of the normal modes were calculated at the B3LYP/6-311 + G(d,p) level and the reported values were scaled by the standard scaling factor of 0.9688 [45].

3. Results and discussion

3.1. DSC

Examples of DSC thermograms as obtained for 5 wt% D_2O solutions of block copolymers of PEO and PNIPAm, as well as PNIPAm homopolymer, are shown in Fig. S4 in the Supplementary material. Endothermic transition was observed in all cases upon heating. The peak temperature T_{peak} and enthalpy ΔH of the transition were extracted from the thermograms and are shown in Table 1 where the last column shows ΔH values related to PNIPAm monomer unit. From Fig. S4 and Table 1 it follows that the shape of thermograms and transition temperatures T_{peak} are virtually the same for PNIPAm homopolymer and block copolymers with exception of Y-shape PEO_{114}-$(PNIPAm_{47})_2$ block copolymer where the transition is significantly broader and shifted 2 K towards higher temperatures. We did not confirm suggestion by Tang et al. [36] that transition temperature depends on the content of PEO units; though PEO content in the PEO_{114}-$PNIPAm_{109}$ diblock copolymer is almost twice larger in comparison with the PEO_{114}-$PNIPAm_{249}$ copolymer, transition

Table 1
Parameters obtained on D_2O solutions (c = 5 wt%) of investigated block copolymers and neat PNIPAm from DSC measurements, where T_{peak} is the peak temperature and ΔH is the enthalpy of the transition.

Sample	T_{peak} (K)	ΔH (J/g) of solution	ΔH (kJ/mol) of PNIPAm units
PNIPAm	307.5	2.43	5.5
PEO_{114}-*b*-$PNIPAm_{249}$	307.5	1.55	4.1
PEO_{114}-*b*-$PNIPAm_{154}$	308.0	1.15	3.4
PEO_{114}-*b*-$PNIPAm_{109}$	307.5	1.26	4.0
PEO_{114}-*b*-$(PNIPAm_{165})_2$	307.7	0.97	2.5
PEO_{114}-*b*-$(PNIPAm_{47})_2$	309.5	0.76	2.5

temperatures are the same in both cases. We assume that 2 K higher T_{peak} value found for the PEO_{114}-$(PNIPAm_{47})_2$ block copolymer is mainly due to the fact that the PNIPAm block is here relatively short; similar effect was reported also for low-molecular-weight PNIPAm homopolymers [46]. Looking on the ΔH (per PNIPAm monomer unit) values in the last column of Table 1, also in this case no direct dependence on the PEO content is visible. Values of ΔH (PNIPAm monomer unit) are the same for PEO_{114}-$PNIPAm_{249}$ and PEO_{114}-$PNIPAm_{109}$, and similarly the same for PEO_{114}-$(PNIPAm_{165})_2$ and PEO_{114}-$(PNIPAm_{47})_2$, though the PEO content in the second copolymer (in wt%) in these two pairs of the samples is twice or three times larger. On the other hand there is a clear effect of the presence of PEO block on ΔH values which are for block copolymers significantly smaller in comparison with the PNIPAm homopolymer. We can divide ΔH (PNIPAm monomer unit) values into three groups. The largest value ΔH = 5.5 kJ/mol was found for the PNIPAm homopolymer (similar ΔH values were reported for PNIPAm homopolymers also by other authors [5,47]). The second group are linear diblock copolymers where the average ΔH = 3.8 kJ/mol and the third group with the lowest ΔH = 2.5 kJ/mol are Y-shape triblock copolymers. These results unambiguously confirm significant effect of copolymer architecture on the energetics of the phase transition of PNIPAm segments. Tang et al. [36] also assumed such effect but they studied only one linear diblock copolymer and two Y-shaped triblock copolymers and therefore they could not exclude potential effect of the length of the PNIPAm block on the phase transition of diblock copolymers.

3.2. NMR spectroscopy

^{1}H NMR spectra of the Y-shape PEO-*b*-$(PNIPAm_{47})_2$ triblock copolymer in D_2O solution (c = 5 wt%) measured under the same instrumental conditions at two temperatures are shown in Fig. 2. The most meaningful effect observed in the spectrum measured at 320.6 K, i.e., above the LCST of PNIPAm homopolymer (around 306 K [1–3]), is a pronounced reduction of integrated intensities of all PNIPAm signals which virtually disappeared from the spectrum. Evidently, at 320.6 K the mobility of PNIPAm units is significantly reduced and the corresponding signals escape detection in high-resolution NMR spectra [28]. In contrast, the intensity of the PEO signal is not influenced by heating to 320.6 K. The same behavior as shown in Fig. 2 was observed also for other investigated block copolymers. This behavior at elevated temperatures is consistent with formation of micelles where immobilized PNIPAm blocks form a rather compact core and mobile PEO blocks form a shell of micelles [48].

From the temperature dependent integrated intensities of NMR signals it is possible to obtain the values of fraction p of PNIPAm units with substantially reduced mobility, i.e., units in the micellar core, using equation [28]

$$p = 1-(I/I_0) \quad (1)$$

where I is the integrated intensity of the definite PNIPAm signal at temperatures during or above the LCST transition and I_0 is the integrated intensity of this signal if no LCST transition occurs. For I_0 we took integrated intensities as obtained for the respective solution at 292.7 K and taking into account that the integrated intensities should decrease with reciprocal absolute temperature T [28], i.e., $I_0(T) = I_0^{292.7}(292.7/T)$ [34,49]. Temperature dependences of the fraction p for D_2O solutions (c = 5 wt%) of the investigated PEO - PNIPAm block copolymers and neat PNIPAm are shown in Fig. 3. We have found that temperature dependences of the fraction p determined from integrated intensities of various PNIPAm signals are the same so proving that p-fraction relates to PNIPAm units as a whole. From Fig. 3 it follows in accord with DSC results that the transition temperatures in most of the block copolymers are only slightly higher (up to ~ 1 K as indicated temperatures at $p_{max}/2$) with exception of the Y-shape PEO_{114}-*b*-$(PNIPAm_{47})_2$ copolymer where the transition is shifted 3 K towards higher temperatures. While the transition for the solution of PNIPAm is rather sharp (transition width 2 K), for block copolymers the transitions are broader (e.g., for PEO_{114}-*b*-$PNIPAm_{109}$ diblock the transition is approx. 7 K broad), and the largest transition width 12 K is again shown by the PEO_{114}-*b*-$(PNIPAm_{47})_2$ copolymer. For this sample maximum value of the p-fraction is reduced to p_{max} = 0.9; here 10% of PNIPAm units which retain high mobility probably correspond to PNIPAm blocks which are too short to participate in the phase transition [28].

Fig. 4 illustrates the effect of copolymer concentration on transition temperatures. While for the linear diblock copolymer (Fig. 4a) increase of the concentration to 20 wt% shifts the transition by 3.5 K towards lower temperatures, for the Y-shape triblock copolymer PEO-*b*-$(PNIPAm_{165})_2$ the effect of polymer concentration on the transition temperature is about twice smaller (1.5 K shift towards lower temperature for c = 20 wt%) (Fig. 4b). Behavior of this copolymer is similar to behavior of the PNIPAm homopolymer where increase of polymer concentration to 20 wt% results in the 1.3 K shift (Fig. 4c). Fig. S5 in the Supplementary Material then illustrates the fact that for all investigated block copolymers, i.e., both for diblock and Y-shape triblock copolymers, we did not observe any hysteresis when temperature dependences of ^{1}H NMR spectra were recorded during gradual heating and subsequent gradual cooling.

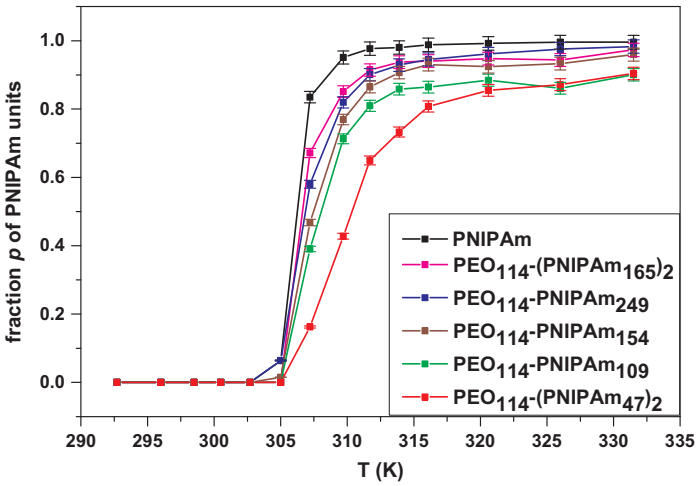

Fig. 3. Temperature dependences of the fraction p (relative error ± 2%) of PNIPAm units with significantly reduced mobility (units in micellar core) for block copolymers of PEO and PNIPAm, and for neat PNIPAm, in D_2O solutions (c = 5 wt%) during gradual heating.

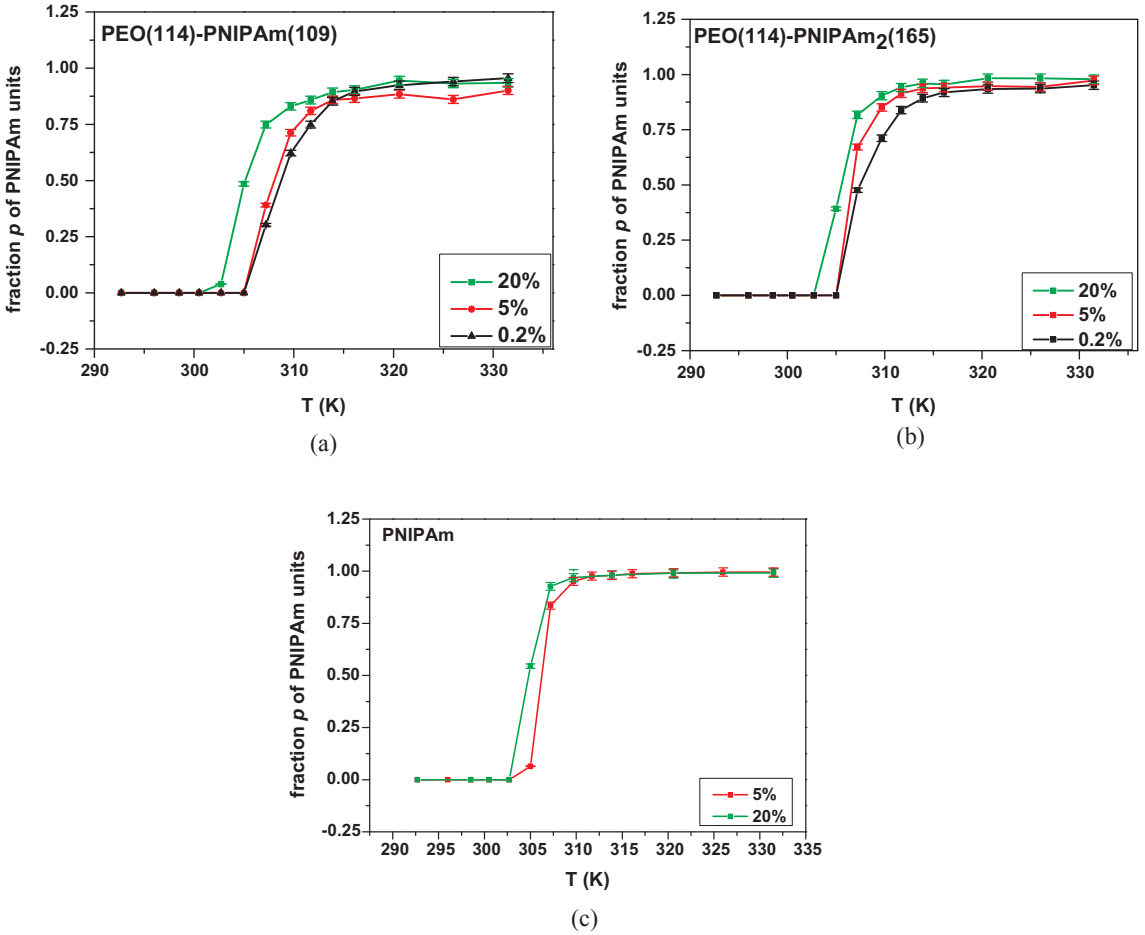

Fig. 4. Temperature dependences of the p-fraction (relative error ± 2%) of PNIPAm units for D_2O solutions of the block copolymers PEO_{114}-*b*-$PNIPAm_{109}$ (a) and PEO_{114}-*b*-$(PNIPAm_{165})_2$ (b), and for the PNIPAm homopolymer (c) with various polymer concentration during gradual heating.

Somewhat unexpected was our finding that there was no hysteresis even in the PNIPAm/D_2O solution (c = 5 wt%) (Fig. S5c in the Supplementary Material), although such hysteresis is frequently reported for aqueous solutions of PNIPAm and some other thermosensitive polymers [4,31,49–52].

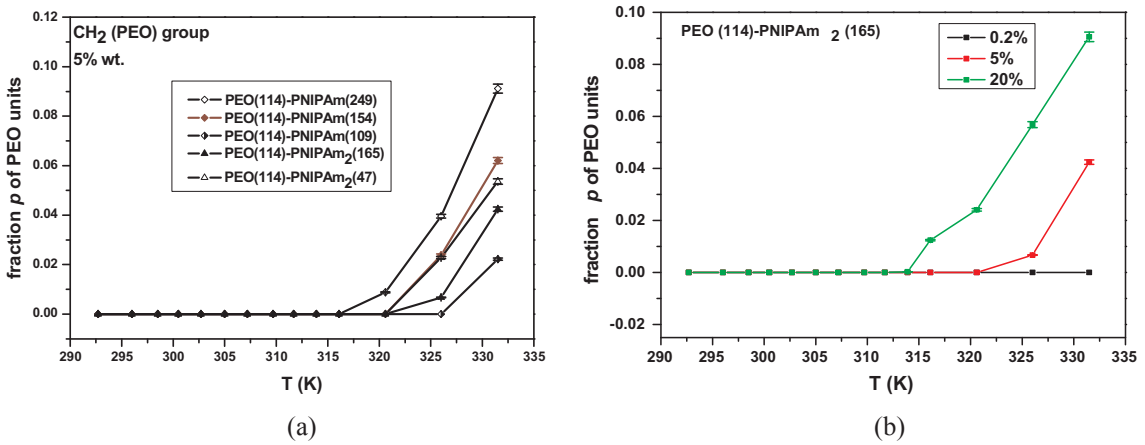

Fig. 5. Temperature dependences of the *p*-fraction (relative error ± 2%) of PEO units for various investigated block copolymers in D_2O solutions (c = 5 wt%) (a) and for the PEO_{114}-*b*-$(PNIPAm_{165})_2$ block copolymer in D_2O solutions with various polymer concentration (b).

Though both the shape and intensity of PEO signal is virtually unchanged at temperatures below 320 K, we revealed that its integrated intensity is reduced at higher temperatures. Temperature dependences of the *p*-fraction of PEO units which show significantly reduced mobility are for D_2O solutions (c = 5 wt%) of the investigated PEO – PNIPAm block copolymers depicted in Fig. 5a. Depending on the sample, the values of the *p*-fraction of PEO are at highest temperature (332 K) in the range 0.02–0.09. For diblock copolymers these values increase with increasing length of the PNIPAm block, while values of the *p*-fraction for two Y-shape block copolymers are very similar. As illustrated in Fig. 5b, *p*-fraction of PEO units significantly increases with increasing copolymer concentration so indicating a connection with aggregation of micelles which is promoted at higher concentrations.

Information on behavior of water during temperature-induced phase transition in D_2O solutions of thermoresponsive polymers can be obtained from measurements of ^1H spin-spin relaxation times T_2 of HDO molecules [28,49,53,54]. Fig. 6 shows that T_2 values of HDO in D_2O solutions of the diblock PEO_{114}-*b*-$PNIPAm_{249}$ copolymer and Y-shape PEO_{114}-*b*-$(PNIPAm_{165})_2$ triblock copolymer are at temperature 325 K (above the phase transition) significantly shorter than those at 295 K (below the transition). This shows that in these systems at temperatures above the transition there is a portion of HDO bound (confined) in a rather compact micellar core formed by PNIPAm segments. In all cases there was a single line of HDO in ^1H NMR spectrum and the T_2 relaxation curves were monoexponential, indicating a fast exchange between bound and free sites. The observed relaxation rates T_2^{-1} at temperatures above the transition are then given as [53,54]

$$(T_2)^{-1} = (1-f)(T_{2F})^{-1} + f\,(T_{2B})^{-1} \tag{2}$$

where subscripts F and B correspond to free and bound states, respectively, and f is the fraction of bound HDO. Fig. 6 shows also time

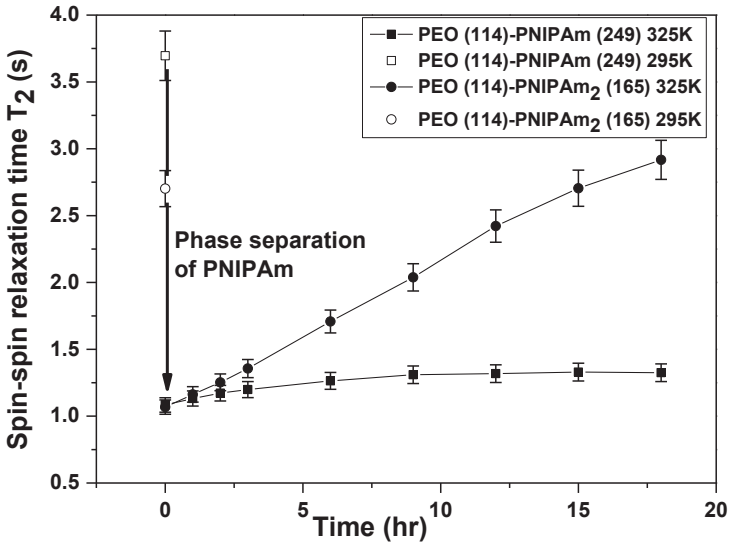

Fig. 6. Time dependences of ^1H spin-spin relaxation time T_2 (relative error ± 5%) of HDO in D_2O solutions (c = 5 wt%) of the PEO_{114}-*b*-$PNIPAm_{249}$ and PEO_{114}-*b*-$(PNIPAm_{165})_2$ block copolymers measured at 325 K. Open symbols show the respective T_2 values at 295 K.

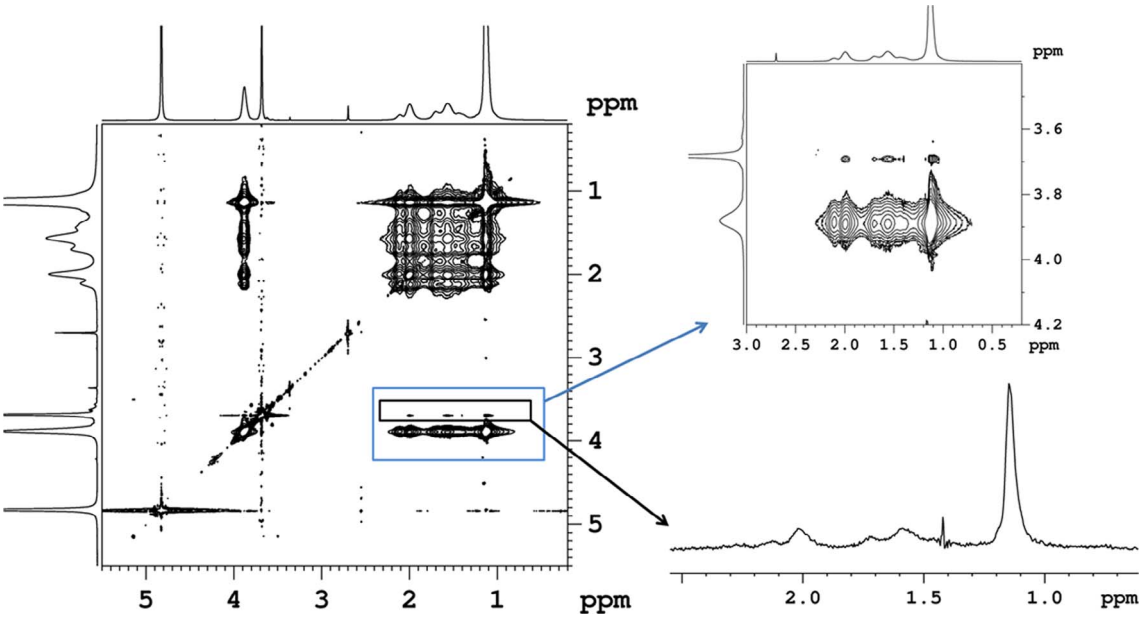

Fig. 7. 2D NOESY spectrum of PEO_{114}-*b*-$(PNIPAm_{165})_2$ Y-shape triblock copolymer in D_2O solution (c = 20 wt%) measured at 292.7 K with mixing time 400 ms. On the right up there are in detail crosspeaks between PEO protons and PNIPAm protons (main chain CH, CH_2 and isopropyl CH_3), on the right down there is 1D slice spectrum extracted from the PEO signal of the NOESY spectrum.

dependences of the T_2 values of HDO; during these measurements the sample was kept for all the time at 325 K. A very different behavior was found for solutions of the diblock copolymer and Y-shape triblock copolymer. In latter case a continuous increase of T_2 values with time was observed showing that water originally bound in the micellar core is with time slowly released from these structures. Similar behavior was observed recently for PVCL/D_2O solutions [49]. On the other hand, T_2 values of HDO in D_2O solution of diblock copolymer were virtually constant for 18 h and no release of water from micellar cores was detected during this period. Behavior of the diblock copolymer resembles behavior of PNIPAm homopolymer where at temperature above the LCST transition T_2 values of HDO were constant for 75 h [28,53].

In addition to temperature dependences of 1D NMR spectra, we measured also temperature dependences of 2D ^1H-^1H NOESY spectra. NOESY spectrum of the Y-shape PEO_{114}-*b*-$(PNIPAm_{165})$ triblock copolymer is shown in Fig. 7. The existence of cross-peaks between PEO protons and various PNIPAm protons, which are depicted in detail on the right side of the Fig. 7, implies that distances between respective protons are smaller than 0.5 nm. Fig. 8 then shows temperature dependences of the absolute integrated intensities of PNIPAm signals in 1D slices, extracted from the PEO signal of the 2D NOESY spectra measured with mixing time 400 ms for D_2O solution of the Y-shape PEO_{114}-*b*-$(PNIPAm_{165})$ triblock copolymer. Dependences of the respective integrated intensities in 1D slices extracted from NOESY spectra measured with mixing time 100 ms as well as dependences obtained using the volume integrals of the

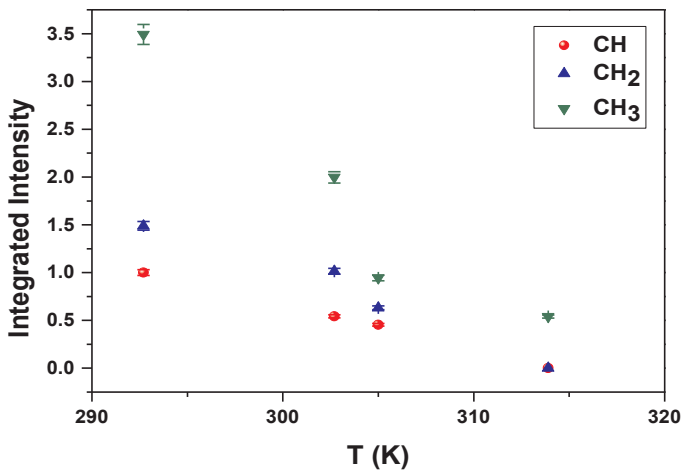

Fig. 8. Temperature dependences of integrated intensities (estimated relative error ± 3%) of various PNIPAm signals in 1D slices extracted from the PEO signal of the NOESY NMR spectra of D_2O solution (c = 20 wt%) of PEO_{114}-*b*-$(PNIPAm_{165})_2$ block copolymer. Main chain CH is depicted in the figure.

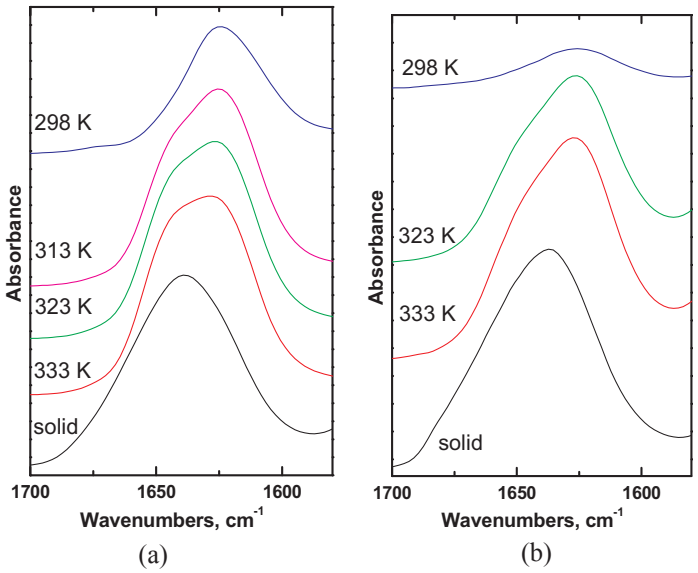

Fig. 9. ATR FTIR spectra (Amide I region) of D_2O solutions (c = 10 wt%) of the PEO_{114}-*b*-$(PNIPAm_{165})_2$ (a) and PNIPAm homopolymer (b) at various temperatures. This region in solid samples is also shown for the comparison.

respective cross-peaks were very similar. While for PEO_{114}-*b*-$PNIPAm_{109}$ diblock copolymer an increase in intensity of cross-peaks between PEO protons and protons of PNIPAm units (main chain CH and CH_2, and isopropyl CH) was detected after increasing the temperature from 292.7 K to 301.6 K, so showing some conformation changes in the pretransition region [34], intensities of cross-peaks in Fig. 8 continuously decrease with temperature. This reveals that Y-shape triblock copolymer cannot form similar conformation as observed for diblock copolymer at 301.6 K, probably from steric reasons. This finding again evidences important role of the architecture of the block copolymer on its behavior in aqueous solution.

3.3. FTIR spectroscopy and DFT calculations

FTIR spectroscopy can provide information on dehydration of PNIPAm segments during the temperature-induced phase transition [12,31,49]. ATR FTIR spectra of the D_2O solutions (c = 10 wt%) of all samples of block copolymers of PEO and PNIPAm, as well as the PNIPAm homopolymer, were measured in the temperature range 298–333 K. Two regions of the IR spectra of PNIPAm units were followed: the region of the C═O stretching vibrations, Amide I (1700–1580 cm^{-1}) and the region of the CH_3 stretching vibrations (around 2975 cm^{-1}). Those regions are not influenced by the spectrum of the solvent (D_2O). The positions of the individual peaks in the overlapped band envelopes were identified using the second derivative of the spectra. Fig. 9 shows the temperature dependences of the Amide I region for solutions of the PEO_{114}-*b*-$(PNIPAm_{165})_2$ Y-shape triblock copolymer (a) and PNIPAm homopolymer (b). At elevated temperatures formation of a new component with higher wavenumber is clearly visible for both samples. The wavenumber of the new component is virtually the same as wavenumber of the Amide I band in respective solid sample (cf. Fig. 9) so evidencing that this component relates to dehydrated carbonyl groups. Fig. 10 shows temperature dependence of the region of CH_3 stretching vibrations for solution of the PEO_{114}-*b*-$(PNIPAm_{165})_2$ Y-shape triblock copolymer. During the heating of the solution the CH_3 stretching band is shifted towards lower wavenumber, i.e., in direction to the wavenumber of the respective solid sample. It corresponds to the partial dehydration of the hydrophobic CH_3 groups at temperatures above the transition due to disruption of local structure of water molecules surrounding these groups (hydrophobic hydration); this process proceeds in parallel with dehydration of C═O groups. The same behavior as shown in Figs. 9 and 10 was found also for other samples of the investigated block copolymers. No significant changes with increasing temperature were detected for the band of C—O—C stretching vibrations of PEO units at ~1085 cm^{-1}.

In order to characterize the Amide I band in more detail, the measured spectra were fitted to several overlapping components of the Voigt profile and the results are displayed in Fig. 11. While two components were sufficient to fit very well the shape of the Amide I band in the PNIPAm homopolymer and Y-shape triblock copolymer, five components were necessary for least squares deconvolution of this band in diblock copolymer. This analysis therefore suggests for the diblock copolymer five types of C═O groups situated in different distinguishable environments.

In recent papers it has been demonstrated that *ab initio* DFT calculations provide a very helpful complementary tool to the investigation of changes in hydration of segments of thermosensitive polymers during phase transition by the methods of vibrational spectroscopy [49,55]. Therefore we performed DFT calculations on model hydrogen bonded complexes of the PNIPAm segments with or without water molecules. *N*-isopropyl-2 methylpropanamide (NIPMPA) was used as the simplest model of the PNIPAm unit. At the same time we also took into account the fact that polymer-polymer hydrogen bonds between C═O and N—H groups can exist especially at temperatures above the transition [31,51]. The structures of the PNIPAm segments and their hydrated complexes were

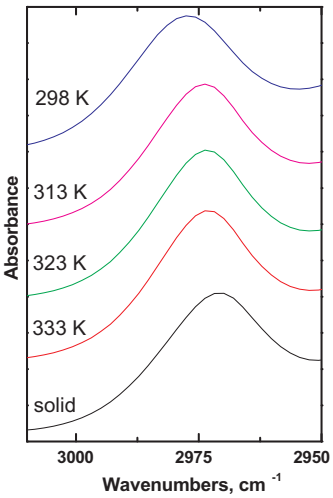

Fig. 10. ATR FTIR spectra (region of CH_3 vibrations) of D_2O solutions (c = 10 wt%) of the PEO_{114}-*b*-$(PNIPAm_{165})_2$ Y-shape triblock copolymer at various temperatures. This region in solid sample is also shown for the comparison.

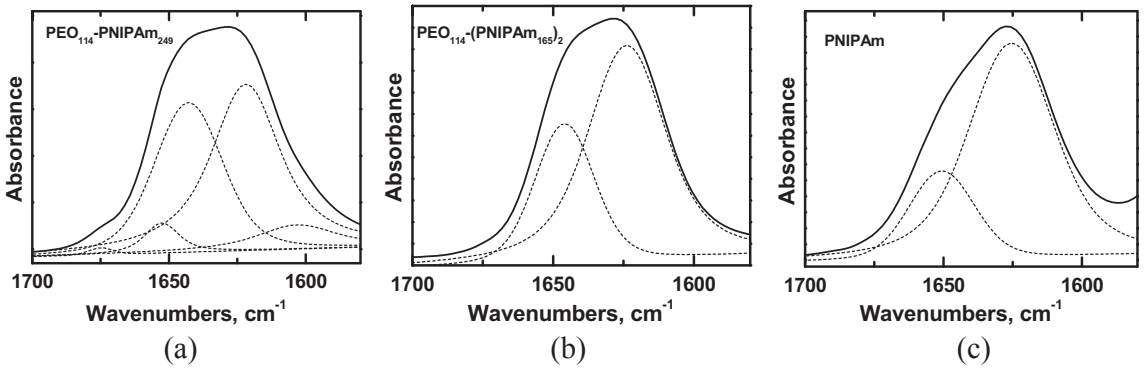

Fig. 11. Amide I region of ATR FTIR spectra of the D_2O solutions (c = 10 wt%) of the PEO_{114}-*b*-$PNIPAm_{249}$ (a), PEO_{114}-*b*-$(PNIPAm_{165})_2$ (b) and PNIPAm homopolymer (c) measured at 333 K, together with Voigt profile components obtained by the least squares deconvolution.

fully optimized without any geometrical constraint. Results of DFT calculations are shown in Fig. 12. From these results it follows that for hydrated model complexes the frequency of the C═O stretching vibration is predominantly determined by the number of direct hydrogen bonds of the C═O group with water molecules (Fig. 12c and d). For dehydrated polymer-polymer model complexes the Amide I frequency somewhat changes when the number of C═O..H−N hydrogen bonds of the given PNIPAm segment is one or two (Fig. 12a and b). DFT calculations also show that Amide I component with highest wavenumber (1675 cm^{-1}) corresponds to the stretching vibrations of free, non-hydrogen-bonded C═O groups (Fig. 12a and b). It should be mentioned that wavenumbers calculated for structures depicted in Fig. 12 agree well with values of the five components obtained by deconvolution of the Amide I band for D_2O solution of the PEO_{114}-*b*-$PNIPAm_{249}$ diblock copolymer so showing that two components with lowest wavenumbers correspond to hydrated C═O groups while three components with larger wavenumbers correspond to dehydrated C═O groups. From comparison of Figs. 11 and 12 it also follows that two components obtained by deconvolution of the Amide I band for the PEO_{114}-*b*-$(PNIPAm_{165})_2$ triblock copolymer and the PNIPAm homopolymer correspond to not very extensively hydrated C═O groups (component with lower wavenumber) and to dehydrated C═O groups (component with higher wavenumber). DFT calculations have shown that values of the extinction coefficients for structures depicted in Fig. 12 do not differ significantly (they are within ± 15% of the average value) with exemption of the extinction coefficient of the band of free, non-hydrogen bonded C═O groups which is about twice smaller. Taking into account that intensity of the component of free C═O groups (which was observed only for the diblock copolymer, cf. Fig. 11a), is very small, it is possible to obtain with reasonable precision values of the degree of dehydration at 333 K for both types of the block copolymers and the PNIPAm homopolymer. In comparison with the PNIPAm homopolymer where this analysis shows 21% of dehydrated C═O groups, the values of the degree of dehydration obtained for both types of block copolymers of PEO and PNIPAm are significantly larger. At the same time effect of the copolymer architecture is important. While this analysis shows 33% of dehydrated C═O groups in PEO_{114}-$(PNIPAm_{165})_2$ Y-shape triblock copolymer, there is 43% of dehydrated C═O groups in PEO_{114}-$PNIPAm_{249}$ diblock copolymer. Higher values of the degree of dehydration of C═O groups found for block copolymers in comparison with PNIPAm homopolymer suggest some variations in inner structures (including hydrogen-bonded water molecules) of micellar cores formed by PNIPAm blocks of the block copolymers and mesoglobules of the PNIPAm homopolymer.

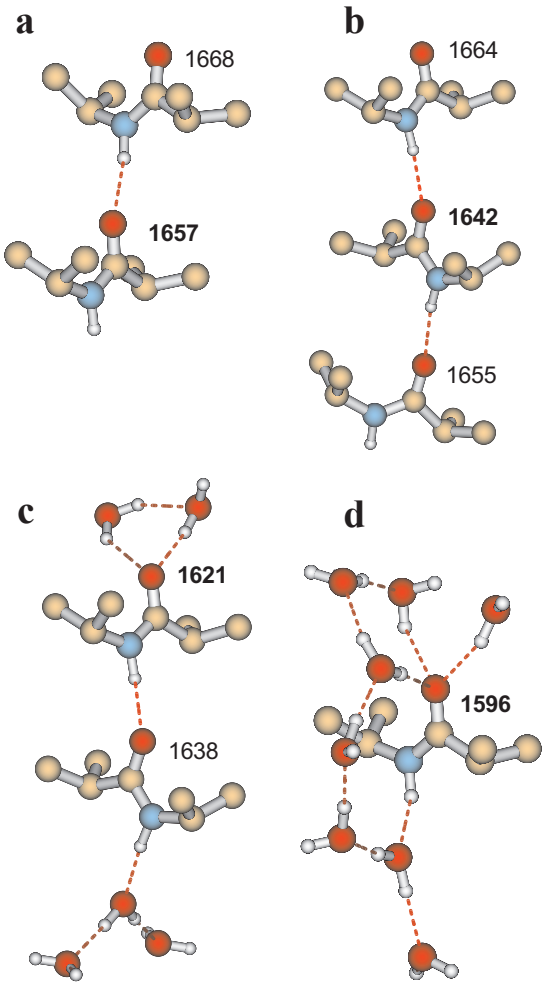

Fig. 12. DFT (B3LYP/6-311 + G(d,p)) optimized structures of the hydrogen bonded complexes of the PNIPAm model segments (NIPMPA) with and without water molecules together with calculated Amide I frequencies (in cm^{-1}). Hydrogen atoms in PNIPAm units are omitted for clarity.

We also followed time dependence of the IR spectra when the sample of the PEO_{114}-*b*-$(PEO_{165})_2$ Y-shape triblock copolymer was kept for 8 h at 325 K; in this sample a slow release of the originally bound water with time was detected by NMR T_2 measurements (cf. Fig. 6). We did not observe any change in the shape of the Amide I band with time so showing that the fraction of hydrated C═O groups is constant. We assume that water released from micellar cores formed by PNIPAm blocks with time, as revealed from NMR T_2 measurements, is mainly indirectly bound water, i.e., water interacting with water molecules directly hydrogen bonded to PNIPAm units. Similar result we recently obtained for PVCL/D_2O solution [56].

4. Conclusions

In the present study we investigated temperature behavior of D_2O solutions of thermoresponsive diblock PEO-*b*-PNIPAm copolymers and Y-shape triblock PEO-*b*-$(PNIPAm)_2$ copolymers in comparison with behavior of PNIPAm homopolymer by combination of NMR and ATR FTIR spectroscopy, DSC and model quantum-chemical calculations. This is a first in-depth study of structural changes and interactions on series of samples of block copolymers of PEO and PNIPAm with different architecture at various temperatures. Though at polymer concentrations $c \leq 5$ wt% the transition temperatures are for block copolymers and PNIPAm homopolymer nearly the same, with exception of the PEO_{114}-*b*-$(PNIPAm_{47})_2$ sample with shorter PNIPAm blocks, we have found that the phase transition and structures of PNIPAm component are significantly affected not only by the presence of the PEO block but also by copolymer architecture. This holds, e.g., for values of the enthalpy ΔH of the transition which are smaller for block copolymers in comparison with neat PNIPAm. At the same time ΔH is larger for diblock copolymers in comparison with Y-shape triblock copolymers. A different behavior between both types of the block copolymers was found by NMR also in connection with influence of the polymer concentration on the phase transition of PNIPAm blocks: while 3.5 K shift towards lower temperatures was detected for diblock when concentration was increased to 20 wt%, for Y-shape triblock this shift was much smaller (1.5 K) and comparable with effect of concentration found for the neat PNIPAm. Aggregation of micelles is then probably responsible for the increase of the values

of the fraction of PEO units with significantly reduced mobility with increasing polymer concentration at temperatures above 320 K.

The existence of water bound in micellar cores formed by PNIPAm blocks was revealed for investigated block copolymers by NMR measurements of spin–spin relaxation times T_2 of HDO molecules and by ATR FTIR spectra. From T_2 measurements it follows that for Y-shape triblock copolymer the originally bound water is slowly released with time from micellar cores formed by PNIPAm segments; comparison with FTIR spectra suggests that the released water can be mainly indirectly bound water. On the other hand, no release of water with time was detected by T_2 measurements for diblock copolymer. IR spectra indicate that changes in hydrophilic and hydrophobic interactions in investigated block copolymers proceed simultaneously. ATR FTIR spectra together with model quantum-chemical DFT calculations showed somewhat different shape of the band of the C═O stretching vibrations for PEO_{114}-*b*-$PNIPAm_{249}$ diblock on the one hand and for PEO_{114}-*b*-$(PNIPAm_{165})_2$ triblock and PNIPAm homopolymer on the other hand. The degree of dehydration of C═O groups as obtained for both types of block copolymers is significantly higher in comparison with PNIPAm homopolymer. At the same time the effect of the copolymer architecture is also important: the degree of dehydration of C═O groups is larger for diblock copolymer in comparison with Y-shape triblock copolymer. We hasten to add that the effect of the copolymer architecture on behavior of block copolymers of PEO and PNIPAm need not be due only to architecture itself (in connection with, e.g., steric reasons) but bound water confined in somewhat different way in respective micellar cores can be also important in this respect. The different behavior of both types of the block copolymers was shown also in 2D NOESY NMR spectra. While in the solution of the PEO-*b*-PNIPAm block copolymer they revealed some conformation changes already in the pretransition region [34], no similar conformation change was detected for the PEO-*b*-$(PNIPAm)_2$ triblock copolymer.

Acknowledgment

Support by the Czech Science Foundation (Project 15-13853S) is gratefully acknowledged. R.K. acknowledges the Charles University, Faculty of Science for providing the opportunity to pursue his PhD studies. Authors thank Eliézer Jäger and Miloš Netopilík for their help with SEC measurements, and Peter Černoch for DLS measurements.

Appendix A. Supplementary material

Supplementary data associated with this article can be found, in the online version, at http://dx.doi.org/10.1016/j.eurpolymj.2017.07.034.

References

[1] H.G. Schild, Poly(N-isopropylacrylamide): experiment, theory and application, Prog. Polym. Sci. 17 (1992) 163–249.
[2] V.O. Aseyev, H. Tenhu, F.M. Winnik, Temperature dependence of the colloidal stability of neutral amphiphilic polymers in water, Adv. Polym. Sci. 196 (2006) 1–85.
[3] S. Fujishige, K. Kubota, I. Ando, Phase transition of aqueous solutions of poly(*N*-isopropylacrylamide) and poly(*N*-isopropylmethacrylamide), J. Phys. Chem. 93 (1989) 3311–3313.
[4] X. Wang, X. Qiu, C. Wu, Comparison of the coil-to-globule and the globule-to-coil transition of a single poly(*N*-isopropylacrylamide) homopolymer chain in water, Macromolecules 31 (1998) 2972–2976.
[5] H.G. Schild, D.A. Tirrell, Microcalorimetric detection of lower critical solution temperatures in aqueous polymer solutions, J. Phys. Chem. 94 (1990) 4352–4356.
[6] K. Otake, H. Inomata, M. Konno, S. Saito, Thermal analysis of the volume phase transition with *N*-isopropylacrylamide gels, Macromolecules 23 (1990) 283–289.
[7] R. Liu, M. Fraylich, B.R. Saunders, Thermoresponsive copolymers: from fundamental studies to applications, Colloid Polym. Sci. 287 (2009) 627–643.
[8] M.D.C. Topp, P.J. Dijkstra, H. Talama, J. Feijen, Thermosensitive micelle-forming block copolymers of poly(ethylene glycol) and poly(N-isopropylacrylamide), Macromolecules 30 (1997) 8518–8520.
[9] J. Virtanen, S. Holappa, H. Lemmetyinen, H. Tenhu, Aggregation in aqueous poly(*N*-isopropylacrylamide)-block-poly(ethylene oxide) solutions studied by fluorescence spectroscopy and light scattering, Macromolecules 35 (2002) 4763–4769.
[10] W. Zhang, L. Shi, K. Wu, Y. An, Thermoresponsive micellization of poly(ethylene glycol)-*b*-poly(*N*-isopropylacrylamide) in water, Macromolecules 38 (2005) 5743–5747.
[11] J. Yan, W. Ji, E. Chen, Z. Li, D. Liang, Association and aggregation behavior of poly(ethylene oxide)-b-poly(N-isopropylacrylamide) in aqueous solution, Macromolecules 41 (2008) 4908–4913.
[12] Q.W.H. Tang, P. Wu, Aqueous solutions of poly(ethylene oxide)-poly(*N*-isopropylacrylamide): thermosensitive behavior and distinct multiple assembly processes, Langmuir 31 (2015) 6497–6506.
[13] J. Zhao, G. Zhang, S. Pispas, Morphological transitions in aggregates of thermosensitive poly(ethylene oxide)-*b*-poly(*N*-isopropylacrylamide) block copolymers prepared via RAFT polymerization, J. Polym. Sci.: Part A: Polym. Chem. 47 (2009) 4099–4110.
[14] A. Papagiannopoulos, J. Zhao, G. Zhang, S. Pispas, A. Radulescu, Thermoresponsive transition of a PEO-b-PNIPAM copolymer: from hierarchical aggregates to well defined ellipsoidal vesicles, Polymer 54 (2013) 6373–6380.
[15] H.H. Lin, Y.L. Cheng, In-situ thermoreversible gelation of block and star copolymers of poly(ethylene glycol) and poly(N-isopropylacrylamide) of varying architectures, Macromolecules 34 (2001) 3710–3715.
[16] R. Motokawa, K. Morishita, S. Koizumi, T. Nakahira, M. Annaka, Thermosensitive diblock copolymer of poly(*N*-isopropylacrylamide) and poly(ethylene glycol) in water: polymer preparation and solution behavior, Macromolecules 38 (2005) 5748–5760.
[17] C. Feng, C. Ren, Y. Ma, The coexisting phase behavior of thermoresponsive copolymer solutions, Soft Matter 10 (2014) 5523–5531.
[18] J. Yan, W.J.E. Chen, Z. Li, D. Liang, Effect of heating rate on thermo-induced aggregation of poly(ethylene oxide)-*b*-poly(*N*-isopropylacrylamide) in aqueous solutions, Chin. J. Polym. Sci. 28 (2010) 437–447.
[19] P. Pramanik, S. Ghosh, Thermoresponsive polymersome from a double hydrophilic block copolymer, J. Polym. Sci.: Part A Polym. Chem. 53 (2016) 2444–2451.
[20] A.J. de Graaf, K.W.M. Boere, J. Kemmink, R.G. Fokkink, C.F. van Nostrum, D.T.S. Rijkers, J. van der Gucht, H. Wienk, M. Baldus, E. Mastrobattista, T. Vermonden, W.E. Hennink, Looped structure of flowerlike micelles revealed by ^{1}H NMR relaxometry and light scattering, Langmuir 27 (2011) 9843–9848.
[21] S.K. Filippov, A. Bogomolova, L. Kaberov, N. Velychkivska, L. Starovoytova, Z. Cernochova, S.E. Rogers, W.M. Lau, V.V. Khutoryanskiy, M.T. Cook, Internal nanoparticle structure of temperature-responsive self-assembled PNIPAm-b-PEG-b-PNIPAm triblock copolymers in aqueous solutions: NMR, SANS, and light scattering studies, Langmuir 32 (2016) 5314–5323.
[22] K. Van Durme, G. Van Assche, V. Aseyev, J. Raula, H. Tenhu, B. Van Mele, Influence of macromolecular architecture on the thermal response rate of amphiphilic copolymers, based on poly(*N*-isopropylacrylamide) and poly(oxyethylene), in water, Macromolecules 40 (2007) 3765–3772.

[23] T. Tokuhiro, T. Amiya, A. Mamada, T. Tanaka, NMR study of poly(*N*-isopropylacrylamide) gels near phase transition, Macromolecules 24 (1991) 2936–2943.
[24] F. Zeng, Z. Tong, H. Feng, N.m.r. investigation of phase separation in poly(N-isopropyl acrylamide)/water solutions, Polymer 38 (1997) 5539–5544.
[25] M. Rusu, S. Wohlrab, D. Kuckling, H. Möhwald, M. Schönhoff, Coil-to-globule transition of PNIPAM graft copolymers with charged side chains: a ^{1}H and ^{2}H NMR and spin relaxation study, Macromolecules 39 (2006) 7358–7363.
[26] R. Plummer, D.J.T. Hill, A.K. Whittaker, Solution properties of star and linear poly(*N*-isopropylacrylamide), Macromolecules 39 (2006) 8379–8388.
[27] P.V. Yushmanov, I. Furó, I. Illiopoulos, Kinetics of demixing and remixing transition in aqueous solutions of poly(*N*-isopropylacrylamide): a temperature-jump ^{1}H NMR study, Macromol. Chem. Phys. 207 (2006) 1972–1979.
[28] J. Spěváček, NMR investigations of phase transition in aqueous polymer solutions and gels, Curr. Opin. Colloid Interface Sci. 14 (2009) 184–191.
[29] J. Chen, X. Gong, H. Yang, Y. Yao, M. Xu, Q. Chen, R. Cheng, NMR study on the effects of sodium *n*-dodecyl sulfate on the coil-to-globule transition of poly(N-isopropylacrylamide) in aqueous solutions, Macromolecules 44 (2011) 6227–6231.
[30] G. Wang, P. Wu, Unusual phase transition behavior of poly(*N*-isopropylacrylamide)-*co*-poly(tetrabutylphosphonium styrenesulfonate) in water: mild and linear changes in the poly(*N*-isopropylacrylamide) part, Langmuir 32 (2016) 3728–3736.
[31] Y. Maeda, T. Higuchi, I. Ikeda, Change in hydration state during the coil-globule transition of aqueous solutions of poly(*N*-isopropylacrylamide) as evidenced by FTIR spectroscopy, Langmuir 16 (2000) 7503–7509.
[32] Y. Wu, F. Meersman, Y. Ozaki, A novel application of hybrid two-dimensional correlation infrared spectroscopy: exploration of the reversibility of the pressure- and temperature-induced phase separation of poly(*N*-isopropylacrylamide) and poly(*N*-isopropylmethacrylamide) in aqueous solution, Macromolecules 39 (2006) 1182–1188.
[33] B. Sun, Y. Lin, P. Wu, H.W. Siesler, A FTIR and 2D-IR spectroscopic study on the microdynamics phase separation mechanism of the poly(N-isopropylacrylamide) aqueous solution, Macromolecules 41 (2008) 1512–1520.
[34] J. Spěváček, R. Konefał, E. Čadová, NMR study of thermoresponsive block copolymer in aqueous solution, Macromol. Chem. Phys. 217 (2016) 1370–1375.
[35] J. Spěváček, R. Konefał, J. Dybal, Temperature-induced phase transition in aqueous solutions of poly(*N*-isopropylacrylamide)-based block copolymer, Macromol. Symp. 369 (2016) 92–96.
[36] X. Tang, X. Liang, Q. Yang, X. Fan, Z. Shen, Q. Zhou, AB_2-type amphiphilic block copolymers composed of poly(ethylene glycol) and poly(*N*-isopropylacrylamide) via single-electron transfer living radical polymerization: synthesis and characterization, J. Polym. Sci.: Part A: Polym. Chem. 47 (2009) 4420–4427.
[37] X. Yu, T. Shi, G. Zhang, L. An, Synthesis of asymmetric H-shaped block copolymer by the combination of atom transfer radical polymerization and living anionic polymerization, Polymer 47 (2006) 1538–1546.
[38] ACD/C + H NMR Predictors and DB 2016.2.2.
[39] F. Ganachaud, M.J. Monteiro, R.G. Gilbert, M.-A. Dourges, S.H. Thang, E. Rizzardo, Molecular weight characterization of poly(*N*-isopropylacrylamide) prepared by living free-radical polymerization, Macromolecules 33 (2000) 6738–6745.
[40] M. Netopilík, P. Kratochvíl, Polystyrene-equivalent molecular weight versus true molecular weight in size-exclusion chromatography, Polymer 44 (2003) 3431–3436.
[41] O. Sedláček, P. Černoch, J. Kučka, R. Konefał, P. Štěpánek, M. Vetrík, T.P. Lodge, M. Hrubý, Thermoresponsive polymers for nuclear medicine: which polymer is the best? Langmuir 32 (2016) 6115–6122.
[42] H.G. Schild, M. Muthukumar, D.A. Tirell, Cononsolvency in mixed aqueous solutions of poly(*N*-isopropylacrylamide), Macromolecules 24 (1991) 948–952.
[43] T.C. Farrar, E.D. Becker, Pulse and Fourier Transform NMR, Academic Press, New York, 1971, pp. 27–29.
[44] M.J. Frisch, G.W. Trucks, H.B. Schlegel, G.E. Scuseria, M.A. Robb, J.R. Cheeseman, G. Scalmani, V. Barone, B. Mennucci, G.A. Petersson, H. Nakatsuji, M. Caricato, X. Li, H.P. Hratchian, A.F. Izmaylov, J. Bloino, G. Zheng, J.L. Sonnenberg, M. Hada, M. Ehara, K. Toyota, R. Fukuda, J. Hasegawa, M. Ishida, T. Nakajima, Y. Honda, O. Kitao, H. Nakai, T. Vreven, J.A. Montgomery, Jr., J.E. Peralta, F. Ogliaro, M. Bearpark, J.J. Heyd, E. Brothers, K.N. Kudin, V.N. Staroverov, R. Kobayashi, J. Normand, K. Raghavachari, A. Rendell, J.C. Burant, S.S. Iyengar, J. Tomasi, M. Cossi, N. Rega, J.M. Millam, M. Klene, J.E. Knox, J.B. Cross, V. Bakken, C. Adamo, J. Jaramillo, R. Gomperts, R.E. Stratmann, O. Yazyev, A.J. Austin, R. Cammi, C. Pomelli, J.W. Ochterski, R.L. Martin, K. Morokuma, V.G. Zakrzewski, G.A. Voth, P. Salvador, J.J. Dannenberg, S. Dapprich, A.D. Daniels, Ö. Farkas, J.B. Foresman, J.V. Ortiz, J. Cioslowski, D.J. Fox, Gaussian 09, Revision D.01, Gaussian, Inc., Wallingford CT, 2013.
[45] J.P. Merrick, D. Moran, L. Radom, An evaluation of harmonic vibrational frequency scale factors, J. Phys. Chem. A 111 (2007) 11683–11700.
[46] S. Furyk, Y. Zhang, D. Ortiz-Acosta, P.S. Cremer, D.E. Bergbreiter, Effects of end group polarity and molecular weight on the lower critical solution temperature of poly(*N*-isopropylacrylamide), J. Polym. Sci.: Part A: Polym. Chem. 44 (2006) 1492–1501.
[47] M. Kano, E. Kokufuta, On the temperature-responsive polymers and gels based on *N*-propylacrylamides and *N*-propylmethacrylamides, Langmuir 25 (2009) 8649–8655.
[48] J. Spěváček, ^{1}H NMR study of styrene-butadiene block copolymer micelles in selective solvents, Makromol. Chem., Rapid Commun. 3 (1982) 697–703.
[49] J. Spěváček, J. Dybal, L. Starovoytova, A. Zhigunov, Z. Sedláková, Temperature-induced phase separation and hydration in poly(*N*-vinylcaprolactam) aqueous solutions: a study by NMR and IR spectroscopy, SAXS, and quantum-chemical calculations, Soft Matter 8 (2012) 6110–6119.
[50] X. Wang, C. Wu, Light-scattering study of coil-to-globule transition of a poly(N-isopropylacrylamide) chain in deuterated water, Macromolecules 32 (1999) 4299–4301.
[51] Y. Maeda, T. Nakamura, I. Ikeda, Changes in the hydration states of poly(N-alkylakrylamide)s during their phase transitions in water observed by FTIR spectroscopy, Macromolecules 34 (2001) 1391–1399.
[52] A. Saeed, D.M.R. Georget, A.G. Mayes, Solution thermal properties of a family of thermo-responsive *N*-isopropyl acrylamide-*co*-hydroxymethyl acrylamide copolymers – aspects intrinsic to the polymers, React. Funct. Polym. 72 (2012) 77–82.
[53] L. Starovoytova, J. Spěváček, Effect of time on the hydration and temperature-induced phase separation in aqueous polymer solutions. ^{1}H NMR study, Polymer 47 (2006) 7329–7334.
[54] B. Sierra-Martín, M.S. Romero-Cano, T. Cosgrove, B. Vincent, A. Fernández-Barbero, Solvent relaxation of swelling PNIPAM microgels by NMR, Collloids Surf. A 270–271 (2005) 296–300.
[55] J. Dybal, M. Trchová, P. Schmidt, The role of water in structural changes of poly(*N*-isopropylacrylamide) and poly(*N*-isopropylmethacrylamide) studied by FTIR, Raman spectroscopy and quantum chemical calculations, Vib. Spectrosc. 51 (2009) 44–51.
[56] J. Spěváček, J. Dybal, Temperature-induced phase separation and hydration in aqueous polymer solutions studied by NMR and IR spectroscopy: comparison of poly(*N*-vinylcaprolactam) and acrylamide-based polymers, Macromol. Symp. 336 (2014) 39–46.

Supplementary material

Thermoresponsive behavior of block copolymers of PEO and PNIPAm with different architecture in aqueous solutions: a study by NMR, FTIR, DSC and quantum-chemical calculations

Jiří Spěváček,* Rafał Konefał, Jiří Dybal, Eva Čadová, Jana Kovářová

Institute of Macromolecular Chemistry, Academy of Sciences of the Czech Republic, Heyrovsky Sq. 2, 162 06 Prague 6, Czech Republic
E-mail: spevacek@imc.cas.cz

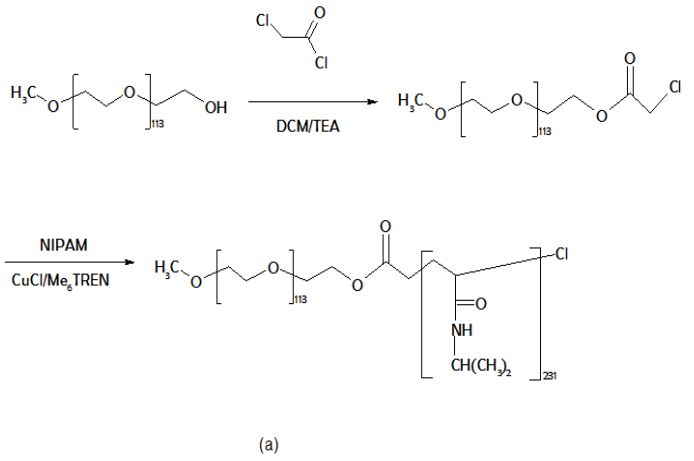

Scheme S1. Synthetic route of diblock copolymers PEO-*b*-PNIPAm (a) and Y-shape triblock copolymers PEO-*b*-(PNIPAm)$_2$ (b).

Materials

N-isopropylacrylamide (NIPAm, Sigma-Aldrich**)** was recrystallized three times from hexane, CuCl (Sigma-Aldrich) was purified by stirring with glacial acetic acid and washing with acetone and drying in vacuum at room temperature, Me6TREN was synthesized according to ref. [1*] , poly(ethylene glycol) monomethyl ether, (PEG, M_n=5000, Sigma-Aldrich) and other chemicals were used as received. Solvents were distilled and stored over molecular sieve.

[1*] M. Ciampolini, N. Nardi, Inorg. Chem. 5 (1966) 41.

Synthesis of the macroinitiators PEG-Cl_2 and PEG-Cl

In a typical experiment for preparation of bifunctional macroinitiator PEG-Cl_2, PEG (M_n=5000, 5.000g, 1mmol) was added to a dried round-bottomed flask, equipped with a magnetic stirring bar and three-way stopcock. Degassed and back-filled carefully with argon three times, 30ml of dried dichloromethane (DCM) and triethylamine (TEA) (1ml, 8.13mmol) were added under argon (solution A). A dropping funnel was placed instead of the three-way stopcock and filled with a solution of DCM (5ml) and dichloroacetyl chloride (DCAC) (0.805ml, 8.37mmol) under argon (solution B). Solution B was added droppwise within 30 min to the solution A, cooling to 0°C. The reaction mixture was left stirring overnight at room temperature, the unsoluble triethylamine hydrobromide salt was removed by filtration and the liquid was shaken three times with diluted HCl, saturated solution of sodium bicarbonate and saturated solution of sodium chloride. The organic part was dried with anhydrous magnesium sulfate and precipitated into ice-cooled diethyl ether. The yield of the precipitated macroinitiator, dried 24 hr at room temperature, was 68%. The amount of chlorine was established by elemental analysis. For attainment of monofunctional macroinitiator PEG-Cl, in addition to chloroacetyl chloride analogous acylation agents like 2-bromoisobutyryl bromide or 2-chloropropionyl chloride were applied.

Synthesis of PEO-*b*-$(PNIPAm)_2$ and PEO-*b*-PNIPAm block copolymers

In a typical experiment for preparation of the Y-shape PEO-*b*-$(PNIPAm)_2$ block copolymer, bifunctional PEG-Cl_2 (0.2195g, 1mmol), NIPAm (2.2632g, 20mmol) and CuCl (19.8mg, 0.2mmol) were added to a round-bottomed flask, equipped with a magnetic stirring bar. After sealing with a three-way stopcock, the flask was degassed and back-filled with argon three times. Subsequently 7ml of solution (DMF/H_2O = 3/1) was added and the mixture was stirred for 15 min, frozen in dry-ice/ethanol bath and degassed by three freeze-pump thaw cycles. After that Me_6TREN was added just before the polymerization, which was carried out at 30°C for 5.5-6 hr. The reaction was rapidly quenched and diluted with 7ml of tetrahydrofuran (THF) and precipitated in diethyl ether (DEE). For achievement of diblock PEO-*b*-PNIPAm copolymer, analogous above mentioned polymerization reactions of NIPAm and monofunctional macroinitiator PEG-Cl were carried out under similar reaction conditions.

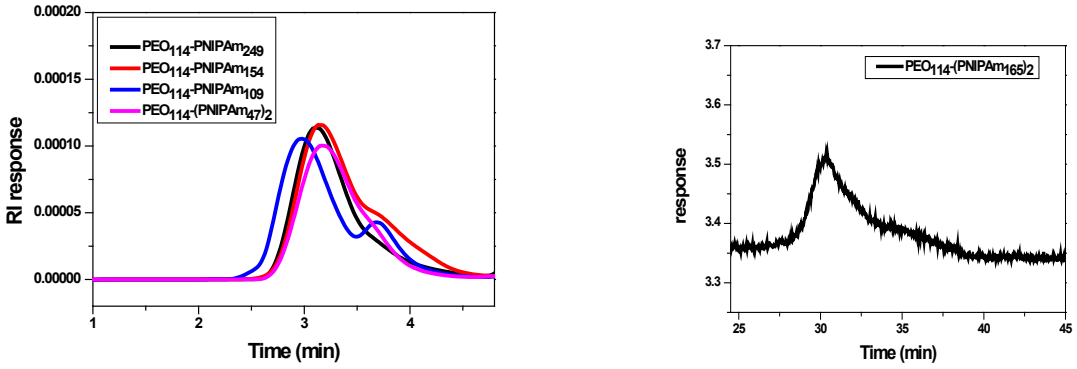

(a) (b)

Fig. S1. SEC traces with methanol /sodium acetate buffer (0.3M, pH 6.5) mixture (80:20 vol%) (a) and DMF (b) as the mobile phase for diblock and Y-shape triblock copolymers of PEO and PNIPAm. Refractive index (a) and light scattering (b) detection.

Table S1.
Values of number-average molecular weight M_n and polydispersity index PDI = M_w/M_n obtained from SEC measurements using methanol /sodium acetate buffer (0.3M, pH 6.5) mixture (80:20 vol%) as the mobile phase. Second column shows M_n values calculated from copolymer composition as determined by NMR.

Sample	M_n (NMR)	M_n (SEC; methanol/buffer; MALS)	PDI (SEC; methanol/buffer; MALS)
PEO_{114}-*b*-$PNIPAm_{249}$	33 137	35 030	1.20
PEO_{114}-*b*-$PNIPAm_{154}$	22 402	22 930	1.44
PEO_{114}-*b*-$PNIPAm_{109}$	17 317	18 330 91 000*	1.06 1.47*
PEO_{114}-*b*-$(PNIPAm_{165})_2$	42 290	63 851**	1.24**
PEO_{114}-*b*-$(PNIPAm_{47})_2$	15 622	27 690	1.21

*Aggregates
**DMF as the mobile phase; calibration on polystyrene standards

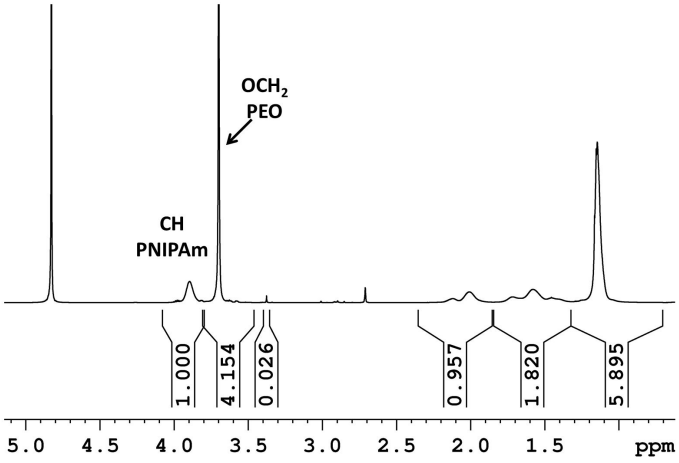

Fig. S2. ^{1}H NMR spectrum of PEO_{114}-*b*-$PNIPAm_{109}$ block copolymer in D_2O solution (*c* = 5 wt%) measured at 292.7 K.

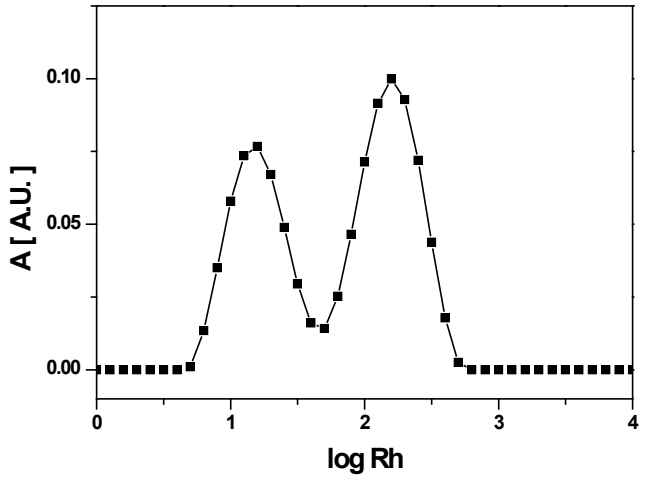

Fig. S3. Hydrodynamic radius R_h distribution as obtained from DLS measurements (ALV-6010 correlator) for PEO_{114}-*b*-$PNIPAm_{109}$ copolymer in methanol/sodium acetate buffer (0.3M, pH 6.5) mixture (80:20 vol%) at room temperature.

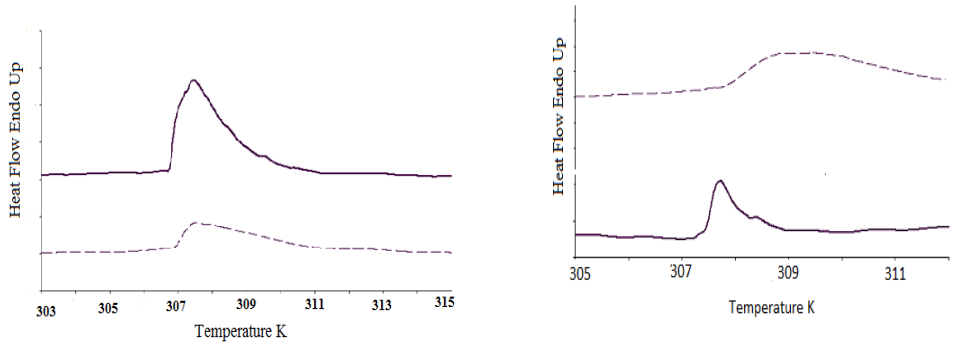

(a) (b)

Fig. S4. DSC thermograms of D_2O solutions (c = 5 wt%) of: (a) PNIPAm homopolymer (full line), PEO_{114}-*b*-$PNIPAm_{249}$ diblock copolymer (dashed line); (b) PEO_{114}-*b*-$(PNIPAm_{47})_2$ (dashed line) and PEO_{114}-*b*-$(PNIPAm_{165})_2$ (full line) Y-shape triblock copolymers.

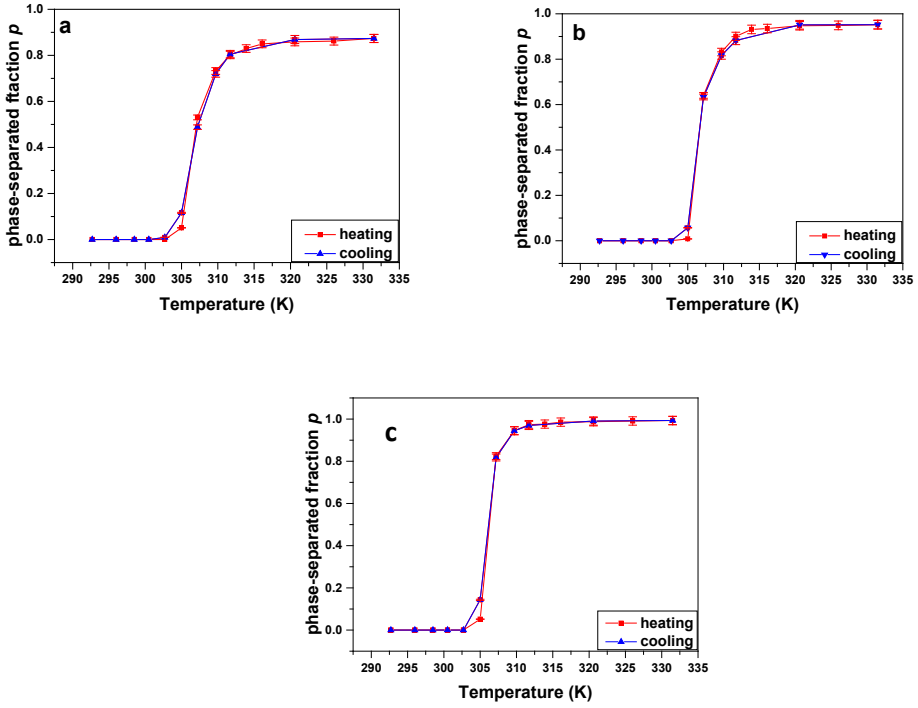

Fig. S5. Temperature dependences of the *p*-fraction (relative error ±2%) of PNIPAm units in D_2O solutions (c = 5 wt%) of PEO_{114}-*b*-$PNIPAm_{249}$ (a) and PEO_{114}-*b*-$(PNIPAm_{165})_2$ (b) block copolymers, and PNIPAm homopolymer (c) measured during gradual heating and subsequent gradual cooling.

Publication 4

J. Spěváček, **R. Konefał**, E. Čadová

NMR study of thermoresponsive block copolymer in aqueous solution.

Macromolecular Chemistry and Physics, **2016**, 217, 1370-1375.

NMR Study of Thermoresponsive Block Copolymer in Aqueous Solution

Jiří Spěváček,* Rafał Konefał, Eva Čadová

Temperature behavior of D_2O solutions of poly(ethylene oxide) $(PEO)_{114}$-*block*-poly(*N*-isopropylacrylamide) $(PNIPAm)_{109}$ is characterized by NMR methods. At temperatures above the lower critical solution temperature (LCST) transition of PNIPAm component, ^1H NMR spectra are consistent with existence of micelles where immobilized PNIPAm blocks form rather compact core and mobile PEO blocks form a shell of micelles. The transition of PNIPAm component shifts toward lower temperatures with increasing polymer concentration. 2D nuclear Overhauser effect spectroscopy spectra which can provide information on proton groups in close spatial contact (<0.5 nm) show an increase in intensity of cross-peaks between PEO protons and main chain CH and CH_2 protons, and isopropyl CH protons of PNIPAm units after increasing the temperature from 292.7 to 301.6 K. The fact that this change occurs at temperature, which is still below the LCST transition of PNIPAm component evidences certain conformation changes in the PEO-*b*-PNIPAm block copolymer already in the pretransition region.

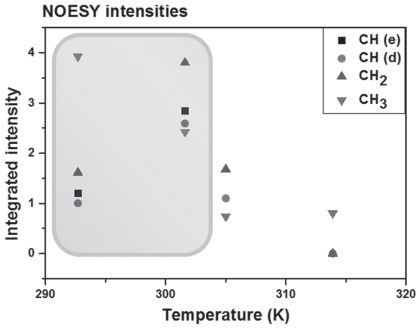

1. Introduction

It is well known that poly(*N*-isopropylacrylamide) (PNIPAm) and other polymers with amphiphilic character exhibit in aqueous solutions a lower critical solution temperature (LCST). They are soluble at lower temperatures but heating above the LCST results in phase separation.[1,2] On the molecular level, both phase separation in solutions and similar volume phase transition in hydrogels of crosslinked polymers are assumed to be a macroscopic manifestation of a coil-globule transition, as was shown for PNIPAm in water, e.g., by light scattering,[3] followed by further aggregation and formation of so-called mesoglobules.[2] The thermoresponsive transition is probably associated with a changed balance between various types of interactions. One contribution is in connection with breakdown of polymer-water hydrogen bonds,[4] while the second contribution is in connection with disruption of local structure of water molecules surrounding hydrophobic groups of polymer segments which promotes hydrophobic interaction.[5] In aqueous solutions of block copolymers poly(ethylene oxide) (PEO)-*b*-PNIPAm heating above the transition temperature of PNIPAm component leads to formation of micelles; the size of the resultant PEO-*b*-PNIPAm micelles decreases with increasing copolymer concentration.[6] Aggregation, self-assembly, and phase behavior of PEO-*b*-PNIPAm block copolymers in water were also studied.[7–12] A rich-phase behavior of these systems was established. At the same time, the phase transition behavior of these copolymers is rather complex.[9–12] Their thermosensitivity makes all these homopolymers and copolymers interesting for miscellaneous biomedical and technological applications.[2,13]

Of various methods used in investigations of thermoresponsive polymers in aqueous solutions, NMR spectroscopy is also an important method providing information on globular structures and interactions in these systems,[14] including block copolymers.[15,16] In addition

Dr. J. Spěváček, R. Konefał, E. Čadová
Institute of Macromolecular Chemistry
Academy of Sciences of the Czech Republic
Heyrovský Sq. 2, 162 06 Prague 6, Czech Republic
E-mail: spevacek@imc.cas.cz

DOI: 10.1002/macp.201600025

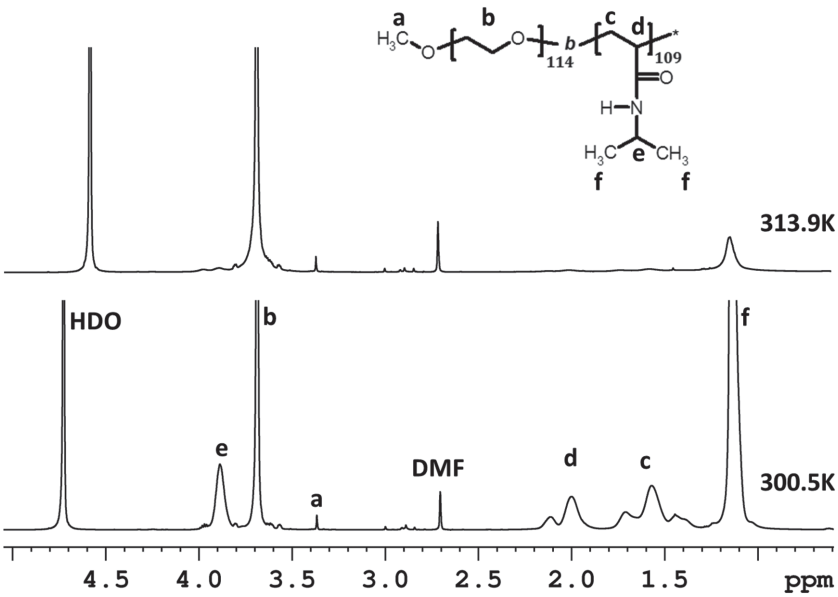

Figure 1. ^{1}H NMR spectra of PEO-*b*-PNIPAm in D_2O solution (c = 5 wt%) measured at 300.5 and 313.9 K under the same instrumental conditions.

to frequently used temperature dependences of 1D NMR spectra and measurements of NMR relaxation times and diffusion coefficients, 2D nuclear Overhauser effect spectroscopy (NOESY), which can provide information on the spatial proximity (distances < 0.5 nm) between respective nuclei, has been also applied in some cases. Chen et al.[17,18] applied NOESY to study interactions between anionic surfactant sodium *n*-dodecyl sulfate and PNIPAm in aqueous solution at various temperatures, while Zhang et al.[19] used this method to obtain information on structural changes in aqueous solution of poly(ethylene glycol) methyl ether methacrylate and 2,2,2-trifluoroethyl acrylate random copolymer during LCST transition. In the present work we used both 1D NMR spectra and especially 2D NOESY in investigations of temperature-induced structural changes in D_2O solutions of PEO-*b*-PNIPAm diblock copolymer.

2. Experimental Section

2.1. Materials

The commercial poly(ethylene glycol) monomethyl ether (Fluca, M_n = 5000) was used as received as a starting material for the preparation of macroinitiator. NIPAm (Sigma-Aldrich) was purified by crystallization in toluene.

2.2. Synthesis of PEO-*b*-PNIPAm Diblock Copolymer

Macroinitiator for the synthesis of the PEO-*b*-PNIPAm diblock copolymer was prepared by elimination reaction of poly(ethylene glycol) monomethyl ether (PEG) 5000 with 2-bromoisobutyrylbromide. PEO-*b*-PNIPAm diblock copolymer was synthesized by means of single-electron transfer living radical polymerization method.[20] The polymerization of NIPAm on PEG 5000 macroinitiator was carried out in the mixture dimethylformamide/H_2O = 3/1 in presence of tris(2-(dimethylamino)ethyl)amine (Me_6TREN) and CuCl at 313 K for 19 h; molar ratios of components were PEG macroinitiator/NIPAm/CuCl/Me_6TREN = 1/400/2/4. The product was isolated by repeated precipitation into petrolether and diethylether. Gel permeation chromatography measurements confirmed a unimodal distribution. Molar ratio of PEO and PNIPAm units in the resulting block copolymer was determined from ^{1}H NMR spectra recorded at room temperature by using integrated intensities of signal b of PEO and signal f or e of PNIPAm (cf. Figure 1). Taking into account that the length of PEO block was 114 units, for the length of PNIPAm block we obtained 109 units.

2.3. NMR Measurements

1D ^{1}H NMR spectra were recorded with Bruker Avance III 600 spectrometer operating at 600.2 MHz and equipped with a 5 mm double resonance broad band probe. Typical conditions were as follows: $\pi/2$ pulse width 10 μs, relaxation delay 10 s, spectral width 15 kHz, acquisition time 2.18 s, 16 scans. The integrated intensities were determined with spectrometer integration software with an accuracy of ±1%. 2D ^{1}H–^{1}H NOESY NMR spectra were recorded on the same spectrometer with 4098 Hz spectral window in f_1 and f_2, and mixing times 100 and 400 ms. A total of 16 scans was accumulated over 512 t_1 increments with a relaxation delay of 10 s. In all 1D and 2D NOESY measurements temperature was maintained constant within ±0.2 K in the range 292–333 K using a BVT-3000 temperature unit. Temperature was calibrated using a standard 80% ethylene glycol (DMSO-d_6) sample. The D_2O (Sigma, 99.9% of deuterium) solutions of PEO-*b*-PNIPAm with polymer concentrations c = 5 and 20 wt% were prepared for NMR measurements. The solutions in 5 mm NMR tubes were degassed and sealed under nitrogen; sodium 2,2-dimethyl-2-silapentane-5-sulfonate was used as an internal NMR standard. The samples were kept at the experimental temperature always at least for 15 min before the measurement.

3. Results and Discussion

Figure 1 shows ^{1}H NMR spectra of a PEO-*b*-PNIPAm diblock copolymer in D_2O solution (c = 5 wt%) recorded under the same instrumental conditions at two temperatures. The assignment of resonances to various proton types is shown in the spectrum recorded at 300.5 K, i.e., below the LCST

of PNIPAm homopolymer which is around 306 K.[1–3,21] Strong peak b corresponds to PEO protons, while signals e, d, c, and f with integrated intensities in the ratio 1:1:2:6 correspond isopropyl CH, main chain CH, CH_2 and CH_3 groups of PNIPAm units, respectively. The second spectrum was recorded at 313.9 K, i.e., above the LCST of PNIPAm. The most significant effect observed in this spectrum is a marked reduction of integrated intensities of all PNIPAm signals which, with exception of signal of CH_3 protons, almost completely disappeared from the spectrum. Evidently, at 313.9 K the mobility of PNIPAm units in polymer chains forming rather compact micellar core is reduced to such an extent that the corresponding signals become too broad to be detected in high-resolution NMR spectra.[14] On the other hand, the intensity of the signal of PEO segments, which remain mobile forming a shell of micelles, is not changed by heating to 313.9 K. The behavior of PEO-*b*-PNIPAm micelles in D_2O is therefore basically the same as behavior of micellar solutions of polystyrene-*b*-polybutadiene block copolymer in heptane (selective solvent for polybutadiene), where manifestation of micelles of block copolymers in NMR spectra was reported for the first time.[22]

To quantitatively characterize the LCST transition of PNIPAm blocks, it is possible to calculate the values of fraction of PNIPAm units with significantly reduced mobility, i.e., units in the micellar core, p, using equation[14]

$$p = 1 - (I / I_o) \quad (1)$$

where I is the integrated intensity of the given PNIPAm signal at temperatures during or above the LCST transition and I_0 is the integrated intensity of this signal if no LCST transition occurs. For I_0 we took integrated intensities as obtained for the respective solution at 292.7 K and taking into account the fact that the integrated intensities should decrease with reciprocal absolute temperature T,[14] i.e., $I_0(T) = I_0^{292.7}(292.7/T)$.[23] In Figure 2, the temperature dependences of the fraction p of PNIPAm units with significantly reduced mobility are shown for D_2O solutions of the block copolymer PEO_{114}-*b*-$PNIPAm_{109}$ and polymer concentrations c = 5 and 20 wt%. These dependences were determined from integrated intensities of the signal e; temperature dependences of the fraction p determined from integrated intensities of signals d, c, and f are the same, as shown in Figure S1 in the Supporting Information, so confirming that p-fraction really relates to PNIPAm units as a whole. While for both concentrations the transition is ≈5 K broad, a significant dependence of the transition region on polymer concentration is obvious from Figure 2. For c = 20 wt% the transition appears in the range 302.5–308 K, i.e., at 3 K lower temperatures in comparison with c = 5 wt%. Very recently even larger 8 K shift of the transition was reported on the basis of calorimetric

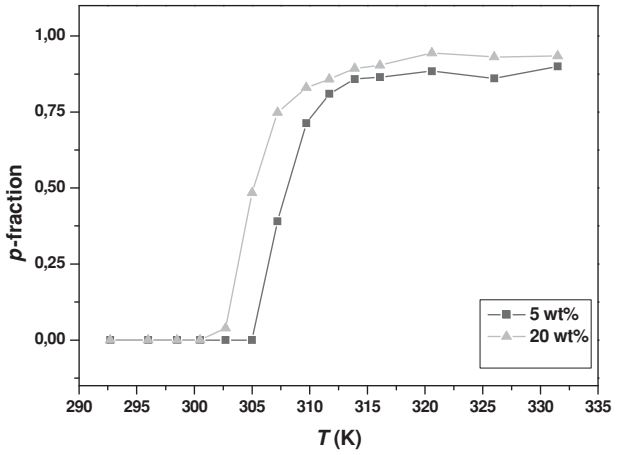

Figure 2. Temperature dependences of the fraction p of PNIPAm units with significantly reduced mobility (units in micellar core) for PEO-*b*-PNIPAm in D_2O solutions of polymer concentrations c = 5 and 20 wt% during gradual heating as determined from integrated intensities of the signal e of isopropyl CH protons.

measurements when concentration of PEO-*b*-PNIPAm increased from 5 to 20 wt%.[12] The difference in magnitude of the concentration effect is probably in connection with different length of the PNIPAm block which is 109 and 19 units in our study and in ref. [12], respectively. The observed dependence of the PNIPAm transition in PEO-*b*-PNIPAm block copolymer on polymer concentration is in contrast with the fact that for acrylamide-based homopolymers (e.g., poly(*N*-isopropylmethacrylamide) and poly(*N*,*N*-diethylacrylamide)), the transition temperatures determined by the same NMR approach are virtually independent of polymer concentration.[14] On the other hand, a similar concentration dependence was recently observed for poly(*N*-vinylcaprolactam) aqueous solutions.[23]

To follow spatial interactions between protons of PEO block and various proton types of PNIPAm block we recorded 2D ^1H-^1H NOESY NMR spectra. Figure 3 shows for illustration the spectrum recorded in D_2O solution (c = 20 wt%) of the studied block copolymer PEO-*b*-PNIPAm; the spectrum was recorded with a mixing time 400 ms at 292.7 K. From Figure 3 it follows that in addition to strong cross-peaks between various proton groups of PNIPAm units, weaker cross-peaks between PEO protons and isopropyl CH, main chain CH, main chain CH_2 and CH_3 protons of PNIPAm units are also visible. The existence of these cross-peaks means that distances between respective protons are smaller than 0.5 nm. Cross-peaks between PEO protons and various proton groups of PNIPAm units were detected also at elevated temperatures up to 305 K, i.e., to the middle of the LCST region (cf. Figure 2, and Figures S2 and S3 in the Supporting Information).

For the quantitative characterization of the intensities of the cross-peaks between PEO and PNIPAm protons we

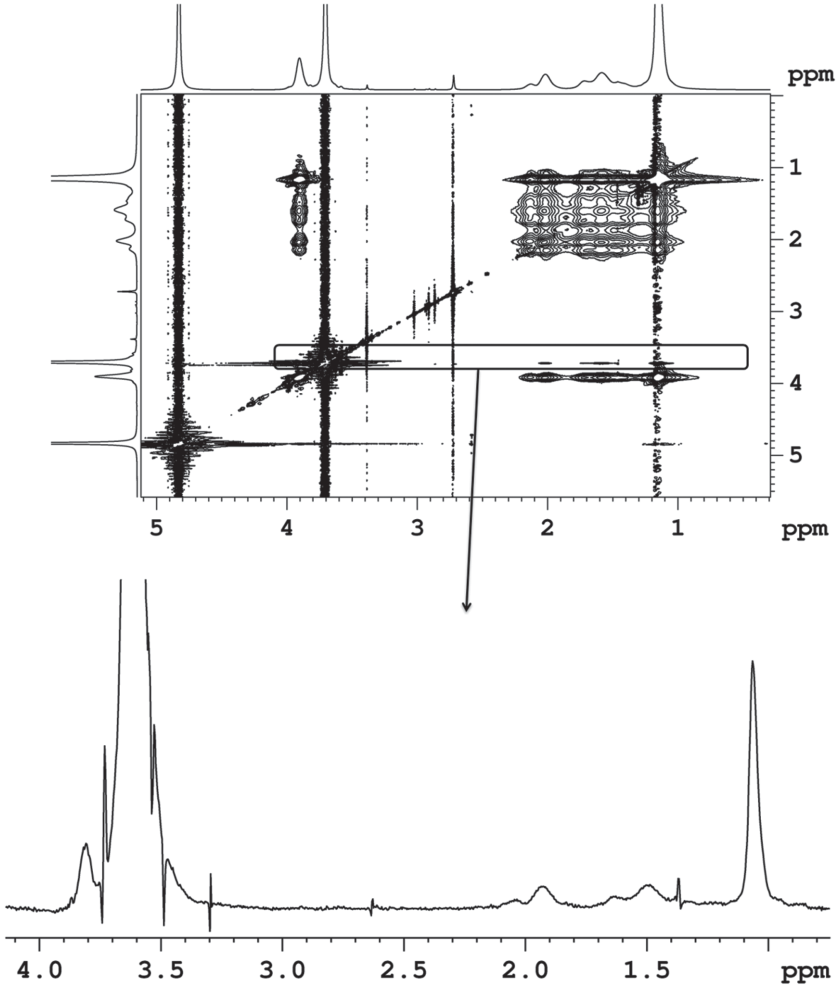

Figure 3. 2D NOESY spectrum of PEO-*b*-PNIPAm in D_2O solution (c = 20 wt%) measured at 292.7 K with mixing time 400 ms. Below there is 1D slice spectrum extracted from the PEO signal of the NOESY spectrum.

used integrated intensities of signals of PNIPAm proton groups (isopropyl CH, main chain CH, main chain CH_2, CH_3) in 1D slices extracted from the PEO signal of the 2D NOESY spectra, as illustrated in the Figure 3 at the bottom. Temperature dependences of the absolute integrated intensities of PNIPAm signals in 1D slices, extracted from 2D NOESY spectra of solution with c = 20 wt% measured with mixing time 400 ms, are shown in Figure 4. Dependences of the respective integrated intensities in 1D slices extracted from NOESY spectra measured with mixing time 100 ms were very similar, only signal/noise ratio in these slices was somewhat lower in comparison with mixing time 400 ms. From Figure 4 it follows that while intensity of the signal of CH_3 protons continuously decreases with increasing temperature, dependences of intensities of main chain CH and CH_2 protons show a maximum at 301.6 K and then decrease to zero. Decrease of the intensity of these protons in the transition region (temperatures > 302.5 K, cf. Figure 2) is evidently in connection with the significantly reduced mobility of PNIPAm segments which form a compact micellar core, as illustrated in Figures 1 and 2. Intensity of the signal of isopropyl CH protons was obtained only for temperatures ≤ 301.6 K, because in the transition region this signal overlaps with strong PEO signal. Nevertheless, also intensity of the signal of isopropyl CH protons is at 301.6 K higher in comparison with its value at 292.7 K, similarly as shown by signals of PNIPAm main chain CH and CH_2 protons. Increase in the intensity at 301.6 K in comparison with 292.7 K was detected also using the volume integrals of the respective cross-peaks between PEO and PNIPAm protons directly in 2D NOESY spectra although the precision is in this case negatively affected by some difficulties connected with phase adjustment. Increased intensity of the respective PNIPAm signals at 301.6 K in comparison with 292.7 K shows that average distance between PEO protons and respective PNIPAm protons (main chain CH and CH_2, and isopropyl CH) is smaller at 301.6 K than at 292.7 K, and/or that number of close contacts between PEO protons and respective PNIPAm protons is significantly increased at 301.6 K. In both cases, this implies a change in conformation of the block copolymer. Important is the fact that this change occurs

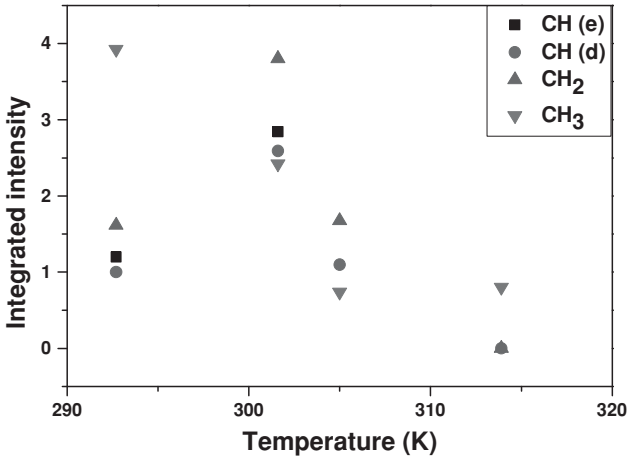

Figure 4. Temperature dependences of integrated intensities of various PNIPAm signals in 1D slices extracted from the PEO signal of the NOESY spectra of PEO-*b*-PNIPAm in D_2O solution (c = 20 wt%).

at temperature which is 1 K lower than the temperature where the LCST transition of PNIPAm component starts (cf. Figure 2). Therefore, Figure 4 evidences certain conformation changes in the PEO-*b*-PNIPAm block copolymer already in the pre-transition region. The fact that increase in the intensity at 301.6 K was not detected for CH_3 protons (cf. Figure 4) indicates that local contacts between PEO and PNIPAm blocks in the changed conformation are of such type that CH_3 protons are already more remote from PEO protons.

Some changes at temperatures below the LCST of the PNIPAm block, which might be relevant to results of the present study, were reported for aqueous solutions of PEO-*b*-PNIPAm block copolymers recently. Abnormal aggregation below LCST was observed by light scattering.[7] Fluorescence measurements showed that hydrophobicity starts to increase already around 290 K.[9] Small angle neutron scattering showed a three-level hierarchical structure below the LCST of PNIPAm which involves the unperturbed PEO-*b*-PNIPAm chains, intermediate-size aggregates, and large clusters.[10] Our results are in accord with results of recent study by Tang and Wu[12] who studied aqueous solutions of PEO-*b*-PNIPAm block copolymers using advanced techniques of 2D infrared spectroscopy. They discussed observed changes in the spectra at temperatures 300–302 K in evolution of PNIPAm from their own domains to loose aggregations with PEO shells. In accord with our results they reported that main chains of PNIPAm respond earlier. One can speculate if conformation changes observed by us and by Tang and Wu already in the pre-transition region are specific only for PEO-*b*-PNIPAm block copolymers, or if this feature is more general and appears, e.g., also in aqueous solutions of thermoresponsive homopolymers. Nevertheless, a further study is necessary to answer this question.

4. Conclusions

In the present study we report some results obtained by NMR spectroscopy on aqueous solutions of PEO-*b*-PNIPAm block copolymer. Heating samples and reaching the LCST transition of PNIPAm component results in reduction of integrated intensities of PNIPAm signals while intensity of PEO signal remains unchanged. This behavior is in accord with existence of micelles where immobilized PNIPAm blocks form rather compact core and mobile PEO blocks form a shell of micelles. In contrast with some acrylamide-based homopolymers where temperatures of the LCST transition are independent of polymer concentration, for PEO_{114}-*b*-$PNIPAm_{109}$ block copolymer the transition shifts to 3 K lower temperatures when polymer concentration is increased from 5 to 20 wt%.

Temperature dependences of 2D NOESY spectra were recorded to obtain information on spatial correlations between protons of PEO blocks and various proton types of PNIPAm blocks. In addition to strong cross-peaks between various proton groups of PNIPAm units, weaker cross-peaks between PEO protons and isopropyl CH, main chain CH, main chain CH_2 and CH_3 protons of PNIPAm units were also detected. In 1D slices extracted from 2D NOESY spectra, an anomalous increase in integrated intensity of signals of main chain CH and CH_2 protons, and isopropyl CH protons of PNIPAm units was revealed after increasing the temperature from 292.7 to 301.6 K. This increase shows that average distance between PEO protons and respective PNIPAm protons is smaller at 301.6 K than at 292.7 K, and/or that number of close contacts (<0.5 nm) between PEO protons and respective PNIPAm protons is significantly increased at 301.6 K. In both cases, this implies a change in conformation of the block copolymer. The fact that this change occurs at temperature which is still below the LCST transition of PNIPAm component evidences certain conformation changes in the PEO-*b*-PNIPAm block copolymer already in the pre-transition region.

Supporting Information

Supporting Information is available from the Wiley Online Library or from the author.

Acknowledgements: Support by the Czech Science Foundation (Project 15-13853S) is gratefully acknowledged. R.K. acknowledges the Charles University, Faculty of Science for providing the opportunity to pursue his PhD studies.

Received: January 21, 2016; Revised: February 17, 2016; Published online: March 15, 2016; DOI: 10.1002/macp.201600025

Keywords: aqueous solutions; NMR; NOESY; poly(ethylene oxide)-*block*-poly(*N*-isopropylacrylamide) block copolymers; stimuli-sensitive polymers

[1] H. G. Schild, *Prog. Polym. Sci.* **1992**, *17*, 163.
[2] V. O. Aseyev, H. Tenhu, F. M. Winnik, *Adv. Polym. Sci.* **2006**, *196*, 1.
[3] S. Fujishige, K. Kubota, I. Ando, *J. Phys. Chem.* **1989**, *93*, 3311.
[4] H. G. Schild, D. A. Tirrell, *J. Phys. Chem.* **1990**, *94*, 4352.
[5] K. Otake, H. Inomata, M. Konno, S. Saito, *Macromolecules* **1990**, *23*, 283.
[6] W. Zhang, L. Shi, K. Wu, Y. An, *Macromolecules* **2005**, *38*, 5743.
[7] J. Yan, W. Ji, E. Chen, Z. Li, D. Liang, *Macromolecules* **2008**, *41*, 4908.
[8] J. Zhao, G. Zhang, S. Pispas, *J. Polym. Sci., Part A: Polym. Chem.* **2009**, *47*, 4099.

[9] R. Motokawa, K. Morishita, S. Koizumi, T. Nakahira, M. Annaka, *Macromolecules* **2005**, *38*, 5748.
[10] A. Papagiannopoulos, J. Zhao, G. Zhang, S. Pispas, A. Radulescu, *Polymer* **2013**, *54*, 6373.
[11] C. Feng, C. Ren, Y. Ma, *Soft Matter* **2014**, *10*, 5523.
[12] Q. W. H. Tang, P. Wu, *Langmuir* **2015**, *31*, 6497.
[13] R. Liu, M. Fraylich, B. R. Saunders, *Colloid Polym. Sci.* **2009**, *287*, 627.
[14] J. Spěváček, *Curr. Opin. Colloid Interface Sci.* **2009**, *14*, 184 and references therein.
[15] Z. Cao, W. Liu, G. Ye, X. Zhao, X. Liu, P. Gao, K. Yao, *Macromol. Chem. Phys.* **2006**, *207*, 2329.
[16] W. Hiller, N. Engelhardt, A.-L. Kampmann, P. Degen, R. Weberskirch, *Macromolecules* **2015**, *48*, 4032.
[17] J. Chen, X. Gong, H. Yang, Y. Yao, M. Xu, Q. Chen, R. Cheng, *Macromolecules* **2011**, *44*, 6227.
[18] J. Chen, H. Xue, Y. Yao, H. Yang, A. Li, M. Xu, Q. Chen, R. Cheng, *Macromolecules* **2012**, *45*, 5524.
[19] C. Zhang, H. Peng, S. Puttick, J. Reid, S. Bernardi, D. J. Searles, A. K. Whittaker, *Macromolecules* **2015**, *48*, 3310.
[20] X. Tang, X. Liang, Q. Yang, X. Fan, Z. Shen, Q. Zhou, *J. Polym. Sci., Part A: Polym. Chem.* **2009**, *47*, 4420.
[21] L. Starovoytova, J. Spěváček, M. Ilavský, *Polymer* **2005**, *46*, 677.
[22] J. Spěváček, *Makromol. Chem., Rapid Commun.* **1982**, *3*, 697.
[23] J. Spěváček, J. Dybal, L. Starovoytova, A. Zhigunov, Z. Sedláková, *Soft Matter* **2012**, *8*, 6110.

Supporting Information

NMR Study of Thermoresponsive Block Copolymer in Aqueous Solution

Jiří Spěváček*, Rafał Konefał, Eva Čadová

Institute of Macromolecular Chemistry, Academy of Sciences of the Czech Republic, Heyrovský Sq. 2, 162 06 Prague 6, Czech Republic; E-mail: spevacek@imc.cas.cz

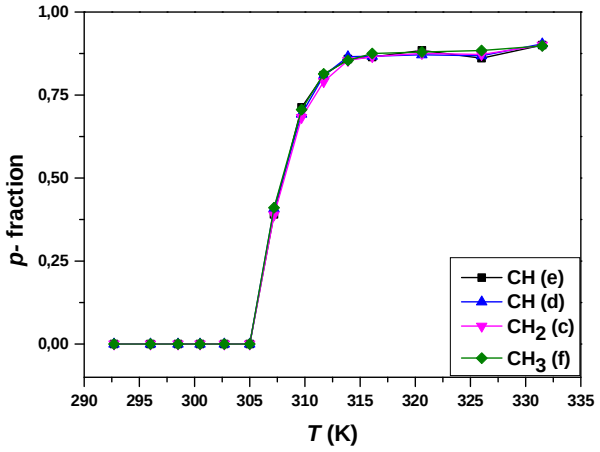

Figure S1. Temperature dependences of the fraction *p* for PEO-*b*-PNIPAm in D_2O solution (*c* = 5 wt%) during gradual heating as determined from integrated intensities of signals of various proton groups of PNIPAm units.

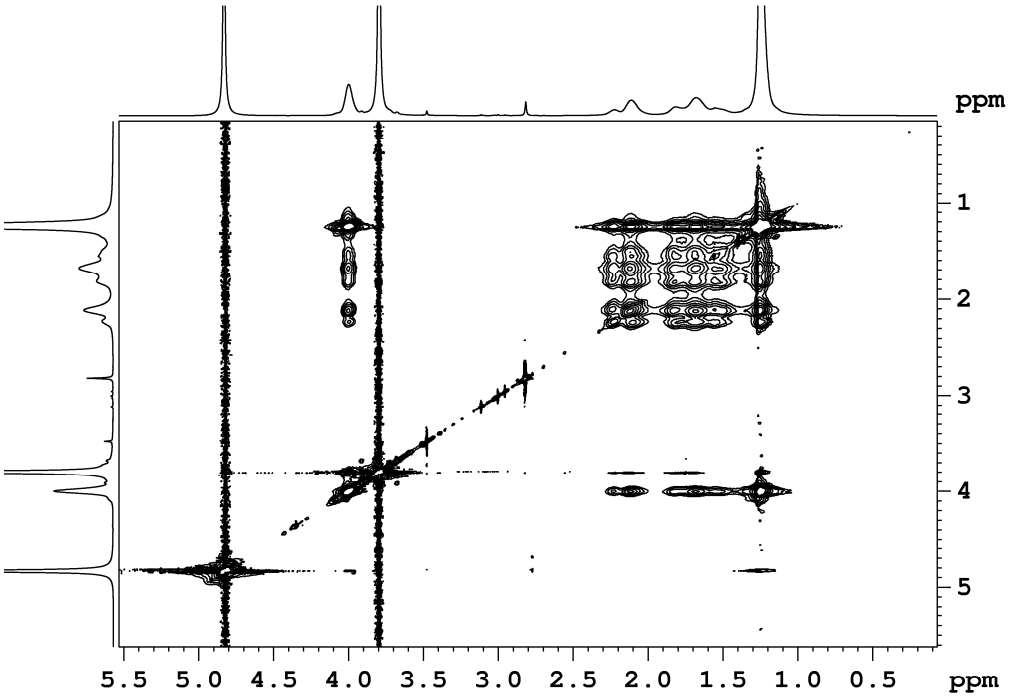

Figure S2. 2D NOESY spectrum of PEO-*b*-PNIPAm in D_2O solution (*c* = 20 wt%) measured at 301.6 K with mixing time 400 ms.

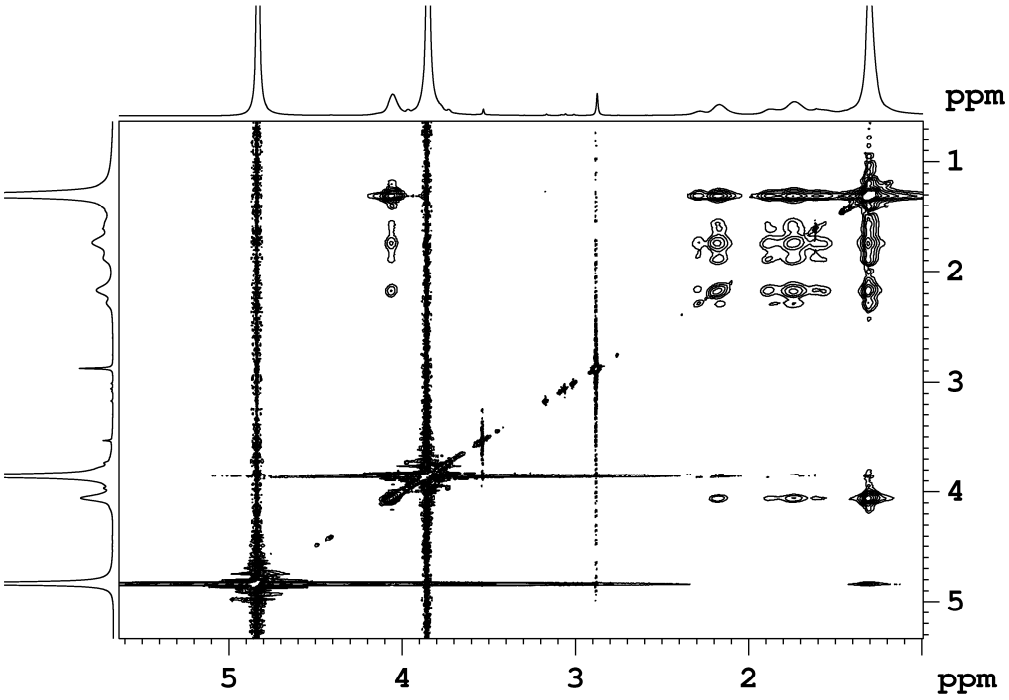

Figure S3. 2D NOESY spectrum of PEO-*b*-PNIPAm in D_2O solution (*c* = 20 wt%) measured at 305 K with mixing time 400 ms.

Publication 5

J. Spěváček, **R. Konefał**, J. Dybal

Temperature-induced phase transition in aqueous solutions of poly(N-isopropylacrylamide)-based block copolymer.

Macromolecular Symposia, **2016**, 369, 92-96.

 DOI: 10.1002/masy.201600058

Temperature-Induced Phase Transition in Aqueous Solutions of Poly(*N*-isopropylacrylamide)-Based Block Copolymer

Jiří Spěváček, Rafał Konefał, Jiří Dybal*

Summary: Temperature-induced phase transition in D_2O solutions of the poly(ethylene oxide)(PEO)-*b*-poly(*N*-isopropylacrylamide)(PNIPAm) block copolymer was investigated and compared with the LCST transition of the PNIPAm homopolymer. We confirmed that the temperature behavior of solutions of the PEO-*b*-PNIPAm in NMR spectra is in accord with existence of micelles where immobilized PNIPAm blocks form rather compact core and mobile PEO blocks form a shell of micelles. By combination of NMR and IR spectroscopy, and DSC we have found that the phase transition and globular structures of the PNIPAm component are significantly affected by the presence of the PEO block. E.g., at temperatures above the phase transition the degree of dehydration of PNIPAm segments (C=O groups) is two times larger in the block copolymer in comparison with the neat PNIPAm. 2D NOESY spectra revealed certain conformation changes in the solution of the PEO-*b*-PNIPAm block copolymer already in the pretransition region.

Keywords: aqueous solutions; block copolymers; micelles; NMR; thermoresponsive polymers

Introduction

It is well known that poly(*N*-isopropylacrylamide) (PNIPAm) and some other amphiphilic polymers show in aqueous solutions a lower critical solution temperature (LCST). They are soluble at lower temperatures but heating above the LCST results in phase separation which makes solutions milk-white turbid.[1–3] When these polymers are chemically crosslinked their hydrogels undergo around this temperature a volume phase transition (collapse) when the gel volume decreases substantially. On the molecular level, both phase separation in solutions and volume phase transition in hydrogels of crosslinked polymers are assumed to be a macroscopic manifestation of a coil-globule transition followed by further aggregation and formation of so-called mesoglobules.[2] Their thermosensitivity makes thermoresponsive polymers interesting for miscellaneous biomedical and technological applications, e.g., as drug release polymers.[2,4] PNIPAm is the most often studied thermoresponsive polymer.

Among various multicomponent thermoresponsive polymer systems, aqueous solutions of block copolymers poly(ethylene oxide) (PEO)-*b*-PNIPAm were also studied. Their heating above the transition temperature of PNIPAm component leads to formation of micelles.[5] At the same time, the phase transition behavior of these copolymers is rather complex.[6–9] In the present paper we provide some results which we obtained recently in investigations of temperature-induced structural changes in D_2O solutions of diblock copolymer PEO-PNIPAm, mainly using NMR and infrared (IR) spectroscopy. We also discuss these results from the point of view of the

Institute of Macromolecular Chemistry, Academy of Sciences of the Czech Republic, Heyrovsky Sq. 2, 162 06 Prague 6, Czech Republic
Fax: +420 296 809 410; E-mail: spevacek@imc.cas.cz

comparison with LCST behavior of the neat PNIPAm homopolymer.

Results and Discussion

Sample of PEO-*b*-PNIPAm diblock copolymer was synthesized by means of single-electron transfer living radical polymerization method[10] when poly(ethylene glycol) monomethyl ether 5000 was used for the preparation of the macroinitiator. An unimodal distribution of molecular weights was confirmed by GPC. Molar ratio of PEO and PNIPAm units in the block copolymer was determined from ^{1}H NMR spectra recorded in $CDCl_3$ at room temperature. Taking into account that the length of PEO block is 114 units, for the length of PNIPAm block we obtained 109 units.

It is now well established that reaching the LCST transition resulting in the formation of rather compact globular structures is accompanied by significant broadening of NMR signals of polymer segments included in mesoglobules.[11] This then results in a marked reduction of integrated intensities of polymer signals in high-resolution NMR spectra recorded on a liquid-state NMR spectrometer. For D_2O solutions of the PEO-PNIPAm block copolymer such behavior was really observed for PNIPAm segments where all PNIPAm signals almost completely disappeared from the ^{1}H NMR spectrum after heating the solution above 312 K.[12] On the other hand the intensity of the signal of PEO protons is not changed by heating to 320 K. This behavior is consistent with existence of micelles where immobilized PNIPAm blocks form rather compact core and mobile PEO blocks form a shell of micelles.[13]

From the temperature dependent integrated intensities of NMR signals it is possible to calculate the values of fraction p of PNIPAm units with significantly reduced mobility;[11] for PEO-PNIPAm block copolymers this is a fraction of units in the micellar core. Temperature

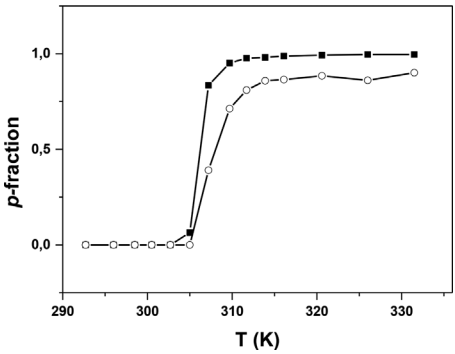

Figure 1.
Temperature dependences of the fraction p of PNIPAm units with significantly reduced mobility for PEO_{114}-*b*-$PNIPAm_{109}$ (○) and neat PNIPAm (■) in D_2O solutions of polymer concentration $c = 5$ wt% during gradual heating.

dependences of the fraction p for D_2O solutions ($c = 5$ wt%) of the PEO_{114}-$PNIPAm_{109}$ block copolymer and neat PNIPAm are then shown in Figure 1. These dependences were determined from integrated intensities of the signal of isopropyl CH protons; temperature dependences of the fraction p determined from integrated intensities of signals of other types of PNIPAm protons are the same so confirming that p-fraction relates to PNIPAm units as a whole. From Figure 1 it follows that while the transition temperature is in both cases almost the same (difference in temperatures of $p_{max}/2$ is ~ 1 K), the width of the both transitions differs significantly. While transition for solution of PNIPAm is rather sharp (transition width 2 K), for PEO_{114}-*b*-$PNIPAm_{109}$ the transition is approx. 7 K broad. Much broader transition for D_2O solution of PEO-PNIPAm block copolymer in comparison with PNIPAm solution we observed also in DSC measurements where the phase transition is manifested by endothermic peak. Moreover, also enthalpies of the transition differ substantially in both cases: $\Delta H = 5.5$ and 4.0 kJ/mol of PNIPAm units for D_2O solution ($c = 5$ wt%) of PNIPAm and PEO_{114}-*b*-$PNIPAm_{109}$, respectively. Differences in the behavior of aqueous

solutions of the neat PNIPAm and PEO-PNIPAm block copolymer exist also concerning a relation between transition temperatures and polymer concentration. In contrast with neat PNIPAm and some other acrylamide-based homopolymers (poly(*N*-isopropylmethacrylamide) and poly(*N*,*N*-diethylacrylamide)) where temperatures
of the LCST transition are virtually independent of polymer concentration, for PEO_{114}-*b*-$PNIPAm_{109}$ block copolymer the transition shifts to 3 K lower temperatures when polymer concentration is increased from 5 wt% to 20 wt%.[12]

Information on the degree of dehydration of PNIPAm segments during the LCST transition can be obtained by IR spectroscopy. Figure 2 shows the temperature dependence of the region of the C=O stretching vibrations (Amide I band) in ATR FTIR spectra of D_2O solution of the PEO_{114}-$PNIPAm_{109}$ block copolymer ($c = 10$ wt%); this region in the solid sample is also shown for the comparison. Two components can be identified in Amide I at temperatures above the phase transition. The wavenumber 1645 cm^{-1} of the new component is the same as in the solid block copolymer showing that this component corresponds to fully dehydrated carbonyl groups. While at temperatures above the transition the values of *p*-fraction are comparable for D_2O solutions of the neat PNIPAm and PEO_{114}-*b*-$PNIPAm_{109}$ block copolymer ($p = 0.9$ for the block copolymer is even slightly smaller in comparison with the neat PNIPAm where $p = 1.0$, cf. Figure 1), from comparison with ATR FTIR spectra of PNIPAm/D_2O solution[14,15] it follows that at temperature above the phase transition (333 K) the degree of dehydration of PNIPAm segments (C=O groups) is substantially higher in the block copolymer in comparison with suspension of the neat PNIPAm. Fitting of the ATR FTIR spectra measured at 333 K to several components of the Voigt profile shows that there are approx. 40% and 20% of dehydrated C=O groups in PEO_{114}-*b*-$PNIPAm_{109}$ and PNIPAm homopolymer, respectively. These results indicate certain differences in internal structures (inclusive of hydrogen-bonded water molecules) of mesoglobules of the neat PNIPAm and micellar cores formed predominantly by PNIPAm blocks of the block copolymer.

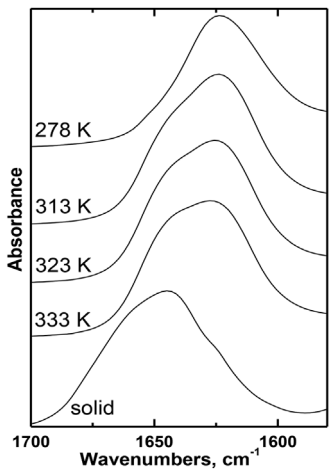

Figure 2.
Temperature dependences of the ATR FTIR spectra (Amide I region) of the D_2O solution ($c = 10$ wt%) of the PEO_{114}-*b*-$PNIPAm_{109}$; this region in solid sample is also shown for the comparison.

In addition to temperature dependences of one-dimensional (1D) NMR spectra, temperature dependences of two-dimensional (2D) ^1H-^1H nuclear Overhauser effect spectroscopy (NOESY) spectra were also recorded. They can provide information on the spatial proximity between protons of PEO block and various proton types of PNIPAm block. Figure 3 shows for illustration the spectrum recorded in D_2O solution ($c = 20$ wt %) of the studied block copolymer PEO_{114}-*b*-$PNIPAm_{109}$; the spectrum was recorded at 301.6 K. From Figure 3 it follows that in addition to strong cross-peaks between various proton groups of PNIPAm units, weaker cross-peaks between PEO protons (signal at 3.8 ppm) and isopropyl CH (4.0 ppm), main chain CH (2.1 ppm), main chain CH_2 (1.7 ppm) and CH_3 (1.25 ppm)

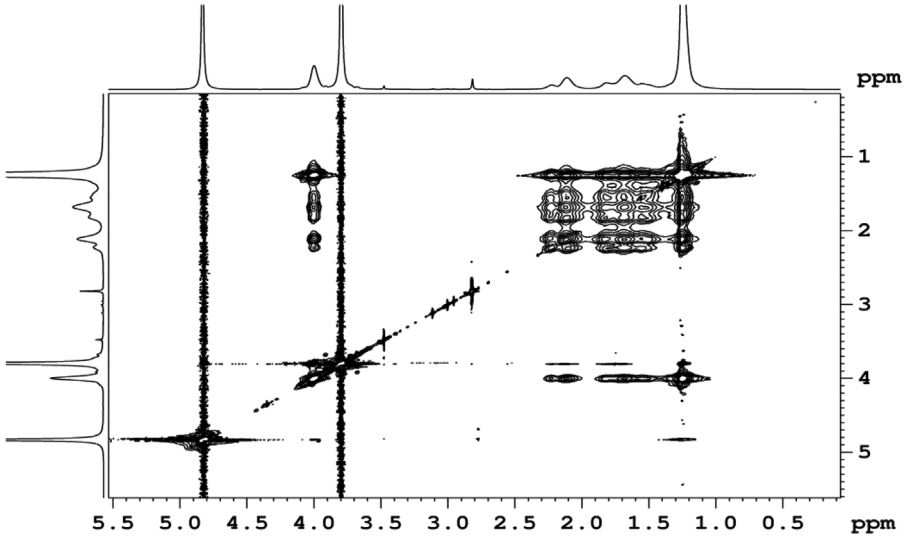

Figure 3.
2D NOESY spectrum of PEO-*b*-PNIPAm in D_2O solution ($c = 20$ wt%) measured at 600 MHz and 301.6 K with mixing time 400 ms.

protons of PNIPAm units are also visible. The existence of these cross-peaks means that distances between respective protons are smaller than 0.5 nm. In the transition region (temperatures >302.5 K) intensity of these cross-peaks decreases, evidently in connection with the significantly reduced mobility of PNIPAm segments which form a compact micellar core. At temperatures above the transition these cross-peaks are not detectable. Interestingly enough, an anomalous increase in intensity of cross-peaks between PEO protons and main chain CH and CH_2 protons, and isopropyl CH protons of PNIPAm units was revealed after increasing the temperature from 292.7 K to 301.6 K.[12] This increase shows that average distance between PEO protons and respective PNIPAm protons is smaller at 301.6 K than at 292.7 K, and/or that number of close contacts (<0.5 nm) between PEO protons and respective PNIPAm protons is significantly increased at 301.6 K. In both cases this implies a change in conformation of the block copolymer. The fact that this change occurs at temperature which is still below the LCST transition of PNIPAm component evidences certain conformation changes in the PEO-*b*-PNIPAm block copolymer already in the pretransition region.[12]

Conclusion

We discussed here phase transition phenomenon in aqueous solutions of the PEO-*b*-PNIPAm block copolymer and compared it with the LCST transition of the PNIPAm homopolymer. The temperature behavior of solutions of the PEO_{114}-*b*-$PNIPAm_{109}$ in NMR spectra is in accord with existence of micelles where immobilized PNIPAm blocks form rather compact core and mobile PEO blocks form a shell of micelles. By combination of NMR spectroscopy, IR spectroscopy and DSC we have found that phase transition and globular structures of PNIPAm component are significantly affected by the presence of the PEO block. This is manifested by larger transition width and reduced value of the enthalpy of the transition, and dependence of transition region on polymer concentration. Moreover, at temperatures above the phase transition the degree of dehydration of PNIPAm segments (C=O groups)

forming core of micelles is two times larger in the block copolymer in comparison with the neat PNIPAm. 2D NOESY spectra revealed certain conformation changes in the solution of the PEO-*b*-PNIPAm block copolymer already in the pretransition region.

Acknowledgements: Support by the Czech Science Foundation (Project 15-13853S) is gratefully acknowledged. R.K. acknowledges the Charles University, Faculty of Science for providing the opportunity to pursue his PhD studies.

[1] H. G. Schild, *Prog. Polym. Sci.* **1992**, *17*, 163.
[2] V. O. Aseyev, H. Tenhu, F. M. Winnik, *Adv. Polym. Sci.* **2006**, *196*, 1.
[3] V. O. Aseyev, H. Tenhu, F. M. Winnik, *Adv. Polym. Sci.* **2011**, *242*, 29.
[4] R. Liu, M. Fraylich, B. R. Saunders, *Colloid Polym. Sci.* **2009**, *287*, 627.
[5] W. Zhang, L. Shi, K. Wu, Y. An, *Macromolecules* **2005**, *38*, 5743.
[6] J. Yan, W. Ji, E. Chen, Z. Li, D. Liang, *Macromolecules* **2008**, *41*, 4908.
[7] R. Motokawa, K. Morishita, S. Koizumi, T. Nakahira, M. Annaka, *Macromolecules* **2005**, *38*, 5748.
[8] A. Papagiannopoulos, J. Zhao, G. Zhang, S. Pispas, A. Radulescu, *Polymer* **2013**, *54*, 6373.
[9] Q. W. H. Tang, P. Wu, *Langmuir* **2015**, *31*, 6497.
[10] X. Tang, X. Liang, Q. Yang, X. Fan, Z. Shen, Q. Zhou, *J. Polym. Sci.: Part A: Polym. Chem.* **2009**, *47*, 4420.
[11] J. Spěváček, *Curr. Opin. Colloid Interface Sci.* **2009**, *14*, 184.
[12] J. Spěváček, R. Konefał, E. Čadová, *Macromol. Chem. Phys.* **2016**, DOI: 10.1002/macp.201600025
[13] J. Spěváček, *Makromol. Chem., Rapid Commun.* **1982**, *3*, 697.
[14] J. Dybal, M. Trchová, P. Schmidt, *Vib. Spectrosc.* **2009**, *51*, 44.
[15] J. Spěváček, J. Dybal, *Macromol. Symp.* **2014**, *336*, 39.

Publication 6

B. Strachota, L. Matejka, A. Zhigunov, **R. Konefał**, J. Spevacek, J. Dybal, R. Puffr

Poly(N-isopropylacrylamide)-clay based hydrogels controlled by the initiating conditions: evolution of structure and gel formation.

Soft Matter, **2015**, 11, 9291-9306.

Soft Matter

PAPER

View Article Online
View Journal | View Issue

Cite this: *Soft Matter*, 2015, **11**, 9291

Poly(*N*-isopropylacrylamide)–clay based hydrogels controlled by the initiating conditions: evolution of structure and gel formation†

Beata Strachota, Libor Matějka,* Alexander Zhigunov, Rafał Konefał, Jiří Spěváček, Jiří Dybal and Rudolf Puffr

Received 10th August 2015,
Accepted 15th September 2015

DOI: 10.1039/c5sm01996f

www.rsc.org/softmatter

The formation of the hydrogel poly(*N*-isopropylacrylamide)–clay (LAPONITE®) by redox polymerization was investigated, and the main factors governing the gel build-up were determined. The significant effect of the redox initiating system ammonium peroxodisulfate (APS) and tetramethylethylenediamine (TEMED) on gel formation and structure was established, making it possible to control the structure of the gel. Moreover, the pre-reaction stage involving the quality of the clay exfoliation in an aqueous suspension and the interaction of reaction components with the clay play a role in controlling the polymerization and gel structure. The molecular and phase structure evolution during polymerization was followed *in situ* by the following independent techniques: Fourier transform infrared spectroscopy (FTIR), chemorheology, small-angle X-ray scattering (SAXS) and ultraviolet-visible spectroscopy (UV/Vis). The combination of these methods enabled us to describe in detail particular progress stages during the gel formation and determine the correlation of the corresponding processes on a time and conversion scale. The mechanism of gel formation was refined based on these experimental results.

1. Introduction

Stimuli-responsive polymer hydrogels have attracted increasing attention as very promising soft materials because of their ability to undergo significant changes in volume in response to external stimuli. The most typical thermosensitive poly(*N*-isopropylacrylamide) (PNIPA)-based hydrogels are used for various applications. However, the PNIPA hydrogels, with covalently cross-linked network structures, are fragile materials and possess a low degree of swelling at higher crosslinking densities. Therefore, for practical applications, the mechanical properties of the soft materials should be improved.

Soft PNIPA-based hydrogels showing extraordinary tensile properties and mechanical toughness were reported by Haraguchi *et al.*[1–3] The gels were formed by *in situ* radical polymerization in the presence of clay. The low-temperature polymerization was initiated by the redox system potassium peroxodisulfate and *N*,*N*,*N*′,*N*′-tetramethylethylenediamine (TEMED). The clay platelets exfoliated in an aqueous solution act as a polyfunctional crosslinker of flexible polymer chains. The generally accepted gel formation mechanism in the PNIPA–clay hybrid[4–7] involves the formation of the "clay-brush particles", *i.e.*, clay aggregates with polymer chains anchored on the surface of clay platelets, in the early polymerization stage. This process is accompanied by a reduction of optical transmittance. Linking of these clay brushes takes place to form large assemblies[8–10] and microgel clusters followed by gelation of the system. Continuation of the polymerization and formation of long grafted chains result in a gradual homogenization and an increase in the transparency of a system. The model of the gelation mechanism was based on measurements of viscosity[4] in the early pregel stage, changes in transparency during polymerization and dynamic light scattering (DLS) and small angle neutron scattering (SANS)[8] data analysis. However, the mechanism is still a subject of discussion. The questions arise as to the nature of the interaction between the clay platelets and polymerization components, the way of system crosslinking, and other issues. In particular, the effect of the redox initiating system on the formation and properties of a polymer/clay gel is not understood.

The aim of this paper was to develop a better understanding of the formation process of PNIPA–clay gels. To gain complex insight into the mechanism of gel build-up, we followed the evolution of both molecular and phase structures during polymerization. The novelty of the investigation is based on the time and conversion correlation of all stages of gel formation determined *in situ* by different independent experimental techniques.

Institute of Macromolecular Chemistry, Academy of Sciences of the Czech Republic, Heyrovsky Sq. 2, 162 06 Prague 6, Czech Republic. E-mail: matejka@imc.cas.cz; Tel: +420 296 809 281

† Electronic supplementary information (ESI) available: TEM micrograph of the dried gel PNIPA-XLS, 30X. See DOI: 10.1039/c5sm01996f

The structure evolution and characterization of particular polymerization stages, including the determination of the gel point, was followed by *in situ* monitoring using Fourier transform infrared spectroscopy (FTIR), rheology, small-angle X-ray scattering (SAXS) and ultraviolet-visible spectroscopy (UV/Vis). In addition to reaction kinetics, the molecular, supramolecular and morphological structures were evaluated. To date, no complex *in situ* time correlation of the processes involved in the corresponding gel formation has been described in the literature. Okay and Oppermann[11,12] studied the formation of a polymer–clay nanocomposite gel by chemorheology. However, the phase structure evolution or conversion correlation of the proposed polymerization stages was not followed. A detailed investigation of gelation was reported by Shibayama *et al.*[8] using an *in situ* method: time-resolved DLS in addition to contrast-variation SANS measurements.

In our study, we investigated the factors governing the formation and properties of the PNIPA–clay gel to determine the formation–structure–property relationships and fine-tune the gel synthesis and properties. The importance of the pre-reaction state of the aqueous clay suspension is discussed, including the quality of the clay dispersion and the interactions of components of the reaction mixture with the clay. Substantial attention is paid to the effect of initiating conditions on the structure build-up and the role of the redox initiating system ammonium peroxodisulfate–*N*,*N*′-tetramethylethylenediamine (APS–TEMED). Usually, gel formation and properties are controlled by the clay and monomer content, while the effect of the initiators has been followed only in few papers. Thermal initiations with AIBN or photopolymerization were reported by Wang *et al.*[13] and Ferse *et al.*,[7] respectively. However, as to the redox system only recently Nigmatullin *et al.*[14] demonstrated using reaction mixtures with high monomer and low clay concentrations that the properties of polyacrylamide–clay hydrogels significantly vary, depending on the initiating conditions during the synthesis. They found that the composition of the redox initiating system affects the polymerization kinetics and the mechanical properties of the hydrogels. The observed trend was attributed to the increase in the degree of self-crosslinking of polyacrylamides due to chain transfer, which was influenced by the composition of the initiating system. In our study, however, we determined a very strong effect of the redox initiator even in solutions of low monomer concentration and relatively high clay concentrations, and we suggest an alternative interpretation of the phenomenon. The effect of the initiator system described in this work makes it possible to efficiently control the polymerization process and thus tune the structure and properties of the final product in a relatively wide range.

Haraguchi *et al.* have mainly used the LAPONITE® XLG clay in their studies. This type of clay, however, is prone to aggregation in water at higher concentrations due to clay platelets assembling to form the so-called ''house of cards'' structures. This phenomenon is a result of attractive interactions between oppositely charged edges and surfaces of the platelets. To prepare aqueous dispersions of high clay content, which would not aggregate, we used pyrophosphate-modified LAPONITE® XLS clay. This approach provided better clay exfoliation and reduced the viscosity of the reaction mixtures.

2. Experimental

2.1 Materials

N-Isopropylacrylamide (NIPA), ammonium peroxodisulfate (APS), *N*,*N*,*N*′,*N*′-tetramethylethylenediamine (TEMED) and hydrofluoric acid were purchased from Aldrich and used as received. The synthetic hectorite clay, LAPONITE® XLS $Na_{0.7}{}^{+}[(Si_8Mg_{5.5}Li_{0.3})O_{20}(OH)_4]^{0.7-}$, consisting of approximately circular platelets (diameter ~30 nm, thickness ~1 nm) and modified with pyrophosphate ions $(P_2O_7)^{4-}$ was donated by Rockwood Ltd. The XLS powder contained 10 wt% water, which was taken into account in the calculation of reactants and solvent amounts for the syntheses of hydrogels.

2.2 Preparation of nanocomposite hydrogels

In the first synthesis step, LAPONITE® XLS (''XLS'') was put into a glass vial and homogeneously dispersed in water *via* mechanical stirring. During this step, the XLS/water mixture was cooled in an ice-water bath at +4 °C, and the stirring time was 1 h for standard samples. To investigate the exfoliation process, the duration of the XLS dispersion step was varied between 2 min and 48 h for selected samples. In the second step, the monomer (NIPA) was added and stirred until dissolution (*ca.* 5 min) and the reaction mixture was purged with argon to remove oxygen. Then, TEMED was added, and the mixture was purged again with Ar. As the last component, the radical initiator APS was added in the form of a 1% aqueous solution cooled to +4 °C, and the mixture was purged with Ar. Finally, the reaction mixture was transferred into a cuvette or fixture, in which the structure development was investigated at 25 °C (using SAXS, NMR, FTIR, and rheology). Solid gel specimens were prepared by transferring the reaction mixtures in argon-filled 5 mL ampoules with an inner diameter of 1 cm.

The concentration of NIPA in solution was 0.75 mol L^{-1}, corresponding to 8.5 wt% in the reaction mixture. As an exception the concentrations 0.5 M and 1 M were also applied. Four clay concentrations, C_{XLS}, were used: 2, 3, 5, and 10 wt% in the reaction mixture, corresponding to approximately 20, 30, 40, and 60 wt% clay in dry poly(NIPA)/clay nanocomposites. The initial clay dispersions, prepared prior to the addition of the other reaction components, had concentrations of 2.6, 4, 6.5 and 13 wt%, respectively. The concentrations of the initiator APS and the activator TEMED were characterized with respect to the monomer content as a molar ratio [APS]/[NIPA] = $[APS]_r$ and [TEMED]/[NIPA] = $[TEMED]_r$, respectively. The sample designation was generated using clay concentration in dry gels and relative concentrations of TEMED and APS. For example, ''30X–0.028–0.0087'' describes the sample with 30 wt% XLS in the dry nanocomposite with $[TEMED]_r$ = 0.028 and $[APS]_r$ = 0.0087.

2.3 Methods

Nuclear magnetic resonance (NMR) measurements. ^{1}H NMR spectra were recorded using a Bruker Avance III 600 spectrometer operating at 600.2 MHz. All NMR spectra and relaxation times were measured on samples in 5 mm NMR tubes that were

degassed and sealed under nitrogen; sodium 2,2-dimethyl-2-silapentane-5-sulfonate (DSS) was used as an internal NMR standard. Typical conditions for measurement of the spectra were as follows: π/2 pulse width 10 μs, relaxation delay 10 s, spectral width 15 kHz, acquisition time 2.18 s, 32 scans. The ^{1}H spin–spin relaxation times T_2 were measured using the CPMG[15] pulse sequence 90_x°–(t_d–180_y°–t_d)$_n$ – acquisition with t_d = 0.5 ms, relaxation delay 60 s and 2 scans. The obtained relaxation curves were monoexponential. For systems wherein the NMR signal of TEMED was very broad (linewidth $\Delta\nu \geq 100$ Hz), T_2 values were determined from the linewidths using the relation $T_2 = (\pi\Delta\nu)^{-1}$.

Zero shear viscosity. For the determination of the zero shear viscosity of solutions, steady-rate sweep tests were performed at shear rates in the range 0.001–100 s^{-1}, and the zero shear viscosity value was extrapolated.

ζ-Potential. The ζ-potentials of the clay–water dispersions were measured at 25 °C using a Malvern Zetasizer Nano ZS, Malvern Instruments. Each data point is an average of approximately 6 measurements.

Shear modulus of gels. The shear moduli (G) of gels were measured on an ARES-G2 (TA Instruments) between parallel plates in slow uniaxial compression mode at room temperature. The uniaxial compression was increased from 0% to 10% in 2 min, while the applied force compression F was recorded. The shear modulus G was calculated using the following equation:[16]

$$G = F/S_0(\lambda^{-2} - \lambda)$$

where S_0 is the initial cross-section of the sample before measurement, $\lambda = l/l_0$, and l and l_0 are compressed and initial heights of samples, respectively. The geometry of the samples was cylindrical, with 10 mm diameter and 10 mm height.

Molecular weight determination of PNIPA chains in the network. PNIPA was separated from the PNIPA–clay gels by dissolving the clay platelets in hydrofluoric acid using the procedure described by Haraguchi.[17] The molecular weight of the PNIPA was determined *via* viscosity measurements using the Mark–Houwink–Sakurada equation,

$$[\eta] = KM_v^a$$

where $[\eta]$ is the intrinsic viscosity, and K and a are constants for a given polymer–solvent–temperature system. The values K = 14.5 × 10^{-2} and a = 0.50 were used for aqueous PNIPA solutions at 20 °C.[18] The viscosity average M_v was determined in this way, which is close to M_w.

***In situ* monitoring of the polymerization**

FTIR. Fourier transform infrared (FTIR) spectra were recorded on a Thermo Nicolet NEXUS 870 spectrometer with a DTGS TEC detector. The spectra with a resolution of 4 cm^{-1} were recorded every 10 s, and 9 scans were averaged. The reaction solution just after initiation was placed in a demountable liquid-cell between two CaF_2 windows separated by a 20 μm teflon spacer. The integrated intensity of the band at ~1417 cm^{-1} assigned to the C–H in-plane-bending vibration of the vinyl group was used in the quantitative analysis of the decrease of C=C double bonds.

Chemorheology. Rheological properties were investigated at 25 °C on a strain-controlled ARES-G2 rheometer (TA Instruments, USA) using a parallel plate fixture with a diameter of 40 mm. Silicone oil was applied on the edge of the plates to prevent water evaporation. Dynamic shear storage modulus $G'(t)$ and loss modulus $G''(t)$ were measured during polymerization by time sweep oscillatory measurements at a frequency of 1 Hz and 0.1% strain amplitude. The strain was kept low enough to be in the linear deformation region and to prevent breakage of the growing structure.

The gel point was determined using the multifrequency sweep measurement ranging from 1 to 64 rad s^{-1} and by applying the Winter–Chambon criterion[19] for a power-law rheological behaviour at the critical state, $G' \sim G'' \sim \omega^n$. This criterion implies that the $\tan\delta$ curves obtained at different frequencies during polymerization intersect in the point of gelation.

Small-angle X-ray scattering (SAXS). The experiments were performed using a pinhole camera (Molecular Metrology SAXS System) attached to a microfocused X-ray beam generator (Osmic MicroMax 002) operating at 45 kV and 0.66 mA (30 W). The camera was equipped with a multiwire, gas-filled area detector with an active area diameter of 20 cm (Gabriel Design). Two experimental setups were used to cover the q range of 0.004–1.1 Å^{-1}, where $q = (4\pi/\lambda)\sin\theta$ (λ is the wavelength and 2θ is the scattering angle). The scattering intensities were put on an absolute scale using a glassy carbon standard.

UV/Vis spectrometry. Changes in transparency during the polymerization were detected using a UV/Vis spectrophotometer (Perkin-Elmer Lambda 20 UV-Vis) at 600 nm wavelength at 25 °C.

3. Results and discussion

3.1 Clay dispersion in water

The properties of nanocomposite hydrogels crosslinked with the clay platelets are dependent on, among other factors, the initial state of the reaction mixture. The quality of a clay dispersion in water, the extent of exfoliation of clay particles and the stability of a clay dispersion prior to the polymerization are crucial for the reproducible synthesis and the final hydrogel properties. We used LAPONITE® XLS instead of LAPONITE® XLG, which does not flocculate to form a gel at low clay content, but still the quality of a clay dispersion is an important factor. For the preparation of a clay dispersion, the clay LAPONITE® XLS was suspended in water and stirred for a time t_{mix}.

The dispersion of clay in water requires hours or even days.[11,20] We investigated the dispersion process of the clay powder in water and the stability of the dispersion by SAXS and measurement of viscosity as well as ζ-potential. Fig. 1a illustrates SAXS profiles of the clay powder before and during dispersion in water. The "dry" powder containing 10% water (see Experimental) shows an interference maximum at q_{max} = 0.50 Å^{-1} corresponding to the interlayer distance d = 13 Å. The figure displays a very quick exfoliation of the particles in water.

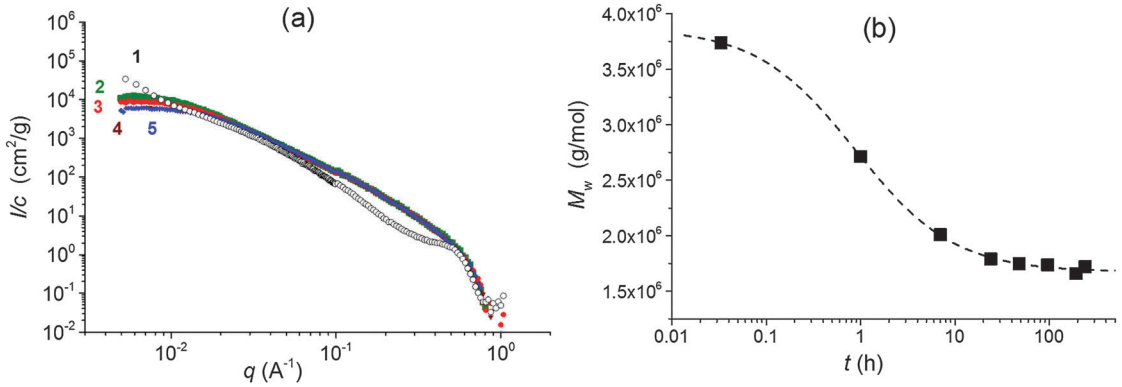

Fig. 1 (a) Evolution of SAXS profiles during mixing of clay suspensions; sample 30X curves (1; ○) – dry, *t*(mixing) = 0 (2; ■) – 2 min, (3; ●) – 1 h, (4; ▲) – 24 h, and (5; ◆) – 48 h; (b) evolution of the molecular weight M_w of clay particles/platelets during mixing, sample 30X.

After only 2 min of stirring, the maximum disappeared, and the individual clay platelets were detected in the 4 wt% suspension (sample 30X before addition of solution of APS). The SAXS profiles of dilute suspensions follow a power law $I(q) \sim q^{-x}$, with $x = 2$ suggesting thin layer shaped objects. The particles' exfoliation, however, is not complete in 2 minutes of stirring. The Guinier analysis of the SAXS profiles in the early mixing stage provides the molecular weight of the silicate nanoparticles of $M_w = 3.9 \times 10^6$. Such a value corresponds to stacks of 2 or 3 clay layers, taking into account the molecular weight of the single platelet $M_w = 1.7 \times 10^6$ reported in the literature.[10] LAPONITE® clay particles containing two or three tightly bound platelets were previously demonstrated.[21–23] The SAXS profiles in Fig. 1a show a decrease in the scattered intensity (I_o) during mixing which is assigned to a decrease of molecular weight. Fig. 1b illustrates the gradual lowering of the determined molecular weight of silicate clusters, implying a disintegration of the stacks of layers upon further stirring. A complete exfoliation of clay in water is achieved in 24–48 h. The molecular weight then approaches the value corresponding to a single platelet. The SAXS results are corroborated by viscosity measurements in Fig. 2, showing a drop in the viscosity of clay suspensions during the mixing. The exfoliation process of clay particles depends on the concentration of an aqueous dispersion and, as expected, it takes a longer time in a more concentrated system of higher viscosity. However, even in the case of the highest clay content in the sample 60X (13 wt% – before addition of solution of APS) the clay particles were completely exfoliated in 48 h. In the literature, the stable dispersion of RDS LAPONITE® (5 wt%) was reported to be formed in 1 day[11] or even in 1 h.[10] The development of a clay dispersion over time was also followed by measurement of the ζ-potential. The exfoliation of clay particles is a result of clay wetting and hydration of Na^+ interlayer ions that are released, thus leading to an increase in the negative charge of the ζ-potential as shown in Table 1. The platelet repulsion then prevails, and viscosity decreases. The clay dispersion and exfoliation were also proved by transmission electron microscopy (TEM). The TEM micrograph of the dried gel 30X in Fig. S1 (ESI†) shows that the gel is homogeneous and the clay platelets are exfoliated well.

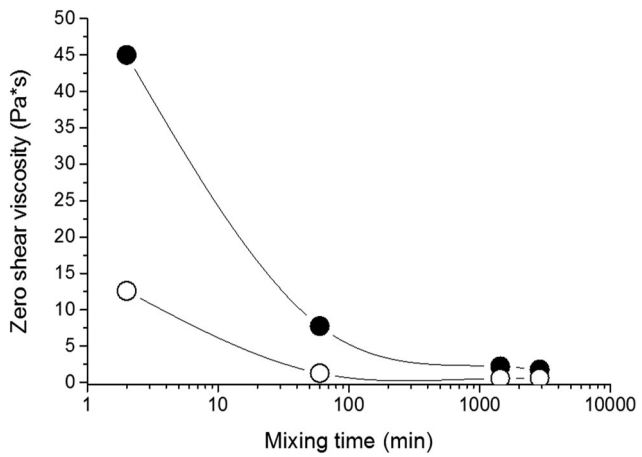

Fig. 2 Zero shear viscosity of clay suspensions as a function of mixing time; curves ○ 30X and ● 60X.

The time for the preparation of a clay suspension and the corresponding degree of clay exfoliation and dispersion was found to be a crucial parameter in hydrogel synthesis. The moduli of hydrogels significantly depend on the mixing time, mainly in systems with high clay concentration as shown in the next paper.[24] For instance, the modulus of the gel 60X is more than 50% higher when the reaction mixture was mixed for 24 h prior to the polymerization compared to that undergoing mixing for only 1 h.

3.2 Interaction of clay with reaction constituents

The clay dispersion is also affected by the reaction mixture components due to their mutual interaction. The monomer NIPA is known to adsorb onto clay surfaces due to H-bonding and

Table 1 ζ-Potential of the clay water dispersions, sample 30X

Mixing time of aqueous clay dispersion	ζ-Potential (mV)
2 min	−23
1 h	−55
2–14 days	−50
1 h + NIPA	−31

dipolar interactions which prevent the clay aggregation and improve the clay dispersion. On the contrary, Haraguchi *et al.*[4] reported that both initiators ammonium persulfate and TEMED promote aggregation of the clay XLG. Both are located near the clay surface due to strong ionic interactions of persulfate or tertiary amine–clay interactions that are not well specified in the case of TEMED.

We checked the effect of the individual reaction mixture agents on dispersion of the XLS in comparison with XLG and the effect of clay concentration and time of mixing on the reaction suspension. The clay XLS used in this paper exhibited a better dispersion in aqueous solution with respect to XLG clay. Fig. 3 displays the viscosity of different mixtures containing low (4 wt%) and high (13 wt%) amounts of clay, corresponding to the samples 30X and 60X, respectively, prepared by mixing for 1 h. In both systems, 30X and 60X, the viscosity of the clay suspension decreased after the addition of NIPA, due to the diminishing extent of clay–water interaction. The initiator APS only slightly augmented the viscosity in contrast to a dramatic increase reported in the case of the XLG suspension. However, the TEMED effect on viscosity growth at high clay content was very significant. The interpretation of this phenomenon is given below.

The interaction of the reaction mixture components NIPA, TEMED and polymer PNIPA with clay was studied by ^{1}H NMR analysis. The analysis proved a very strong interaction for TEMED–clay resulting in immobilization of the TEMED molecule. This effect is demonstrated in Fig. 4, which shows the disappearance of the peaks corresponding to TEMED in the presence of clay. The signals at 2.50 and 2.22 ppm assigned to CH_2 and CH_3 groups of TEMED (see Fig. 4a) were also observed and found to be sharp in the mixture with NIPA (Fig. 4b) and even in the polymerization mixture containing the polymer PNIPA (Fig. 4c). The position of the corresponding peaks was slightly shifted to 2.75 and 2.40 ppm in the polymer solution in contrast to the mixture with monomer only. This effect is a result of an interaction of the TEMED molecule in solution with a polymer, likely due to adsorption. The TEMED fragment covalently bound to a polymer as an initiating end group was not detectable because the molecular weight of the polymer was too high (see below).

In the reaction suspension involving clay, however, the TEMED signals were very broad (Fig. 4d). During polymerization in the presence of clay (Fig. 4e) the situation was the same; in the gel, the TEMED signals were almost not detectable (Fig. 4f). The position of these broad bands appears to be shifted during polymerization by interaction with the polymer in the same way as in the absence of clay.

The disappearance of the peaks in the presence of clay is due to immobilization of the TEMED molecule by strong adsorption onto a clay surface. On the contrary, the peaks corresponding to both NIPA (vinyl═CH and ═CH_2 at 5.73 ppm and 6.18 ppm, respectively, as well as isopropyl CH and CH_3 at 3.98 ppm and 1.17 ppm, respectively) and PNIPA (main chain CH and CH_2 at 2.01 ppm and 1.57 ppm, respectively, as well as isopropyl CH and CH_3 at 3.89 ppm and 1.14 ppm, respectively) were still present in the spectra of the clay containing systems (Fig. 4d–f) in spite of NIPA and PNIPA also being adsorbed onto clay. The NMR results thus prove that the clay–TEMED interaction was much stronger compared to clay–NIPA and clay–PNIPA.

For a quantitative evaluation of the TEMED immobilization and thus the interaction strength with the clay in comparison with the interactions clay–NIPA and clay–PNIPA we determined the T_2 relaxation times characterizing the mobility of the corresponding CH_2 and CH_3 protons. Table 2 shows that T_2 values of TEMED were reduced by almost 3 orders of magnitude in the clay suspension and even more in the polymerized clay suspension and in the gel. The relaxation times of NIPA and PNIPA in the presence of clay were at least 10 times longer than that of TEMED revealing a higher mobility because of a weaker interaction with the clay. Moreover, the ratio of relaxation times corresponding to the TEMED molecule $T_2(NCH_3)/T_2(NCH_2)$ for the clay–TEMED mixture was appreciably higher (~ 2) than that for free TEMED (<1). This finding implies a stronger slowing down of the mobility of CH_2 protons with respect to that of CH_3 by adsorption onto clay. TEMED is often used as a bidentate

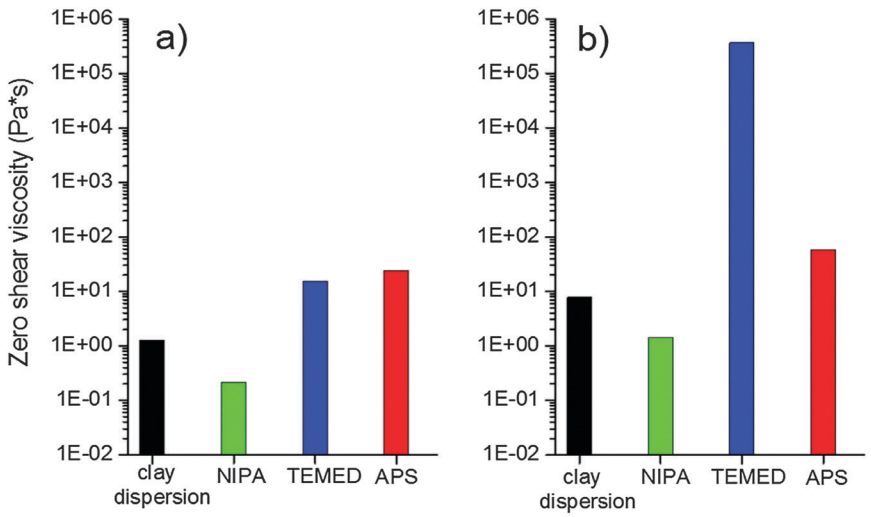

Fig. 3 Effect of reaction components on the viscosity of clay dispersions for different clay contents, mixing time = 1 h: (a) 30X and (b) 60X.

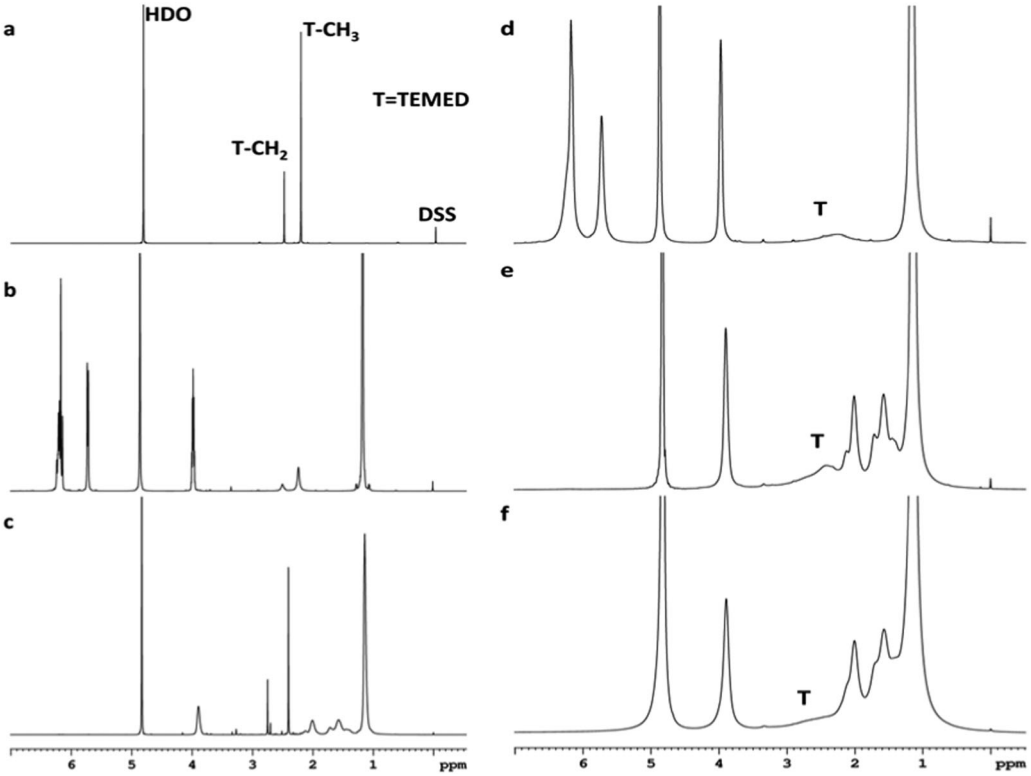

Fig. 4 ^{1}H NMR spectra of TEMED (a), NIPA–TEMED (b), PNIPA–TEMED (c), reaction mixture 30X, clay–NIPA–TEMED/APS (3 : 1), *t*(reaction) = 0 (d), reaction mixture *t* = 20 min (e), and gel 30X (f). All spectra were recorded in D_2O at room temperature.

ligand for metal ions, and the redox initiation is also supposed to proceed through a cyclic intermediate including both TEMED nitrogens (see below). Therefore, we assume that both nitrogens are also involved in the interaction with a silicate layer by N-coordination to exchangeable cations or by H-bonds through a H_2O bridge on an oxygen containing clay surface to form a stable coordination cycle with mainly the CH_2 groups being severely immobilized. The compound dimethylethyleneamine (DMEA) was used as a mononitrogen model of TEMED to test this hypothesis. The higher T_2 values of DMEA in Table 2 compared to TEMED demonstrate a weaker bonding through one nitrogen only and may support the idea of a strong cyclic-type TEMED interaction on the clay surface.

Another possibility of the interaction involving both nitrogens is an interplatelet bridge giving rise to the formation of plate doublets. Such an increase in doublet formation explains the dramatic increase in viscosity of a clay suspension after the addition of TEMED as shown in Fig. 3b. This phenomenon occurs only at a high clay content of 60X (13 wt%), where the platelets are close to each other and could be bridged by the TEMED molecule. No significant increase in viscosity was observed at a lower clay amount, 30X (4 wt%), as shown in Fig. 3a.

Unfortunately, it was not possible to follow the interaction of the initiator APS in a similar way as the behaviour of TEMED because in ^{1}H NMR spectra the signal of APS was overlapped by the signal of the solvent (residual HDO). Moreover, due to low

Table 2 ^{1}H spin–spin relaxation times T_2 of TEMED, DMEA, NIPA and PNIPA molecules

	T_2 [ms]					
	TEMED (or DMEA)		NIPA (or PNIPA)			
Sample	NCH_2	NCH_3	CH_2=	CH=	NCH	CH_3
TEMED	945	868				
NIPA			805	648	1343	722
TEMED–NIPA	26	24	111	104	287	71
TEMED–clay	1.1[a]	2.2[a]				
DMEA–clay	3.0[a]	3.8[a]				
Reaction mixture, *t* = 0 TEMED–NIPA–clay	0.9[a,b]		10	9	24	15
Polymerization, *t* = 20 min TEMED–NIPA–PNIPA–clay	0.8[a,b]				7[c]	
Final gel	0.5[a,b]				7[c]	7[c]

[a] Determined after deconvolution from the linewidth $\Delta\nu$ using the relation $T_2 = (\pi\Delta\nu)^{-1}$. [b] One broad band for both NCH_3 and NCH_2 protons. [c] PNIPA.

sensitivity of the ^{15}N nuclei signal, APS was undetectable in the ^{15}N NMR spectra.

3.3. Hydrogel formation

Gelation is the crucial step of network formation. Moreover, in the multiphase hybrid systems the relative rate of gelation with respect to phase structure evolution, such as aggregation or reaction induced microphase separation, governs the structure and morphology of a hybrid network. Therefore, determination of a correlation between molecular and phase structure development is a way to understand the mechanism of formation and the structure of the hybrid gel. We followed the formation of the PNIPA–clay hybrid hydrogel in all the process complexity using several complementary experimental methods that allowed us to monitor *in situ* both molecular and phase structures and evaluate the corresponding correlation.

3.3.1. Molecular structure evolution. The molecular structure features and evolution during polymerization are characterized by,

(i) the kinetics of polymer growth,

(ii) the molecular weight M_w of the polymer, and

(iii) crosslinking, gelation and the postgel stage.

In situ FTIR and chemorheology measurements were the techniques used to gain the corresponding information.

Polymerization. Polymerization of NIPA is initiated by the redox system involving APS as the initiator and TEMED as an activator promoting the decomposition of APS into free radicals. TEMED decreases the activation energy E_a of polymerization making the reaction possible at low temperatures. While E_a = 62 kJ mol^{-1} in the polymerization initiated with APS, the initiating system APS/TEMED reduces the activation energy to E_a = 22 kJ mol^{-1}.[25] The initiation mechanism proposed by Feng *et al.*[26] is shown in Scheme 1. The reaction scheme is assumed to proceed *via* a charge transfer complex and a cyclic transient state to form two main types of primary initiating radicals.

In addition, hydroxyl radicals formed by hydrolysis ($^*OSO_3H + H_2O \rightarrow H_2SO_4 + HO^*$) are considered to be responsible for initiation.

In the presence of clay minerals, the polymerization process is affected and inhibition[27] as well as catalysis[28,29] of free radical polymerization by clay have been described in the literature.

The reaction kinetics of NIPA polymerization were monitored *in situ* by FTIR spectroscopy. Fig. 5 shows the progress of conversion of the NIPA monomer during the reaction evaluated using the peak at 1417 cm^{-1} attributed to the presence of C=C bonds in vinyl groups. Polymerization initiated by the redox system at 25 °C was relatively fast under the used reaction conditions. Seventy percent conversion was reached in 15 min and the complete conversion in approximately 40 min in the case of the reaction mixture with the following composition: 30X–0.028–0.0043, *i.e.*, [NIPA] = 0.75 M, C_{XLS} = 3 wt%, $[TEMED]_r$ = 0.028, and $[APS]_r$ = 0.0043 (see Fig. 5a).

Initiation stage. The reaction exhibited an induction period that was lengthened by the decreasing content of initiators APS and TEMED (Fig. 5b). A comparison of the curves 1 and 2 shows the effect of the initiators on the neat NIPA polymerization, and curves 3–5 illustrate the polymerization in the presence of clay. Curves 3 and 4 prove the influence of a decreasing content of APS and curve 5 shows the polymerization under diminished concentration of both APS and TEMED. Fig. 5a reveals that the polymerization was slowed down and the induction period was longer in the presence of clay. This period corresponds to an initiation stage that is considered to involve two steps: generation of primary radicals by decomposition of the initiator and production of the first monomer radical by the reaction of the monomer and the primary radical. A slight consumption of the monomer up to 5% can be observed during this induction period.

The initiation is the rate determining step in free radical polymerization. It is dependent on the concentration of the initiator [I], the rate of decomposition k_d and the efficiency of initiation f_i characterizing an effective radical concentration.

$$R_i \sim 2k_d f_i[I], \quad (1)$$

where R_i is the rate of initiation.

In the redox polymerization, usually the initiator and the activator are applied in a constant ratio of concentrations, r = [activator]/[initiator]. In particular, in the case of PNIPA–clay gel preparation, the ratio r = [TEMED] : [APS] = 3 : 1 is often used in the literature. We have thus determined the rate of initiation as a function of the initiators' concentration $[TEMED, APS]_{r=3}$ while keeping the ratio constant at r = 3. The rates of initiation were evaluated as being inversely proportional to the corresponding induction period (t_{ind}); $R_i \sim 1/t_{ind}$. The following dependencies were established for polymerization of neat NIPA and the PNIPA–clay system 60X:

$$R_i(\text{PNIPA}) \sim [\text{TEMED, APS}]_{r=3}^{1.2} \quad (2a)$$

$$R_i(60X) \sim [\text{TEMED, APS}]_{r=3}^{0.8} \quad (2b)$$

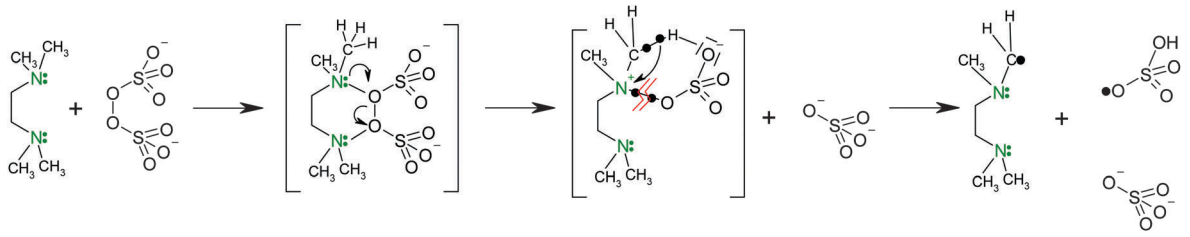

Scheme 1 Mechanism of the primary radical formation in redox initiation by APS and TEMED.[26]

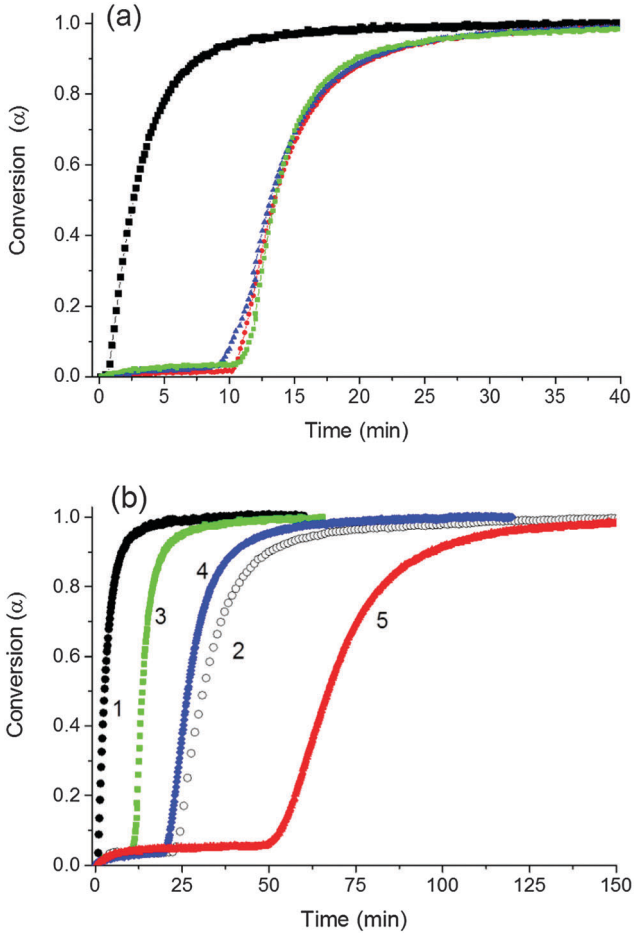

Fig. 5 Kinetics of NIPA conversion during polymerization in systems with a different content of clay and initiators, T = 25 °C (a) the effect of clay content; (■) 0X neat PNIPA, (●) 30X, (▲) 40X, (■) 60X [TEMED]$_r$ = 0.028, [APS]$_r$ = 0.0043; (b) the effect of TEMED and APS content; 1(●) 0X–0.028–0.0043, 2 (○) 0X–0.01–0.0014, 3 (■) 60X–0.028–0.0043, 4 (◆) 60X–0.028–0.0014, and 5 (▲) 60X–0.01–0.0014.

The reaction order for NIPA polymerization was lower in the case of the PNIPA–clay reaction mixture. This effect is a result of lower initiation efficiency in the presence of clay due to the termination of primary radicals. During the polymerization of NIPA in the clay suspension, the initiation is affected by adsorption of both initiators and the monomer onto the LAPONITE® surface. This interaction depends on the type of LAPONITE®. In the case of XLG clay, the persulfate anion is adsorbed by a strong ionic bond to positive charges at the platelet edges while in XLS the edge charges are neutralized by pyrophosphate anions. The interaction is thus much weaker in XLS, as revealed in Fig. 3 showing only a small increase in viscosity by the addition of APS to the clay. The sulfate anions remaining in solution cannot decompose into radicals during the reaction at room temperature because of the corresponding high activation energy (see above). These anions must diffuse to the clay surface to meet the TEMED activator adsorbed onto the clay, to form a charge transfer complex and generate primary radicals (see Scheme 1). Due to strong TEMED adsorption, the formation of primary radicals could be slowed down for steric reasons. Mainly, a high viscosity of clay suspensions may affect the rate of initiation. The formed primary radicals may be more prone to recombination by the solvent cage effect that leads to a reduction of the initiation efficiency and a longer induction period. The induction period is usually associated with an inhibition effect of oxygen or some impurities. The effect of oxygen in the presence of clay was determined by evaluation of the reaction kinetics of the model sample prepared without purging with argon before polymerization. It was proved that mainly the systems with high clay content and a low concentration of APS were very sensitive to the inhibition. Moreover, the influence was much more pronounced on the surface than in the bulk of the gel. The induction period monitored inside such a bulk gel was determined to be significantly prolonged, while at the gel surface the polymerization did not proceed at all. Inhibition by clay has also been reported previously and attributed to electron transfer from initiating or propagating radicals to the clay's Lewis acid sites.[27,28]

Propagation stage. After primary radical formation, the polymerization of nearby adsorbed NIPA monomers begins, and the slow initiation step is followed by a fast propagation, the rate of which is less dependent on the clay and initiators (see Fig. 5). The growing polymer chains are physically bound to clay platelets by coordination and dipolar interactions of the chain end groups from the initiation radicals. Moreover, adsorption of chain segments onto the clay surface also occurs. The molecular weight of a polymer generally increases with increasing monomer concentration [M] and decreasing initiator content as follows from the general expression,

$$P_n \sim k_p[M]/2(k_t f_i k_d[I]_{init}[I]_{act})^{1/2} \quad (3)$$

where P_n is the degree of polymerization; k_p and k_t are propagation and termination rate constants, respectively, and $[I]_{init}$ and $[I]_{act}$ are concentrations of the initiator and the activator, respectively.

Haraguchi *et al.*[30] proved that the M_w of PNIPA during the free NIPA polymerization corresponds to a theoretical dependence on the monomer content with the power equal to 0.98. The theoretical prediction as to the effect of the initiator was proved by Feng *et al.*[26] who determined a decrease in the molecular weight of poly(acrylamide) with increasing TEMED content.

The effect of clay in reducing the amount of initiating radicals should give rise to the generation of fewer growing chains of higher length. Haraguchi, however, determined that clay does not affect the M_w of the polymer which is constant regardless of the clay concentration. We investigated the effect of clay and the effect of initiators upon polymerization in the presence of clay. Our experiments revealed substantially higher values of molecular weight of PNIPA in the gel compared to the linear PNIPA particularly at higher clay content in accordance with a lower efficiency of initiation in the presence of clay. Fig. 6 displays the M_v of PNIPA formed during the linear free NIPA polymerization as well as the M_v of the chains in the hybrid network as a function of concentration of TEMED or APS initiators.

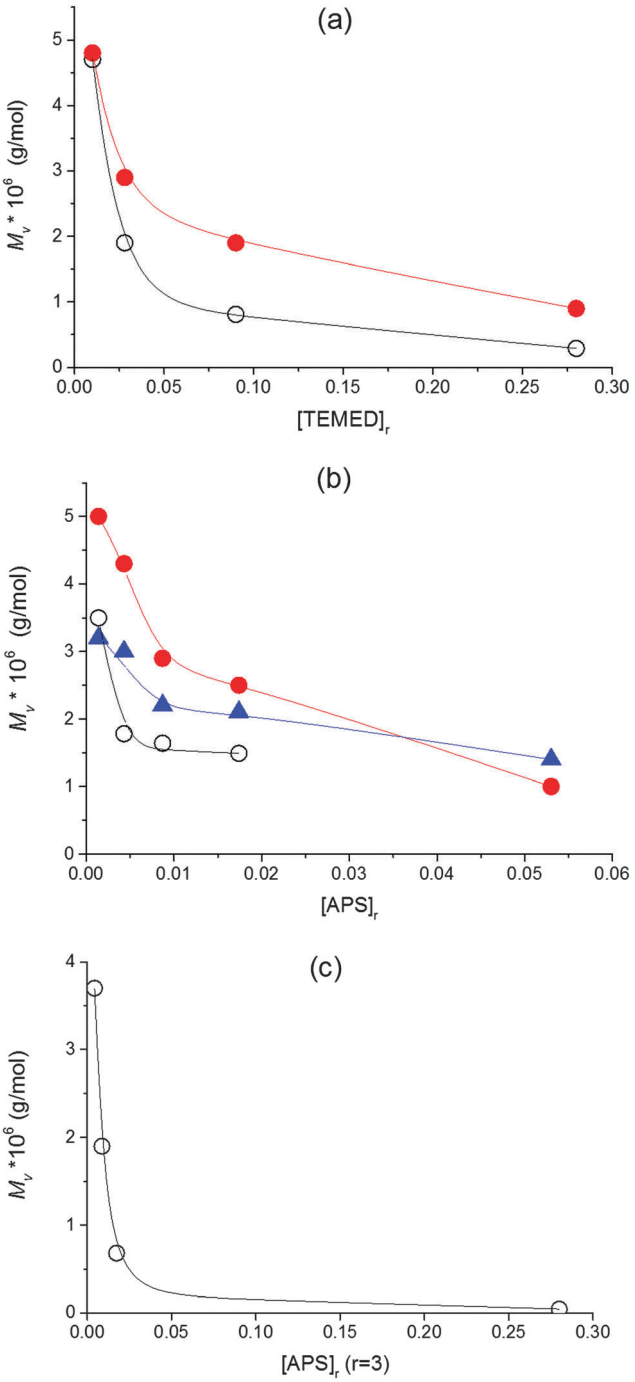

Fig. 6 Molecular weight M_v of PNIPA during linear NIPA polymerization and in the clay based gel as a function of (a) the content of TEMED at constant $[APS]_r$ = 0.0087, (b) the content of APS at constant $[TEMED]_r$ = 0.028, and (c) the content of APS and TEMED at a constant ratio r(=[TEMED]/[APS]) = 3. (○) free PNIPA, (●) PNIPA in gel 30X, and (▲) PNIPA in gel 60X.

The molecular weights of the network chains were determined by a technique used previously by Haraguchi *et al.*[17] (see Experimental). The M_v in Fig. 6 decreased with increasing amount of initiators. At low APS and TEMED content ($[APS]_r < 0.0087$, $[TEMED]_r < 0.028$), the molecular weight reached the value 5×10^6, while it is lower by two orders of magnitude, $M_v = 4.6 \times 10^4$, at high concentrations ($[APS]_r = 0.087$, $[TEMED]_r = 0.28$). The power dependencies determined from double logarithmic plots, however, were smaller compared to the theoretical power 1/2 in eqn (3).

$$M_v(\text{PNIPA}) \sim [\text{TEMED}]^{-0.4}[\text{APS}]^{-0.2} \quad (4a)$$

$$M_v(60\text{X}) \sim [\text{TEMED}]^{-0.35}[\text{APS}]^{-0.1} \quad (4b)$$

At high clay content (60X), the M_v of a polymer is less dependent on the APS concentration. This fact could be related to the more important inhibition effect at high clay amount and low APS content. In this case and in the presence of traces of oxygen, a low conversion and a low fraction of a polymer were determined by FTIR and NMR analyses mainly at the surface of a sample. Also Mauroy *et al.*[31] reported phase segregation and formation of a polymer deficient phase at the surface of the gel PNIPA–LAPONITE® system during polymerization under a controlled amount of oxygen. As a result, an inhomogeneous distribution of a polymer fraction inside the gel and at the surface occurs, giving rise to a broad distribution of molecular weights and a smaller increase in average M_v at low APS content.

In the literature the redox initiators' ratio r is often considered to be crucial in affecting the redox polymerization and the final gel properties, while, typically, the constant ratio is used in the preparation of polymer–clay gels. Adrus *et al.*[32] found that increasing the ratio ($r > 1$) decreases gel times in nonlinear PNIPA polymerization while the low ratio results in a long induction period. Also Nigmatullin *et al.*[14] reported the effect of the ratio on the rate of polymerization/gelation of the polyacrylamide–clay system. They observed a faster polymerization with increasing r at a constant initiator APS concentration, while the polymerization speed was decreased with an increasing r at constant activator content (fastest at $r < 1$). In all these cases, however, the polymerization was accelerated by an increasing overall concentration of the initiator or activator regardless of the ratio of their content. We found, however, that the optimum ratio $r = 3$ promotes the formation of the PNIPA–clay gels displaying the best properties.[24] Taking this into account, we followed the effect of the concentration of initiators while keeping the ratio constant at $r = 3$. Fig. 6c shows that such a dependence of M_v is very dramatic, thus revealing that the overall concentration of both initiators is important for the initiation stage and control of the forming polymer structure. The M_v decreases mainly if the content of both the initiator and activator is high. In this case, termination of primary radicals is favoured.[33]

The molecular weight of the polymer chains between cross-links, *i.e.*, the length of elastically active chains between clay platelets in our case, is an important structural parameter of a gel. This factor determines the structure as well as mechanical and swelling properties of gels. Therefore, the initiators affect not only the rate of polymerization but also the polymer structure. Consequently, the initiating conditions, *i.e.*, the concentration of initiators or their composition, can be used to efficiently control the polymer structure and the final gel properties.[24]

Similar to the initiators, clay also exhibits an effect on the polymerization process and polymer structure. A lower efficiency

of the initiation during NIPA polymerization in the presence of clay results in a decrease of the polymerization speed with respect to the free NIPA reaction and higher molecular weights of polymer chains in a gel.

Crosslinking and gelation. Crosslinking in the PNIPA–clay system could occur by several different ways. The most typical is termination by the recombination of two chains from different clay platelets thus forming a bridge between the platelets that acts as an elastically active network chain. The formation of physically trapped entanglements of two chains anchored on different platelets is another and a very important way of crosslinking. This type of physical bridging of the clay sheets is indirectly experimentally proved by the perfect self-healing properties of these clay–polymer gels.[34] Another possibility is a chain termination in a "radical centre" on another or the same platelet to create an elastically active chain or inactive cycle. In the later stage, however, the access of the chain end to a primary radical on another platelet is limited due to an absorbed polymer layer on the surface of the majority of clay platelets (see below). An unlikely possibility is termination by disproportionation at room temperature polymerization due to the high temperature dependence of this reaction. The self-crosslinking by radical transfer to a chain is typical of free acrylate polymerization.[35,36] Nigmatullin *et al.*[14] reported self-crosslinking at a high monomer concentration even in the presence of a low clay amount. Haraguchi *et al.*, however, excluded such a crosslinking in the systems containing clay above a certain critical concentration.[17] In addition to elastically active chains inactive loops and dangling chains are formed.

Chemorheology, *i.e.*, dynamic shear rheology of a system performed during a chemical reaction, is a reliable and applicable method to follow the *in situ* evolution of a molecular structure, crosslinking and gelation during polymerization. The determined time of gelation t_{gel} is the most important parameter characterizing network formation. However, only few papers have described the chemorheology investigation of PNIPA–clay and similar hydrogel formation. Okay and Oppermann[11] monitored the development of complex shear moduli $G'(t)$ and $G''(t)$ during redox polymerization of acrylamide in an aqueous dispersion of LAPONITE® RDS. They observed that the crosslinking reaction, characterized by a fast growth of the G' modulus, is promoted by an increasing content of LAPONITE®. However, the overall kinetics of structure evolution, including the pregel stage and gelation times, were not determined because the initial period of the reaction exhibiting low moduli below the detection level was not taken into account. In the case of NIPA–XLS polymerization, Okay *et al.*[12] showed a very unusual progress during the crosslinking reaction consisting of an initial abrupt increase in the modulus followed by a continuous decrease with polymerization time. This behaviour was interpreted by inhomogeneity of the gel and the existence of clusters of clay platelets. Nigmatullin *et al.*[14] studied by means of rheology the rate of polymerization of acrylamide in the presence or absence of montmorillonite clay. The rate was characterized by the duration of the initial induction period to reach a certain value of modulus (G' = 3 Pa). This period is not equivalent to the polymerization induction period corresponding to the initiation stage because it includes the rheological behaviour of the polymer. The systems were also characterized by dynamics of the storage modulus evolution in the gelation and postgelation stages.

We monitored the *in situ* crosslinking and gelation of the PNIPA–XLS system by following the evolution of the complex moduli $G'(t)$ and $G''(t)$. None of the abnormalities reported by Okay *et al.*[12] were observed. During polymerization both moduli increased and the system classically progressed through the three stages illustrated in Fig. 7. In the pregel stage $G'' > G'$, in the postgel stage $G' > G''$ and at the gel point $G' \cong G''$. The precise determination of the gel times t_{gel} was based on the Winter–Chambon criterion of the critical state[19] (see Experimental). The gel times are given in Table 3 together with induction periods of polymerization for the selected systems for comparison. For the sake of simplicity, however, only the evolution of the dynamic storage modulus $G'(t)$ is displayed in the following figures. The increase of $G'(t)$ during polymerization of a series of reaction mixtures with different contents of clay (20X–60X), APS and TEMED is shown in Fig. 8. The pregel stage includes an induction period of the polymerization governed by the initiation process (see above) as well as propagation of a polymer chain. An increase in the modulus was relatively small in this stage and was detected under our experimental conditions only during the slow reactions showing a high enough pregel modulus. This enhancement of the modulus is a result of the increasing fraction of a polymer and probably also a result of bridging of the platelets by the growing polymer, thereby forming polymer–clay clusters. The steep increase in the modulus corresponds to the onset of gelation. Gelation is accelerated by an increase in the monomer NIPA concentration (Table 3) and concentrations of the initiators APS and TEMED (Fig. 8) as expected due to the faster kinetics (*cf.* Fig. 5). Moreover, Fig. 8a reveals that gelation was slowed down by the increasing content of clay.

The sharp increase in the modulus at the gel point is typical for fast reacting chemical systems mainly at low viscosity reaction mixtures. In contrast, during the gelation of LAPONITE®

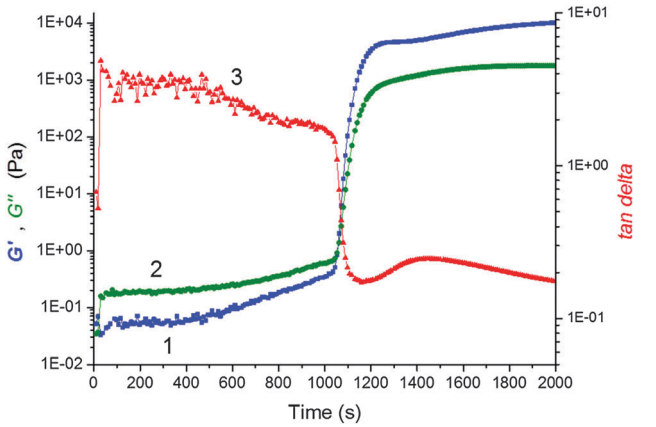

Fig. 7 Evolution of complex moduli $G'(t)$ and $G''(t)$ and the loss factor tan δ during polymerization of the system 60X–0.01–0.0087; 1-(blue ■) storage modulus, 2-(green ●) loss modulus, and 3-(red ▲) loss factor tan δ.

Table 3 Gelation times (t_{gel}) and induction periods (t_{ind}) during the formation of the PNIPA–clay gel $[APS]_r$ = 0.0087 (0.0043), $[TEMED]_r$ = 0.028, T = 25 °C

[NIPA] [mol L^{-1}]	Sample	t_{ind} [min]	t_{gel} [min]
0.75	20X–0.028–0.0087		3
	30X–0.028–0.0087	4	4
	40X–0.028–0.0087	5	6
	60X–0.028–0.0087	5	9
	20X–0.028–0.0043		14
	30X–0.028–0.0043	10	18
	40X–0.028–0.0043	9	22
	60X–0.028–0.0043	10.5	25
0.5	30X–0.028–0.0087		11
1	30X–0.028–0.0087		2.5

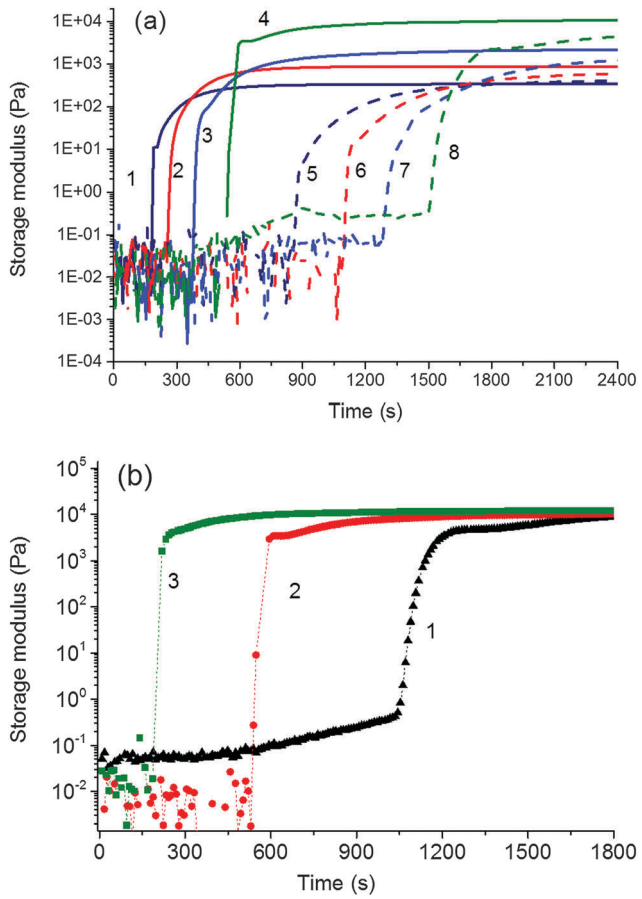

Fig. 8 Evolution of the storage modulus $G'(t)$ during polymerization of the system NIPA–clay at 25 °C, [NIPA] = 0.75 mol L^{-1} (a) effect of clay and APS content, $[TEMED]_r$ = 0.028; curves 1 – 20X, $[APS]_r$ = 0.0087; 2 – 30X, $[APS]_r$ = 0.0087; 3 – 40X, $[APS]_r$ = 0.0087; 4 – 60X, $[APS]_r$ = 0.0087; 5 – 20X, $[APS]_r$ = 0.0043; 6 – 30X, $[APS]_r$ = 0.0043; 7 – 40X, $[APS]_r$ = 0.0043; 8 – 60X, $[APS]_r$ = 0.0043; (b) the effect of TEMED content, $[APS]_r$ = 0.0087, 60X; curves 1(▲) $[TEMED]_r$ = 0.01, 2(●) $[TEMED]_r$ = 0.028, and 3(■) $[TEMED]_r$ = 0.09.

without polymer, Tanaka *et al.* found that the complex viscosity changed much more smoothly at the gelation point.[37] This difference in rheology evolution reflects the different types of gelation.[38,39]

While LAPONITE® undergoes aggregation, physical gelation, the PNIPA–XLS gelation, is the chemical process, mainly the recombination of PNIPA chains. Colloidal gelation occurring *via* noncovalent bonds is often controlled by diffusive transport, whereas the chemical gelation is reaction limited and realized by covalent bond percolation.[40] Diffusion control could lead to a smooth change in viscosity at the gel point of LAPONITE®. On the contrary, the PNIPA–clay gelation is reaction rate limited resulting in a faster evolution of rheology close to the gel point. The PNIPA–clay is a physical gel because of physical interactions of clay–PNIPA. However, the crosslinking proceeds by combination of chemical reactions and physical interactions. In the early stage and during gelation, the chemical reactions dominate resulting in the steep increase in the modulus at the gel point. Consequently, the structure growth and gelation of the PNIPA–clay system can be treated as chemical crosslinking and gelation.

The rate of gel formation is generally determined mainly by the kinetics of the crosslinking reaction and the content and functionality (f) of a crosslinker governing the critical conversion at the gel point $\alpha_c = 1/(f-1)$. At high functionality the gelation occurs earlier at a low conversion. In our case two opposite factors played a role. The clay serves as a multifunctional crosslinker and increasing its amount should accelerate the gelation of a system. On the other hand, the clay slows down the polymerization of NIPA, thus delaying gelation. The kinetics are decelerated in the presence of clay; however, this effect is independent of clay content (Fig. 5 and Table 3) contrary to gelation (Fig. 8 and Table 3). Hence, another factor must be responsible for the deceleration of gelation with increasing clay content. The polymerization is initiated at the clay surface by TEMED (or APS) radical fragments. At a constant TEMED concentration and increasing content of clay, the average number of initiating sites on the clay platelet, *i.e.*, a theoretical functionality of the plate $f_{th(platelet)}$ ($\sim$[TEMED–APS]/C_{XLS} under full initiating efficiency) is reduced (see Scheme 2). Gelation of the system, *i.e.*, the time of gelation, depends on an average theoretical functionality of a clay platelet. Therefore, $t_{gel} \sim 1/f_{th(platelet)} = C_{XLS}/[TEMED–APS]$. Consequently, at a constant TEMED (and APS) concentration and increasing content of clay,

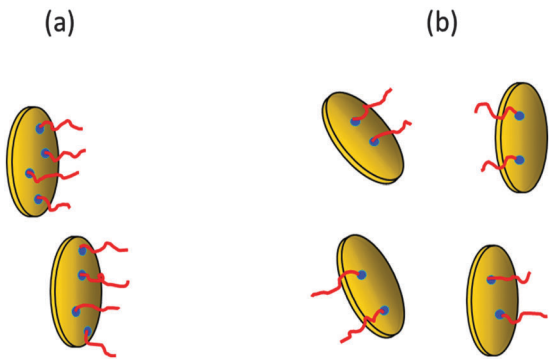

Scheme 2 Functionality of clay platelets corresponding to the number of issuing polymer chains at (a) low clay content and (b) high clay content, for polymerization at a constant concentration of initiators.

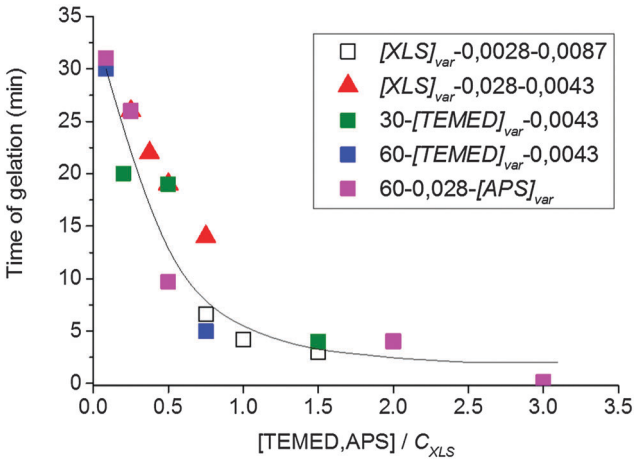

Fig. 9 Gel time as a function of the ratio of concentrations [TEMED–APS]/C_{XLS} corresponding to the theoretical functionality of the platelet.

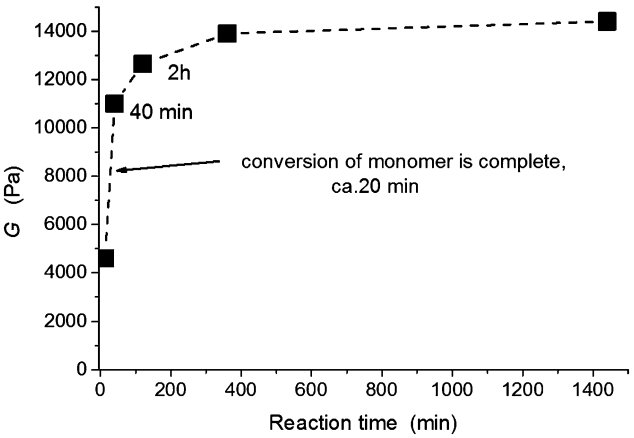

Fig. 10 Evolution of the modulus in the postgel stage during polymerization of the system 60X, the content of initiators $[APS]_r$ = 0.0087, $[TEMED]_r$ = 0.028 (T = 25 °C).

the gelation speed is decreased. This hypothesis is supported by the plot in Fig. 9. The master curve of the dependence of gel times on theoretical functionality of the platelet describes relatively well the gelation of all studied systems with different contents of clay, TEMED and APS. The ratio C_{XLS}/[TEMED–APS] in different systems is considered relatively with respect to the standard mixture 30X–0.028–0.0087 (see Experimental).

The ratio is determined relatively with respect to the standard mixture 30X–0.028–0.0087.

Postgel stage. In the postgel stage the modulus continues to grow as the crosslinking density gradually increases and finally reaches a plateau. Fig. 8a shows the complexity of the gel formation. While the time of gelation is delayed with increasing clay content, the modulus in the postgel stage is enhanced. The interpretation of this fact and discussion of the mechanical properties are given in the next paper.[24] The chemorheology measurements of hydrogels, however, are not well suited for a long monitoring of the polymerization because of water evaporation and a corresponding change in the degree of swelling. Therefore, a long time evolution of the modulus in the postgel stage, displayed in Fig. 10, was determined by measuring the separate samples polymerized *ex situ* in closed vials for a particular reaction time. The majority of modulus enhancement occurred within 1 h during the polymerization of the 60X sample. A slight increase, however, continued up to 24 h despite the fact that the radical polymerization was finished, *i.e.*, the monomer completely reacted in less than 30 min. We suggest that this increase of modulus was brought about by a slow formation of trapped entanglements thus generating additional physical crosslinking.

3.3.2. Phase structure evolution. The phase structure and its evolution during polymerization were investigated by SAXS and UV/Vis providing generally information on a small size scale (0.5–20 nm) and on a large one (>100 nm), respectively.

The development of the phase structure during polymerization followed by *in situ* time resolved SAXS is illustrated in Fig. 11. One can see the appearance and growth of a shoulder at

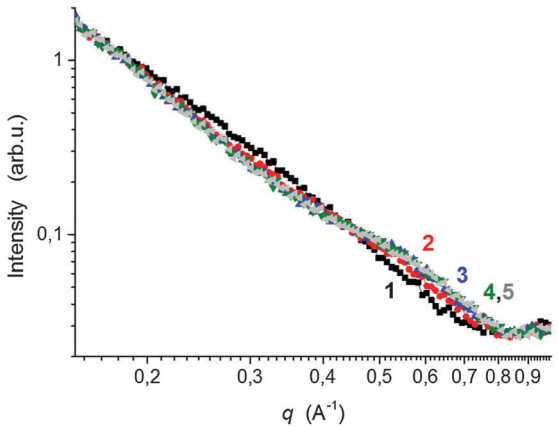

Fig. 11 SAXS profiles during polymerization of PNIPA–clay at 25 °C, (60X–0.028–0.0043). The curves are indicated according to the reaction time; 1 (■) 10 min, 2 – (●) 20 min, 3 – (▲) 30 min, 4 – (▼) 40 min, and 5 – (◀) 100 min.

high q values (~0.5 Å^{-1}) of the SAXS profiles in the early polymerization stage. This shoulder is attributed to the formation of a polymer layer on clay platelets. The radius of gyration of the adsorbed polymer determined by the function of a generalized Gaussian coil was found to be R_g = 6.3 Å, which roughly corresponds to the polymer layer thickness D = 16 Å [geometrical diameter of a particle $D = (5/3)^{1/2}2R_g$ under an assumption of a spherical shape, which reflects an upper limit of the layer thickness]. This finding is in agreement with literature data as Shibayama *et al.*[8] reported the polymer layer with a thickness of *ca.* 10 Å and Nelson *et al.*[41] determined the monolayer of polyethers on the clay surface of 11–16 Å thickness. R_g of the layer is approximately constant for all the time, thus proving that no further polymer adsorption takes place after saturation of the clay surface by a monolayer. The gradual increase in the SAXS intensity in the shoulder region is in accordance with an increase in the number of clay platelets covered with a polymer layer. In approximately 30 min, the intensity reaches a plateau, likely revealing that all the accessible platelets are covered as in the

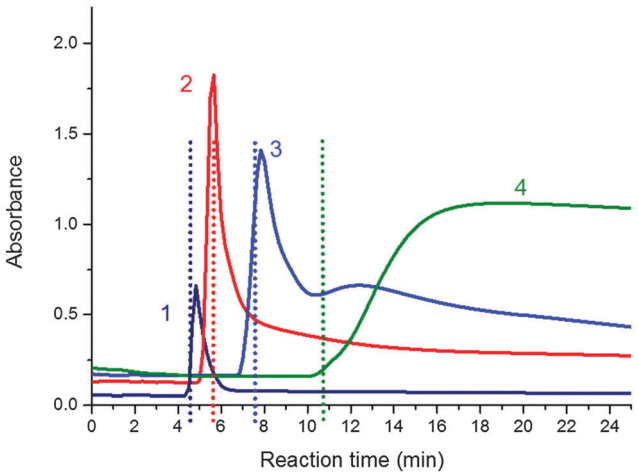

Fig. 12 Evolution of absorbance at 600 nm measured by UV-Vis spectrometry during polymerization of the PNIPA–clay system at 25 °C, $[APS]_r$ = 0.0087, $[TEMED]_r$ = 0.028; curves: 1 – 20X, 2 – 30X, 3 – 40X, and 4 – 60X. Dashed lines show the gelation point.

case of the sample 0.75N–60X–0.028–0.0043. This phase structure evolution was compared with the molecular structure evolution determined by chemorheology. Fig. 8a shows that the corresponding system gelled at approximately 25 min, which approximately corresponds to the time of coverage of the majority of the clay platelets.

In situ UV/Vis spectrometry measurements were conducted during polymerization to examine the turbidity in the PNIPA–clay system as described in the literature[7] and correlate it with molecular structure evolution. Fig. 12 illustrates the evolution of the absorbance at 600 nm of the reaction dispersions during polymerization of four systems with different clay contents (20X–60X). The initially homogeneous transparent reaction mixtures exhibited a sharp drop in transparency followed by a period of turbidity and the recovery of a partly transparent state revealing a final homogenization. The evolution of turbidity was compared with the gel points of the systems determined by chemorheology. The mixtures became cloudy shortly before the gel point. The dashed lines in the figure display gelation. The increasing clay amount in the mixtures shifted the appearance of turbidity to longer reaction times in agreement with the corresponding shift of gelation. The cloudy period was relatively short, being only 1.5 min for the sample 20X, however, the period was lengthened with increasing clay content in the gel. Also the transparency of the finally cured gels decreases at a higher amount of clay. Moreover, very cloudy systems were formed in the case of high concentration of the APS initiator.

These results related to the phase structure are in agreement with literature data[4,8] generated using DLS and SANS. The novelty of our investigation consists in the precise time correlation of these phenomena with molecular structure development, such as the initiation of polymerization, growth of the polymer fraction, gelation and postgel increase in the crosslinking density as determined by independent techniques.

3.3.3 Mechanism of PNIPA–clay hydrogel formation. Based on the complementary results refinement and a slight modification of the generally accepted model of the mechanism of the PNIPA–clay hybrid gel formation are proposed. The build-up of the gel involves the following consecutive stages (see Scheme 3):

(a) Pregel stage. The initial slow reaction stage is determined by the formation of primary radicals and the initiation of the NIPA polymerization in the aqueous suspension of well-dispersed and exfoliated clay platelets. The redox type initiation is manifested by the induction period, which is the rate determining step of the process. An increasing content of initiators, APS and

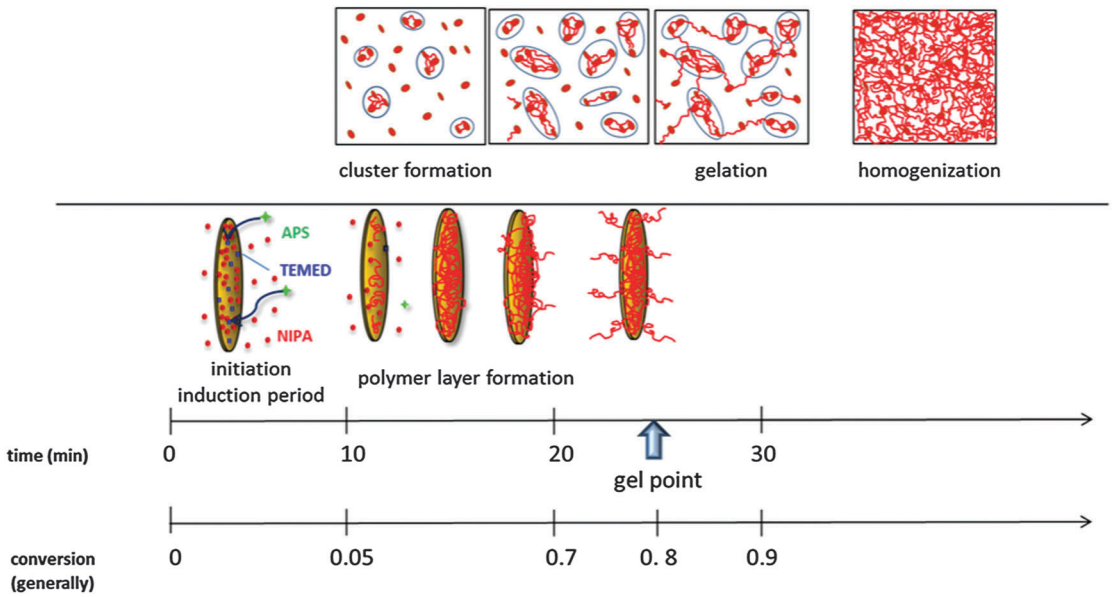

Scheme 3 Progress of gel formation during polymerization. The time and conversion scales determined for polymerization of the sample 0.75N–60X–0.028–0.0043 at T = 25 °C.

TEMED, reduces the induction period and accelerates the polymerization thus enabling control of the polymerization rate. On the contrary, the presence of clay in a reaction mixture results in inhibition of polymerization and lengthening of the induction period, t_{ind} (Fig. 5) due to the mobility and steric restrictions to form the active redox complex APS–TEMED (see Scheme 1). The strong adsorption of TEMED onto a clay surface and a high medium viscosity could play a role.

The induction period is followed by a fast polymerization and polymer fraction growth (Fig. 5). The formed polymer chains adsorb onto the clay platelets and create a polymer monolayer of a constant thickness of ~1.5 nm on their surface. The fraction of the covered clay sheets gradually increases until all accessible sheets are grafted with a polymer layer (t_{layer}) (*cf.* Fig. 11).

After saturation of the clay platelet surface, the grafted chains continue to grow outward from the platelet into the solution interplatelet space. Only then can the polymer chains issuing from different platelets crosslink and form a bridge between platelets, most likely by a chemical reaction, such as recombination and formation of entanglements. The bridging of the clay sheets gives rise to the formation of clusters and results in system heterogeneity due to the irregular density of growing crosslinked domains (clusters). This phenomenon is manifested by a slight increase in the modulus in the pregel stage (Fig. 8) (also an increase in the polymer fraction contributes to this modulus enhancement) and the appearance of turbidity (Fig. 12). The gradual increase of the modulus, likely characterizing the formation and growth of clusters (one of the possible interpretations), sets early in the pregel stage ($t_{clustering}$) immediately after the induction period (*cf.* Fig. 5 and 8) and continues until gelation. The process occurs in the conversion region of the monomer $\alpha \sim 0.1$–0.8. The turbidity, however, is observed only just before gelation in the conversion of ~0.7 when large clusters detectable by UV/Vis spectrometry are created ($t_{turbidity}$) (*cf.* Fig. 8 and 12). In the case of XLG clay, Shibayama and Haraguchi reported[4,8] a distinct reduction in transparency already in the early stage and a monomer conversion $\alpha = 0.07$ at a minimum transparency. Both crosslinking and the appearance of turbidity are delayed by increasing the content of clay. This finding is contrary to the results of Chen and Xu[42] who observed an earlier turbidity period in systems with a higher concentration of clay LAPONITE® RD. This difference could be related to the clay type as RD LAPONITE® is prone to form "house of cards" structures at higher clay content unlike the XLS LAPONITE®. The heterogeneity is more pronounced in gels prepared with a high content of initiators. In this case, the extremely fast polymerization leads to excessive clustering and build-up of a microgel-like structure, which is manifested by strong turbidity. This phenomenon is discussed in the next paper.[24]

(b) Gelation. Gelation of the system sets in at a relatively high conversion of the monomer, *i.e.*, the fraction of the polymer being ~0.7–0.9 (*cf.* Fig. 5 and 8) (this is not the conversion of the crosslinking reaction).

A large fraction of polymer first covers the clay platelets, and only after the surface saturation by the polymer layer does the crosslinking and clustering occur. The clusters are gradually interconnected, mainly by the reaction (recombination) of PNIPA chains, and gelation of the system occurs by bond percolation (t_{gel}) as in the typical chemical gelation. The delay of gelation by clay is a result of the inhibition effect of clay and a slower polymerization, as well as by decreasing the functionality of clay platelets with increasing clay concentration.

(c) Postgel stage. Gradually all clay sheets are covered by a polymer layer (Fig. 11) and issue polymer chains forming bridges between platelets. They are thus incorporated into the gel and enhance the gel fraction. The increasing crosslinking density in the postgel stage and continuous bridging of the clusters within the gel results in homogenization of the system and recovery of transparency (Fig. 12). The recovery is delayed by a high clay content. In the late postgel stage, even after termination of the radical polymerization, the crosslinking density is slowly enhanced by the formation of trapped entanglements (*cf.* Fig. 5 and 10).

The particular progress stages were characterized by the reaction times t_x and conversion α during polymerization. While the time scale is applicable for a particular system only, the conversion scale could be more general. The experimentally determined development during polymerization of the sample 0.75N–60X–0.028–0.0043 at $T = 25$ °C is as follows:

t_{ind} = 11 min, α_{ind} = 0–0.05 – induction period (FTIR)

t_{layer} = 11–30 min, α_{layer} = 0.05–0.8 – formation of a polymer layer on the clay platelet up to all covered platelets (SAXS)

$t_{clustering}$ = 11–25 min, $\alpha_{clustering}$ = 0.1–0.8 – bridging of platelets, formation of clusters (chemorheology)

$t_{turbidity}$ = 22.5 min (maximum at 30 min), $\alpha_{turbidity}$ = 0.8–0.85 – formation of large clusters (UV/Vis)

t_{gel} = 25 min, α_{gel} = 0.8–0.9 – gelation of the system (chemorheology)

$t_{transparency} > 35$ min, $\alpha_{transparency} > 0.9$ – a gradual increase in transparency due to homogenization of the gel (UV/Vis)

$t_{ent} \geq 60$ min, $\alpha_{ent} = 1$ – formation of entanglements dominates this stage (DMA).

Scheme 3 illustrates the progress in gel formation involving time and conversion correlations of the experimentally determined processes.

4. Conclusions

In situ monitoring of the gel formation by several independent methods (FTIR, chemorheology, SAXS, and UV/Vis) enabled the detailed time and conversion correlation of molecular and phase structure evolution during gel formation. Such a correlation has not been performed to date. Using these complementary methods, 7 progress stages of the gel formation were experimentally determined during polymerization and were then characterized and correlated to each other: (1) induction period (FTIR), (2) polymer propagation and coverage of clay platelets by a polymer monolayer (FTIR and SAXS), (3) saturation of the clay surface followed by crosslinking and bridging of clay platelets resulting in clustering (SAXS and chemorheology),

(4) large cluster generation giving rise to the formation of an inhomogeneous structure and the appearance of turbidity (UV/Vis), (5) gelation by interconnection of clusters and bond percolation, including precise determination of the gel point (chemorheology), (6) postgel stage structure homogenization (UV/Vis) and (7) postgel growth of crosslinking density by entanglement formation (FTIR and DMA).

The crucial factors determining structure evolution are discussed, and their effect on the formation and properties of PNIPA–clay hydrogel is clarified. The gel formation and properties are known to be determined by the content of clay and monomer in an aqueous suspension. In this and the next paper we show, in addition, very efficient control of both gel build-up (this work) and the gel properties (next paper)[24] by reaction conditions, including the redox initiator system and the prereaction stage of clay suspension preparation. Moreover, the complex effect of clay on NIPA polymerization and gel formation was clarified.

Dispersion of the XLS clay powder in the prereaction stage is fast; however, stacks of 2 or 3 clay layers are present for a long time in the clay suspension mainly at high clay content. A perfect exfoliation takes time, and a careful preparation of a clay suspension is therefore necessary as the degree of exfoliation prior to polymerization strongly determines the final gel properties.[24]

The process of polymerization and gel formation is significantly affected by the redox initiating system, the initiator APS and the activator TEMED. They control not only the rate of polymerization but also the polymer structure. Their initiation efficiency is manifested in the early stage of the polymerization by the induction period corresponding to the formation of primary radicals. Reducing the concentration of the initiators leads to a decrease in the speed of polymerization. However, on the other hand, this reduction also leads to the generation of higher molecular weight chains. This finding implies the possibility of controlling the chain length between crosslinks in the gel independently of the crosslinking density determined by the clay content.

The clay acts in the gel formation not only as a crosslinker and reinforcing nanofiller but also influences the polymerization process as well. The presence of clay promotes the inhibition of polymerization by lowering the efficiency of the initiators. This effect is attributed mainly to sterical and mobility restrictions for the formation of primary radicals in a high viscosity medium. A very strong interaction of the activator TEMED with the clay platelets of a coordination type likely plays a role. Moreover, increasing the clay content at a constant initiator concentration results in a delay of gelation due to the decreasing functionality of the clay platelet despite an improvement in the mechanical properties.

Acknowledgements

The authors acknowledge the financial support of the Grant Agency of the Czech Republic (Projects P108/12/1459 and 13-23392S). B.S. and R.K. acknowledge the Charles University Faculty of Science for providing the opportunity to pursue their PhD studies.

References

1 K. Haraguchi, T. Takehisa and S. Fan, *Macromolecules*, 2002, **35**, 10162.
2 K. Haraguchi and H. J. Li, *Macromolecules*, 2006, **39**, 1898.
3 K. Haraguchi, H. J. Li, H. Y. Ren and M. Zhu, *Macromolecules*, 2010, **43**, 9848.
4 K. Haraguchi, H. J. Li, K. Masuda, T. Takehisa and E. Elliott, *Macromolecules*, 2005, **38**, 3482.
5 K. Haraguchi, *Colloid Polym. Sci.*, 2011, **289**, 455.
6 K. Haraguchi and Y. J. Xu Colloid, *Polym. Sci.*, 2012, **290**, 1627.
7 B. Ferse, S. Richter, F. Eckert, A. Kulkarni, C. M. Papadakis and K. F. Arndt, *Langmuir*, 2008, **24**, 12627.
8 S. Miyazaki, H. Endo, T. Karino, K. Haraguchi and M. Shibayama, *Macromolecules*, 2007, **40**, 4287.
9 S. Abdurrahmanoglu, V. Can and O. Okay, *J. Appl. Polym. Sci.*, 2008, **109**, 3714.
10 J. Nie, B. Du and W. Oppermann, *Macromolecules*, 2005, **38**, 5729.
11 O. Okay and W. Oppermann, *Macromolecules*, 2007, **40**, 3378.
12 S. Abdurrahmanoglu and O. Okay, *J. Appl. Polym. Sci.*, 2010, **116**, 2328.
13 Y. Wang, J. Ma, S. Yang and J. Xu, *Colloids Surf., A*, 2011, **390**, 20.
14 R. Nigmatullin, M. Bencsik and F. Gao, *Soft Matter*, 2014, **10**, 2035.
15 T. C. Farrar and E. D. Becker, *Pulse and Fourier transform NMR*, Academic Press, New York, 1971, p. 27.
16 M. Ilavský, *Adv. Polym. Sci.*, 1993, **109**, 173.
17 K. Haraguchi, Y. Xu and G. Li, *Macromol. Rapid Commun.*, 2010, **31**, 718.
18 S. Fujishige, *Polym. J.*, 1987, **19**, 297.
19 H. H. Winter and M. Mours, *Adv. Polym. Sci.*, 1997, **134**, 165.
20 C. Martin, F. Pignon, A. Magnin, M. Meireles, V. Lelièvre, P. Lindner and B. Cabane, *Langmuir*, 2006, **22**, 4065.
21 J. Fripiat, J. Cases, M. Francois and M. Letellier, *J. Colloid Interface Sci.*, 1982, **89**, 378.
22 L. Rosta and H. R. von Gunten, *J. Colloid Interface Sci.*, 1990, **134**, 397.
23 J. M. Saunders, J. W. Goodwin, R. M. Richardson and B. Vincent, *J. Phys. Chem. B*, 1999, **103**, 9211.
24 B. Strachota, J. Hodan and L. Matějka, submitted.
25 X. Guo, K. Qiu and X. Feng, *Chin. J. Polym. Sci.*, 1989, **7**, 165.
26 X. D. Feng, X. Q. Guo and K. Y. Qiu, *Makromol. Chem.*, 1988, **189**, 77.
27 D. H. Solomon and J. D. Swift, *J. Appl. Polym. Sci.*, 1967, **11**, 2567.
28 P. Bera and S. K. Saha, *Polymer*, 1998, **39**, 1461.
29 A. S. Badran, A. A. Abdelhakim, A. B. Moustafa and M. A. Abdelghaffar, *J. Polym. Sci., Part A: Polym. Chem.*, 1988, **26**, 609.
30 Y. Xu, G. Li and K. Haraguchi, *Macromol. Chem. Phys.*, 2010, **211**, 977.

31 H. Mauroy, Z. Rozynek, T. S. Plivelic, J. O. Fossum, G. Helgesen and K. D. Knudsen, *Langmuir*, 2013, **29**, 371.
32 N. Adrus and M. Ulbricht, *React. Funct. Polym.*, 2013, **73**, 141.
33 G. S. Misra and U. D. N. Bajpai, *Prog. Polym. Sci.*, 1982, **8**, 61.
34 K. Haraguchi, K. Uyama and H. Tanimoto, *Macromol. Rapid Commun.*, 2011, **32**, 1253.
35 J. Gao and B. J. Frisken, *Langmuir*, 2003, **19**, 5212.
36 J. Gao and B. J. Frisken, *Langmuir*, 2003, **19**, 5217.
37 H. Tanaka, S. Jabbari-Farouji, J. Meunier and D. Bonn, *Phys. Rev. E: Stat., Nonlinear, Soft Matter Phys.*, 2005, **71**, 021402.
38 A. Zaccone, J. J. Crassous and M. Ballauff, *J. Chem. Phys.*, 2013, **138**, 104908.
39 A. Zaccone, H. H. Winter, M. Siebenburger and M. Ballauff, *J. Rheol.*, 2013, **58**, 1219.
40 S. Coresszi, D. Rioretto and F. Sciortino, *Soft Matter*, 2012, **8**, 11207.
41 A. Nelson and T. Cosgrove, *Langmuir*, 2004, **20**, 2298.
42 Y. Chen and W. Xu, *J. Mater. Res.*, 2014, **29**, 820.

Publication 7

B. Strachota, L. Matějka, A. Sikora, J. Spěváček, **R. Konefał**, A. Zhigunov, M. Šlouf

Insight into the cryopolymerization to form poly(N-isopropylacrylamide)/clay macroporous gel. Structure and phase evolution.

Soft Matter, **2017**, 13, 1244-1256.

Soft Matter

PAPER

View Article Online
View Journal | View Issue

Cite this: *Soft Matter*, 2017, 13, 1244

Insight into the cryopolymerization to form a poly(*N*-isopropylacrylamide)/clay macroporous gel: structure and phase evolution†

Beata Strachota, Libor Matějka,* Antonín Sikora, Jiří Spěváček, Rafał Konefał, Alexander Zhigunov and Miroslav Šlouf

Received 7th October 2016,
Accepted 17th December 2016

DOI: 10.1039/c6sm02278b

www.rsc.org/softmatter

The cryopolymerization and formation of a macroporous poly(*N*-isopropylacrylamide) (PNIPA)/clay cryogel were investigated. The mechanism of the cryopolymerization and cryogel formation was elucidated. Two processes, cryostructuration and cryopolymerization, proceed simultaneously and their relative rates determine the structure evolution and the cryogel morphology – porosity. The cryostructuration in the PNIPA/clay system during freezing, controlled by the freezing temperature and the rate of cooling, includes both water and NIPA crystallization, formation of a highly concentrated non-frozen liquid phase (NFLP) and clay aggregation. The rate of cryopolymerization and gelation is governed by the following effects: by a low polymerization temperature and after freezing, by the high cryoconcentration and a steric confinement, manifested by a reduced reagent mobility. Moreover, it depends on the cooling rate and the evolution of cryostructuration. The progress of cryostructuration and cryopolymerization during freezing was described and experimentally proved step by step. Both the phase development during freezing and the progress of cryopolymerization including gelation were monitored *in situ* by NMR, DSC, chemorheology and SAXS. The morphology and porosity of the cryogels were characterized by SEM and TEM.

1. Introduction

Smart hydrogels exhibiting volume changes in response to specific external stimuli,[1] such as temperature, solvent quality or pH, have been widely studied. For some practical applications, there are two main drawbacks in contemporary stimuli responsive hydrogels: low mechanical strength and a slow rate of response to a stimulus.

In order to obtain a gel with a high mechanical performance, many attempts were made.[2] Recently, a lot of attention has been paid to polymer/clay nanocomposite hydrogels. Haraguchi *et al.* synthesized the nanocomposite hydrogel poly(*N*-isopropylacrylamide) (PNIPA)/clay showing excellent mechanical properties.[3–6] The gels are formed by radical polymerization of NIPA in the water suspension of clay where the exfoliated clay platelets serve as multifunctional crosslinking agents. In our previous paper[7] we have discussed in detail the mechanism of PNIPA/clay gel formation by the redox initiated radical polymerization and the mechanical properties of the gel.[8]

The PNIPA gel is a thermoresponsive system displaying a temperature induced volume transition from the swollen state below LCST at about 32 °C to the deswollen collapsed state above LCST. The rate of the swelling–deswelling processes is an important parameter determining the rate of the gel response to a change in temperature. The gel response is generally accelerated by introducing porosity using different techniques.[9–12] Freezing cryopolymerization[13–18] is a simple and efficient method to prepare macroporous gels.[19–22] The principle of this strategy consists of solvent (water) freezing to form ice, polymerization in a semi-frozen state and subsequent ice thawing. The freezing polymerization to build hydrogels results in the formation of two phases: ice crystals and a non-frozen liquid phase (NFLP) containing all solutes where the polymerization takes place and the polymer grows. Thawing of the crystalline phase after polymerization leads to the appearance of macropores within the cryogel structure.

Several research groups investigated the formation of porous acrylamide based gels by cryopolymerization.[23–26] Kirsebom *et al.*[27,28] studied by NMR spectroscopy the cryopolymerization of dimethylacrylamide cross-linked with PEG diacrylate. They evaluated the concentration of the NFLP depending on the concentration of the starting monomers and the freezing temperature. Lozinsky *et al.*[20] investigated the cryopolymerization

Institute of Macromolecular Chemistry, Academy of Sciences of the Czech Republic, v.v.i., Heyrovsky Sq. 2, 162 06 Prague 6, Czech Republic.
E-mail: matejka@imc.cas.cz; Tel: +420 296 809 281

† Electronic supplementary information (ESI) available. See DOI: 10.1039/c6sm02278b

of acrylamides and determined the effect of freezing temperature and thermal history of the reaction on the yield, conversion and molecular weight of the linear polymer.[19] Okay *et al.*[29] prepared the macroporous gel of poly(2-acrylamido-2-methylpropane sulfonic acid) crosslinked with bisacrylamide (BAA) at temperatures varying between −22 and 25 °C. They reported the critical temperature T = −8 °C below which the gels exhibit interconnected micropores enabling the fast transport of water by convection through the pores. We[16] prepared the PNIPA based cryogel crosslinked with BAA and reinforced with *in situ* formed nanosilica. The two-step polymerization procedure was applied involving polymerization at T = 15 °C followed by the cryopolymerization at T = −18 °C. The gel showed improved mechanical properties and very fast swelling–deswelling kinetics.

So far, however, mainly the cryopolymerization of chemically crosslinked PNIPA gels was studied. These porous cryogels display a fast swelling–deswelling response to an external stimulus, however the mechanical properties are poor. Only two papers[30,31] report the cryopolymerization of the nanocomposite based PNIPA/clay system exhibiting a high porosity and a very high extensibility.

Tong *et al.*[30] synthesized the PNIPA/clay gel by the cryopolymerization of NIPA at T = −18 °C in the aqueous clay suspension. They described the dependence of gel properties on clay content and on the time of ice thawing at T = 20 °C after cryopolymerization before taking out of the glass tube. The deswelling and reswelling rate of the cryogels was significantly accelerated due to the macropore structure in the case of clay content >6 wt%. In these cryogels the pore sizes are approximately 20–50 μm, while they are smaller than 10 μm in the case of the low clay content. Xu *et al.*[31] prepared by freezing polymerization the PNIPA/clay nanocomposite gels with an ultrarapid response and excellent mechanical properties. They applied the two-step polymerization procedure consisting of polymerization at T = 20 °C followed by freezing and cryopolymerization at T = −28 °C. The authors studied the evolution of structure and properties during polymerization with respect to the time of start the freezing. The chain growth and network formation are sterically hindered by ice crystals.

In view of the excellent mechanical properties of the nanocomposite PNIPA/clay hydrogels and a generally high porosity of cryogels, we decided to prepare macroporous PNIPA/clay cryogels showing both extraordinary mechanical properties and a very fast thermoresponsive swelling–deswelling kinetics. In this paper, we provide a deep insight into the cryopolymerization and formation of the nanocomposite based cryogel. The investigation involves a detailed study of the cryostructuration in the PNIPA/clay system during cooling and freezing, and the simultaneous redox initiated cryopolymerization and gel formation. The relative rates of these processes govern the final structure and properties of the cryogel. For the first time, the evolution of both the phase and the molecular structure during cryostructuration and cryopolymerization was determined. The processes were followed *in situ*. The polymerization kinetics was monitored by NMR and DSC, while the gel formation by chemorheology experiments. The phase development was determined by DSC, SAXS and NMR. The final structure and morphology of cryogels were characterized by SEM and TEM. Steric confinement and restriction of mobility due to freezing and clay aggregation are discussed. The factors governing the rate of cryopolymerization and the cryogel structure are evaluated. Moreover, the effect of freezing and the rate of freezing on the polymerization kinetics and the porosity of cryogels were determined.

The mechanism of formation of a cryogel is still not completely understood. Therefore, the main goal consists of a contribution to the general understanding of the mechanism of cryogel build-up. For the elucidation of the formation of the nanocomposite PNIPA/clay cryogel, the specific character of redox initiation and crosslinking of this nanocomposite, as well as clay aggregation at a low temperature, is taken into account. In the future, we will investigate the properties of the porous PNIPA/clay cryogels including the accelerated thermoresponsive swelling–deswelling kinetics and their mechanical properties.

2. Experimental

Materials

N-Isopropylacrylamide (NIPA), ammonium peroxodisulfate (APS), and *N*,*N*,*N*′,*N*′-tetramethylethylenediamine (TEMED) were purchased from Aldrich and used as received. The synthetic hectorite clay, LAPONITE® XLS $Na^{+}_{0.7}[(Si_8Mg_{5.5}Li_{0.3})O_{20}(OH)_4]^{0.7-}$, consisting of approximately circular platelets (diameter ∼ 30 nm and thickness ∼ 1 nm) and modified with pyrophosphate ions $(P_2O_7)^{4-}$ was donated by Rockwood Ltd.

Preparation of macroporous hydrogels

PNIPA/clay cryogels were prepared by polymerization of NIPA in aqueous suspension of clay LAPONITE® XLS at a freezing temperature. A homogeneous dispersion of aqueous clay was made by stirring the clay with cold water (around 4 °C) for 1 h. Next, the monomer NIPA was added to the solution and dissolved. Subsequently, the catalyst TEMED and initiator APS, in a form of a 1% aqueous solution, were admixed. Immediately, the reaction mixture was transferred into argon-filled 5 mL ampoules with an inner diameter of 1 cm (in the case of NMR, SAXS or DSC investigations, the reaction mixture was transferred into NMR tubes, X-ray capillaries or DSC pans, respectively) and the radical polymerization was allowed to proceed for 1 min at 15 °C. Then the temperature was lowered down to −20 °C and the cryopolymerization proceeded for 24 h. All operations were carried out under an argon atmosphere. Two basic variants were applied: approaching −20 °C with a slow cooling rate (5 °C min^{-1}) with samples in a freezer, or fast cooling to −20 °C in a cryostat bath (cooling rate: 50 °C min^{-1}). In addition, the isothermal cryopolymerizations at different freezing temperatures were also performed. After the reaction, the prepared gel was taken out of the reaction ampoule and immersed in water at 25 °C.

The composition of the polymerization system is as follows: the concentration of NIPA vinyl groups in the solution was

0.75 mol L^{-1}, which corresponds to 8.5 wt% of NIPA in water. The clay concentration was 3 wt% in the reaction mixture corresponding to 4 wt% suspension in water. The amounts of initiator (APS) and activator (TEMED) were defined with respect to the monomer content using the molar ratios [APS]/[NIPA] = $[APS]_r$ and [TEMED]/[NIPA] = $[TEMED]_r$, which were equal to 0.0087 and 0.028, respectively.

Differential scanning calorimetry (DSC)

The DSC analyses were performed using a TA Q2000 differential scanning calorimeter. The instrument was calibrated with pure indium. The DSC scans of the aqueous NIPA solution, as well as of the polymerization reaction were carried out at the cooling rate of 1 °C min^{-1} until the temperature reached −20 °C; thereafter the DSC scans were continued at a constant temperature (−20 °C). The modulated temperature differential scanning calorimetry (MTDSC) experiment was performed in the isothermal region at −20 °C. The modulation parameters p = 60 s and ΔT = 1 °C were used.

The ice fraction in the samples cooled down to −20 °C was estimated from their melting enthalpy (see the details in the ESI†). The weight fraction of ice ('extent of crystallinity') in an aqueous mixture was calculated according to the following expression:

$$w_{ice} = \frac{\Delta H_m^{exp}}{\Delta H_{m,water}^{\circ}}$$

where ΔH_m^{exp} is the experimentally measured enthalpy of ice melting and $\Delta H_{m,water}^{\circ}$ is the enthalpy of melting of pure ice, as determined by using our cryopolymerization protocol, which was found to be equal to 322.3 J g^{-1}.

Evaluation of the concentration of NIPA in the non-frozen liquid phase is described in the ESI.†

NMR spectroscopy

NMR spectroscopy was used to monitor the monomer conversion and the reaction kinetics *in situ*. Moreover, NMR methods also enabled us to follow the changes in the mobility of the monomer, polymer and water during cooling and subsequent freezing. ^{1}H NMR spectra were recorded using a Bruker Avance III 600 spectrometer operating at 600.2 MHz. All NMR spectra and relaxation times were measured on samples in 5 mm NMR tubes which were degassed and sealed under nitrogen; sodium 2,2-dimethyl-2-silapentane-5-sulfonate (DSS) was used as an internal NMR standard. D_2O was applied as the solvent in most cases. Typical conditions for measurements of the spectra are as follows: a π/2 pulse width of 10 μs, a relaxation delay of 10 s, a spectral width of 15 kHz, an acquisition time of 2.18 s, and 4 scans. The spectra of the supercooled and semi-frozen solutions were recorded with 1 scan and without deuterium lock. The ^{1}H spin–spin relaxation times T_2 were measured using the CPMG[32] pulse sequence $90^\circ_x - (t_d - 180^\circ_y - t_d)_n -$ acquisition with t_d = 0.5 ms, relaxation delay 100 s and 1 scan. The obtained relaxation curves were monoexponential. In all the measurements the temperature was maintained constant within ±0.2 °C using a BVT-3000 temperature unit. Temperature was calibrated using a sample of 4% solution of methanol in [D_4]-methanol and a standard 80% ethylene glycol (DMSO-d_6) sample.

Determination of monomer conversion – *ex situ*

The monomer conversion was determined gravimetrically *ex situ*, as the fraction of the formed polymer for the cases of the polymerization in the freezer or in the cryostat. First, the reaction was inhibited by hydroquinone after certain time periods. Thereafter, the polymer was precipitated from this inactive reaction mixture by increasing the temperature up to 60 °C, and subsequently it was separated and dried at 100 °C under vacuum until the constant weight was reached. The mass of dry polymer was determined, and thus the time-dependent monomer conversion to polymer was obtained.

Fraction of the gel and swelling degree

The gels were extracted in water for 60 days and then they were dried under vacuum at 120 °C till the constant weight. The gel fraction w_g was determined as $w_g = m_e/m_0$, where m_e is the mass of the extracted and dried sample and m_0 is the theoretical gel mass corresponding to the masses of the incorporated components.

The equilibrium swelling degree Q of the hydrogels was defined as the ratio of the mass of the swollen gel (m_s) to the mass of the dry gel (m_d): $Q = (m_s/m_d)$.

Small-angle X-ray scattering (SAXS)

SAXS experiments were performed using a pinhole camera (modified Molecular Metrology System, Rigaku, Japan) attached to a microfocused X-ray beam generator (Rigaku MicroMax 003) operating at 50 kV and 0.6 mA (30 W). The camera was equipped with a vacuum version of the 'Pilatus 300K' detector. Two experimental setups were used to cover the q range of the scattering vector q = 0.005–1.1 $Å^{-1}$ (q is defined as: $q = (4\pi/\lambda)\sin\theta$, where λ is the wavelength and 2θ is the scattering angle). We collected images every 15 seconds. Usually four images were averaged. In order to observe the melting process, the samples were sealed in capillaries and frozen. Dry ice pieces were put into the sample chamber in order to avoid overly rapid thawing. After that, the capillaries with the samples were installed inside the X-ray chamber and observed. The pressure in the chamber was kept near 5×10^{-3} mbar.

Chemorheology

Evolution of rheological properties during polymerization was measured at 0 °C and 15 °C on a strain-controlled ARES-G2 rheometer (TA Instruments, USA), using a parallel plate fixture with a diameter of 25 mm. Silicone oil was applied on the edge of the plates to prevent water evaporation. Dynamic shear storage modulus $G'(t)$ and loss modulus $G''(t)$ were determined during polymerization by time sweep oscillatory measurements at a frequency of 1 Hz and a strain amplitude of 0.1%. The strain was kept low enough to be in the linear deformation region and to prevent breakage of the growing structure. Precise determination of the gel point was performed by multifrequency

sweep measurements ranging from 1 to 64 rad s^{-1} and applying the Winter–Chambon criterion[33] for a power-law rheological behaviour in the critical state, $G' \sim G'' \sim \omega^n$. This criterion implies that loss factor tan δ is independent of frequency ω at the gel point, *i.e.* the $\tan\delta$ curves measured at different frequencies during polymerization intersect in the point of gelation.

Scanning and transmission electron microscopy (SEM and TEM)

The morphology of the hydrogels was visualized using SEM. All micrographs were obtained using a SEM microscope Quanta 200 FEG (FEI, Czech Republic). The hydrogels were observed both in the dried and in the wet/frozen state. The dry hydrogels (dried at 80 °C under vacuum) were fractured at room temperature, fixed on a conductive support and sputtered with a thin platinum layer (vacuum sputter coater SCD 050, Leica, Austria). The fracture surfaces were then observed in a high-vacuum SEM (HV-SEM), using a secondary electron detector and an accelerating voltage of 10 kV. The wet (swollen) hydrogels were cut into small cubes flash-frozen with liquid nitrogen and transferred onto a Peltier cooling stage of the SEM microscope, which was pre-cooled at −10 °C. The cut surfaces of the cubic samples were observed under low vacuum (p = 100 Pa) and at low temperature (T = −10 °C; Cryo-LV-SEM) using a LFD detector (detects both secondary and backscattered electrons) and an accelerating voltage of 10 kV.

TEM was employed in order to characterize the incorporated clay platelets in cryohydrogels. The hydrogel samples were dried at 100 °C under vacuum for 24 h. Ultrathin slices (approximately 60 nm thick) of dried hydrogels were subsequently cut using an Ultracut UTC ultramicrotome from Leica. The slices were put on supporting Cu grids and observed using a Tecnai G2 Spirit Twin 12 microscope (FEI, Czech Republic) in the bright field mode at an accelerating voltage of 120 kV.

Molecular weight determination of PNIPA

The molecular weights of the PNIPA were determined *via* viscosity measurements by using the Mark–Houwink–Sakurada equation

$$[\eta] = KM_v^a$$

where $[\eta]$ is the intrinsic viscosity, and K and a are constants for a given polymer–solvent–temperature system. The values $K = 14.5 \times 10^{-2}$ and a = 0.50 were used for aqueous PNIPA solutions at 20 °C.[34] The viscosity average M_v is determined in this way, which is close to M_w.

3. Results and discussion

The macroporous nanocomposite PNIPA/clay gels were prepared by the cryopolymerization of NIPA in the clay containing aqueous solution. The build-up of the cryogel includes the simultaneous cryostructuration during the cooling and the cryopolymerization. Both these processes were investigated. The slow and fast cooling of the reaction solution was applied in order to determine the effect of cooling conditions on the cryogel formation and the final gel properties.

3.1. Cryostructuration

The cryopolymerization of NIPA in a water solution was performed at the temperature T = −20 °C. While cooling the mixture, involving NIPA and clay, the water crystallization takes place. The process was followed at slow and fast cooling rates in the freezer (rate of cooling = 5 °C min^{-1}) and the cryostat (50 °C min^{-1}), respectively. Fig. 1 shows the decrease in temperature during cooling of the mixture down to T = −20 °C under both conditions. Crystallization of water is manifested by the steep temperature increase due to the corresponding exotherm. During cooling, the solution is in a metastable state, far from equilibrium. The liquid is supercooled and crystallization occurs at the temperature $T \sim -7$ °C in 5.5 min in the freezer and within 25 s in the cryostat. Due to system instability, the process of crystallization and the extent of crystallinity depend on experimental conditions, such as the cooling rate, the freezing temperature, the specimen geometry, the material and the surface character of vessel walls, the concentration of solution components, the viscosity of a medium, *etc.*[15] Therefore, the crystallization times are not well reproducible. Under the quiet conditions and using the small samples, *e.g.* in DSC equipment, the crystallization initiation is slower. Regarding the cooling rates, the reaction temperature T = −20 °C is reached within 3 min in the cryostat, while it takes 45 min in the freezer.

The crystalline fraction, determined by DSC, is dependent on the rate of cooling; it reaches 84% at a slow cooling rate and slightly decreases down to 81% under conditions of the fast cooling rate. Moreover, the fraction of a crystalline phase increases with decreasing freezing temperature and with a storage time at low temperature.

The freezing of water in the solution results in a separation of the system into an immobilized ice phase and a mobile liquid phase containing NIPA, initiators, clay and alternatively a polymer. By ^{1}H NMR spectroscopy we investigated the NIPA solution at T = +15 °C, at T = −8 °C prior to freezing and at

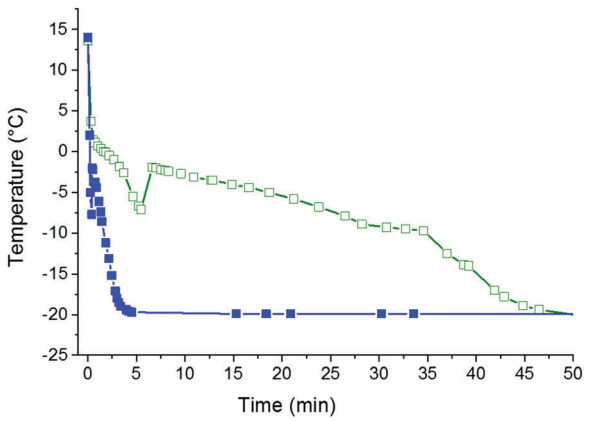

Fig. 1 Temperature decrease during cooling of the nonreactive (without initiator) reaction mixture NIPA/clay in the freezer (□) and in the cryostat (■).

$T = -13.5$ °C after freezing. The results are illustrated in the ESI,† Fig. SI1. The decrease in temperature down to $T = -8$ °C does not affect appreciably the mobility of components in the supercooled solution, as revealed by narrow signals. After freezing, the signal of water is dramatically reduced and all signals are broadened. However, both the signal of residual water at 5.1 ppm and the signals corresponding to NIPA (at 6.3, 5.6, 4.0 and 1.2 ppm) are still observed, implying the presence of a non-frozen liquid phase involving water and NIPA. Broadening of the signals means a significant decrease in mobility in the semi-frozen state. For quantifying the effect, the T_2 relaxation times, characterizing the mobility of the protons in the CH_2 group of NIPA, were determined and are given in Table 1. The T_2 relaxation time is somewhat shortened by decreasing temperature. Reducing the temperature by 20 °C leads to shortening of the relaxation time in the supercooled solution by 45%. However, after freezing, the T_2 value immediately becomes smaller by almost two orders of magnitude.

The NMR analysis shows that in addition to the decrease in the water peak the intensity of NIPA signals also diminished. To determine the mobile fraction of NIPA and water (HDO) at various temperatures we compared absolute integrated intensities of the respective signals in NMR spectra measured under the same instrumental conditions; at the same time we also took into account the fact that integrated intensities should depend on the absolute temperature T (in Kelvin) as $1/T$.[35] The analysis displays a sharp drop in the mobile fraction of water and a gradual decrease in the fraction of the mobile NIPA liquid monomer during cooling (see the ESI,† Fig. SI2). The partial NIPA immobilization is a result of NIPA crystallization.

3.1.1. Phase evolution of NIPA solution during cryo-structuration. During cooling, the system undergoes a cryostructuration as shown in the phase diagram of the NIPA solution in Fig. 2. The diagram construction was based on the experimental data from the study of Sasaki *et al.*[36] The limited miscibility of NIPA and water at temperatures above $T = 25$ °C is characterized using the binodal curve. The metastable part of the binodal continues in the region below $T = 25$ °C (dashed curves). Moreover, the solid–liquid (s–l) curves of NIPA and the equilibrium water crystallization (ewc) curve are shown. We experimentally proved that the presence of a small amount of clay (3 wt%) does not change the phase diagram. Consequently, this diagram can be used to describe the phase evolution of the NIPA/clay/H_2O system during cooling.

The initial system corresponds to point A in Fig. 2, *i.e.* 8.5 wt% NIPA solution. Upon cooling under equilibrium conditions, water crystallizes from the solution just below $T = 0$ °C on the equilibrium crystallization curve of water (ewc) and the NIPA concentration in a solution increases up to the eutectic concentration (point D). In this case, under equilibrium conditions, all water and NIPA would crystallize and no reaction could be possible because of the absence of any non-frozen liquid phase. Under metastable conditions, however, the solution is supercooled and water crystallizes only at a lower temperature in point B, (B′) depending on experimental conditions, such as the cooling rate, sample volume, material of vessels, *etc.* In the case of large vessel volumes in a freezer or a cryostat, crystallization takes place at $T = -7$ °C (point B) (conf. Fig. 1), while in small DSC pans at $T = -15$ °C (point B′). Due to the crystallization exotherm, the solution temperature increases in the freezer or cryostat up to $T = -2$ °C (see Fig. 1) reaching point C in the phase diagram. As a result of ice crystallization, a volume fraction of the non-frozen liquid becomes smaller and the solution is cryo-concentrated. The system is moving along the crystallization curve, ewc. Continuous crystallization of the metastable supercooled water leads to an increase in the concentration of NIPA solution up to the concentration on the metastable binodal. In the case of the slow cooling the

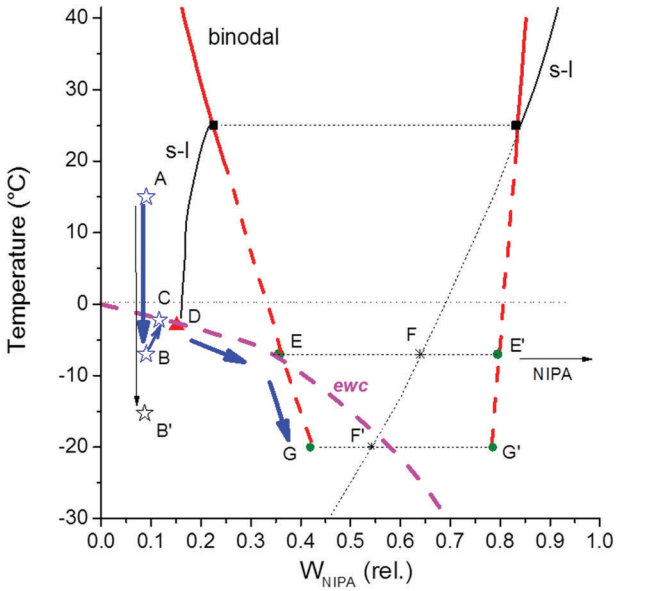

Fig. 2 Phase diagram of NIPA solution (based on the experimental dates of Sasaki *et al.*[36]) Curves: ewc (dashed) – equilibrium crystallization of water, s-l – solid–liquid curve of NIPA (dotted – metastable part), and binodal (dashed – metastable part). The diagram is not affected by the presence of clay (3 wt%).

Table 1 ^{1}H spin–spin relaxation times T_2 of NIPA molecules (CH_2═ protons) in D_2O

	T_2 [ms]					
Sample	$T = 15$ °C	$T = 0$ °C	$T = -3$ °C unfrozen	$T = -5$ °C unfrozen	$T = -10$ °C semi-frozen	$T = -15$ °C semi-frozen
NIPA solution[a]	1677	1074	986	937	20	12
NIPA/clay suspension[b]	15		8.2			2.5

[a] 8.5 wt% of NIPA. [b] 8.5 wt% of NIPA, 3 wt% of clay.

crystalline fraction reaches 84% and the corresponding reduction of the liquid phase volume results in an increase in the concentration of the solution from initial 8.5% up to 39% in the cryoconcentrated phase. After reaching a high concentration at point E on the binodal curve, the solution should be separated into less and more concentrated phases (E, E′). This phase segregation was experimentally proved by DSC as shown in the ESI.† The small phase separation endotherm (points E, in Fig. SI3a, ESI†) following after the crystallization exotherm (B–C, in Fig. SI3a and b, ESI†) was detected in the DSC thermogram. The more concentrated phase E' in the phase diagram (Fig. 2), however, lies outside the metastable part of the s–l curve of NIPA (concentration F). Therefore, in the moment of the formation of the more concentrated phase E', the metastable NIPA starts to crystallize and the liquid phase keeps the concentration of the more diluted branch of the metastable binodal. The temperature continues to decrease down to the reaction temperature, $T = -20$ °C, and a shift along the binodal curve down to the point G occurs. In the metastable state, there is a coexistence of the liquid cryo-concentrated phase G, ice crystallites and the crystalline NIPA.

3.1.2. Clay dispersion/aggregation in aqueous suspension. The formation of PNIPA/clay cryogels proceeds in a suspension of clay in water. The clay arrangement in the water suspension and its change during cooling were determined by SAXS.

The SAXS profile of dry clay particles in Fig. 3 (curve 1) exhibits the maximum at $q_{max} = 0.48$ Å^{-1} corresponding to the interplatelet distance in a clay particle $d = 13$ Å ($d = 2\pi/q_{max}$) in agreement with the literature.[31] After suspension in water prior to polymerization, the clay platelets are completely exfoliated (curve 2). The slope x of the profile equals $x = 2$ implying plate-like structures and the scattered intensity levels off at low angles as a result of the absence of aggregates.[7] The profiles 3–5 show the arrangement of clay platelets upon freezing. The sample cooled down to $T = -20$ °C and frozen (curve 3) displays a significant interference maximum at $q_{max} = 0.31$ Å^{-1} revealing an ordered structure. During cooling and water crystallization,

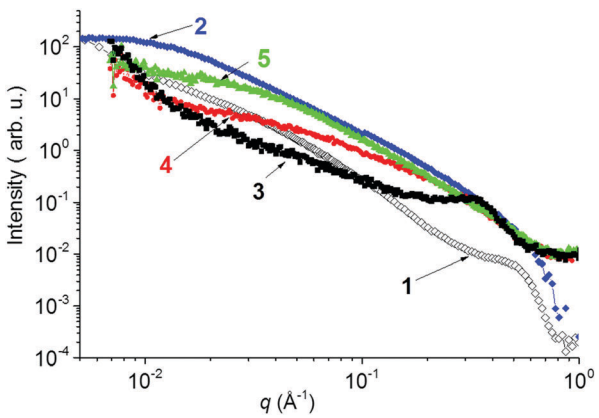

Fig. 3 SAXS profiles of the clay suspension (4 wt%) in water upon cooling. Curves: 1 – dry clay particle, 2 – clay suspension in water prior to polymerization, $T = 15$ °C, 3 – semi-frozen suspension, $T = -20$ °C, 4 – ice thawing (5 min), and 5 – ice thawing (11 min).

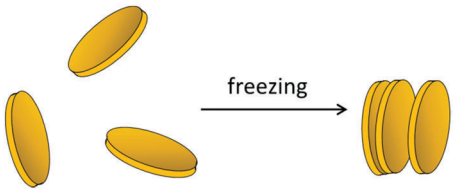

Scheme 1 Clay aggregation during freezing of water suspension.

the platelets separate into non-frozen liquid phases. Due to the densification of this phase, the exfoliated clay platelets aggregate in the confined conditions to form ordered structures of platelet stacks as illustrated in Scheme 1. The formation of aggregates is obvious from the steeply increasing intensity at low angles. The SAXS maximum corresponds to the inter-platelet correlation distance $d = 20$ Å. Due to an experimental impossibility to follow structure evolution *in situ* during freezing, we have determined the development of the clay structure in the reverse process upon increasing temperature from the frozen state. The time resolved profiles reveal a gradual structure disordering (disappearance of the maximum) and a transition from the confined aggregates at a low temperature into the state of randomly exfoliated plates as restructuralization takes place upon slow ice melting (curves 4 and 5).

3.2. Cryopolymerization

The cryopolymerization proceeds simultaneously with cryo-structuration during cooling. However, the macroporous cryogel could be formed only when freezing occurs in the pregel stage. Therefore, the relative rates of both processes are important and determine the evolution of the structure and final gel properties. Both the kinetics of polymerization and the rate of gel formation on one side, and the freezing procedure, such as the rate of freezing and freezing temperature on the other side, can be controlled in order to find the optimum conditions for the synthesis of macroporous cryogels with good mechanical properties.

The evolution of the molecular structure during cryo-polymerization was monitored by NMR, chemorheology and DSC, while phase structure development was followed by SAXS and DSC. The factors governing the rate of cryopolymerization and gel formation were investigated.

3.2.1. Kinetics of cryopolymerization. The radical polymerization of NIPA was initiated with the redox system APS/TEMED. The rate of the cryopolymerization of NIPA and the NIPA/clay system depends on several factors:

(a) effect of low temperature slowing down the polymerization,

(b) cryoconcentration effect due to freezing resulting in the acceleration of the reaction in the concentrated liquid phase of the semi-frozen system, and

(c) steric confinement and reduction of mobility of reactive species due to densification of a solution and a clay aggregation after freezing, affecting negatively the reaction rate.

Kinetics of the cryopolymerization, characterized as the conversion of the monomer NIPA, was monitored *in situ* by NMR spectroscopy. Monomer NIPA signals of CH_2= and/or

CH═ groups (*cf.* Fig. SI1, ESI†) were used for this purpose. The above mentioned effects on the rate of cryopolymerization were investigated.

Effect of temperature in the homogenous solution. The polymerization at a low temperature was followed in the metastable supercooled state in the absence of crystallization in order to exclude the effect of cryoconcentration and to determine only the effect of decreasing temperature. Fig. 4 shows the kinetics of polymerization of NIPA (Fig. 4a) and the NIPA/clay system (Fig. 4b) at different temperatures T_c = 15 °C, 0 °C and −10 °C (curves 1, 2 and 3). The decrease in polymerization temperature results in slowing down the polymerization and an appearance of the pronounced induction period. Moreover, the polymerization is slower and the induction period is longer in the PNIPA/clay gel forming mixture compared to the linear NIPA polymerization.

The induction period corresponds to the initiation stage of polymerization, which is the rate determining step of a radical polymerization. The initiation process consists of the generation of a primary radical from the initiator followed by its reaction with a monomer to form the first monomer radical. The rate of initiation R_i depends on the concentration of the initiator [I], the decomposition rate of the initiator k_d and the efficiency of initiation f_i; $R_i \sim 2k_d f_i[I]$. The induction period changes due to the existence of inhibitors or other impurities. However, under the same experimental conditions, in a rough approximation, one can consider the change in the length of the induction period as inversely proportional to the change in the rate of initiation.

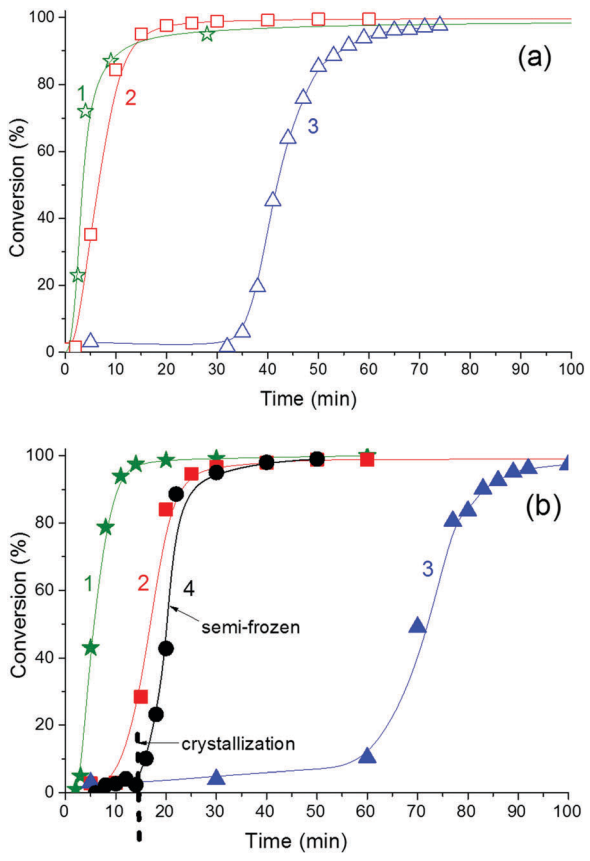

Fig. 4 Kinetics of polymerization of (a) NIPA and (b) NIPA/clay system at different temperatures. Curves: 1 – 15 °C, 2 – 0 °C, 3 – (−10) °C, unfrozen state, and 4: (−10) °C semi-frozen state, and the dashed line indicates crystallization.

The slower polymerization and the longer induction period during polymerization of NIPA in the presence of clay were discussed in our previous paper.[7] Both the monomer NIPA and the activator TEMED tend to be adsorbed on the clay surface. The initiator APS must diffuse into clay in order to form an active complex with TEMED and to generate the primary radical. The adsorption of TEMED, moreover, could result in a steric hindrance to the formation of primary radicals. In addition, due to a high viscosity of a clay suspension, the primary radicals may recombine by the solvent cage effect. These facts lead to a reduction of the initiation efficiency f_i, thereby slowing down the initiation and lengthening the induction period in the presence of clay.

The decrease in the polymerization temperature slows down the radical formation. Moreover, an increase in viscosity results in the reduced initiation efficiency from the above mentioned reason. This is manifested by the longer induction period. Whereas, there is a relatively small difference between the rates at T = 15 °C and 0 °C (curves 1 and 2), the slowing down of initiation is very pronounced in the supercooled solution at the temperature T = −10 °C (curve 3) both in NIPA and NIPA/clay polymerization. The induction period is 5–8 times longer at T = −10 °C compared to the reaction at T = 0 °C. Moreover, the viscosity increase could hinder the diffusion of the monomer to the growing chain end and also slow down the propagation. In the case of NIPA, once the polymerization is initiated, the propagation is relatively fast and the final conversion approaches $\alpha \rightarrow 1$. However, in the presence of clay in the NIPA-clay system, the propagation is slower at T = −10 °C.

Cryoconcentration effect. The cryostructuration upon freezing involves an increasing concentration of the non-frozen solution, *i.e.* cryoconcentration, a steric confinement of a polymer in the non-frozen liquid phase between ice crystallites and a clay aggregation occurring after the water crystallization. The effect of freezing on polymerization is revealed in Fig. 4b by comparing the polymerization kinetics of the NIPA/clay system at T = −10 °C in the semi-frozen (curve 4) and unfrozen supercooled (curve 3) states. The polymerization is much faster in the semi-frozen state. The fast propagation sets in just after crystallization indicated by the dashed line. The freezing is detected by a sudden decrease in the intensity of the NMR water signal.

The shortening of the induction period as well as the higher propagation rate are the results of the increased cryoconcentration in the non-frozen liquid phase including both initiators and monomer NIPA. The concentration of the liquid phase is increased about 4–5 times by water crystallization, from 8.5 wt% up to 39 wt%. Accordingly, the concentration of initiators increases. The polymerization starts and it is accelerated just after water crystallization when this cryoconcentrated phase is formed.

The NIPA crystallization, proved by NMR upon cooling of the nonreactive NIPA solution (without initiator), is gradual and

slower compared to water crystallization (see Fig. SI2, ESI†). Therefore, the cryopolymerization, mainly starting just after water freezing, likely begins before NIPA crystallization. The onset of the reaction thus occurs in the cryoconcentrated phase (~39%). The fast NIPA consumption by polymerization then restricts the NIPA crystallization during polymerization.

Steric confinement. Polymerization in the cryo-concentrated phase proceeds under confined conditions due to the reduced volume fraction of the non-frozen liquid phase between ice crystallites and the aggregation of clay.

The mobility of both the monomer and the polymer chains significantly decreases after water crystallization. The effect of solution freezing on the steric confinement and the mobility of solution components is determined by NMR spectroscopy (see the ESI†). During polymerization at $T = -10$ °C prior to water crystallization (in the supercooled system) the NMR spectrum in Fig. SI4a (ESI†) shows narrow peaks of water, monomer NIPA and catalyst TEMED, as well as somewhat broader peaks corresponding to the PNIPA polymer. It means that all the substances of the polymerization mixture display a quite good mobility in the supercooled solution at $T = -10$ °C. The freezing is characterized by a dramatic reduction of the water signal in Fig. SI4b (ESI†). After freezing, all signals significantly broaden revealing a reduction of the mobility of all substances due to a steric confinement and a viscosity increase (*cf.* Table 1). The polymer signals completely disappeared implying that the confined conditions affect more the mobility of polymer chains. The lower mobility in the semi-frozen system is in agreement with a slower diffusion compared to supercooled samples as reported by Kirsebom *et al.*[27]

In the presence of clay in the NIPA/clay system, the clay aggregation takes place to form layered stacks of platelets upon freezing as shown above (see Fig. 3 and Scheme 1). Fig. 5 displays the SAXS profiles of the layered aggregates at a low temperature (curve 1) with the interference maximum at q_{max} = 0.31 Å^{-1} corresponding to the interplatelet distance d = 20 Å. The initiation of polymerization occurs on the clay surface because of TEMED adsorption on the platelets and the growing polymer chains are adsorbed on the platelet surface.[5,7] In the case of the cryopolymerization, this mechanism results in a polymer intercalation into the layered structure of the clay stacks, thus leading to the increasing interplatelet distance and a partial distortion of the ordered arrangement. SAXS curve 2 proves the shift of the maximum to the lower q value during polymerization down to q_{max} = 0.20 Å^{-1}, corresponding to the increased interplatelet distance d = 31 Å. Moreover, the maximum becomes less pronounced due to a less regular arrangement after the polymer intercalation.

In the system NIPA/clay, the interaction of reagents with clay is an important parameter affecting the polymerization. It was proved that both NIPA and the polymer as well as the initiator TEMED are strongly adsorbed on the clay surface.[7] As a result, their mobility is reduced. This is revealed by NMR analysis of the NIPA/clay polymerization mixture in the ESI.† The NIPA and polymer peaks are broad, and the TEMED signals almost

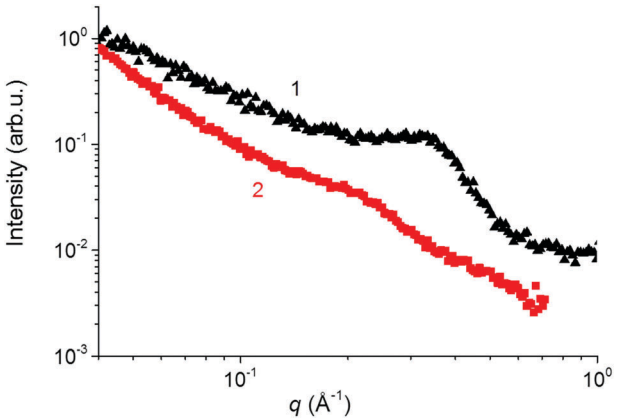

Fig. 5 SAXS profiles of the semi-frozen NIPA/clay suspension (4wt%) at T = −20 °C. Curves: 1 – prior to polymerization (without initiator) and 2 – during polymerization.

disappeared in the spectrum of the supercooled solution in Fig. SI4c (ESI†). After freezing, the NIPA peaks further broaden as shown in Fig. SI4d (ESI†) while the polymer peaks disappear. Table 1 shows the significant shortening of the T_2 relaxation time of NIPA by two orders of magnitude in the presence of clay. The decrease in temperature and freezing result in further diminishing of the relaxation time. The presence of the ordered clay in the non-frozen liquid phase brings about a 5-fold shortening of the NIPA relaxation time with respect to the solution without a clay. The results show that both cryoconcentration after freezing and the presence of clay significantly reduce the mobility of the NIPA monomer and polymer chains, the mobility of which however could not be quantified by the determination of the T_2 relaxation time. Nevertheless, Fig. 4b (curve 4) reveals that the restriction of the reagent mobility in the confined space after freezing and clay aggregation does not affect significantly the polymerization kinetics. The acceleration effect due to the high cryo-concentration of reactants prevails.

Effect of the cooling rate. The rate of cooling of the reaction mixture is the factor governing the rate and the extent of cryostructuration and thereby the progress of polymerization. Fig. 6 displays the kinetics of NIPA polymerization taking place in the freezer (curve 1) and in the cryostat (curve 2), corresponding, respectively, to the slow (5 °C min^{-1}) and fast (50 °C min^{-1}) cooling during polymerization (*cf.* Fig. 1). The kinetics was analysed *ex situ* by the determination of NIPA conversion from the fraction of the formed polymer (see the Experimental section). The reaction is substantially faster in the freezer, *i.e.* applying the slow cooling. The length of the induction period is 3–4 min in the freezer while it is 30 min in the cryostat. Also the following rate of polymerization is much slower in the cryostat.

The comparison of Fig. 1 and 6 reveals that in the freezer, the crystallization sets in about 5 min leading to cryoconcentration of the solution and the acceleration of the polymerization. The reaction in the freezer mainly proceeds at a temperature in the range between $T \sim 0$ °C and $T = -10$ °C which is attained at a

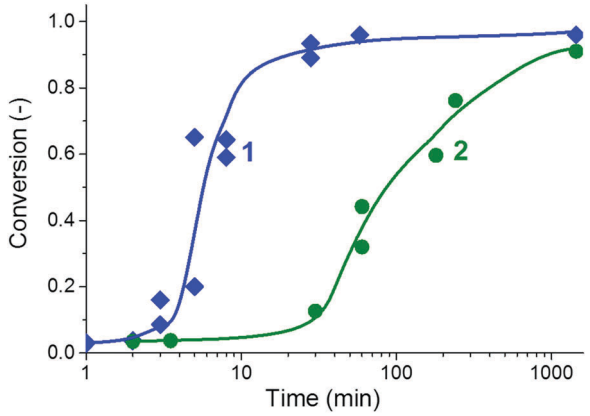

Fig. 6 Kinetics of PNIPA polymerization upon cooling down to $T = -20$ °C. Curves: 1 – in the freezer and 2 – in the cryostat.

slow cooling rate within 30 min when the conversion reaches the value $\alpha \sim 0.9$. Upon fast cooling in the cryostat, a low temperature $T = -20$ °C is achieved within 3 min. Despite crystallization, the polymerization in this case is very slow. The induction period lasts for 30 min, the conversion $\alpha = 0.5$ is reached only in 100 min and even in 24 h the reaction is incomplete, $\alpha = 0.9$. The high viscosity and immobilization of reactive species slowing down the polymerization dominate at the low temperature $T = -20$ °C.

3.2.2. Phase changes and reaction progress during cryopolymerization. The complex view of the cryostructuration and cryopolymerization was obtained by DSC. Fig. 7a shows the DSC thermogram displaying a series of exotherms occurring during cooling and cryopolymerization of the NIPA/clay system at $T = -20$ °C. These exotherms are assigned to crystallization of water and to the polymerization. The first strong exotherm at the beginning corresponds to water crystallization upon cooling. The non-frozen liquid phase, composed of NIPA, clay, water and the redox initiator, is cryo-concentrated and the accelerated cryopolymerization follows as shown in Fig. 4b (curve 4). The reaction exotherm during polymerization is overlapped by the dominating crystallization thermal effect and only the small reaction exotherms appear in the thermogram.

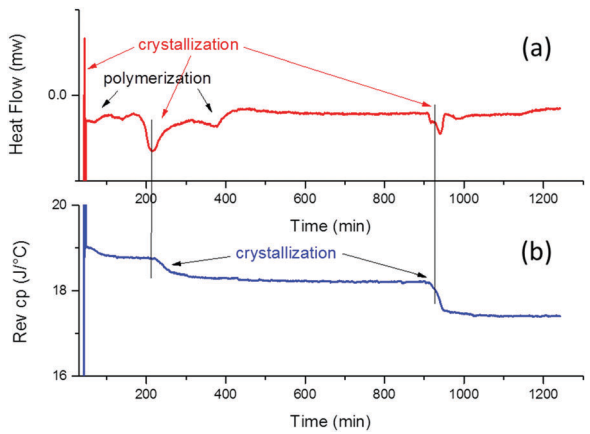

Fig. 7 DSC thermogram of the cryopolymerization of the NIPA/clay system at $T = -20$ °C. (a) Heat flow and (b) reverse Cp.

The heat of reaction was estimated by subtracting the crystallization heat flux from the total heat flow during isothermal polymerization of NIPA. This crystallization thermal effect was obtained by measuring the heat flow in the solution containing the already reacted polymer PNIPA under the same conditions under which polymerization was carried out. In this case only crystallization takes place while no polymerization is observed. The heat of reaction, free from the crystallization thermal effect, reflecting the course of polymerization at $T = -20$ °C, is illustrated in the ESI,† Fig. SI5. The reaction heat $\Delta H_r = -98.5$ J g^{-1}, determined in such a way, closely agrees with that of polymerization at room temperature.

The consumption of NIPA in the liquid phase during the polymerization results in an expulsion of water from this phase in order to keep a phase concentration according to the binodal curve in the phase diagram (see Fig. 2). This expelled water crystallizes and the second large exotherm in the DSC thermogram in Fig. 7a emerges. The assignment of this exotherm to the crystallization, *i.e.* the phase change and not the reaction heat, is confirmed by the simultaneous decrease in reverse Cp measured by MTDSC as shown in Fig. 7b. Several such exotherms coupled with the Cp decrease occur during cryopolymerization as a result of the crystallization of water expelled step by step from the reaction phase. Moreover, such separated discontinuous crystallization exotherms also appear in the nonreactive system, *i.e.* in the absence of initiators. This could be a result of a gradual water crystallization in a metastable state upon cooling along the path C–G in the phase diagram (Fig. 2). Both these processes, the crystallization of water expelled from the liquid phase and the gradual freezing of a metastable water, occur during cryopolymerization.

During cooling, the partial crystallization of NIPA also takes place as proved by NMR (in the concentration F of the phase diagram (Fig. 2)). Upon cryopolymerization, the reactive monomer NIPA involved in the liquid phase is gradually depleted. In order to keep the NIPA phase concentration according to the binodal curve (along the path C–G), the metastable crystalline NIPA melts and dissolves. This melting is manifested during the polymerization by endotherm maxima at around 600 and 1100 min as shown in Fig. SI5 in the ESI.†

3.2.3. Gel formation. The growth of the molecular structure, crosslinking and formation of the PNIPA/clay gel were followed by chemorheology experiments. Fig. 8 illustrates the evolution of the storage shear modulus $G'(t)$ during polymerization of the PNIPA/clay system at two temperatures, $T = 15$ °C and $T = 0$ °C (curves 1 and 2). In addition, the kinetic curves of conversion of the NIPA monomer, reflecting the progress of polymerization, are given in the figure (curves 3 and 4) in order to enable correlation between the polymer growth and the gel formation. The structure development is characterized by a low modulus in the pregel stage, by the steep increase in modulus corresponding to gelation and by levelling off the modulus in the postgel stage. Precise determination of the gel point was performed by multifrequency sweeps (see the Experimental section). The rates of polymerization characterized by the length of the induction period t_{ind} and by the reaction time to reach the conversion

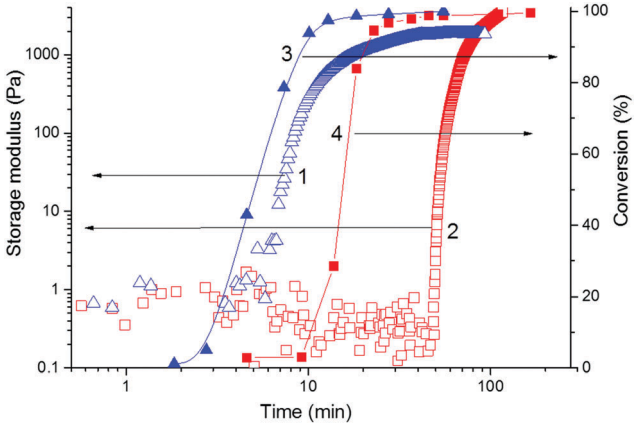

Fig. 8 Evolution of the storage modulus (G') (left axis) and conversion of the NIPA monomer (α) (right axis) during polymerization of the system NIPA/clay at the temperatures, T = 15 °C and T = 0 °C. Curves: 1 – G' at T = 15 °C, 2 – G' at T = 0 °C, 3 – α at T = 15 °C, and 4 – α at T = 0 °C.

α = 0.5, *i.e.* t (α = 0.5), as well as rates of gelation characterized by time of gelation t_g are given in Table 2. In addition, the critical conversion at the gel point, α_c, is also determined, as an important characteristic of gel formation.

Both kinetics of polymerization and gel formation are slower at a lower temperature. However, Fig. 8 and Table 2 reveal that the decrease in temperature affects more the gelation than the kinetics of NIPA conversion. While the polymerization is slowed down about 3 times by decreasing temperature from T = 15 °C down to T = 0 °C, the gelation is slowed down almost 10 times (see Table 2).

In order to understand this behaviour it is necessary to take into account the mechanism of structure growth and gelation.[7] During the polymerization, the induction period is followed by the polymer chain growth and formation of a polymer monolayer adsorbed on the clay platelet. After saturation of the platelet surface, the chains grow outwards into the interplatelet space. Only then the crosslinking occurs by recombination of chains growing from different platelets or by formation of entanglements. This process leads to bridging of the platelets and formation of clusters of clay platelets resulting finally in chain percolation and gelation. Xu *et al.*[31] followed the evolution of the polymerization and gelation by UV/VIS spectroscopy from decreasing transmittance of the solution which was attributed to the formation of clay-brush particles and start of gelation. Our direct determination of gelation by chemorheology in combination with the evaluation of the monomer conversion during polymerization by NMR makes it possible to elucidate the mechanism of cryogel formation and the effect of temperature on gelation.

Table 2 Rates of polymerization and gelation as functions of temperature

	T = 15 °C	T = 0 °C
t_{ind}, min	3	10
t (α = 0.5), min	5	18
t_g, min	5.5	50
α_c	0.7	0.95

t_{ind} – time of induction period, t_g – gelation time, α_c – critical conversion.

Fig. 8 and Table 2 show that gelation sets in at a relatively high conversion of NIPA; α_c = 0.7–0.95. Most of the monomer is consumed to form a polymer layer on the clay platelet and the system gels only in the late polymerization stage after platelet saturation. The critical conversion, moreover, increases with decreasing temperature (see Table 2). At the temperature T = 0 °C, the gel is formed only when almost all NIPA is consumed. This is a result of an increasing viscosity at a low temperature leading to a decrease in the polymer mobility and slowing down chain entangling and recombination of macroradicals. In contrast to the slow crosslinking, the polymer propagation is less affected by the viscosity increase and the deceleration of the polymerization rate at a low temperature is less significant. It is due to the fact that the mobility of a polymer chain is more restricted than that of the low molecular weight monomer NIPA at a low temperature as determined by NMR. Consequently, the more significant restriction of gelation than monomer conversion at decreasing temperature supports the suggested mechanism of gelation because crosslinking and gelation are governed by the mobility of polymer chains while polymer growth is controlled mainly by the diffusion of a monomer approaching the chain end.

The gelation after freezing was not directly followed, however, one can expect a severe delay of gelation in this case because of confined conditions which strongly restrict polymer crosslinking. Moreover, after freezing, the gel formation is sterically hindered by the presence of crystallites restricting the interconnection of polymer domains growing in non-frozen liquid phases.

During the gel formation, not all PNIPA chains are involved in crosslinking and as a result some sol fraction w_s exists in the cured samples. However, the fraction of the gel w_g (=1 − w_s) = 0.92 in the studied porous cryogels is higher than that in the gels prepared at positive temperatures, with w_g = 0.83.

The polymerization is initiated by the redox system APS/TEMED. APS serves as an initiator and TEMED acts as an activator promoting the decomposition of APS into free radicals.[37] The polymerization initiated with APS alone displays the activation energy E_a = 62 kJ mol^{-1}, however, in the presence of TEMED, the activation energy decreases down to E_a = 22 kJ mol^{-1}.[38] Therefore, a majority of polymer chains are initiated and grow at the clay surface because of the preferred initiation with the participation of TEMED, which is adsorbed on clay as discussed above. However, a small fraction is initiated by APS alone in a water medium. These polymer chains are not attached at the clay surface, do not contribute to crosslinking through clay platelets and can be therefore extracted from the gel. Due to the high activation energy of initiation by APS, the fraction of the corresponding chains growing in water is smaller in the case of a low reaction temperature. Consequently, the cryogels show a minor sol fraction compared to gels formed at a higher temperature.

3.3. Structure of cryopolymers

A low reaction temperature affects not only the polymerization kinetics but also the polymer structure. The cryopolymerization

in semi-frozen media results in the polymers of a higher molecular weight, M_v, compared to the synthesis at a temperature above the freezing point of a medium.[39] In the case of a polymer network and a gel, the length of polymer chains between cross-links is an important structural characteristic governing the properties of the gel. In the previous papers[7,8] we controlled the M_v of PNIPA by the concentration of initiators and proved a close correlation between the molecular weight and the mechanical properties of the corresponding nonporous gels.

In this work, we followed the effect of temperature and the rate of cooling on the molecular weight of PNIPA as important parameters to be applied for the control of the structure and properties of porous cryogels. In addition to the reaction at T = 25 °C and 0 °C, three types of cryopolymerization conditions were used: (i) isothermal polymerization at T = −10 °C, (ii) polymerization in the freezer applying a slow cooling down to T = −20 °C and (iii) polymerization in the cryostat with a fast cooling down to T = −20 °C. The results, given in Table 3, reveal a pronounced increase in M_v of PNIPA cryopolymers with respect to the polymer prepared at T = 25 °C.

The rate of cooling during the cryopolymerization governs the temperature range in which the major fraction of a polymer is formed. During fast cooling in the cryostat, all reactions proceed at T = −20 °C, which is reached within 3 min (*cf.* Fig. 6 and Fig. 1). In contrast, in the freezer, the major fraction of the polymer grows within 8 min (see Fig. 6), which corresponds, under the slow cooling rate, to the temperature range T = −2 °C down to T = −7 °C (see Fig. 1). The highest molecular weight polymer was prepared at T = −10 °C. This is in agreement with the study of Lozinsky[20] who found that the maximum of conversion, yield and molecular weight of the polymer was achieved at T = −12 °C. At a very low reaction temperature the polymer molecular weight distribution broadens as a result of increasing heterogeneity of the reaction medium because the polymerization proceeds both in the non-frozen liquid phase and at the liquid–ice interface.[20]

The degree of polymerization P_n of PNIPA is generally expressed as

$$P_n \sim k_p[\mathrm{NIPA}]/2(k_t f_i k_d[\mathrm{I}]_{init}[\mathrm{I}]_{act})^{1/2}$$

Based on this expression, the dependence of the molecular weight on the polymerization temperature results from the following opposite factors. At a low temperature, M_v should increase due to (a) the decrease in initiation efficiency f_i as discussed above, and (b) the increase in NIPA concentration because of the cryoeffect. In contrast, M_v should decrease due to (c) the increasing concentration of initiators in the liquid phase, and (d) the reduction of propagation rate constant k_p at a low temperature, because of a higher viscosity and the lower reagent mobility. As a result of these opposite effects, the molecular weight passes through the maximum depending on temperature.

Table 3 Molecular weights of PNIPA prepared at different temperatures

PNIPA, 0.75 mol L^{-1}	$M_v \times 10^6$
T = 25 °C	2.1
T = 0 °C	2.4
T = −10 °C	6.8
Freezer T = −20 °C	6.4
Cryostat T = −20 °C	4.2

M_v – determined from viscosity – see the Experimental section.

3.4. Morphology – porosity of cryogels

The cryopolymerization results in the macroporous gels the SEM micrographs of which are displayed in Fig. 9. The high porosity was achieved despite a low content of clay in the reaction mixture, 3 wt%, in contrast Tong *et al.*[30] reported large pores only in the cryogels with a clay content >6 wt%. In our case, the morphology of cryogels, *i.e.* the extent and character of porosity, depends on the conditions of the cryopolymerization. We found that the rate of cooling is crucial for the final gel morphology and porosity. Fig. 9a and b show the porous PNIPA/clay cryogels prepared in the freezer and the cryostat under the conditions of the slow and fast cooling, respectively. At the slow cooling rate in the freezer, the large ice crystallites are formed resulting in the large channel-like open pores in the gel after the crystallite thawing. The pore size reaches *ca.* 100 μm. In contrast, only small crystallites grow upon fast cooling, thus

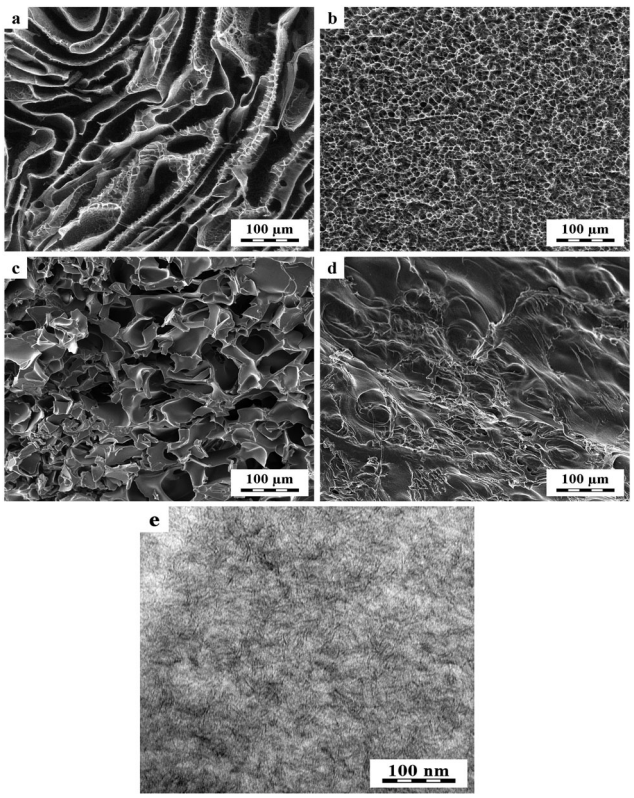

Fig. 9 SEM (a–d) and TEM (e) micrographs of the PNIPA/clay samples synthesized in the (a) freezer (slow cooling), (b) cryostat (fast cooling), (c) freezing in the pregel stage, and (d) freezing in the postgel stage. The wet (a and b) and dried (c and d) samples were visualized using Cryo-LVSEM and HVSEM microscopy, respectively (see the Experimental section). The TEM micrograph (e) corresponds to the sample shown in (a).

leading to the cryogels with closed pores of the small size, about 5–10 μm.

Moreover, the relative rates of cryostructuration and polymerization/gelation determine the gel porosity. The fast and early freezing before gelation of PNIPA/clay results in the macroporous cryogel with the interpenetrating pores of size 50–100 μm as illustrated in Fig. 9c. In contrast, the late freezing only after gelation leads to a gel with a low porosity in Fig. 9d.

The cryogels prepared in the freezer show a higher swelling capacity than those formed by the fast cooling in the cryostat due to larger porosity. Surprisingly, however, the porous cryogels, both from the freezer and the cryostat, swell less than the nonporous gels. The corresponding swelling degrees are Q = 0.31 (freezer), 0.17 (cryostat) and 0.35 (nonporous gel), respectively. This is a result of a higher crosslinking density and a higher modulus of the cryogels because of the cryoconcentration effect, which reduce the swelling capability. The swelling and mechanical properties of cryogels will be discussed in detail in the next paper.

The TEM micrograph in Fig. 9e, displaying 1000 times smaller scale than the SEM micrograph, shows the morphology of the pore wall of the cryogel. It is obvious that the clay platelets are relatively well dispersed in the polymer matrix. Only small clusters involving several platelets are present, however no large clay aggregates are observed.

The prepared cryogels show very fast swelling–deswelling kinetics due to the presence of the large interconnected pores and moreover they exhibit perfect mechanical properties. Both the porosity and the mechanical strength can be tuned by controlling the relative rates of cryostructuration and cryopolymerization.

4. Conclusions

The cryopolymerization of the PNIPA/clay system was studied and the mechanism of formation of the macroporous nanocomposite cryogel was determined. The process of the cryogel formation includes cryostructuration of a reaction solution during cooling and the simultaneous polymerization under cryoconditions. The relative rates of these processes govern the final gel structure, morphology and properties. Both phase and molecular structure evolution including gelation were monitored *in situ* by NMR, DSC, chemorheology and SAXS.

The cryostructuration involves successively crystallization of water, formation of the cryoconcentrated non-frozen liquid phase (NFLP), aggregation and ordering of clay, phase separation, monomer NIPA crystallization and its melting during cryopolymerization. The presence of the NFLP in the semi-frozen system was proved by NMR. The concentration of the solution increases from initial 8.5 wt% up to 39 wt% in the NFLP. The clay platelets in the nanocomposite mixture aggregate into layered ordered stacks. Consequently, the cryoconcentration and a clay aggregation result in severely confined conditions for a polymerization. The solutes in the NFLP (NIPA, initiator, polymer) show a significant decrease in mobility after freezing. The rate of cryopolymerization, proceeding under conditions of the cryostructuration, is controlled by the opposite effects: (i) slowing down at a low temperature due to the increase in viscosity and the decrease in efficiency of the redox initiation affecting the induction period, and (ii) acceleration due to cryoconcentration.

The mechanism of cryogel formation and effect of decreasing temperature on gelation were elucidated. Crosslinking and gelation are governed by the mobility of polymer chains that is severely limited at a low temperature, while a polymer growth is controlled mainly by the mobility of a monomer which is less affected.

The macroporous cryogels with the channel-like open pores of size ~100 μm were prepared. The gel porosity depends on the cooling rate and the relative rates of cryostructuration and polymerization/gelation. The highest cryogel porosity was achieved by slow cooling and freezing of the solution before gel formation.

Acknowledgements

The authors acknowledge the financial support of the Grant Agency of the Czech Republic (Project 13-23392S). L. M. acknowledges the COST Action MP1202 HINT (Ministry of Education, Youth and Sports LD14010). B. S. and R. K. acknowledge the Charles University, Faculty of Science for the opportunity to pursue their PhD studies.

References

1 M. Shibayama and T. Tanaka, *Adv. Polym. Sci.*, 1993, **109**, 1.
2 A. M. S. Costa and J. F. Mano, *Eur. Polym. J.*, 2015, **72**, 344.
3 K. Haraguchi, T. Takehisa and S. Fan, *Macromolecules*, 2002, **35**, 10162.
4 K. Haraguchi and H. J. Li, *Macromolecules*, 2006, **39**, 1898.
5 K. Haraguchi, H. J. Li, K. Masuda, T. Takehisa and E. Elliott, *Macromolecules*, 2005, **38**, 3482.
6 K. Haraguchi, *Adv. Polym. Sci.*, 2015, **267**, 187.
7 B. Strachota, L. Matějka, A. Zhigunov, R. Konefał, J. Spěváček, J. Dybal and R. Puffr, *Soft Matter*, 2015, **11**, 9291.
8 B. Strachota, J. Hodan and L. Matějka, *Eur. Polym. J.*, 2016, **77**, 1.
9 T. Serizawa, K. Wakita and M. Akashi, *Macromolecules*, 2002, **35**, 10.
10 S. Dutta and D. Dhara, *J. Appl. Polym. Sci.*, 2015, **132**, 42749.
11 X. Z. Zhang, Y. Y. Yang and T. S. Chung, *Langmuir*, 2002, **18**, 2538.
12 M. Lutecki, B. Strachotová, M. Uchman, J. Brus, J. Pleštil, M. Šlouf, A. Strachota and L. Matějka, *Polym. J.*, 2006, **38**, 527.
13 W. Xue, I. W. Hamley and M. B. Huglin, *Polymer*, 2002, **43**, 5181.
14 S. L. Lim, W. N. H. Tang, C. W. Ooi, E. S. Chan and B. T. Tey, *J. Appl. Polym. Sci.*, 2016, **133**, 43515.
15 V. I. Lozinsky, *Russ. Chem. Rev.*, 2002, **71**, 489.

16 B. Strachotová, A. Strachota, M. Uchman, M. Šlouf, J. Brus, J. Pleštil and L. Matějka, *Polymer*, 2007, **48**, 1471.
17 G. Huerta-Angeles, K. Hishchak, A. Strachota, B. Strachota, M. Šlouf and L. Matějka, *Eur. Polym. J.*, 2014, **59**, 341.
18 K. Depa, A. Strachota, M. Šlouf and J. Hromadková, *Eur. Polym. J.*, 2012, **48**, 1997.
19 V. I. Lozinsky and O. Okay, *Adv. Polym. Sci.*, 2014, **263**, 49.
20 R. V. Ivanov and V. I. Lozinsky, *Polym. Sci., Ser. A*, 2006, **48**, 1232.
21 H. Kirsebom and B. Mattiasson, *Polym. Chem.*, 2011, **2**, 1059.
22 Q. Zhao, J. Z. Sun, X. F. Wu and Y. T. Lin, *Soft Matter*, 2011, **7**, 4284.
23 V. I. Lozinsky, E. A. Kalinina, V. Ya. Grinberg, N. V. Grinberg, V. V. Chupov and N. A. Plate, *Vysokomol. Soedin., Ser. A*, 1997, **39**, 1972.
24 O. Okay and V. I. Lozinsky, *Adv. Polym. Sci.*, 2014, **263**, 103.
25 W. Xue, S. Champ, M. B. Huglin and T. G. J. Jones, *Eur. Polym. J.*, 2004, **40**, 467.
26 H. Kirsebom, D. Topgaard, I. Yu. Galaev and B. Mattiasson, *Langmuir*, 2010, **26**, 16129.
27 H. Kirsebom, G. Rata, D. Topgaard, B. Mattiasson and I. Y. Galaev, *Macromolecules*, 2009, **42**, 5208.
28 H. Kirsebom, G. Rata, D. Topgaard, B. Mattiasson and I. Y. Galaev, *Polymer*, 2008, **49**, 3855.
29 M. M. Ozmen and O. Okay, *Polymer*, 2005, **46**, 8119.
30 S. Zheng, T. Wang, D. Liu, X. Liu, C. Y. Wang and Z. Tong, *Polymer*, 2013, **54**, 1846.
31 Y. Chen and W. Xu, *J. Mater. Res.*, 2014, **29**, 820.
32 T. C. Farrar and E. D. Becker, *Pulse and Fourier transform NMR*, Academic Press, New York, 1971, p. 27.
33 H. H. Winter and M. Mours, *Adv. Polym. Sci.*, 1997, **134**, 165.
34 S. Fujishige, *Polym. J.*, 1987, **19**, 297.
35 J. Spěváček, *Curr. Opin. Colloid Interface Sci.*, 2009, **14**, 184.
36 S. Sasaki, S. Okabe and Y. Miyahara, *J. Phys. Chem. B*, 2010, **114**, 14995.
37 X. D. Feng, X. Q. Guo and K. Y. Qiu, *Makromol. Chem.*, 1988, **189**, 77.
38 X. Guo, K. Qiu and X. Feng, *Chin. J. Polym. Sci.*, 1989, **7**, 165.
39 V. I. Lozinsky and R. V. Ivanov, in *Synthesis and Modification of Polymers*, ed. Y. B. Monakov, Khimiya, Moscow, 2003, p. 68.

Supplementary information

Insight into the cryopolymerization to form poly(N-isopropylacrylamide) / clay macroporous gel. Structure and phase evolution

Beata Strachota, Libor Matějka*, Antonín Sikora, Jiří Spěváček, Rafał Konefał, Alexander Zhigunov, Miroslav Šlouf

Institute of Macromolecular Chemistry, Academy of Sciences of the Czech Republic, v.v.i., Heyrovsky Sq. 2, 162 06 Prague 6, Czech Republic

Experimental

Differential scanning calorimetry

Due to the fact that the samples never totally crystallize, it was not possible to discern the contributions of ice and of crystalline NIPA to the total melting enthalpy of the sample. Therefore, for an estimate of the fraction of ice, we assumed that the measured enthalpy of melting stems from the ice melting only (this is acceptable in view of the relatively low concentration of NIPA, and of its low melting enthalpy in comparison to ice).

The concentration of NIPA in the non-frozen liquid phase is given by formula:

$$w_{NIPA} = \frac{w^{\circ}_{NIPA}}{w^{\circ}_{NIPA} + w^{\circ}_{NIPA}\left(1 - \frac{\Delta H^{exp}_{m}}{\Delta H^{\circ}_{m,\,water}}\right)}$$

where w°_{NIPA} is the weight fraction of NIPA in the initial NIPA solution.

Results and Discussion

3.1. Cryostructuration

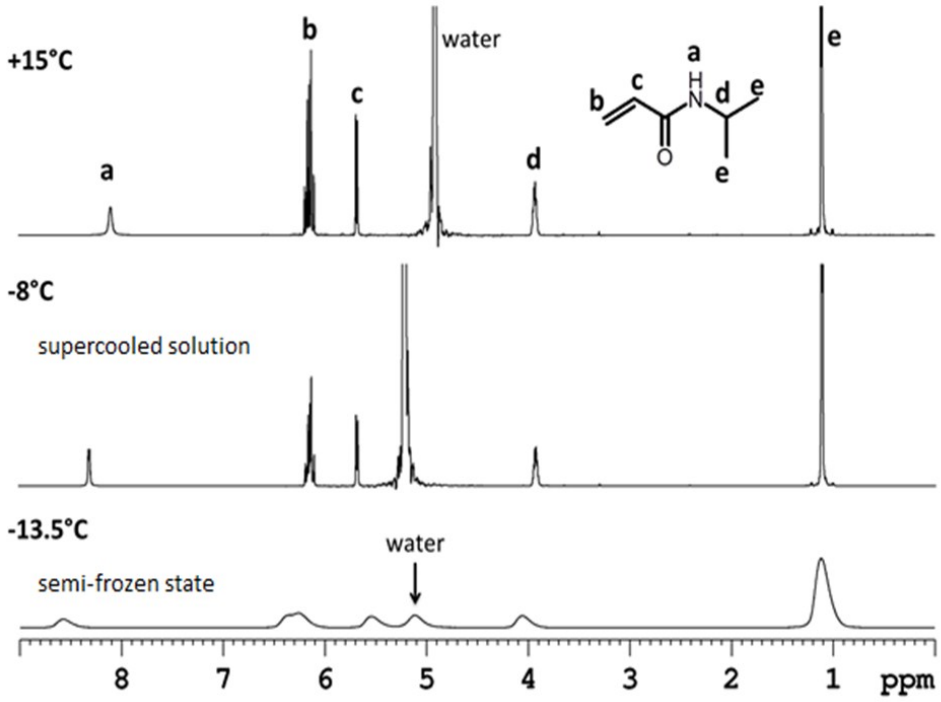

Fig. SI 1 ^{1}H NMR spectrum of the 8.5 wt.% NIPA solution in H_2O/D_2O (80/20) mixture at cooling (a) *T*= 15 °C, (b) *T*= -8 °C, prior to crystallization, (c) *T*= -13.5 °C, after crystallization. Mixture H_2O/D_2O (80/20) was used as the solvent in this case in order to detect better the signal of residual water also after freezing. The peaks assignment of NIPA and water is described in the figure.

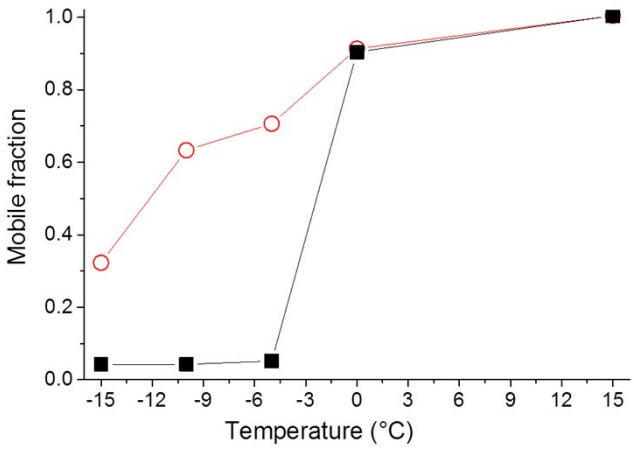

Fig. SI 2 Mobile fraction of water (■) and NIPA (ᔓ) as a function of temperature. NIPA/D_2O solution (8.5 wt. % of NIPA). Virtually the same dependence was obtained for various proton groups of NIPA.

3.1.1. Phase evolution of NIPA solution during cryostructuration

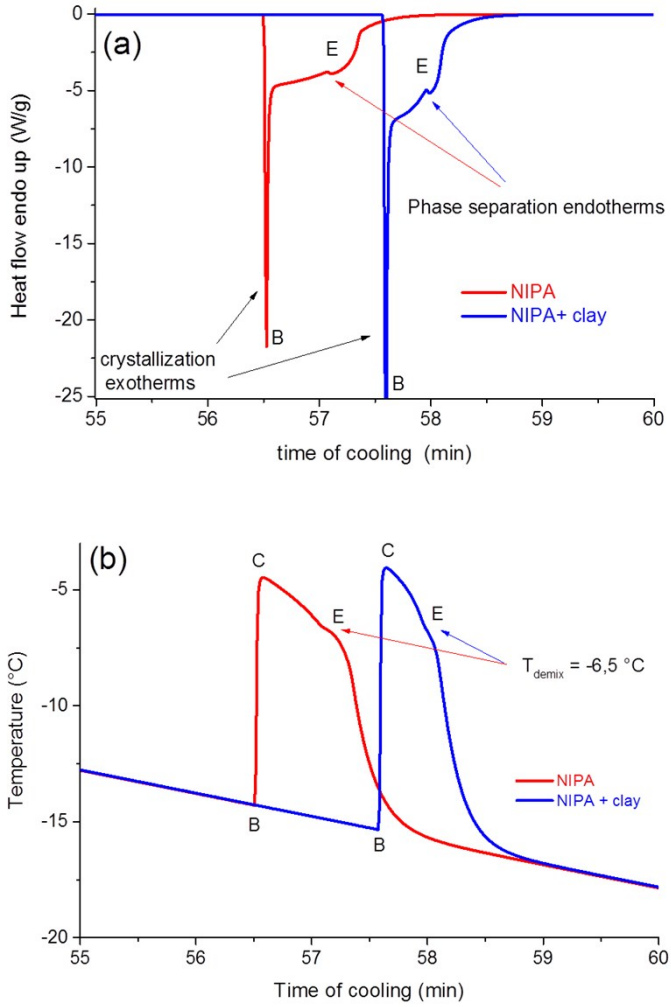

Fig. SI 3 The heat flow (a) and temperature (b) as functions of cooling time at heterogeneous crystallization of mixtures NIPA/H_2O and NIPA/clay/H_2O. Samples cooled at a cooling rate 1 °C/min.

B,C,E – points correspond to the phase diagram in Fig.2

3.2. Cryopolymerization

3.2.1. Kinetics of cryopolymerization

Steric confinement

The polymer mobility is revealed from Fig. SI4 displaying ^{1}H NMR spectra taken during polymerization of NIPA (Fig. SI4 a,b) and the NIPA/clay system (Fig. SI4 c,d) at *T*= -10 °C prior and after water crystallization.

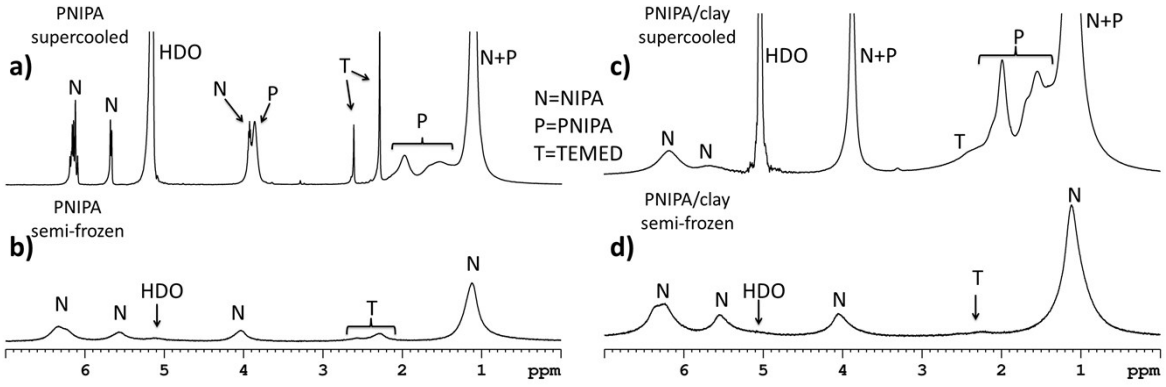

Fig. SI 4 ^{1}H NMR spectra of NIPA and NIPA/clay polymerization mixtures in D_2O at *T*= -10 °C. a) PNIPA unfrozen solution, b) PNIPA semi-frozen solution, c) PNIPA/clay unfrozen solution, d) PNIPA/clay semi-frozen solution. P–polymer, N–NIPA, T-TEMED.

The polymer is characterized by the broader signals which are designated by P. The peaks at 2.22 and 2.50 ppm correspond to the activator TEMED.

3.2.2 Phase changes and reaction progress during cryopolymerization

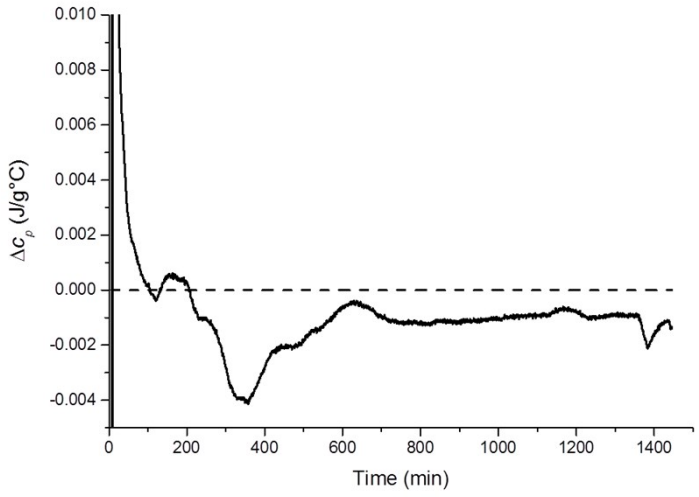

Fig. SI 5 Heat of reaction during polymerization of NIPA at *T*= -20 °C. Dash line indicates the baseline determined by subtraction of crystallization.

Publication 8

L. Starovoytova, J. Šťastná, A. Šturcová, **R. Konefał**, J. Dybal, N. Velychkivska, M. Radecki, L. Hanyková

Additive effects on phase transition and interactions in poly(vinyl methyl ether) solutions.

Polymers, **2015**, 7, 2572-2583.

polymers

MDPI

Article

Additive Effects on Phase Transition and Interactions in Poly(vinyl methyl ether) Solutions

Larisa Starovoytova [1], Julie Šťastná [2], Adriana Šturcová [3], Rafal Konefal [1], Jiří Dybal [3], Nadiia Velychkivska [1], Marek Radecki [2] and Lenka Hanyková [2,*]

Received: 27 August 2015; Accepted: 30 November 2015; Published: 4 December 2015
Academic Editor: Richard Hoogenboom

[1] Department of NMR Spectroscopy, Institute of Macromolecular Chemistry AS CR, v.v.i., Heyrovského Sq. 2, 162 06 Prague, Czech Republic; larisa@imc.cas.cz (L.S.); konefal.rafal@gmail.com (R.K.); velychkivska@imc.cas.cz (N.V.)
[2] Department of Macromolecular Physics, Faculty of Mathematics and Physics, Charles University in Prague, V Holešovičkách 2, 180 00 Prague 8, Czech Republic; chamky@seznam.cz (J.Š.); radecki.m@seznam.cz (M.R.)
[3] Department of Vibrational Spectroscopy, Institute of Macromolecular Chemistry AS CR, v.v.i., Heyrovského Sq. 2, 162 06 Prague, Czech Republic; sturcova@imc.cas.cz (A.Š.); dybal@imc.cas.cz (J.D.)
* Correspondence: Lenka.Hanykova@mff.cuni.cz; Tel.: +420-2-2191-2368; Fax: +420-2-2191-2350

Abstract: A comparative study of thermal response of poly(vinyl methyl ether) in the presence of different hydrophilic and hydrophobic additives was performed by Nuclear magnetic resonance (NMR) spectroscopy, Fourier-transform infrared (FTIR) spectroscopy, differential scanning calorimetry (DSC), and optical microscopy. The effect of polymer concentration and additive content on the appearance and extent of the phase transition was determined. A detailed study of interaction mechanism in solutions with two hydrophobic additives showed differences in the way in which polymer globules are formed. For solutions containing *t*-butyl methyl ketone and *t*-butanol, measurements of ^{1}H spin-spin relaxations showed the presence of water and additive molecules bound in PVME globular structures. These originally-bound molecules are then slowly released from the globular-like structures. Incorporation of molecules into the globules disrupts the cooperativity of the transition and affects the size of globular structures.

Keywords: additives; LCST; poly(vinyl methyl ether); thermal properties

1. Introduction

The applications of stimuli-responsive polymers are becoming more and more diversified. The ability of the polymers to change their behavior according to external conditions, and the possibility to moderate this effect, make such systems interesting for drug delivery applications, as sensors, and in cosmetics [1–4]. Investigations of the transition phenomena in model systems can offer knowledge that is of practical use. Poly(vinyl methyl ether) (PVME) is a non-ionic water-soluble polymer with useful properties, such as biocompatibility, non-toxicity, low glass transition temperature and thermoresponsive behavior with lower critical solution temperature (LCST) around 308 K [5–7]. The phase transition effects for this polymer have been widely investigated by different experimental techniques, such as differential scanning calorimetry (DSC) [8–10], Nuclear magnetic resonance (NMR) spectroscopy [11,12], and Fourier-transform infrared (FTIR) spectroscopy [6,13,14].

Modification of the transition conditions (such as the transition temperature) of thermoresponsive polymers can be achieved in different ways, such as variation of the hydrophobicity of the polymer chain by copolymerization with hydrophobic or hydrophilic co-monomers or changes in the composition of the solvent by mixing the aqueous polymer solution with small molecules (additives) that alter the polymer-water interaction [15–18].

Additive molecules can sometimes be used as a crude model of a medical drug for examining drug delivery systems [19,20]. The ability of an additive compound to interact with the polymer chain on the one hand and to bind water molecules on the other hand plays an important role in its influence on the transition mechanism [11]. In particular, the ability of the additive to be embedded into the polymer globules affects the mechanism of their formation and the kinetics of water release and, possibly, also the additive release from the globular structures. Based on their influence on polymer structure, it is possible to distinguish two types of additives, namely those that either stabilize or destabilize the hydration structure surrounding the polymer chain [21].

In previous studies of similar systems, it was found that even a small amount of an additive can change the transition temperature and the mechanism of the phase separation in PVME solutions. For example, although propanol has almost no effect on this polymer behavior, lower molecular weight alcohols are able to relatively stabilize the polymer structure, whereas higher alcohols and simple inorganic salts tend to destabilize the structure, *i.e.*, lead to lower transition temperatures [18,22].

In this work we perform a comparative analysis of the phase separation of PVME in the presence of structurally similar additives, *t*-butyl methyl ketone (TBMK), *t*-butyl methyl ether (TBME), *t*-butylamine (TBAm), and *t*-butanol (TBOH) differing in individual chemical groups (carbonyl, ether, amine, and hydroxyl group, respectively). Several experimental techniques were used in this investigation. NMR and FTIR were used to individually analyze the additive, water, and polymer segments and analyze their mobility and interactions during the transition. DSC and optical microscopy were used to characterize the macroscopic behavior of the sample as a whole. Differences in the mechanism of transition because of the presence of these additives are discussed.

2. Experimental Section

2.1. Materials

PVME was purchased from Sigma-Aldrich (St. Louis, MO, USA) and was supplied as 50 wt % aqueous solution (molecular weight determined by SEC in THF was M_w = 60,500, $M_w/M_n \approx 3$). *t*-Butyl methyl ketone, *t*-butyl methyl ether, *t*-butylamine, and *t*-butanol (see Figure 1 for the structures) were purchased from Sigma-Aldrich (St. Louis, MO, USA) and were used as obtained. After drying, the polymer was used to prepare PVME in D_2O (99.96% of deuterium) solutions with polymer concentrations c_P = 0.5−10 wt % and concentrations of additives c_{ad} = 0−10 wt %. All the PVME/D_2O samples in 5 mm NMR tubes were degassed and were sealed under argon; sodium 2,2-dimethyl-2-silapentane-5-sulfonate (DSS) was used as an internal NMR standard.

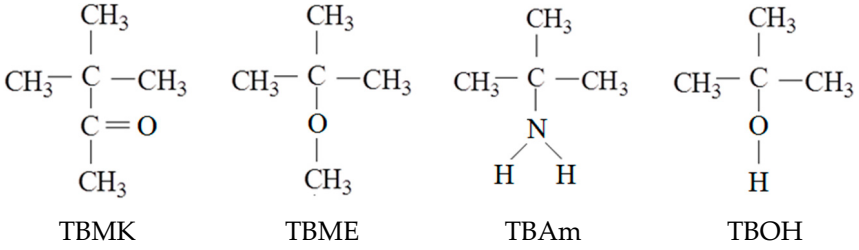

Figure 1. Structural formulae of *t*-butyl methyl ketone (TBMK); *t*-butyl methyl ether (TBME); *t*-butylamine (TBAm); and *t*-butanol (TBOH).

2.2. NMR Mesurements

^{1}H NMR spectra were measured with a Bruker 600 MHz Avance III spectrometer (Billerica, MA, USA, 5 mm NMR tubes were used). The integrated signal intensities were determined with the spectrometer integration software with an accuracy of ±1%. The temperature was kept constant within ±0.2 K with a BVT 3000 temperature unit. The typical measurement conditions for ^{1}H were as follows: a spectral width of 6 kHz, a pulse width of 10 μs (90° pulse) and a relaxation

delay of 20 s. The ^{1}H spin-spin relaxation times T_2 were measured with the CPMG pulse sequence 90°_x-(t_d-180°_x-t_d)$_n$-acquisition, for t_d = 0.5 ms.

2.3. Infrared Spectroscopy

Attenuated total reflectance (ATR) FTIR spectra of the PVME solution, neat PVME (containing a small amount of absorbed water), TBME, and TBMK solutions were collected with a Nicolet Nexus 870 FTIR spectrometer (Thermo Fisher Scientific, Waltham, MA, USA) purged with dry air and equipped with a cooled mercury-cadmium-telluride (MCT) detector. The samples were measured on a horizontal ATR Golden Gate unit (SPECAC Ltd., Orpington, UK) with a diamond prism and a controlled heated top plate; the spectral resolution was 4 cm^{-1}. All the spectra were processed with the advanced ATR correction with OMNIC^{TM} software (Thermo Fisher Scientific, Waltham, MA, USA). The spectrum of neat D_2O at the corresponding temperature was subtracted to better visualize the dissolved compounds. In addition, the spectrum of PVME at the corresponding temperature was subtracted from spectra in Figure 8d,e to visualize the TBME additive only; this subtraction is responsible for the baseline distortion. The spectra were scaled.

2.4. DSC

DSC measurements were performed with a differential scanning calorimeter, Pyris 1 (Perkin-Elmer, Waltham, MA, USA); two complete cycles with heating and cooling rates of 5 K· min^{-1} over a range of 275–325 K were performed. Samples of approximately 10 mg were encapsulated in aluminum pans. The transition was characterized by calculation of the enthalpy changes per unit mass of PVME through integration of the experimental DSC thermograms.

2.5. Optical Microscopy

Optical microscope measurements were carried out under nitrogen atmosphere with a Nikon Eclipse 80i (Nikon Instruments, Amsterdam, Netherlands); a camera, PixeLINK PL-A662 (PixeLINK, Ottawa, ON, Canada); and a temperature cell, Linkam LTS350 (Linkam Scientific Instruments, Surrey, UK). Development of the morphology was observed for a thin sample layer placed between a support glass slide and a cover slip, with 50-fold magnification. The heating rate was 1 K· min^{-1}, and before each experiment, the samples were always maintained at the experimental temperature for 1 min.

3. Results and Discussion

3.1. Influence of Additives on the Phase Transition

The intensity and shape of the polymer, additive, and water HDO signals in NMR spectra vary with temperature. The polymer signal vanishes from the high-resolution NMR spectra because of broadening (often extreme) of the polymer peak due to the restriction in the mobility of polymer chains upon formation of the solid-like globules [5,11]. Figure 2 shows ^{1}H NMR spectra as detected for the neat PVME solution and solutions of PVME with additives at temperatures above the transition of each particular system. The shapes of the peaks in the spectra are different for individual additives and for the pure PVME solution.

We can distinguish two types of polymer peaks [5]. The first type corresponds to flexible polymer segments which are not involved in compact globular structures (the narrow part of the CH_3O peak at 3.5 ppm in spectrum a, Figure 2). The second type is assigned to the major part of polymer units which form solid-like globular structures (the broad part of the same peak from 4 to 5 ppm). The presence of additives strongly affects the shape of both polymer band components. As shown in Figure 2, the signal of the units in globular structures is extremely broadened, so it is no longer visible in the spectra (spectra in Figure 2b–e); this disappearance suggests that the polymer units involved in globules formed in solutions with additives show higher immobilization in comparison with collapsed units in the solution of neat PVME. Further, it follows from Figure 2 that the shape of NMR signal

corresponding to PVME group $CHOCH_3$ depends on the additive. The solution with TBME shows quite narrow $CHOCH_3$ peak whereas, for solutions with others additives, this peak broadens.

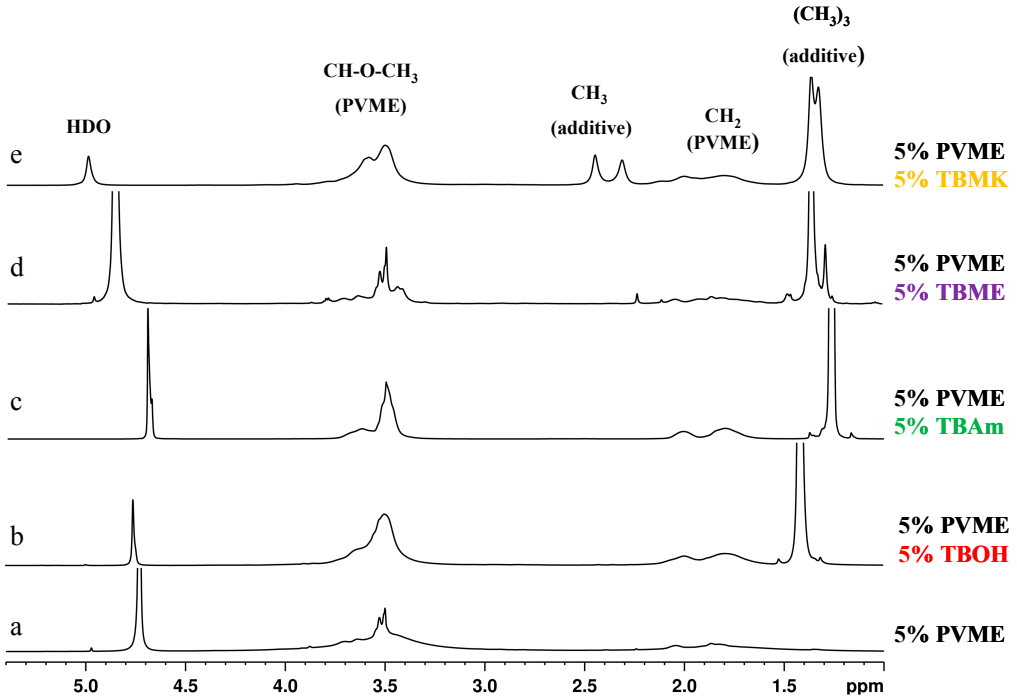

Figure 2. High-resolution ^{1}H NMR spectra of D_2O solutions of neat PVME (c_P = 5 wt %) (**a**); and solutions with additives TBOH (**b**); TBAm (**c**); TBME (**d**); and TBMK (**e**) (c_P = 5 wt %, c_{ad} = 5 wt %) measured at temperatures above the transition of each particular system.

For further analysis, we shall define the phase separated fraction as the fraction of PVME units in concentrated, polymer-rich phase. We have determined the values of the fraction of phase-separated PVME units from the following relation

$$p\,(T) = 1 - \frac{I}{I_0} \tag{1}$$

where I is the integrated intensity of the given polymer line in a partly phase-separated system and I_0 is the integrated intensity of this line if no phase separation occurs [11,23].

Temperature dependences of the fraction p as obtained from integrated intensities of $CHOCH_3$ protons of PVME are shown for neat PVME solution (c_P = 5 wt %) and PVME solutions with c_{ad} = 5 wt % in Figure 3. For all polymer and additive concentrations investigated, the solutions show a qualitatively similar behavior of the polymer $CHOCH_3$ proton intensities. From Figure 3 it follows that all solutions with additives exhibit broader transition region than the solution with neat PVME; this effect is the most significant in PVME/TBMK solution where the transition is ~12 K broad. Transition temperature was detected as the temperature in the middle of the transition, *i.e.*, where the signal has decreased by 50%. Figure 4 shows the dependence of transition temperature on additive concentration for solutions with c_P = 5 wt %. For TBAm and TBOH, increasing concentration was observed to lead to a slight shift of transition temperature to higher values; at the same time the transition extent (fraction p above the transition in Figure 3) decreases as compared with the neat PVME. TBAm and TBOH molecules obviously stabilize polymer-solvent interactions and prevent hydrophobic polymer-polymer interactions. Such stabilizing effect was detected in aqueous solutions of PVME and lower molecular weight alcohols [15,18,22].

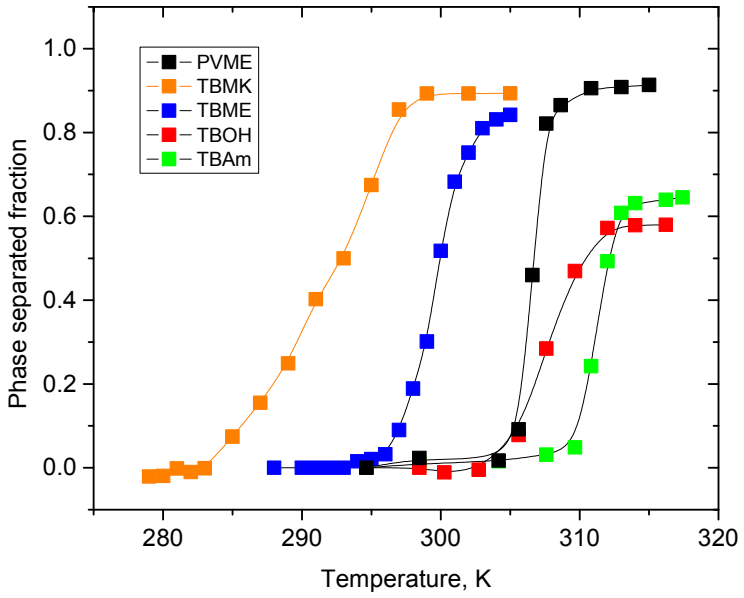

Figure 3. Temperature dependences of the fraction p as obtained from integrated intensities of $CHOCH_3$ protons of PVME in neat PVME solution (c_P = 5 wt % in D_2O) and PVME/additives solutions (c_P = 5 wt %, c_{ad} = 5 wt % in D_2O).

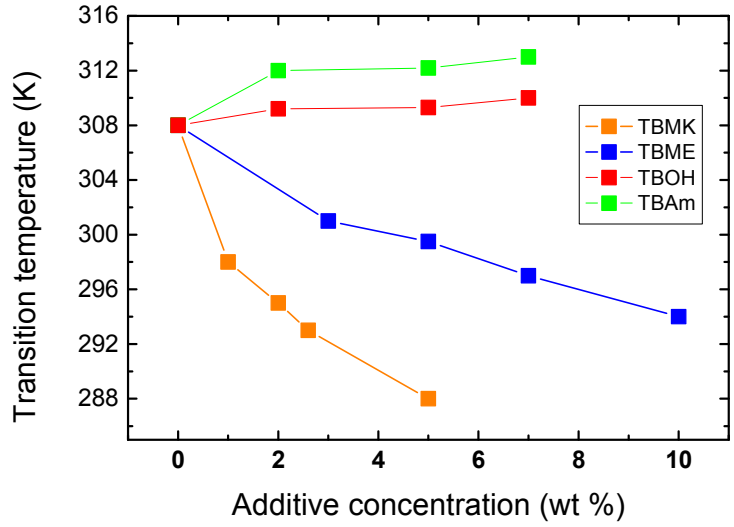

Figure 4. Concentration dependence of the transition temperature for PVME/additives solutions (c_P = 5 wt % PVME in D_2O).

On the other hand, increasing the concentration of the additives TBMK and TBME in the system promotes destabilization of the hydration structure surrounding the polymer chain; increasing this concentration significantly decreases the transition temperature. As shown in Figure 4, this effect is more pronounced for TBMK. The presence of the ether additive only results in changes of the transition temperature, and no broadening of the transition region was observed. Similarly as TBMK and TBME, higher alcohols, and simple inorganic salts tend to destabilize the structure, *i.e.*, lead to lower transition temperatures in aqueous solutions of PVME [18]. The values of fraction p above the transition in PVME/TBMK and PVME/TBME solutions reach ~0.9 similarly as the values in neat PVME solution. We assume that the remaining minority mobile component (~10%), which does not take part in the phase transition, comes from low-molecular weight oligomers as it was shown for PVME/D_2O solutions [24].

The effect of polymer concentration on the phase transition of solutions with hydrophilic and hydrophobic additives (TBAm and TBME, respectively) is seen in Figure 5. For higher PVME concentrations (c_p = 10 wt %) in PVME/TBAm solution, the dependence is shifted by ~4 K to lower values. This shift of the transition is probably a consequence of the preferred polymer-polymer contacts at higher concentration, allowing hydrophobic interactions to predominate at lower temperatures. More complicated behavior was detected for solutions with hydrophobic TBME. An increase of the transition temperature is observed for additive concentration c_{ad} = 3 wt % and higher polymer concentration, apparently since the number of hydrophobic additive molecules per polymer segment decreases and, thus, hydrophobic interactions of the additive with the chain are reduced. Subsequently, for more concentrated polymer solutions and c_{ad} > 5 wt %, the transition temperature decreases by ~4 K. The solvent quality for such high TBME concentrations is probably reduced and the phase transition occurs already at lower temperatures. These two different mechanisms controlling LCST shift were described for aqueous solutions of poly(*N*-isopropylacrylamide) and hydrophobic benzaldehydes [19].

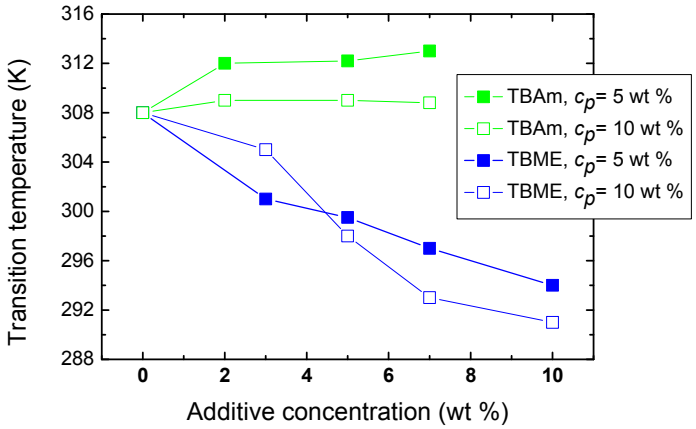

Figure 5. Concentration dependence of the transition temperature for PVME/TBME and PVME/TBAm solutions for two various polymer concentrations c_P = 5 and 10 wt % PVME in D_2O.

3.2. Mobility of Water and Additive Molecules during Phase Transition

The mobilities of the additive and water molecules were studied using NMR spin-spin relaxation time T_2 [5,11]. To follow the changes in the behavior of the water and additive in the presence of the polymer, a comparative analysis of T_2 was performed at temperatures below and above the transition. In this respect it is useful to define T_{2im} as the ratio of the measured T_2 values in the polymer-additive system $T_{2(pvme+additive)}$ and in the corresponding additive/D_2O solution $T_{2(additive)}$ at the same temperature (T_{2im} = $T_{2(pvme+additive)}/T_{2(additive)}$) [20]. The value of T_{2im} gives temperature-independent information about the extent of the immobilization of the water and additive molecules caused by the presence of the polymer. The comparison of these quantities for HDO molecules and for the *t*-butyl group of the additives is given in Table 1. If no interaction with the polymer occurs, the value of T_{2im} should be equal to 1 (if the effects of viscosity can be neglected). The lower the resulting value, the higher the immobilization effect caused by the polymer–water or polymer–additive interaction.

Table 1. T_{2im} parameters for the PVME/additive solutions (c_P = 5 wt %, c_{ad} = 5 wt %).

Temperature	TBMK		TBME		TBOH		TBAm	
	HDO	$(CH_3)_3$	HDO	$(CH_3)_3$	HDO	$(CH_3)_3$	HDO	$(CH_3)_3$
below LCST	0.16	0.42	0.78	0.78	0.65	0.92	0.60	0.88
above LCST	0.14	0.32	0.60	0.54	0.34	0.30	0.83	0.79

Relaxation parameters T_{2im} detected in PVME/TBOH and PVME/TBAm solutions below LCST reach similar values, see Table 1. T_{2im} values of the additive *t*-butyl group are almost equal to 1, values as obtained for water molecules are somewhat lower which could indicate a slight interaction with the polymer as well as the influence of chemical exchange. Different relaxation behavior of molecules in solutions with hydrophilic additives was found at elevated temperatures above LCST. T_{2im} values of molecules in PVME/TBAm solution remain high even above the transition while a reduction of T_{2im} values was observed for water and additive molecules in PVME/TBOH solution. The greater immobilization above the transition temperature for TBOH and water can be attributed to the effect of incorporation of a certain portion of these molecules into the globular structures.

Changes in the mobility of solvent molecules as a function of time were found to arise from the effects of solvent molecules being released from the polymer globular structure. The investigated samples were kept for the whole time in the magnet of NMR spectrometer at elevated temperature and the time dependence of T_2 values was measured. Figure 6a shows that T_2 values of HDO and *t*-butyl group in the PVME/TBOH solution very slowly increased with time, reaching after tens of hours a value similar to that observed at temperatures below the transition. These results provide evidence that water and additive originally bound in globules are, over time, very slowly released (squeezed out) from the globular structures. Such behavior was previously detected in aqueous solutions of neat PVME solutions [5,11]. In contrast, for TBAm solutions no such changes in T_2 as a function of time were observed, confirming the idea that globules formed in these solutions do not contain bound water or/and additive.

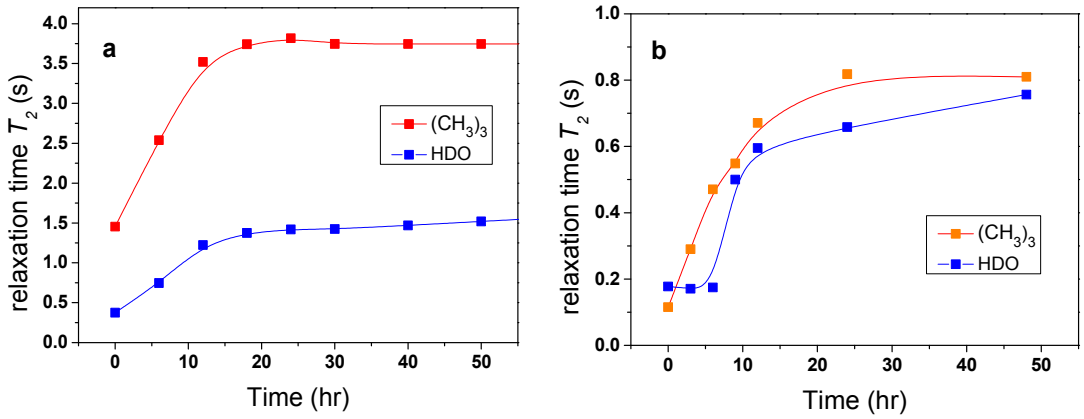

Figure 6. Time dependences of the spin-spin relaxation time T_2 of HDO and $(CH_3)_3$ protons of additive in PVME/TBOH (**a**) and PVME/TBMK (**b**) solutions (c_P = 5 wt %, c_{ad} = 5 wt % in D_2O) measured above the phase transition.

It follows from Table 1 that, for the solution with TBMK, T_{2im} of water and *t*-butyl group reach substantially lower values indicating that water and additive molecules are strongly involved in interactions with the polymer at temperatures both below and above LCST. For TBME, the solvent and additive molecules are only slightly affected by the presence of the polymer. Similarly as in the case of PVME/TBOH solutions, a time-dependent experiment (Figure 6b) confirmed that molecules originally bound in collapsed polymer structures of PVME/TBMK solution are slowly released.

3.3. FTIR Spectroscopy

As indicated by the concentration dependences of the transition temperature in Figure 4 and NMR relaxations, solutions with TBMK and TBME showed substantial differences during phase transition. A detailed FTIR study confirmed different interaction mechanisms taking place in these solutions. On the other hand, no or negligible differences were recorded in FTIR spectra of PVME/TBOH and PVME/TBAm solutions and they were, thus, no longer analyzed.

Corrected ATR FTIR spectra of TMBK systems are presented in Figure 7. In the presence of two PVME bands that are assigned to the stretching vibration of the carbonyl group of TBMK are present at 278 K (spectrum d in Figure 7); one band is at 1705 cm^{-1}, which is close to the position of the band for the neat form of the compound (spectrum a) [25], and a second band is at 1688 cm^{-1}, which corresponds to the hydrated form of TBMK (spectra b and c). As the temperature increases to 301 K (well above LCST), only the band that represents the neat form is present at 1707 cm^{-1}. In the presence of PVME, the positions the symmetric CH_3 deformation bands are almost identical to the locations of the bands in the neat TBMK (1365 cm^{-1} and 1355 cm^{-1}). The above observations could signify that below the transition temperature, domains rich in TBMK and attached to the polymer exist. The surfaces of these domains interact with water molecules through hydrogen bonds with the carbonyl groups of TBMK; thus, two carbonyl bands are present in the spectra below the transition—a hydrated band and a band similar to the neat TBMK. Above the transition temperature, the methyl groups remain in the same environment, whereas the carbonyl groups experience an environment similar to that of the neat TBMK and are no longer in contact with water molecules—this result could be consistent with the entrance of TBMK into the interior of the collapsed PVME globules.

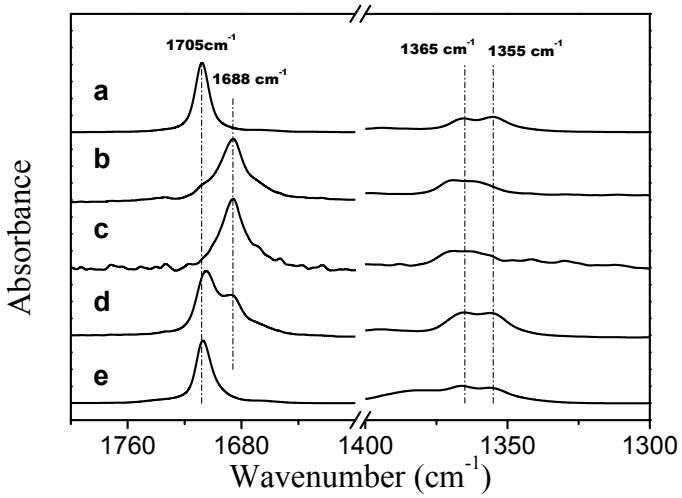

Figure 7. Corrected ATR FTIR spectra of TMBK at a temperature of 301 K (**a**); TBMK in D_2O at a concentration of 5 wt % and a temperature 278 K (**b**); TBMK in D_2O at a concentration of 5 wt % and a temperature 301 K (**c**); PVME/TBMK/D_2O at c_P = 0.5 wt % and c_{ad} = 5 wt % and a temperature of 278 K (**d**); and PVME/TBMK/D_2O at c_P = 0.5 wt % and c_{ad} = 5 wt % and a temperature of 301 K (**e**).

In the spectrum of neat TBME, the CH_3 symmetric deformation bands are located at 1386 and 1364 cm^{-1} (spectrum Figure 8a). In the presence of PVME the positions of these two bands are identical to the locations of the bands in the spectra of TBME hydrated with D_2O at 278 K. Upon an increase in temperature to 301 K (above LCST), these two bands shift to positions identical to those in neat TBME. In the spectrum of neat TBME, the band assigned to the C–O stretching vibration of the methoxy group is located at 1086 cm^{-1} [26]. An appearance of the second band at 1046 cm^{-1}, in the presence of PVME, most likely corresponds to the hydrated form of TBME. The above observations confirm that below the transition temperature the methyl groups of TBME are hydrated. Above the transition temperature, the methyl groups are located in an environment similar to neat TBME. The two C–O stretching vibration bands in the methoxy group that are present in the spectra below and above the transition temperature (spectra Figure 8d,e) indicate the presence of two types of additive molecules; the α band most likely corresponds to TBME molecules that are isolated from each other and in which the dipole-dipole intermolecular interaction has been eliminated. The β band at the lower wavenumbers probably corresponds to hydrated TBME molecules in which the methoxy oxygen is involved in hydrogen bonds with the solvating D_2O molecules.

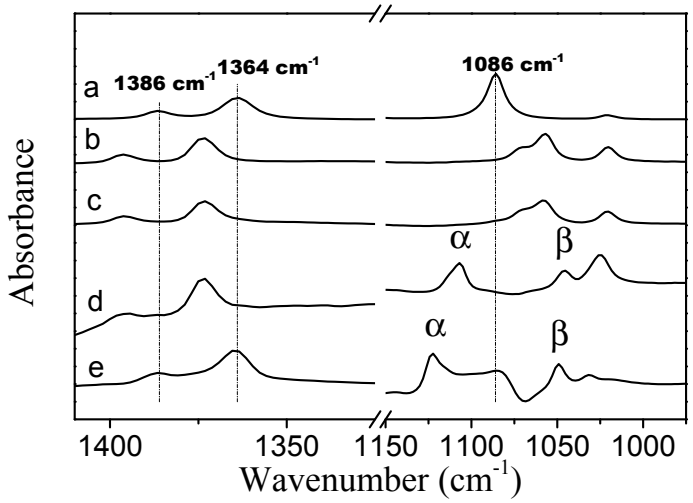

Figure 8. Corrected ATR FTIR spectra of (**a**) TBME at a temperature of 301 K; (**b**) TBME in D_2O at a concentration of 5 wt % and a temperature of 278 K; (**c**) TBME in D_2O at a concentration of 5 wt % and a temperature of 301 K; (**d**) PVME/TBME/D_2O at c_P = 10 wt % and c_{ad} = 5 wt % and a temperature of 278 K; and (**e**) PVME/TBME/D_2O at c_P = 10 wt % and c_{ad} = 5 wt % and a temperature of 301 K.

From the results obtained from NMR relaxation and FTIR experiments, we can suggest that globular structures formed in TBME solutions above LCST do not contain a substantial amount of bound water or additive molecules; the slight mobility restriction of water and TBME could be caused by interactions of these molecules with the surface of the polymer globules. On the other hand, for TBMK solutions we observe a strong mobility reduction of the additive and water molecules. This fact can be explained by the interactions between the polymer chain and the TBMK carbonyl group that are mediated by one or more water molecules.

3.4. Cooperativity of the Phase Transition

The temperature dependences of *p*-fraction shown in Figure 3 can be used for determining the enthalpy and entropy changes during phase transition, considering this process as the competition between non-phase separated (coil) and phase separated (globule) states governed by the Gibbs free energy. The van´t Hoff equation describes temperature changes of the equilibrium constant *K* of the coil-globule transition as follows:

$$\ln K = -\frac{\Delta H_{NMR}}{RT} + \frac{\Delta S_{NMR}}{T} \quad (2)$$

where ΔH_{NMR} and ΔS_{NMR} are the changes in enthalpy and entropy, respectively, and R is the gas constant. In relation to the *p*-fraction the equilibrium constant K can be written as the ratio:

$$K = \frac{p}{p_{max} - p} \quad (3)$$

where p_{max} are values of fraction p above the transition. The dependences of $R \ln(p/(p_{max} - p))$ on $-1/T$ were fitted with linear regression according to Equations (2) and (3) and the parameters ΔH_{NMR} are summarized in Table 2. Table 2 contains also enthalpy changes ΔH_{DSC} as obtained from DSC measurements and recalculated to mol of monomer units where the enthalpy data for neat PVME quite well agree with the literature [27,28]. Enthalpy values ΔH_{DSC} can be compared with those determined from NMR. Assuming that the phase transition is a cooperative process and the polymer chain consists of cooperative units (domains) which undergo transition as a whole [29–31], the values ΔH_{NMR} are thus related to mol of cooperative units. The ratio $\Delta H_{NMR}/\Delta H_{DSC}$ represents the average number

of monomer units in one cooperative domain and can provide a quantitative analysis of the degree of cooperativity (*cf.* Table 2). For the 5 wt % solution of neat PVME and solutions of PVME with TBME and TBAm (c_{ad} = 5 wt %), the size of the domains agrees quite well with the average degree of polymerization (D_P of PVME ~348), thus showing that, in this case, the cooperative unit is the whole polymer chain. For solutions with TBMK and TBOH (c_{ad} = 5 wt %), these domains are smaller and consist of only 140 and 170 monomer units, respectively. As follows from relaxation experiments, a certain amount of water and additive molecules is incorporated into the globules formed in these two solutions. This process is obviously time-consuming and disrupts the cooperativity of the transition; cooperative units are smaller and the phase transition is broader.

Table 2. Thermodynamic parameters determined by NMR and DSC and the number of monomer units in the domain for mixtures of 5 wt % PVME.

Sample	ΔH_{NMR} MJ/mol	ΔH_{DSC} kJ/mol	Number of Mon. Units in Domain
PVME	1.32	4.05	326
TBMK	0.32	2.23	143
TBME	0.78	2.32	336
TBOH	0.40	2.30	174
TBAm	0.58	1.98	293

The difference in the structure and size of the polymer globules in the presence of the additives can be demonstrated by the optical microscopy images shown in Figure 9. This figure demonstrates that globular structures formed above LCST transition in aqueous PVME/TBMK and PVME/TBOH solutions are somewhat smaller than those observed for solutions with other additives and neat PVME. This finding corresponds to the data in Table 2 where size of cooperative domains as calculated for PVME/TBOH and PVME/TBMK solutions is about twice smaller in comparison with domains formed in other solutions and this is obviously macroscopically manifested in smaller polymer aggregations. Interestingly enough, polymer agglomerates formed in PVME/TBME solutions show strong separation and well-defined surfaces. This could be the consequence of the fact that 90% of polymer chains are involved in the collapsed structures, as follows from the fraction p above the transition, and at the same time these structures do not contain any bound water or additive.

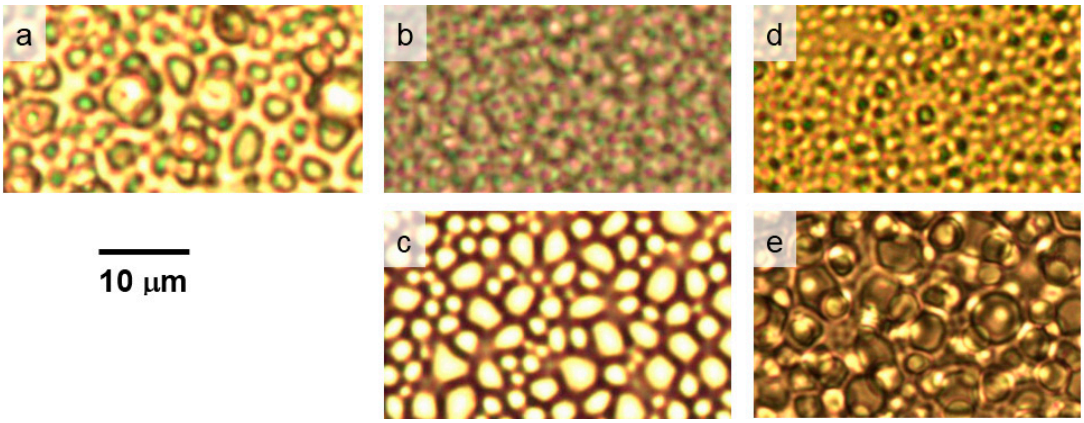

Figure 9. Photomicrographs of the neat PVME solution (c_P = 5 wt % in D_2O) (**a**) and solutions with additives TBMK (**b**); TBME (**c**); TBOH (**d**); and TBAm (**e**) (c_P = 5 wt %, c_{ad} = 5 wt %) recorded at temperatures above the transitions of the particular systems.

4. Conclusions

Temperature-induced phase separation of PVME in the presence of small additives was investigated with various techniques. It has been shown that the interactions and dynamics during the phase transition are significantly influenced by the chemical structure of an additive molecule and hydrophobic additives more strongly affect polymer transition than additives with hydrophilic character. A slight stabilizing effect of hydrogen bonding was manifested in the presence of hydrophilic additives TBOH and TBAm in PVME solution by the shift of the transition region towards higher temperatures and by a decrease of the fraction of PVME units involved in globular structures. A clear pronounced decreasing effect on the LCST was found for hydrophobic TBME and TBMK additives, which obviously facilitate the phase separation process. Detailed FTIR analysis showed that TBMK is in a strong interaction with the carbonyl group of the additive and the ether group of the polymer even before phase transition, in contrast to TBME, with which no polymer interaction occurs before the transition. Two different mechanisms controlling LCST shift were suggested from polymer concentration dependences.

From comparison of thermodynamical parameters, as obtained from NMR and DSC, the size of the cooperative units undergoing the transition as a whole was determined. Cooperative domains in PVME/TBOH and PVME/TBMK solutions are about twice smaller in comparison with those formed in other solutions, and this is macroscopically manifested in smaller polymer aggregations. NMR relaxation experiments confirmed that a certain portion of water and additive molecules remained bound in PVME globules in the solutions with TBOH and TBMK. The incorporation of water and additive molecules into the globules, thus, leads to reduced cooperativity of the transition and influences the size of polymer aggregations formed above LCST. The originally-bound molecules are, over time, very slowly released from phase-separated globules.

Acknowledgments: Support by the Czech Science Foundation (Project 13-23392S) is gratefully acknowledged.

Author Contributions: Larisa Starovoytova, Nadiia Velychkivska and Rafal Konefal performed NMR experiments and analyzed NMR data; Julie Šťastná performed experiments on optical microscopy; Adriana Šturcová and Jiří Dybal performed FTIR experiments and analyzed FTIR data; Marek Radecki performed experiments on optical microscopy and DSC; Lenka Hanyková and Larisa Starovoytova wrote the paper.

Conflicts of Interest: The authors declare no conflict of interest.

References

1. Liu, R.; Fraylich, M.; Saunders, B.R. Thermoresponsive copolymers: From fundamental studies to applications. *Colloid Polym. Sci.* **2009**, *287*, 627–643. [CrossRef]
2. Aseyev, V.O.; Tenhu, H.; Winnik, F.M. Temperature dependence of the colloidal stability of neutral amphiphilic polymers in water. *Adv. Polym. Sci.* **2006**, *196*, 1–85.
3. Schild, H.G. Poly(*N*-isopropylacrylamide)—Experiment, theory and application. *Prog. Polym. Sci.* **1992**, *17*, 163–249. [CrossRef]
4. Aseyev, V.O.; Tenhu, H.; Winnik, F.M. Non-ionic thermoresponsive polymers in water. *Adv. Polym. Sci.* **2011**, *242*, 29–89.
5. Spěváček, J.; Hanyková, L.; Starovoytova, L. ^{1}H NMR relaxation study of thermotropic phase transition in poly(vinyl methyl ether)/D_2O solutions. *Macromolecules* **2004**, *37*, 7710–7718. [CrossRef]
6. Zeng, X.; Yang, X. A study of interaction of water and model compound of poly(vinyl methyl ether). *J. Phys. Chem. B* **2004**, *108*, 17384–17392. [CrossRef]
7. Pastorczak, M.; Kozanecki, M.; Ulanski, J. Water-polymer interactions in PVME hydrogels—Raman spectroscopy studies. *Polymer* **2009**, *50*, 4535–4542. [CrossRef]
8. Van Durme, K.; Loozen, E.; Nies, E.; Mele, B. Phase behavior of poly(vinyl methyl ether) in deuterium oxide. *Macromolecules* **2005**, *38*, 10234–10243. [CrossRef]
9. Meeussen, F.; Bauwens, Y.; Moerkerke, R.; Nies, E.; Berghmans, H. Molecular complex formation in the system poly(vinyl methyl ether)/water. *Polymer* **2000**, *41*, 3737–3743. [CrossRef]

10. Maeda, H. Dielectric and calorimetric behaviors of poly(viny1 methyl ether)–water systems including unusual relaxation processes at subzero temperatures. *Macromolecules* **1995**, *28*, 5156–5159. [CrossRef]
11. Starovoytova, L.; Spěváček, J. Effect of time on the hydration and temperature-induced phase separation in aqueous polymer solutions. ^{1}H NMR study. *Polymer* **2006**, *47*, 7329–7334. [CrossRef]
12. Hanyková, L.; Spěváček, J.; Ilavský, M. ^{1}H NMR study of thermotropic phase transition of linear and crosslinked poly(vinyl methyl ether) in D_2O. *Polymer* **2001**, *42*, 8607–8612. [CrossRef]
13. Sun, B.; Lai, H.; Wu, P. Integrated microdynamics mechanism of the thermal-induced phase separation behavior of poly(vinyl methyl ether) aqueous solution. *J. Phys. Chem. B* **2011**, *115*, 1335–1346. [CrossRef] [PubMed]
14. Maeda, Y. IR spectroscopic study on the hydration and the phase transition of poly(vinyl methyl ether) in water. *Langmuir* **2001**, *17*, 1737–1742. [CrossRef]
15. Labuta, J.; Hill, J.P.; Hanyková, L.; Ishihara, S.; Ariga, K. Probing the micro-phase separation of thermo-responsive amphiphilic polymer in water/ethanol solution. *J. Nanosci. Nanotech.* **2010**, *10*, 8408–8416. [CrossRef]
16. Van Durme, K.; Rahier, H.; Mele, B. Influence of additives on the thermoresponsive behavior of polymers in aqueous solution. *Macromolecules* **2005**, *38*, 10155–10163. [CrossRef]
17. Housni, A.; Narain, R. Aqueous solution behavior of poly(*N*-isopropylacrylamide) in the presence of water-soluble macromolecular species. *Eur. Polym. J.* **2007**, *43*, 4344–4354. [CrossRef]
18. Horne, R.A.; Almeida, J.P.; Day, A.F.; Yu, N.T. Macromolecule hydration and the effect of solutes on the cloud point of aqueous solutions of polyvinyl methyl ether: A possible model for protein denaturation and temperature control in homeothermic animals. *J. Colloid Interface Sci.* **1971**, *35*, 78–84. [CrossRef]
19. Hofmann, C.; Schonhoff, M. Do additives shift the LCST of poly(*N*-isopropyl acrylamide) by solvent quality changes or by direct interactions? *Colloid Polym. Sci.* **2009**, *287*, 1369–1376. [CrossRef]
20. Hofmann, C.; Schonhoff, M. Dynamics and distribution of aromatic model drugs in the phase transition of thermoreversible poly(*N*-isopropyl acrylamide) in solution. *Colloid Polym. Sci.* **2012**, *290*, 689–698. [CrossRef]
21. Costa, R.; Freitas, R. Phase behavior of poly(*N*-isopropyl acrylamide) in binary aqueous solutions. *Polymer* **2002**, *43*, 5879–5885. [CrossRef]
22. Maeda, Y.; Yamamoto, H.; Ikeda, I. Micro-Raman spectroscopic investigation on the phase separation of poly(vinyl methyl ether)/alcohol/water ternary mixtures. *Langmuir* **2004**, *20*, 7339–7341. [CrossRef] [PubMed]
23. Spěváček, J.; Hanyková, L. NMR study on polymer-solvent interactions during temperature-induced phase separation in aqueous polymer solutions. *Macromol. Symp.* **2007**, *251*, 72–80. [CrossRef]
24. Spěváček, J.; Hanyková, L. ^{1}H NMR relaxation study of polymer-solvent interactions during thermotropic phase transition in aqueous solutions. *Macromol. Symp.* **2003**, *203*, 229–238. [CrossRef]
25. Crowder, G.A. 3,3-Dimethyl-2-butanone: Infrared and Raman spectra, normal coordinate calculations, and calculated structure. *Spectrosc. Lett.* **1997**, *30*, 1353–1367. [CrossRef]
26. Li, Z.; Singh, S. FTIR and ab-initio investigations of the MTBE—Water complex. *J. Phys. Chem. A* **2008**, *112*, 8593–8599. [CrossRef] [PubMed]
27. Maeda, H.J. Interaction of water with poly(vinyl methyl ether). *J. Polym. Sci.* **1994**, *32*, 91–97. [CrossRef]
28. Schafer-Soenen, H.; Moerkerke, R.; Berghmans, H.; Koningsveld, R.; Dušek, K.; Šolc, K. Zero and off-zero critical concentrations in systems containing polydisperse polymers with very high molar masses. 2. The system water—Poly(vinyl methyl ether). *Macromolecules* **1997**, *30*, 410–416. [CrossRef]
29. Tiktopulo, E.I.; Uversky, V.N.; Lushchik, V.B.; Klenin, S.I.; Bychkova, V.E.; Ptitsyn, O.B. "Domain" coil-globule transition in homopolymers. *Macromolecules* **1995**, *28*, 7519–7524. [CrossRef]
30. Tiktopulo, E.I.; Bychkova, V.E.; Ricka, J.; Ptitsyn, O.B. Cooperativity of the coil-globule transition in a homopolymer: Microcalorimetric study of poly(*N*-isopropylacrylamide). *Macromolecules* **1994**, *27*, 2879–2882. [CrossRef]
31. Hanyková, L.; Radecki, M. NMR and thermodynamic study of phase transition in aqueous solutions of thermoresponsive amphiphilic polymer. *Chem. Lett.* **2012**, *41*, 1044–1046. [CrossRef]

Publication 9

S. Petrova, E. Jäger, **R. Konefał**, A. Jäger, C. de Garcia Venturini, J. Spěváček, E. Pavlova, P. Štěpánek

Novel poly(ethylene oxide monomethyl ether)-b-poly(ε-caprolactone) diblock copolymers containing a pH-acid labile ketal group as a block linkage.

Polymer Chemistry, **2014**, 5, 3884-3893.

Polymer Chemistry

PAPER

View Article Online
View Journal | View Issue

Cite this: *Polym. Chem.*, 2014, **5**, 3884

Novel poly(ethylene oxide monomethyl ether)-*b*-poly(ε-caprolactone) diblock copolymers containing a pH-acid labile ketal group as a block linkage†

S. Petrova,* E. Jäger, R. Konefał, A. Jäger, C. G. Venturini, J. Spěváček, E. Pavlova and P. Štěpánek

Received 24th January 2014
Accepted 13th February 2014

DOI: 10.1039/c4py00114a

www.rsc.org/polymers

A new biocompatible and biodegradable diblock copolymer that contains a specific acid-labile degradable linkage (acyclic ketal group) between the hydrophobic poly(ε-caprolactone) (PCL) and the hydrophilic poly(ethylene oxide monomethyl ether) (MPEO) blocks is described herein. A multi-step synthetic method that combines carbodiimide chemistry, a "click" reaction and ring-opening polymerization (ROP) was employed to successfully produce a series of MPEO-*b*-PCL diblock copolymers (herein referred to as $MPEO_{44}$-*b*-PCL_{17} and $MPEO_{44}$-*b*-PCL_{44}). 2-{[2-(2-Azidoethoxy)propan-2-yl]}ethan-1-ol was obtained as a linker between the two blocks through a three-step synthetic approach. Furthermore, a newly developed α-methoxy-ω-hydroxy-poly(ethylene oxide) that contains an acid-labile ketal linkage was designed as a macroinitiator *via* a "click" reaction for the sequential controlled ring-opening polymerization of ε-CL. The newly obtained compounds (precursors, macromer, macroinitiator and final diblock copolymers) were assessed by ^{1}H NMR, ^{13}C NMR and FT-IR spectroscopy and SEC analysis, which are described in this manuscript. Upon dissolution in a mild organic solvent, the $MPEO_{44}$-*b*-PCL_{17} block copolymer self-assembled in water–PBS into regular, spherical, stable nanoparticles (NPs). Furthermore, the presence of the acid-labile ketal linker enabled the disassembly of these nanoparticles in a buffer that simulated acidic cytosolic or endosomal conditions in tumour cells as evaluated by dynamic light scattering (DLS), nanoparticle tracking analysis (NTA) and transmission electron microscopy (TEM) images. This disassembly led to hydrolysis profiles that resulted in neutral degradation products.

Introduction

Currently, the priorities for the development of polymer therapeutics are strictly associated with the production of biocompatible, degradable polymeric nanostructures. The properties of these materials are defined by their structures, compositions, dimensions and functionalities. Over the past several decades, amphiphilic block copolymers (hydrophilic and hydrophobic blocks) have been extensively studied.[1–4] These copolymers are of great interest because of their ability to self-assemble in aqueous media to generate various structure types, shapes and sizes, ranging from nano- to micrometres.[5–7] It is well known that amphiphilic block copolymers are able to form nanosized spherical micelles with a core–shell architecture. The applications of these systems are associated with their several unique properties, such as the possibility of controlling the release of drugs,[8–10] matrices for three-dimensional tissue regeneration,[11–13] diagnostic agents[14,15] and DNA delivery.[16,17] In particular, self-assembled core–shell NPs from amphiphilic block copolymers have attracted considerable attention in the development of drug-delivery systems. Their hydrophobic core is used as a reservoir for lipophilic agents (drugs), whereas their hydrophilic corona creates a highly water-bound barrier that ensures colloidal stability, a reduction in the rate of opsonin adhesion and clearance of the particles from the body.[18] Another relevant consideration for the development of core–shell NPs for drug-release applications is the carriers' ability to release their cargo drug in a controlled manner upon arrival at the target site.[19] For these reasons, many researchers are paying special attention to the design of environmentally triggered polymeric nanoparticles that are capable of releasing the original molecules in their active forms under various chemical and physical stimuli, such as pH, light, temperature, enzyme concentration or redox gradients.[20–22] pH-sensitive degradable polymers have played an integral role in the advancement of drug-delivery technology, such as the delivery of protein-based vaccines and nucleic acids, in the treatment of acute

Institute of Macromolecular Chemistry v.v.i., Academy of Sciences of the Czech Republic, Heyrovsky Sq. 2, 162 06 Prague 6, Czech Republic. E-mail: petrova@imc.cas.cz; Tel: +420 296 809 296

† Electronic supplementary information (ESI) available. See DOI: 10.1039/c4py00114a

inflammatory diseases and especially for tumour targeting.[23,24] Considering the tumour-targeting field of drug delivery, the hydrophobic guest drug molecules must be retained in the inner particle core while in the bloodstream and then be rapidly released at the specific tumour sites.[25] A significant amount of research has demonstrated the association between acidic pH conditions and cancer, as the extracellular pH in most solid tumour sites is more acidic (ranging from pH 5.7 to 7.2) compared to that of normal tissues (buffered at pH 7.4).[26,27] Because of these pH differences, several pH-degradable polymers that contain different acid-labile linkers suitable for triggering drug release, such as ester,[28] hydrazone,[29] carboxydimethylmaleic,[30] orthoester,[31] imine,[32] β-thiopropionate,[33] vinylether,[34] and phosphoramidate,[35] have been widely studied. In particular, acid-degradable (co)polymers and NPs that contain multiple reactive functionalities, such as ketal/acetal labile linkages along the polymer backbone or as pendant groups, are of considerable interest. Ketals and acetals have been demonstrated to be more sensitive to the acidic environment of tumours and phagosomes than esters and hydrazones.[35] Moreover, these linkers are also more stable under physiological conditions (at pH $\sim$ 7.4) than the other aforementioned linkages.[36] In addition, pH-responsive systems containing acid-labile bonds that are degradable under mild acidic conditions, such as those of tumour sites, lead to tuneable hydrolysis profiles, which ultimately result in neutral degradation products that can be easily excreted, thereby avoiding accumulation and inflammatory responses.[37] Although novel and efficient pH-sensitive carriers that contain ketal/acetal linkages have great potential for drug delivery, synthetic challenges have limited the applications of these systems.

Herein, we report the synthesis of a novel class of well-defined biocompatible and biodegradable acid-labile poly(ethylene oxide monomethyl ether) (MPEO)-*b*-poly(ε-caprolactone) (PCL) diblock copolymers that contain ketal groups as block linkers. The PEO and PCL polymers were selected as building blocks because of their special interest for environmental, biomedical and pharmaceutical applications.[38–41] PCL is a aliphatic hydrophobic polyester with great potential as a biomaterial due to its unique combination of biodegradability and biocompatibility,[42] and PEO is a hydrophilic and very flexible biocompatible polymer that is non-toxic and easily eliminated from the body.[43] For the synthesis, an efficient multi-step pathway was employed, which resulted in new block copolymers with reasonable yields. Different synthetic routes (*i.e.*, carbodiimide chemistry, "click" reaction and ring-opening polymerization) were applied for the preparation of low-molecular-weight compounds as precursors for constructing the acid-labile ketal group of the MPEO-*b*-PCL diblock copolymers. In addition, the amphiphilic diblock copolymers self-assembled into regular spherical NPs in aqueous solution and under buffer-simulated physiological conditions (pH $\sim$ 7.4). These nanoparticles were found to be degraded into non-toxic compounds under buffer-simulated acidic cytosolic or endosomal conditions in tumour cells (pH $\sim$ 5.0), revealing their potential as systems that could find applications, *e.g.*, as acid-labile drug-delivery systems.

Experimental

Materials

Ethylene glycol (99%, Sigma-Aldrich), trimethyl orthoacetate (99%, Aldrich), *p*-toluenesulphonic acid monohydrate (98.5%, Fluka), 2-chloroethanol (99%, Aldrich), sodium azide (99%, Fluka), tetrabutylammonium bromide (TBABr, 99%, Fluka), pyridinium *p*-toluenesulphonate (PPTS, 99%, Fluka), 5-hexynoic acid (97%, Aldrich), 4-dimethylaminopyridine (DMAP, 99% Sigma-Aldrich), *N*,*N*′-dicyclohexylcarbodiimide (DCC, 99%, Fluka), CuBr (98%, Fluka), 2-methoxypropene (98%, Aldrich) and molecular sieves (5 Å, Sigma-Aldrich) were used without further purification. ε-Caprolactone (ε-CL, 99%, Sigma-Aldrich) was dried over CaH_2 with continuous stirring at room temperature for 48 h and distilled under reduced pressure before use. Tin(II) bis(2-ethylhexanoate) ($Sn(Oct)_2$, 95%, Aldrich, 0.06 M solution in toluene) and sodium hydroxide (NaOH) were used as received. MPEO ($M_n \sim 1800$ g mol^{-1}) was purchased from Fluka. Triethylamine (Et_3N) (≥99.5%, Sigma-Aldrich) was dried over CaH_2 and distilled under reduced pressure. CH_2Cl_2 (Sigma-Aldrich) was dried by refluxing over a benzophenone–sodium complex and distilled under an argon atmosphere. Toluene (99%, Labscan) and tetrahydrofuran (THF, 99%, Fluka) were refluxed for 24 h over CaH_2 under a dry argon atmosphere and then distilled. All other chemicals were used as received.

Synthesis of compounds 1–5

Compounds **1**,[44,45] **2**,[46] **3**,[45] **4**,[45] and **5**[47] were synthesised according to previous procedures, which are described in detail in the ESI.†

Synthesis of α-methoxy-ω-hydroxy-poly(ethylene oxide) containing a ketal group (compound 6)

The coupling of 2-{[2-(2-azidoethoxy)propan-2-yl]ethan-1-ol (**4**) (0.18 g, 7.78×10^{-4} mol) with α-methoxy-ω-alkyne-poly(ethylene oxide) (**5**) (1.4 g, 7.09×10^{-4} mol) bearing the alkyne was performed in a glass reactor containing dry THF (8 mL). CuI (0.015 g, 7.87×10^{-5} mol) and triethylamine (0.01 mL, 7.91×10^{-5} mol) were added to the polymer solution and allowed to react at 35 °C for 4 h. Subsequently, the reaction mixture was exposed to air, diluted with THF, and passed through a neutral alumina column to remove the copper catalysts. The macroinitiator was recovered by two precipitations in cooled diethyl ether. The product (**6**) was recovered as a white solid. Yield: 1.30 g, 93%.

Synthesis of the MPEO-*b*-PCL diblock copolymer containing a ketal group (compound 7)

In a typical synthesis, 0.127 g (5.7×10^{-5} mol) of α-methoxy-ω-hydroxy-poly(ethylene oxide) (**6**) containing a ketal group was introduced into a 50 mL glass reactor equipped with a magnetic stir bar. The macroinitiator was dissolved in dry toluene and dried three times by azeotropic distillation. A certain amount of freshly distilled ε-CL was added, and after heating, 0.1 mL of 0.06 M $Sn(Oct)_2$ was rapidly injected through a septum. The

polymerization was carried out for 48 h at 110 °C. The reactor was cooled to room temperature, and the reaction mixture was dissolved in toluene. The copolymer (**7**) was collected by precipitation in cooled diethyl ether, filtered and dried overnight under vacuum at 40 °C.

Characterisation techniques

^{1}H NMR and ^{13}C NMR spectra (300 and 75 MHz, respectively) were recorded using a Bruker Avance DPX 300 NMR spectrometer with $CDCl_3$ as the solvent at 25 °C. The chemical shifts are relative to TMS using hexamethyldisiloxane (HMDSO, $\delta = 0.05$ and 2.0 ppm from TMS in ^{1}H NMR and ^{13}C NMR spectra) as the internal standard. The M_n values of compounds **5–7** were determined by ^{1}H NMR spectroscopy. For compound **5**, the M_n was calculated according to eqn (1):

$$M_{n(NMR)} = [(I_b/4)/(I_d/2)] \times 44 + 31 + 95 \quad (1)$$

where I_b and I_d represent the integral values of the peaks at $\delta =$ 3.63 ppm (–CH_2–CH_2–O– of the PEO repeating unit) and at $\delta =$ 4.22 ppm (–CH_2–CH_2–O–C(O)), respectively. The values 31 and 95 represent the molecular weights of the two functional groups at the chain ends CH_3–O– and –C(O)–$C(CH_2)_3$–C≡CH, respectively. The M_n of the macroinitiator (**6**) was calculated according to eqn (2):

$$M_{n(NMR)} = [(I_b/4)/(I_g/2)] \times 44 + 31 + 284 \quad (2)$$

where I_b and I_g represent the integral values of the peaks at $\delta =$ 3.63 ppm (–CH_2–CH_2–O– of the PEO repeating unit) and at $\delta =$ 2.76 ppm (–O–C(O)–CH_2–CH_2–CH_2–), respectively. The values 31 and 284 are the molecular weights of the two functional groups at the chain ends CH_3–O– and –O–C(O)–$(CH_2)_3$–triazole ring–$(CH_2)_2$–$OC(CH_3)_2$–O–$(CH_2)_2$–OH, respectively. The M_n of the MPEO-*b*-PCL diblock copolymers (**7**) was determined by ^{1}H NMR using eqn (3)

$$M_{n(NMR)}\,(\text{MPEO-}b\text{-PCL}) = [(I_r/2)/(I_b/4)] \times DP_{MPEO} \times 114 + M_{n(NMR)}\,(\text{macroinitiator}) \quad (3)$$

where I_r and I_b represent the integral values of the methylene protons of PCL (r) (Fig. 2, top) and of the methylene protons of PEO (b). The value 114 is the molecular weight of the ε-CL unit, DP_{MPEO} is the degree of polymerization of the macroinitiator, and $M_{n(NMR)}$ is the number-average molecular weight of the macroinitiator. Infrared spectra were obtained using a PerkinElmer Spectrum 100 equipped with a universal ATR (attenuated total reflectance) accessory with a diamond crystal. In all cases, the resolution was 4 cm^{-1} and the spectra were averaged over 16 scans. The samples were prepared in the form of KBr pellets. The number-average molecular weights (M_n),

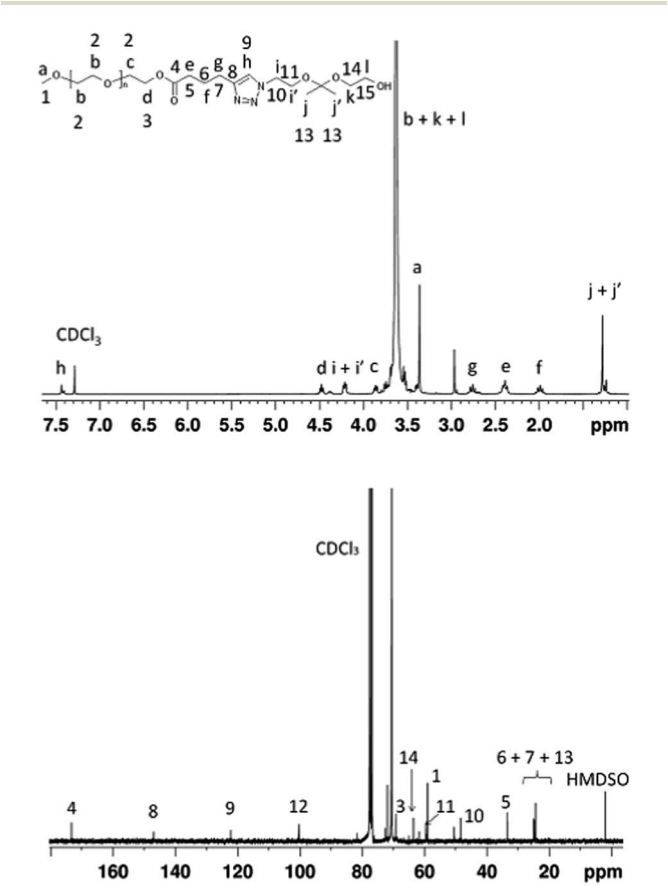

Fig. 1 ^{1}H (top) and ^{13}C (bottom) NMR spectra of the α-methoxy-ω-hydroxy-PEO containing a ketal group in $CDCl_3$.

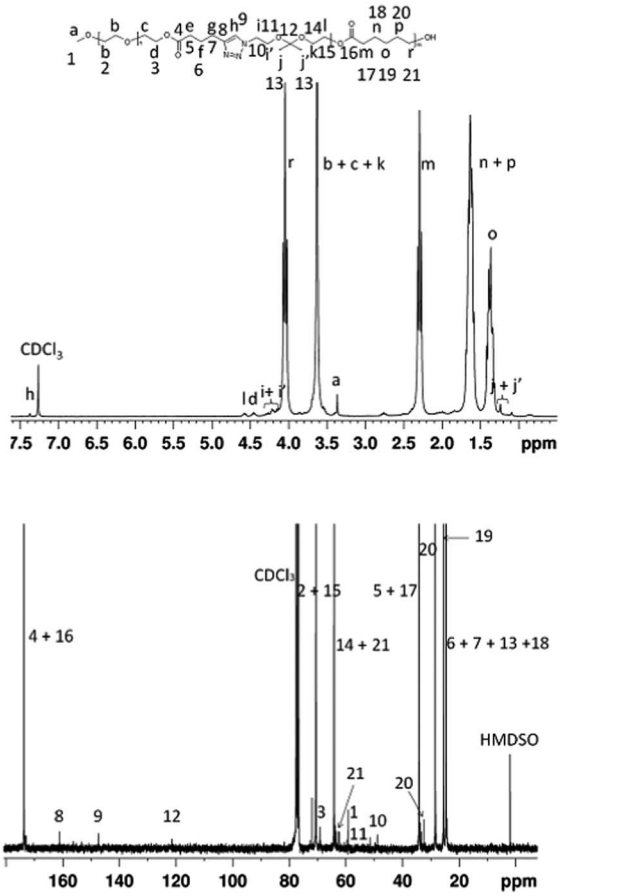

Fig. 2 ^{1}H (top) and ^{13}C (bottom) NMR spectra of the MPEO-*b*-PCL diblock copolymer in $CDCl_3$.

weight-average molecular weights (M_w), and polydispersity indices (M_w/M_n) of the prepared macromer, macroinitiator and block copolymers were determined by size exclusion chromatography (SEC). The analyses were performed using an SDS 150 pump (Watrex, Czech Republic) equipped with refractometric (Shodex RI-101, Japan) and UV (Watrex UVD 250, Czech Republic) detectors. The separation system consisted of two PLgel MIXED-C columns (Polymer Laboratories) and was calibrated with polystyrene standards (PSS, Germany). THF was used as the mobile phase at a flow rate of 1.0 mL min^{-1} at 25 °C. Data collection and processing were performed using the Clarity software package.

Nanoparticle preparation

NPs were prepared using the nanoprecipitation protocol. A preheated (40 °C) acetone solution (5 mL) containing the MPEO-*b*-PCL block copolymer (10 mg) was added drop-wise (EW-74900-00, Cole-Parmer®) into a pre-heated (40 °C) Milli-Q® water solution (10 mL, pH ~ 7.4). The pre-formed NPs were allowed to self-assemble, and then the solution was transferred to a dialysis tube (MWCO = 3500) and dialysed against 5 L of water (pH ~ 7.4) for 24 hours. The final concentration was adjusted to 1 mg mL^{-1} using phosphate-buffered saline (PBS) at pH ~ 7.4.

Nanoparticle characterisation

The NPs were characterised by DLS and NTA. The DLS measurements were performed using an ALV CGE laser goniometer consisting of a 22 mW HeNe linearly polarised laser operating at a wavelength (λ = 632.8 nm), an ALV 6010 correlator, and a pair of avalanche photodiodes operating in the pseudo cross-correlation mode. The samples were filtered through 0.45 μm PVDF membranes (Millex-HV, Millipore®) loaded into 10 mm diameter glass cells and maintained at 25 or 37 ± 1 °C. The data were collected using the ALV Correlator Control software, and the counting time was 30 s. To avoid multiple light scattering, the samples were diluted 100-fold before the measurements.[48] The measured intensity correlation functions $g_2(t)$ were analysed using the algorithm REPES (incorporated in the GENDIST program),[49] resulting in the distributions of relaxation times shown in an equal area representation as $\tau A(\tau)$. The mean relaxation time or relaxation frequency ($\Gamma = \tau^{-1}$) is related to the diffusion coefficient (D) of the nanoparticles as $D = \frac{\Gamma}{q^2}$, where $q = \frac{4\pi n \sin(\theta/2)}{\lambda}$ is the scattering vector with n representing the refractive index of the solvent and θ representing the scattering angle. The hydrodynamic radius (R_H) or the distribution of R_H was calculated using the well-known Stokes–Einstein relation:

$$R_H = \frac{k_B T}{6\pi\eta D} \quad (4)$$

where k_B is the Boltzmann constant, T is the absolute temperature, and η is the viscosity of the solvent. The NTA analyses were performed using the NanoSight LM10 & NTA 2.0 Analytical Software (NanoSight, Amesbury, England). The samples were diluted (4000×, Milli-Q® water or PBS, pH ~ 7.4 and 5.0) and injected into the sample chamber with a syringe (25 °C). The NTA apparatus combines a light scattering microscope with a laser diode (635 nm) camera charge-coupled device, which allows viewing and recording of the NPs in solution. Each video clip was captured over 60 s. The NTA software is able to identify and track individual NPs (10–1000 nm), which are in Brownian motion, and relate their particle movement to a sphere with an equivalent R_H, as calculated using the Stokes–Einstein relation (eqn (4)). The size distribution was expressed by the span value, which was calculated using eqn (5).

$$\text{Span} = \frac{d_{(0.9)} - d_{(0.1)}}{d_{(0.5)}} \quad (5)$$

where $d_{(0.9)}$, $d_{(0.1)}$ and $d_{(0.5)}$ are the diameters at 90%, 10% and 50% cumulative volumes, respectively.

Transmission electron microscopy (TEM)

TEM observations were performed on a Tecnai G2 Spirit Twin at 120 kV (FEI, Czech Republic). The NPs were diluted 100-fold, and 2 μL of the aqueous solution was dropped onto a copper TEM grid (300 mesh) coated with a thin, electron-transparent carbon film. The solution was removed by touching the bottom of the grid with filter paper. This rapid removal of the solution was performed after 1 min to minimise oversaturation during the drying process; this step was found to be necessary to preserve the structure of the NPs. The NPs were negatively stained with uranyl acetate (2 μL of a 1 wt% solution was dropped onto the dried NPs and removed after 15 s in the same manner described above). The sample was left to completely dry at ambient temperature and then observed *via* a TEM using bright-field imaging. Under these conditions, the micrographs displayed a negatively stained background with bright spots, which correspond to the investigated NPs.

Results and discussion

A new synthetic pathway was developed to obtain well-defined amphiphilic copolymers that contain acid-labile, degradable ketal linkages as block linkers that are highly sensitive to pH under physiological conditions. The synthesis of the biocompatible, biodegradable, acid-labile MPEO-*b*-PCL was designed using, for the first time, the combination of a "click" reaction with DCC chemistry and ROP (Scheme 1). This strategy provides new insights into the combination of new "click" chemistry reactions with the classic synthetic pathways in polymer chemistry.

Synthesis of compounds 1 to 5

The compounds ethylene glycol monoacetate (**1**)[44,45] (Fig. S1†), 2-azidoethanol (**2**)[46] (Fig. S2†), 2-{[2-(2-azidoethoxy)propan-2-yl]oxy}ethyl acetate (**3**)[45] (Fig. S3†), 2-{[2-(2-azidoethoxy)propan-2-yl]ethan-1-ol (**4**)[45] (Fig. S4†) and α-methoxy-ω-alkyne-poly(ethylene oxide) (**5**)[47] (Fig. S5†) were synthesised according to previous reports and were characterised by ^{1}H and ^{13}C NMR, FT-IR spectroscopy and SEC analysis (**5**), which are described in detail in the ESI.†

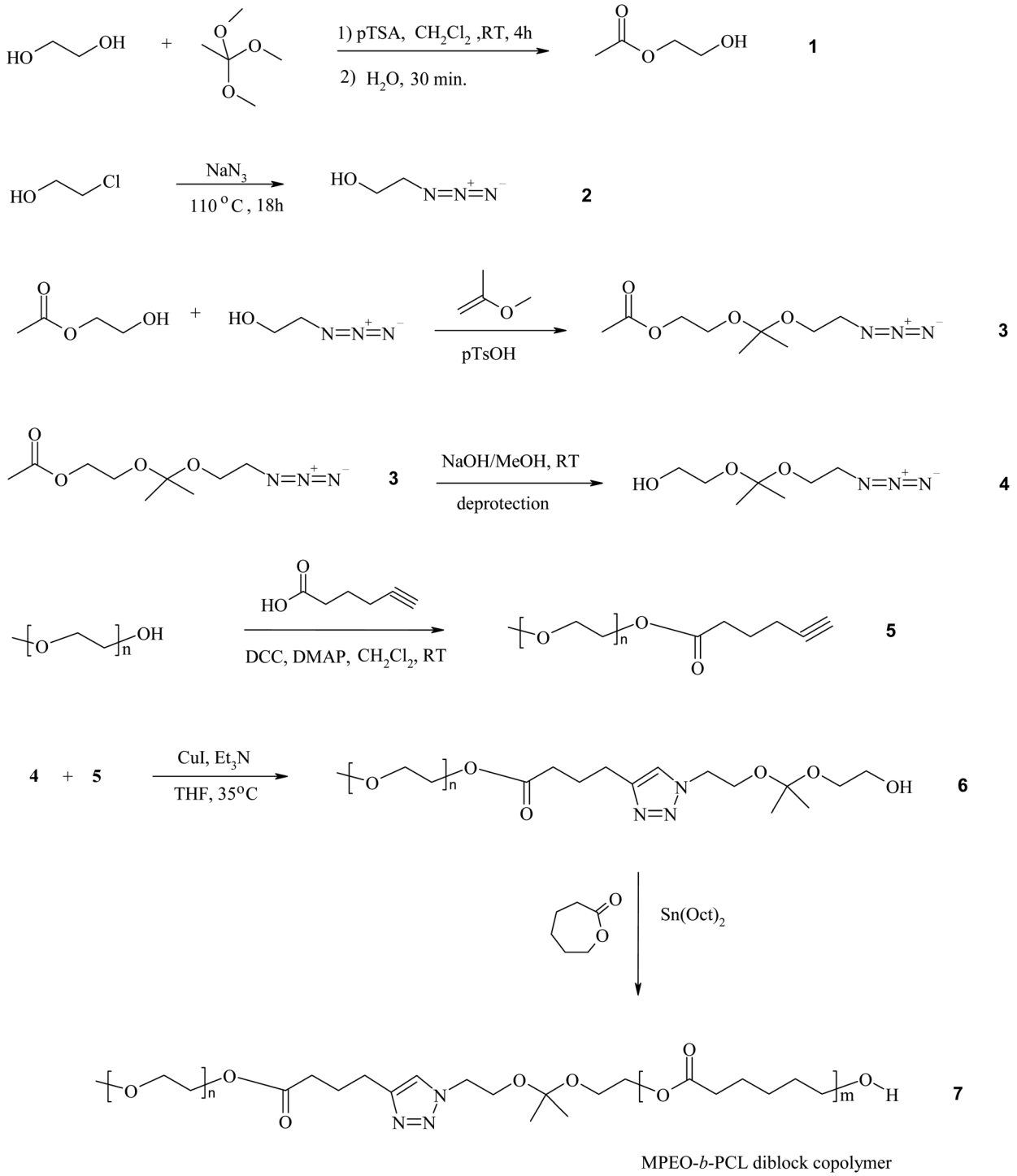

Scheme 1 Synthetic route for the preparation of MPEO-*b*-PCL diblock copolymers.

Synthesis of α-methoxy-ω-hydroxy-poly(ethylene oxide) containing a ketal group (compound 6)

The α-methoxy-ω-hydroxy-poly(ethylene oxide) containing a ketal group (**6**) was prepared as a macroinitiator through a "click" reaction between α-methoxy-ω-alkyne-PEO (**5**) and 2-{[2-(2-azidoethoxy)propan-2-yl]ethan-1-ol (**4**) (see Scheme 1). The azide–alkyne Huisgen cycloaddition was performed in the presence of CuI and Et_3N. After purification, the obtained macroinitiator was characterised by ^1H and ^{13}C NMR, FT-IR spectroscopy and SEC analysis. The ^1H NMR spectrum (Fig. 1, top) confirms that the "click" reaction was complete due to the disappearance of the characteristic signal for the alkyne end-group at $\delta = 1.96$ ppm (h) (Fig. S5†) and the appearance of a new proton signal from the triazole ring at $\delta = 7.40$ ppm (h) in Fig. 1 (top). The signal observed at $\delta = 1.28$ ppm (j + j′) is assigned to

Table 1 Macromolecular characteristics of functional MPEO

MPEO samples	Conversion[a] (%)	M_n[b] (NMR)	M_n[c] (SEC)	M_w/M_n[d] (SEC)
MPEO	—	1800	1464	1.23
Macromer	87	2200	1710	1.24
Macroinitiator	82	2320	1760	1.31

[a] Conversion was calculated by ^{1}H NMR spectroscopy (Fig. S5† and 1, top). [b] M_n was calculated by ^{1}H NMR spectroscopy according to eqn (1) and (2). [c] M_n was determined by SEC calibrated with PS standards. [d] M_w/M_n was determined by SEC calibrated with PS standards.

the six protons of the dimethyl ketal group –OC(CH$_3$)$_2$–O– and demonstrates that the ketal group remains unaffected during the azide–alkyne Huisgen cycloaddition. Furthermore, a singlet signal attributed to CH$_3$–O– was observed at $\delta = 3.39$ ppm (a), and other signals were observed at $\delta = 2.76$ (g), $\delta = 2.39$ (e) and $\delta = 1.96$ ppm (f). Additional signals located in the vicinity of the EO ($\delta = 3.63$ ppm) were also identified: $\delta = 2.85$ ppm (c) is a typical signal of –CH$_2$–CH$_2$–O–C(O), $\delta = 4.21$ ppm (i + i′) is attributed to –N–CH$_2$–CH$_2$–O–, and $\delta = 4.47$ ppm (d) is characteristic of –CH$_2$–CH$_2$–O–C(O). The conversion of the "click" reaction was calculated from the relative intensities of the signals characteristic of both –O–C(CH$_3$)$_2$–O– (j + j′, $\delta = 1.28$ ppm) and –CH$_2$–O–C(O) (d, $\delta = 4.47$ ppm) groups in the ^{1}H NMR spectrum, which gives a quantitative value of ~82% (Table 1).

The ^{13}C NMR spectrum (Fig. 1, bottom) of the α-methoxy-ω-hydroxy-PEO containing a ketal group is further evidence for the successful achievement of the "click" cycloaddition. Signals corresponding to the dimethyl ketal group at $\delta = 24.32$ ppm (**13**) and from the fully substituted carbon –OC(CH$_3$)$_2$–O– at 100.33 ppm (**12**) were clearly observed. Other significant signals were observed at high chemical shifts at $\delta = 122.22$ (**9**) and $\delta = 146.97$ ppm (**8**), which correspond to the carbons from the triazole ring –CH$_2$–CH═CH–N–, and at $\delta = 173.29$ ppm (**4**), which is attributed to the carbonyl carbon from the –CH$_2$–O–C(O)–(CH$_2$)$_3$– group.

Moreover, the effectiveness of the "click" cycloaddition reaction to afford 1,2,3-triazole as a product was confirmed by FT-IR spectroscopy (Fig. S7b†). Complete disappearance of the peak corresponding to the azide group at 2102 cm^{-1} was observed, which indicates the completion of the reaction. The identification of C–N stretching frequencies is generally a very difficult task because the mixing of bands is possible in this region.[50] The absorption bands observed at 1553, 1469 and 1455 cm^{-1} are due to stretching vibrations between carbon and nitrogen atoms. The characteristic absorption band of C–N observed at 1361 cm^{-1} confirms the formation of the triazole ring. Absorption bands for the carbon–hydrogen groups were also observed, thus resulting in C–H stretching absorption in the 2992 to 2700 cm^{-1} region of the IR spectrum. Moreover, in the spectrum of compound **6**, a weak –C═O stretching band at 1735 cm^{-1} was observed, indicating the presence of a carbonyl ester group. Furthermore, distinctive bands from the ether groups of the EO repeating units at 1107 cm^{-1} were also observed (Fig. S7b†). The SEC chromatogram from the corresponding macroinitiator obtained after the cycloaddition reaction shows a monomodal distribution, as indicated by the overlap of the SEC traces (dotted line in Fig. S8†). The molecular weight of the resulting product remains unchanged, except for a slight increase in polydispersity. Nevertheless, after the reaction, the SEC chromatogram from α-methoxy-ω-hydroxy-MPEO containing a ketal group (**6**) clearly demonstrates the absence of side products with higher M_n values that could be formed as a result of alkyne homocoupling.

Synthesis of the MPEO-*b*-PCL diblock copolymer containing a ketal group (compound 7)

The MPEO-*b*-PCL diblock copolymers (**7**) were successfully synthesised by ROP from the ε-CL monomer. The previously synthesised α-methoxy-ω-hydroxy-poly(ethylene oxide) containing a ketal group (**6**) was used as a macroinitiator in the presence of Sn(Oct)$_2$ as a catalyst. The lengths of the PCL blocks were controlled by regulating the ε-CL/macroinitiator molar ratio. After purification, the MPEO-*b*-PCL diblock copolymers were characterised by ^{1}H and ^{13}C NMR, FT-IR spectroscopy and SEC analysis. The structure and composition of the obtained diblock copolymers were also confirmed by FT-IR spectroscopy. The ^{1}H NMR spectrum of the diblock copolymer (Fig. 2, top) shows characteristic signals for protons belonging to ε-CL and EO repeating units. The signals for the methylene protons of the ε-CL units were detected at $\delta = 4.06$ ppm (r) –CH$_2$–OC(O)–, $\delta = 2.29$ ppm (m) –C(O)CH$_2$–, $\delta = 1.58$ ppm (n + p) –C(O)–CH$_2$–CH$_2$–CH$_2$–CH$_2$– and $\delta = 1.34$ ppm (o) –C(O)–CH$_2$–CH$_2$–CH$_2$–CH$_2$–. The methylene protons of the EO repeating units were observed at $\delta = 3.63$ ppm (b), whereas the singlet signal is attributed to the CH$_3$–O– appeared at $\delta = 3.39$ ppm (a). The signal observed at $\delta = 1.31$ ppm (j + j′) attributed to the six protons of the dimethyl ketal group –OC(CH$_3$)$_2$–O– and the resonance signal at $\delta = 7.37$ ppm (h) assigned to the triazole ring demonstrate that the ketal group and the triazole ring remain unaffected following the ROP. Furthermore, there were signals in the spectrum at $\delta = 4.57$ ppm (l), attributed to methylene protons from the –CH$_2$–O–C(O)– fragment; at $\delta = 4.45$ ppm (d), assigned to the last monomer unit of PEO; and at $\delta = 4.21$ ppm (i + i′), attributed to the methylene protons from the fragment between the triazole ring and the ketal group –N–CH$_2$–CH$_2$–O–C(CH$_3$)$_2$–O–. Low intensity signals at $\delta = 2.76$ (g), 2.50 (e) and 2.00 ppm (f) for the protons from the –OC(O)–CH$_2$–CH$_2$–CH$_2$– triazole ring were also present. The experimental degree of ε-CL polymerization agrees well with the theoretical values (Table 2). The ^{13}C NMR spectrum (Fig. 2, bottom) of the diblock copolymers shows

Table 2 Macromolecular characteristics of MPEO-*b*-PCL diblock copolymers

Sample	M_n[a] (NMR)	M_n[b] (NMR)	M_n[c] (SEC)	M_w/M_n[d] (SEC)
MPEO$_{44}$-*b*-PCL$_{17}$	4000	5400	3130	1.45
MPEO$_{44}$-*b*-PCL$_{44}$	7000	6830	7570	1.43

[a] M_n was calculated by the monomer conversion; $M_n = [M]_0/[I]_0 \times 114 + M_n$ α-methoxy-ω-hydroxy-MPEO containing a ketal group (**6**). [b] M_n was calculated by ^{1}H NMR spectroscopy according to eqn (2). [c] M_n is relative to PS standards. [d] M_w/M_n is relative to PS standards.

carbon signals that are consistent with the desired structure. The most important carbon signals are highlighted, *i.e.*, the signals that correspond to carbons from the dimethyl ketal group at $\delta =$ 24.39 ppm (**13**) and the quaternary carbon from the same group –OC$(CH_3)_2$–O– at $\delta = 121.50$ ppm (**12**). Other significant signals were observed at higher frequencies and slightly shifted in comparison with the ^{13}C NMR spectrum from α-methoxy-ω-hydroxy-PEO containing a ketal (**6**) (Fig. 1, bottom). These signals appear at $\delta = 147.44$ (**9**) and $\delta = 161.1$ ppm (**8**) for the triazole ring –CH_2–CH=CH–N– and at $\delta = 173.58$ ppm (**4** + **16**) for the carbon from the carbonyl group –CH_2–O–C(O)–$(CH_2)_3$– next to PEO and for the carbon from carbonyl group in PCL. All of the other remaining signals are attributed to the carbon atoms from the diblock copolymer structure.

Similar bands for the characteristic peaks were found for all samples in the FT-IR spectra (Fig. S7c†).

The molecular weights and polydispersity indices of the synthesised MPEO-*b*-PCL diblock copolymers were determined by SEC. The analysis clearly shows that the obtained curves are monomodal, confirming that the ketal group was not degraded during the ROP of ε-CL. A slight asymmetry is observed at longer elution times in the SEC curve (regular line in Fig. S9†), which strongly suggests that some unreacted MPEO is present. The molecular characteristics of the diblock copolymers are listed in Table 2.

Polymer nanoparticles (NPs)

As a proof-of-concept, polymer NPs were prepared from the block copolymers, and their behaviours under different simulated physiological conditions were evaluated in detail by DLS and NTA. The visual appearance of the colloidal particles immediately after the injection of the MPEO-*b*-PCL block copolymer solutions into water was size-dependent and did not change after the dilution with PBS (pH ~ 7.4) (data not shown). For $MPEO_{44}$-*b*-PCL_{17}, the resulting colloidal solution was fully transparent, whereas the solution was slightly opalescent for the $MPEO_{44}$-*b*-PCL_{44} block copolymer. This result is a visual indication that the particles produced by the nanoprecipitation protocol using the $MPEO_{44}$-*b*-PCL_{44} block copolymer are larger than the particles produced using the $MPEO_{44}$-*b*-PCL_{17} block copolymer.[51] Fig. 3 shows the distribution of R_H for $MPEO_{44}$-*b*-PCL_{17} and $MPEO_{44}$-*b*-PCL_{44} block copolymer micelles after the dialysis process and dilution with PBS, as measured by DLS. The distribution of R_H for $MPEO_{44}$-*b*-PCL_{17} appears as only one single distribution of R_H relative to the presence of the polymer micelles in PBS solution with an average of $R_H = 32.1$ nm (Fig. 3, blue circles). Furthermore, the polydispersity of the $MPEO_{44}$-*b*-PCL_{17} micelles is very low as estimated through the cumulant analysis ($\mu/\Gamma^2 = 0.08 \pm 0.007$). However, for the $MPEO_{44}$-*b*-PCL_{44} block copolymer, a bimodal distribution of R_H was observed with average sizes of $R_H = 18.5$ nm and 99.5 nm, respectively (Fig. 3, red circles). Because the ketal linkage does not affect the physico-chemical properties of the MPEO-*b*-PCL diblock copolymers, the main factors that control the particle size and morphology in crystalline amphiphilic block copolymers that self-assemble in water are the preparation methodology and the polymer properties,

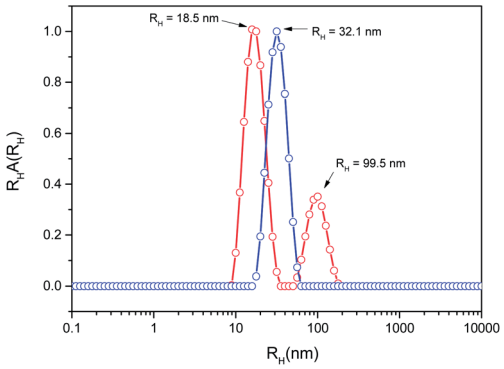

Fig. 3 Distributions of R_H for (○) $MPEO_{44}$-*b*-PCL_{17} and (○) $MPEO_{44}$-*b*-PCL_{44} NPs prepared by the nanoprecipitation protocol and diluted in PBS (pH ~ 7.4), both at a concentration of 1 mg mL^{-1}.

such as the molecular weight and the relative block length.[52] Although the study of the particles' morphology is far beyond the scope of the current investigation, some comparisons with the literature data could be performed. Similar particle sizes were found in a previous study for micelles of the PEO-*b*-PCL diblock copolymer with the same block length prepared through the dialysis method.[53,54] For the PEO_{44}-*b*-PCL_{44} diblock copolymer, mixtures between spherical and cylindrical micelles were found to coexist after dialysis when observed by TEM.[53] Spherical micelles with diameters in the range of 35 ± 5 nm were observed concomitantly with cylinders with a broad size range (greater than 100 nm) and polydispersity. Similar results were obtained by others authors[55] by using the same block and block lengths. The observed bimodal size distribution of R_H for the PEO_{44}-*b*-PCL_{44} block copolymer is related to a morphological mixture of at least two types of particles. According to the aforementioned literature, the most probable morphological structures are the mixture between spherical micelles with an average size of $D_H = 37.0$ nm and cylindrical and/or worm-like micelles with $D_H = 199$ nm. On the other hand, for PEO_{44}-*b*-PCL_{17} block copolymer assemblies, single monodisperse spherical micelles are obtained in most cases.

Note that thermodynamically stable polymeric NPs with hydrodynamic diameters ($2R_H = D_H$) within the range of 20 to 60 nm have been shown to be ideal for tumour drug-delivery applications.[56] They are within the size range that enables renal clearance to be avoided ($D_H > 10$ nm), thereby providing the NPs a potentially prolonged blood circulation time and, considering that their size is below the cut-off size of the leaky pathological vasculature ($D_H < 200$ nm), specific accumulation in solid tumour tissue due to the enhanced permeation and retention (EPR) effect.[57] Moreover, in addition to the role of the particle size in the EPR effect, another important aforementioned target in cancer therapy is the acidic cytosolic or endosomal conditions in tumour cells. Therefore, the sensibility of the polymer NPs containing the acid-labile ketal group was tested by DLS in acidic media (pH ~ 5) under physiological conditions (37 °C) using the $MPEO_{44}$-*b*-PCL_{17} block copolymer. $MPEO_{44}$-*b*-PCL_{17} block copolymer NPs were chosen for evaluating the ketal linkage sensibility *in vitro* because they presented a monodisperse single distribution of R_H with a

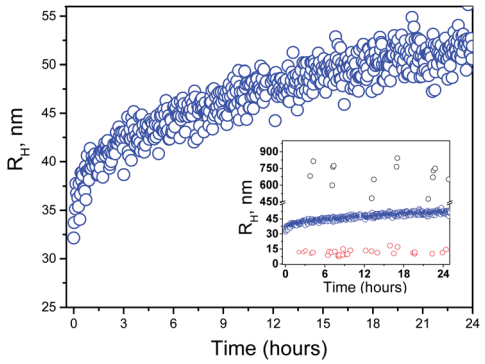

Fig. 4 Temporal dependence on the R_H distribution of $MPEO_{44}$-*b*-PCL_{17} NPs at pH ~ 5.0 and 37 °C. The inset illustrates the R_H distribution as a function of time for (○) aggregate NPs, (○) free PEO chains and (○) loose aggregates.

$D_H = 64.2$ nm, which is within the optimal size for drug-delivery applications. As shown in Fig. 3, the absence of a mixture between distinct morphological structures facilitates the experimental procedures and data analysis. Fig. 4 shows the distribution of R_H for the $MPEO_{44}$-*b*-PCL_{17} block copolymer NPs at pH ~ 5.0 and 37 °C as a function of time.

The results clearly show an increase in the average size of the micellar NPs from $R_H = 32.1$ nm to R_H 52.6 nm in 24 hours, which corresponds to an increase in D_H of approximately 41 nm. To obtain a thorough size distribution and to gain more information to accurately analyse the distribution of monodisperse and polydisperse samples than can be obtained through DLS,[58,59] the $MPEO_{44}$-*b*-PCL_{17} NPs were analysed using NTA at 25 °C. This technique is a powerful tool that complements DLS, and it is particularly valuable for the detection and accurate sizing of a broad range of population ratios. After 24 hours, the $MPEO_{44}$-*b*-PCL_{17} block copolymer NPs showed mean particle sizes of 96 nm and 118 nm under pH ~ 7.4 and pH ~ 5.0, respectively. Fig. 5 depicts the size distributions for the NPs, in which the value of $d(0.1)$ was 64 nm, $d(0.5)$ was 92 nm and $d(0.9)$ was 128 nm (pH ~ 7.4) and $d(0.1)$ was 61 nm, $d(0.5)$ was 92 nm and $d(0.9)$ was 209 nm (pH ~ 5.0). According to eqn (2), these cumulative volumes give span values of 0.69 and 1.57 for pH ~ 7.4 and pH ~ 5.0, respectively.

In addition, it is possible to verify for the $MPEO_{44}$-*b*-PCL_{17} block copolymer NPs the presence of only one sharp peak at pH ~ 7.4 (Fig. 5, upper) and three peaks at pH ~ 5.0 (Fig. 5 bottom). Similarly, the TEM images (Fig. 6) showed a comparable increase in the size of the $MPEO_{44}$-*b*-PCL_{17} block copolymer NPs at pH ~ 5.0 (Fig. 6b) when compared to the NPs at pH ~ 7.4 (Fig. 6a) after 24 hours. The particle sizes determined from the TEM images are clearly smaller than those determined by scattering techniques. This discrepancy can be explained by a combination of two effects: (i) during sample preparation, the particles undergo dehydration and may shrink, and (ii) scattering techniques report an intensity-average dimension, whereas TEM reports a number-average dimension. Therefore, TEM images generally yield smaller sizes relative to DLS data.[60]

The increases in particle size and size distribution, as shown by both scattering techniques and TEM, are strong evidence for

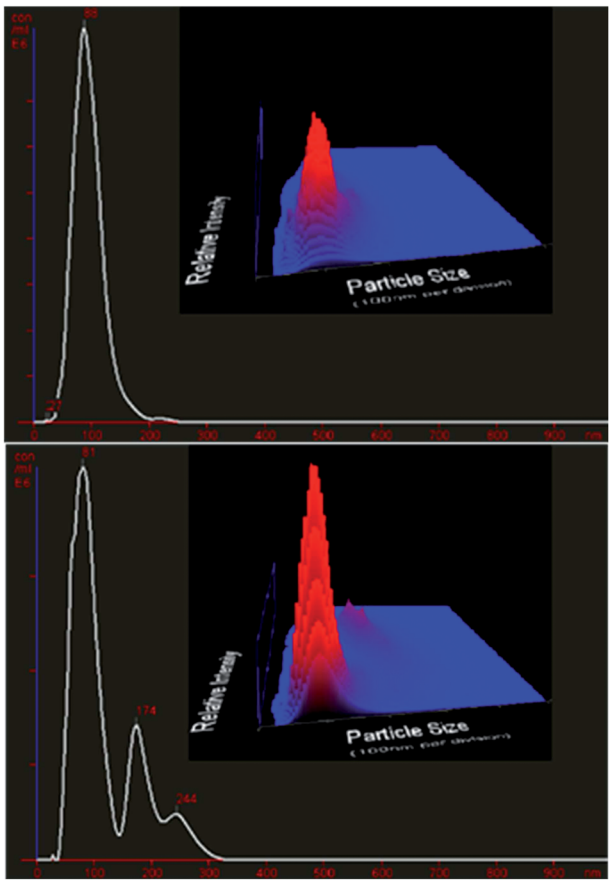

Fig. 5 Size distribution from NTA for the $MPEO_{44}$-*b*-PCL_{17} NPs under pH ~ 7.4 (upper) and pH ~ 5.0 (bottom) after 24 h.

micellar aggregation over time. The aggregation mechanism could be explained through the hydrolysis of the acid-labile ketal linkage in the $MPEO_{44}$-*b*-PCL_{17} block copolymer micelles at pH 5.0. While the hydrolysis of the ketal group occurs at the interface between the PCL core and the PEO shell inside the micelles, the free hydrolysed PEO chains begin to be released into the media (inset of Fig. 4). The decrease in the density of surface PEO chains leads to a decrease in the steric hindrance of the particles and to an increase in the hydrophobicity of the particles, and consequently, particle aggregation.[23] The linear relationship observed between the relaxation rates (Γ) and the square of the wave vector (q^2) for the particles before (37 °C and pH ~ 7.4) and after 24 hours (37 °C and pH ~ 5.0) demonstrates that both NPs and their aggregates are spherical (Fig. S10† and 6), and no distinct micellar structures were observed by DLS, NTA and TEM. Furthermore, no changes in the particle size distributions were observed for the $MPEO_{44}$-*b*-PCL_{17} block copolymer micelle by DLS at pH ~ 7.4 for 24 hours, confirming that the particles are selective to environments with mild acidic conditions (from pH ~ 5 to ~ 6.5) such as tumour tissues (Fig. S11†). Moreover, the degradation of the $MPEO_{44}$-*b*-PCL_{17} diblock copolymer was confirmed by ^{13}C NMR spectroscopy. For the NMR study, 40–50 mg of the $MPEO_{44}$-*b*-PCL_{17} diblock copolymer was dissolved in 0.6 mL of deuterated chloroform followed by the addition of 25 μl of hydrochloric acid-d (DCl).

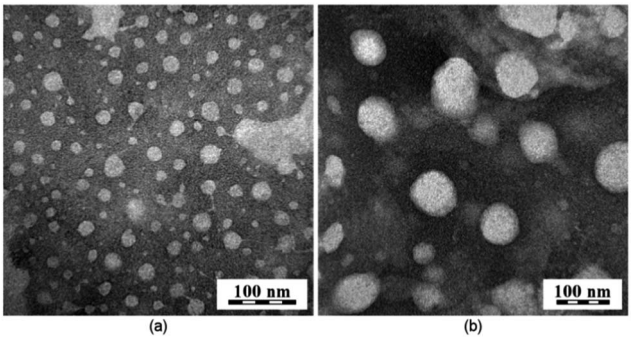

Fig. 6 TEM images of $MPEO_{44}$-*b*-PCL_{17} NPs at pH ~ 7.4 (a) and at pH ~ 5.0 (b) after 24 h.

The degradation was determined based on the disappearance of the signal from the ketal linkage between the PEO and PCL blocks. Fig. S12† shows the ^{13}C NMR spectra of the $MPEO_{44}$-*b*-PCL_{17} copolymer (a) before and (b) after the addition of DCl. The ^{13}C NMR spectra reveal the complete disappearance of the carbon signal from the ketal group linker $-OC(CH_3)_2-O-$ at $\delta =$ 121.50 ppm (**12**, Fig. S12†) after the addition of DCl (**12**, Fig. S12b†). This observation is strong evidence that hydrolytic degradation occurs in the ketal linkage of the $MPEO_{44}$-*b*-PCL_{17} diblock. Unfortunately, the usual degradation products resulting from the acid hydrolysis of a ketal group, such as acetone,[22] could not be detected in the ^{13}C NMR spectrum. Their signal is hidden under that of the ε-CL repeating units in the ^{13}C NMR. According to the ^{13}C NMR spectra, no changes were observed in the signal from ε-CL repeating units after the addition of DCl. The signals from the methylene carbons $-CO-(CH_2)_5-O-$ (**17** to **21** from $\delta = 20$ to $\delta = 65$ ppm, Fig. S12†) and from the carbonyl group (**16** at $\delta = 173$ ppm, Fig. S12†) related to the PCL segments remain unchanged. Moreover, no new signal from side products that could derive from the hydrolysis of ester bonds related to the PCL segments was detected after the acid addition. However, a visible decrease in the methylene signal $-O-(CH_2)_2-O-$ (**2** at $\delta = 70$ ppm, Fig. S12b†) related to MPEO units was observed in the ^{13}C NMR spectra. The decrease in the signal of the MPEO units is related to the experimental procedures. After the addition of DCl to the $MPEO_{44}$-*b*-PCL_{17} block copolymer solution in $CDCl_3$, the NMR tube was vigorously shaken. The formation of an emulsion composed of droplets of D_2O containing the MPEO blocks dissolved in the internal phase and the PCL blocks dissolved in the outer phase ($CDCl_3$, organic phase) spontaneously occurs. While hydrolysis of the ketal group occurs, the released PCL segments are dissolved in the outer organic phase ($CDCl_3$), whereas the MPEO blocks remain dissolved in the emulsion droplets (D_2O) with restricted mobility. The restriction in the mobility of the MPEO chains dissolved in the D_2O droplets decreases the signal intensity in the ^{13}C NMR spectra.[61]

Conclusions

Through the combination of carbodiimide chemistry and ROP mechanisms with a "click" reaction, novel pH-sensitive amphiphilic block copolymers containing acid-labile ketal groups as block linkers were successfully synthesised using a multi-step stage-by-stage synthetic strategy. The acid-cleavable linkage in the block copolymer backbone was used as a junction point for the design of hydrophilic PEO and hydrophobic PCL segments. For this purpose, a 2-{[2-(2-azidoethoxy)propan-2-yl]} ethan-1-ol compound, with a specific degradable linkage (acyclic ketal group), was synthesised for the first time. Subsequently, α-methoxy-ω-hydroxy-PEO containing a ketal group was prepared as a macroinitiator through a "click" reaction between previously synthesised α-methoxy-ω-alkyne-PEO and 2-{[2-(2-azidoethoxy)propan-2-yl]}ethan-1-ol. The obtained macroinitiator was applied for the sequential controlled ROP of ε-CL in the presence of $Sn(Oct)_2$. Different ratios of ε-caprolactone/hydroxyl were used to obtain copolymers with different PCL block lengths. Good control, purity and conversion over each obtained product were achieved without degradation of the acid-labile ketal group. Upon dissolution in a mild organic solvent, the $MPEO_{44}$-*b*-PCL_{17} block copolymer self-assembled in water–PBS into regular spherical NPs, and the presence of the acid-labile ketal group linker allowed the NPs to disassemble and aggregate in buffer that simulated acidic cytosolic or endosomal conditions in tumour cells (pH ~ 5.0), as evaluated by DLS and NTA analyses and TEM images. The synthesised block copolymers could be used in a variety of applications, *e.g.*, as pH-triggered release and drug-delivery systems.

Acknowledgements

This research was supported by the Grant Agency of the Czech Republic (P208/10/1600). E.J., R.K., and A.J. acknowledge Charles University (Prague, CZ) for the financial support and for the opportunity to pursue their Ph.D. studies. C. G. Venturini acknowledges the Program Science Without Borders CAPES/Brazil (Process number 2293/13-7). Electron microscopy was supported through grant TACR TE01020118.

References

1 Y.-Y. Won, H. T. Davis and F. S. Bates, *Science*, 1999, **283**, 960–963.
2 J. K. Kim, E. Lee, Z. G. Huang and M. Lee, *J. Am. Chem. Soc.*, 2006, **128**, 14022–14023.
3 E. Busseron, Y. Ruff, E. Moulin and N. Giuseppone, *Nanoscale*, 2013, **5**, 7098–7140.
4 D. E. Cola, C. Lefebvre, A. Deffieux, T. Narayanan and R. Borsali, *Soft Matter*, 2009, **5**, 1081–1090.
5 A. H. Gröschel, F. H. Schacher, H. Schmalz, O. V. Borisov, E. B. Zhulina, A. Walther and A. H. E. Müller, *Nat. Commun.*, 2012, **3**, 1–11.
6 T. Smart, H. Lomas, M. Massgnani, M. V. Flores-Merino, L. R. Perez and G. Battaglia, *Nano Today*, 2008, **3**, 38–46.
7 R. B. Grubbs and Z. Sun, *Chem. Soc. Rev.*, 2013, **42**, 7436–7445.
8 X.-B. Xiong, A. Falamarzian, S. M. Garg and A. Lavasanifar, *J. Controlled Release*, 2011, **155**, 248–261.

9 W. Shao, K. Miao, H. Liu, C. Ye, J. Du and Y. Zhao, *Polym. Chem.*, 2013, **4**, 3398–3410.
10 W. Wang, H. Sun, F. Meng, S. Ma, H. Liu and Z. Zhong, *Soft Matter*, 2012, **8**, 3949–3956.
11 W. J. Li, C. T. Laurencin, E. J. Caterson, R. S. Tuan and K. K. Frank, *J. Biomed. Mater. Res.*, 2001, **60**, 613–621.
12 W. J. Li, K. G. Danielson, P. G. Alexander and R. S. Tuan, *J. Biomed. Mater. Res., Part A*, 2003, **67**, 1105–1114.
13 C. Drew, X. Wang, L. A. Samuelson and J. Kumar, *J. Macromol. Sci., Part A: Pure Appl.Chem.*, 2003, **40**, 1415–1422.
14 S. V. Trubetskoy, *Adv. Drug Delivery Rev.*, 1999, **37**, 81–88.
15 V. P. Torchilin, *Colloids Surf., B*, 1999, **16**, 305–319.
16 K. Miyata, N. Nishiyama and K. Kataoka, *Chem. Soc. Rev.*, 2012, **41**, 2562–2574.
17 J. H. Jeong and T. G. Park, *J. Controlled Release*, 2002, **82**, 159–166.
18 Y. Ymamoto, Y. Nagasaki, Y. Kato, Y. Sugiyama and K. Kataoka, *J. Controlled Release*, 2001, **77**, 27–38.
19 A. Rösler, G. W. M. Vandermeulen and H.-A. Klok, *Adv. Drug Delivery Rev.*, 2001, **53**, 95–105.
20 Q. Zhang, N. R. Ko and J. K. Oh, *Chem. Commun.*, 2012, **48**, 7542–7552.
21 E. G. Kelley, J. N. L. Albert, M. O. Sullivan and T. H. Epps, *Chem. Soc. Rev.*, 2013, **42**, 7057–7071.
22 S. Binauld and M. H. Stenzel, *Chem. Commun.*, 2013, **49**, 2082–2102.
23 F. C. Giacomelli, P. Štěpánek, C. Giacomelli, V. Schmidt, E. Jäger, A. Jäger and K. Ulbrich, *Soft Matter*, 2011, **7**, 9316–9325.
24 S. Mura, J. Nicolas and P. Couvreur, *Nat. Mater.*, 2013, **12**, 991–1003.
25 E. Jäger, A. Jäger, P. Chytil, T. Etrych, B. Říhova, F. C. Giacomelli, P. Štěpánek and K. Ulbrich, *J. Controlled Release*, 2013, **165**, 153–161.
26 I. F. Tannock and D. Rotin, *Cancer Res.*, 1989, **49**, 4373–4384.
27 H. Yin, E. S. Lee, D. Kim, K. H. Lee, K. T. Oh and Y. H. Bae, *J. Controlled Release*, 2008, **126**, 130–138.
28 S. Sengupta, D. Eavarone, I. Capila, G. Zhao, N. Watson, T. Kiziltepe and R. Sasisekharan, *Nature*, 2005, **436**, 568–572.
29 S. Aryal, C. J. Hu and L. Zhang, *ACS Nano*, 2010, **4**, 251–258.
30 H. Mok, J. W. Park and T. G. Park, *Bioconjugate Chem.*, 2008, **19**, 797–801.
31 A. P. Griset, J. Walpole, R. Liu, A. Gaffey, Y. L. Colson and M. W. Grinstaff, *J. Am. Chem. Soc.*, 2009, **131**, 2469–2471.
32 B. Wang, C. Xu, J. Xie, Z. Yang and S. Sun, *J. Am. Chem. Soc.*, 2008, **130**, 14436–14437.
33 M. M. Ali, M. Oishi, F. Nagatsugi, K. Mori, Y. Nagasaki, K. Kataoka and S. Sasaki, *Angew. Chem., Int. Ed.*, 2006, **45**, 3136–3140.
34 Y. Li and P. I. Lee, *Int. J. Pharm.*, 2010, **383**, 45–52.
35 S. D. Khaja, S. Lee and N. Murthy, *Biomacromolecules*, 2007, **8**, 1391–1395.
36 J. Siepmann and A. Göpferich, *Adv. Drug Delivery Rev.*, 2001, **48**, 229–247.
37 J. H. Jeong, S. W. Kim and T. G. Park, *Bioconjugate Chem.*, 2003, **14**, 473–479.
38 M. A. R. Meier, S. N. H. Aerts, B. B. P. Staal, M. Rasa and U. S. Schubert, *Macromol. Rapid Commun.*, 2005, **26**, 1918–1924.
39 S. Petrova, I. Kolev, S. Miloshev, M. D. Apostolova and R. Mateva, *J. Mater. Sci.: Mater. Med.*, 2012, **23**, 1225–1234.
40 J. Wu and C.-C. Chu, *Acta Biomater.*, 2012, **8**, 4314–4323.
41 J. Nicolas, S. Mura, D. Brambila, N. Mackiewicz and P. Couvreur, *Chem. Soc. Rev.*, 2013, **42**, 1147–1235.
42 J. Rieger, P. Dubois, R. Jérôme and C. Jérôme, *Langmuir*, 2006, **22**, 7471–7479.
43 N. Kumar, M. N. V. Ravikumar and A. J. Domb, *Adv. Drug Delivery Rev.*, 2001, **53**, 23–44.
44 M. Oikawa, A. Wada, F. Okazaki and S. J. Kusumoto, *J. Org. Chem.*, 1996, **61**, 4469–4471.
45 R. A. Shenoi, B. F. L. Lai and J. N. Kizhakkedathu, *Biomacromolecules*, 2012, **13**, 3018–3030.
46 O. Norberg, L. Deng, T. Aastrup and M. Yan, *Anal. Chem.*, 2011, **83**, 1000–1007.
47 H. Freichels, V. Pourcelle, R. Auzély-Velty, J. Marchand-Brynaert and C. Jérôme, *Biomacromolecules*, 2012, **13**, 760–768.
48 P. Štěpánek, *J. Chem. Phys.*, 1993, **99**, 6384–6393.
49 J. Jakes, *Czech. J. Phys.*, 1988, **38**, 1305.
50 V. Krishnakumar and J. R. Xavier, *Spectrochim. Acta, Part A*, 2004, **60**, 709–714.
51 A. M. de Oliveira, E. Jäger, A. Jäger, P. Štěpánek and F. C. Giacomelli, *Colloids Surf., A*, 2013, **436**, 1092–1102.
52 A. Choucair and A. Eisenberg, *Eur. Phys. J. E*, 2003, **10**, 37–44.
53 Z.-X. Du, J.-T. Xu and Z.-Q. Fan, *Macromolecules*, 2007, **40**, 7633–7637.
54 P. Schuetz, M. J. Greenall, J. Bent, S. Furzeland, D. Atkins, M. F. Butler, T. C. B. McLeishd and D. M. A. Buzza, *Soft Matter*, 2011, **7**, 749–759.
55 S. M. Loverde, M. L. Klein and D. E. Discher, *Adv. Mater.*, 2012, **24**, 3823–3830.
56 H. Cabral, Y. Matsumoto, K. Mizuno, Q. Chen, M. Murakami, M. Kimura, Y. Terada, M. R. Kano, K. Miyazono, M. Uesaka, N. Nishiyama and K. Kataoka, *Nat. Nanotechnol.*, 2011, **6**, 815–823.
57 H. Maeda, H. Nakamura and J. Fang, *Adv. Drug Delivery Rev.*, 2013, **65**, 71–79.
58 V. Filipe, A. Hawe and W. Jiskoot, *Pharm. Res.*, 2010, **27**, 796–810.
59 A. E. James and J. D. Driskell, *Analyst*, 2013, **138**, 1212–1218.
60 A. Jäger, D. Gromadzki, E. Jäger, F. C. Giacomelli, A. Kozlowska, L. Kobera, J. Brus, B. Říhova, M. El Fray, K. Ulbrich and P. Štěpánek, *Soft Matter*, 2012, **8**, 4343–4354.
61 J. Spěváček, *Makromol. Chem., Rapid Commun.*, 1982, **3**, 697–703.

Supplementary Information for the Manuscript Entitled

Novel poly(ethylene oxide monomethyl ether)-*b*-poly(ε-caprolactone) diblock copolymers containing a pH-acid labile ketal group as blocks linkage

Svetlana Petrova*, Eliézer Jäger, Rafał Konefał, Alessandro Jäger,

Cristina Garcia Venturini, Jiří Spěváček, Ewa Pavlova and Petr Štěpánek

Institute of Macromolecular Chemistry, Heyrovsky Sq. 2, 162 06 Prague 6, Czech Republic

E-mail: petrova@imc.cas.cz; Tel:+420 296 809322;+420 296 809211

Synthesis of the compounds 1-5.

Synthesis of Ethylene glycol monoacetate ***(compound 1)***

Ethylene glycol monoacetate (**1**) was synthesized according to previous procedures.[44,45] Briefly, ethylene glycol (6.7 mL, 0.121 mol), trimethyl orthoacetate (23.1 mL, 0.182 mol), and p-toluene sulfonic acid monohydrate (0.5 g, 0.121 mol) were dissolved in 150 mL of CH_2Cl_2 and stirred at room temperature for 4 h. Water (3.3 mL, 0.182 mol) was added to the reaction mixture and stirred for an additional 1 h. CH_2Cl_2 was removed under reduced pressure and the obtained crude product was purified by silica gel flash chromatography using $CHCl_3$/acetone (9:1) as a mobile phase. The product, 2-hydroxyethyl acetate (**1**), was recovered as a colorless liquid. Yield: 2.45 g, 40%. ^{1}H-NMR ($CDCl_3$, ppm): 2.09 (s, 3H, C*H*$_3$-C(O)-O-), 3.1 (s, 1H, -CH_2-O*H*), 3.8 (t, 2H, -O-CH_2-C*H*$_2$-OH), 4.18 (t, 2H, -O-C*H*$_2$-CH_2-OH). ^{13}C-NMR ($CDCl_3$, ppm): 20.9, 60.9, 66.11, 171.6.

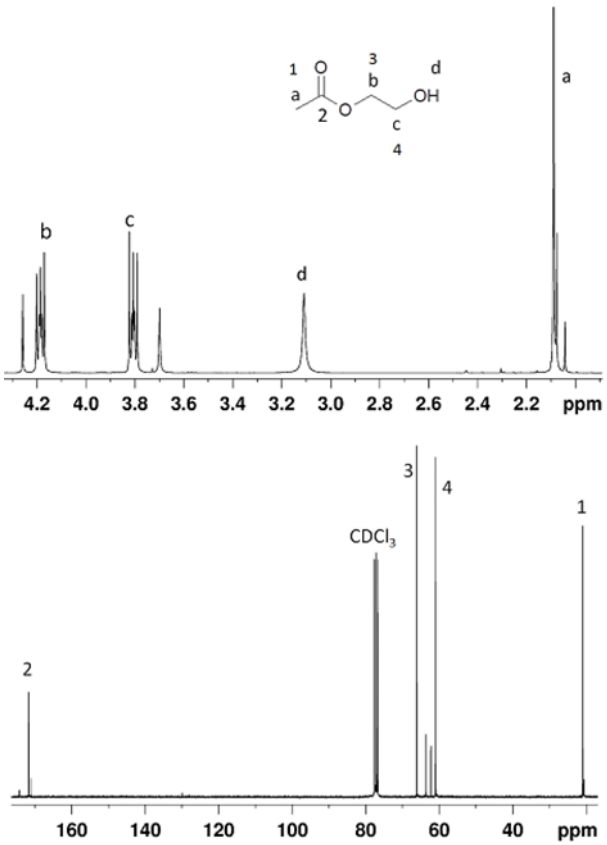

Fig. **S1**. ^{1}H (top) ^{13}C (bottom) NMR spectra of the ethylene glycol monoacetate (**1**) in $CDCl_3$.

Synthesis of 2-Azidoethanol ***(compound 2)***

Compound **2** was synthesized according to the literature.[46] In a typical reaction, 2-chloroethanol (5.22 g, 0.078 mol), sodium azide (15.19 g, 0.234 mol), and TBABr (2.51 g, 0.0078 mol) were mixed in a round-bottom flask equipped with a reflux condenser and stirred at 110 ºC for 18 h (using a safety shield). The mixture was diluted with Et_2O and the solid by-products were filtered off. The solvent was evaporated under reduced pressure (without heating), giving a yellow oil. The crude product was purified by distillation at 12 mbar, yielding 2-azidoethanol (**2**) as a colorless oil. Yield: 2.23 g, 40%. ^{1}H-NMR ($CDCl_3$, ppm): 2.82 (s, 1H, -CH_2-O*H*), 3.45 (t, 2H, -C*H*$_2$-OH), 3.75 (t, 2H, N_3-C*H*$_2$-). ^{13}C-NMR ($CDCl_3$, ppm): 53.58, 61.47.

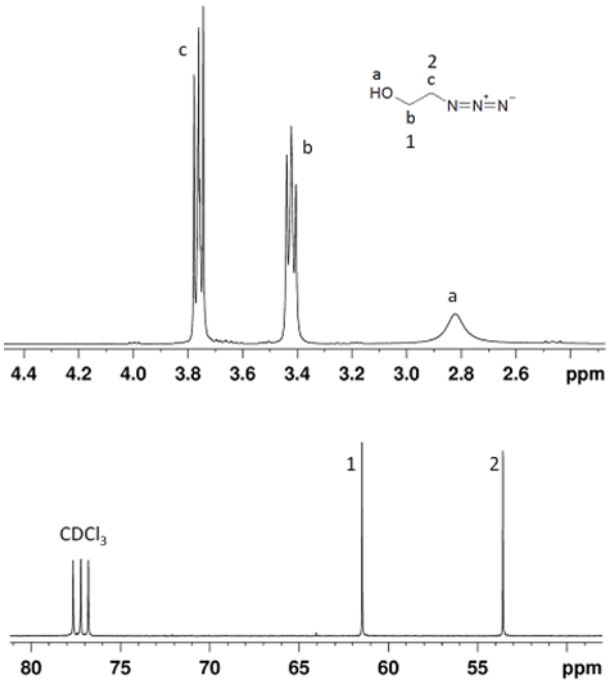

Fig. **S2**. ^{1}H (top) ^{13}C (bottom) NMR spectra of the 2-azidoethanol (**2**) in $CDCl_3$.

Synthesis of 2-{[2-(2-azidoethoxypropan-2-yl]oxy}ethyl acetate ***(compound 3)***

2-{[2-(2-Azidoethoxypropan-2-yl]oxy}ethyl acetate (**3**) was synthesized according to literature procedure.[45] Compound 1 (1.5 g) and 2 (1.3 g) 1/1 mol/mol were dissolved in 50 mL of dry THF. PPTS (0.4 g, 0.00144 mol) was added and stirred for 15 min, followed by addition of molecular sieves (5 Å) (30 g) and additional stirring for 15 min. To this mixture, 2-methoxypropene (1.04 g, 0.0144 mol) was added, and the reaction mixture was stirred at room temperature for 48 h. The reaction mixture was neutralized with solid $NaHCO_3$ and kept over Celite bed. The filtrate was evaporated to obtain the crude product, which was purified by column chromatography on silica gel using EtOAc/Hex (1:9) as eluent. The formation of the new 2-{[2-(2-azidoethoxypropan-2-yl]oxy}ethyl acetate (**3**) was determined by collection of different fractions monitored by TLC. The product was recovered as a colorless liquid. Yield: 1 g, 70%. ^{1}H-NMR ($CDCl_3$, ppm): 1.38 (s, 6H, -O-C(CH_3)$_2$-O-), 2.08 (s, 3H, CH_3-C(O)-O-), 3.35 (t, 2H, -C(CH_3)$_2$-O-CH_2-CH_2-N_3), 3.58-3.68 (m, 4H, -CH_2-O-C(CH_3)$_2$-O-CH_2-CH_2-N_3), 4.19 (t, 2H, CH_3-C(O)-O-CH_2-). ^{13}C-NMR ($CDCl_3$, ppm): 21.10, 24.80, 51.04, 59.11, 60.01, 63.93, 100.46, 171.07.

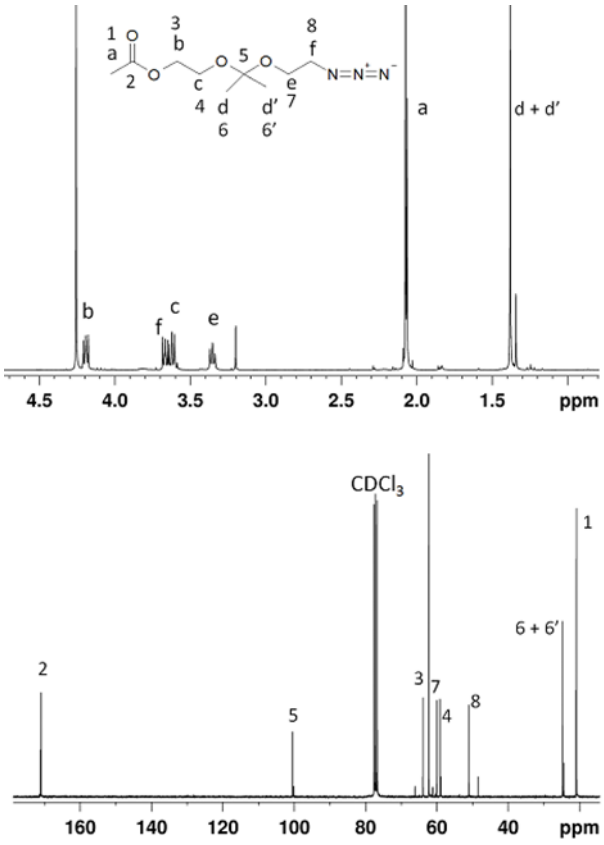

Fig. **S3**. ^{1}H (top) and ^{13}C (bottom) NMR spectra of the 2-{[2-(2-azidoethoxypropan-2-yl]oxy}ethyl acetate (**3**) in $CDCl_3$.

Synthesis of 2-{[2-(2-azidoethoxy)propan-2-yl]ethan-1-ol ***(compound 4)***

Compound **4** was synthesized according to previous procedure.[45] Deprotection of the acetyl group of the compound **3** was carried out by treating with sodium hydroxide in CH_3OH/H_2O at room temperature for 2 h. After the reaction, brine was added and the product was extracted with CH_2Cl_2. The combined organic phases were evaporated under reduced pressure. The product (**4**) was recovered as a colorless liquid. Yield: 0.8 g, 80%. ^{1}H-NMR ($CDCl_3$, ppm): 1.35 (s, 6H, -O-C(CH_3)$_2$-O-), 3.34-3.38 (t, 2H, -C(CH_3)$_2$-O-CH_2-CH_2-N_3), 3.56-3.59 (m, 4H, --C(CH_3)$_2$-O-CH_2-CH_2-OH), 3.62-3.68 (t, 2H, -CH_2-N_3). ^{13}C-NMR ($CDCl_3$, ppm): 21.10, 24.40, 48.62, 51.08, 59.93, 100.35.

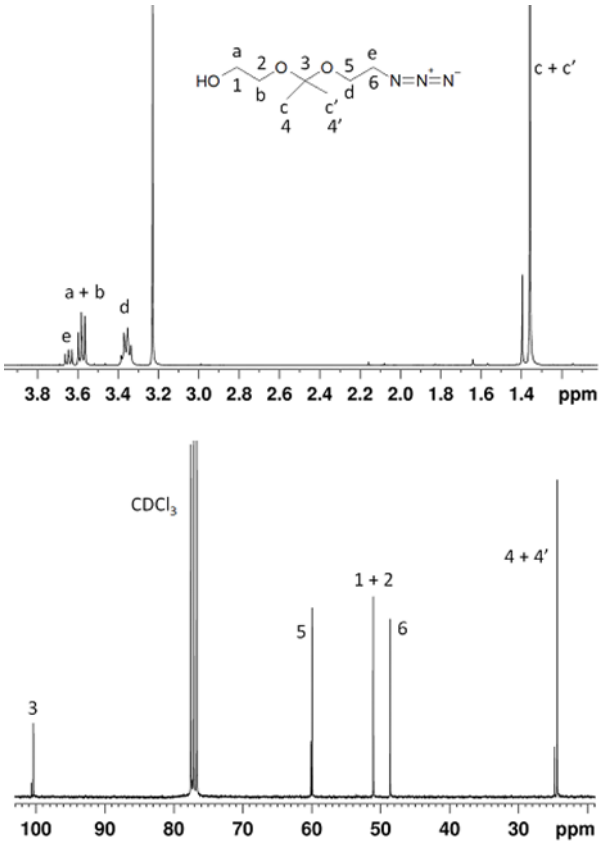

Fig. **S4**. ^{1}H (top) and ^{13}C (bottom) NMR spectra of the 2-{[2-(2-azidoethoxy)propan-2-yl]ethan-1-ol (**4**) in $CDCl_3$.

Synthesis of α-methoxy-ω-alkyne-poly(ethylene oxide) ***(compound 5)***

α-Methoxy-*ω*-alkyne-poly(ethylene oxide) (**5**) was synthesized according to the literature.[47] In a flame-dried and argon-purged two-neck round-bottom flask equipped with three-port valves *α*-methoxy-*ω*-hydroxyl-poly(ethylene oxide) (9g, 0.0045 mol, 1800 g/mol) was dried by repeated azeotropic distillations (three times) of dry toluene. After, 0.5 mL of 5-hexynoic acid (0.0045 mol), 0.055 g of DMAP (0.00045 mol) and 0.93 mg of DCC (0.0045 mol) were transferred to the flask under inert gas blanket followed by the addition of 107 mL of dry CH_2Cl_2 by using a flame-dried and argon-flushed glass syringe equipped with a metallic cannula. The solution was stirred at room temperature for 36 h under argon. The solvent was evaporated under vacuum and the solid residue was dissolved in THF. The resulted solution was filtered to remove the dicyclohexylurea (by-product) and the polymer was precipitated in cold Et_2O. After filtration the solid was dried under vacuum at room temperature. Yield: 8.09 g, 90%. ^{1}H-NMR ($CDCl_3$, ppm): 1.83 (p, 2H, -C*H*$_2$-CH$_2$-C≡H), 1.96 (t, 1H, -C≡*H*), 2.25 (td, 2H, -C*H*$_2$-C≡H), 2.47 (t, 2H, -C*H*$_2$-CH$_2$-CH$_2$-C≡H), 3.39 (s, 3H, -O-C*H*$_3$), 3.63 (m, 4H, -C*H*$_2$-C*H*$_2$-O-), 3.86 (t, 2H, -O-C*H*$_2$-CH$_2$-O-C(O)), 4.22 (t, 2H, -O-CH$_2$-C*H*$_2$-O-C(O)).

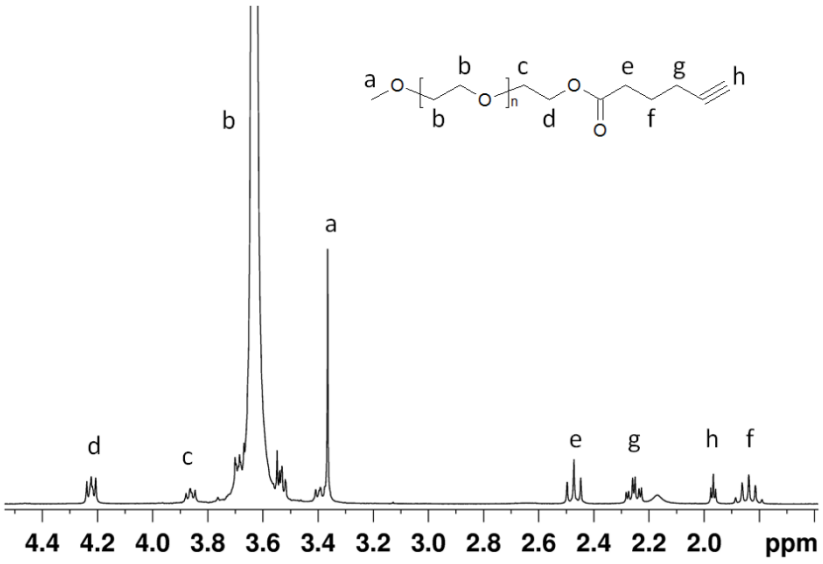

Fig. **S5**. ^{1}H NMR spectrum of the α-methoxy-ω-alkyne-PEO (**5**) in $CDCl_3$.

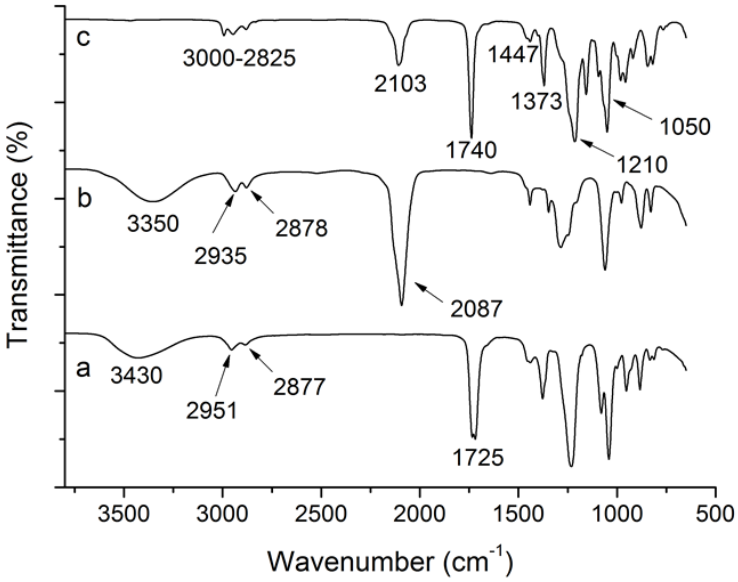

Fig. **S6**. FT-IR spectra of the (a) ethylene glycol monoacetate **(1)**, (b) 2-azidoethanol **(2)**, and (c) 2-{[2-(2-azidoethoxy)propan-2-yl]oxy}ethyl acetate **(3)**.

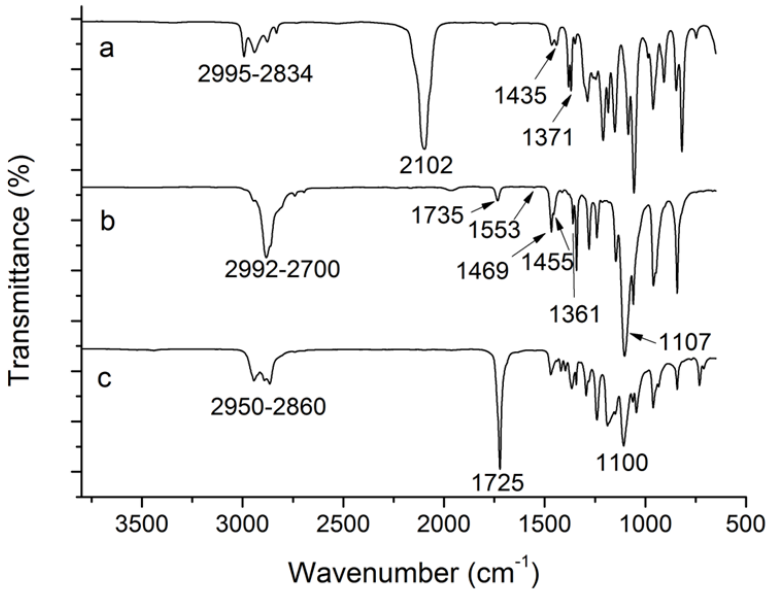

Fig. **S7**. FT-IR spectra of the (a) 2-{[2-(2-azidoethoxy)propan-2-yl]ethan-1-ol (**4**), (b) α-methoxy-ω-hydroxy-poly(ethylene oxide) containing ketal group (**6**), and (c) MPEO-*b*-PCL diblock copolymer (**7**).

The characteristic peaks observed are the following; 1725 cm^{-1} for the ester bond (C=O stretching) from the ε-CL repeated units in the PCL block, 1100 cm^{-1} for the ether bond (C–O–C stretching) of the EO repeated units of the PEO backbone and at 2950 and 2860 cm^{-1} the C–H vibrations bands typical for both monomer units.

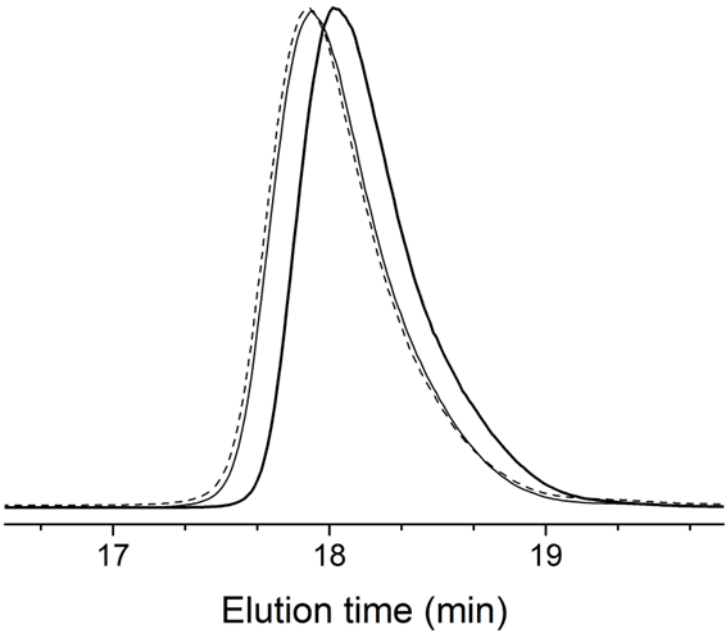

Fig. **S8**. SEC chromatograms in THF of MPEO (bold line), ω-alkyne-MPEO (regular line) and α-methoxy-ω-hydroxy-MPEO containing ketal group (**6**) (dotted line).

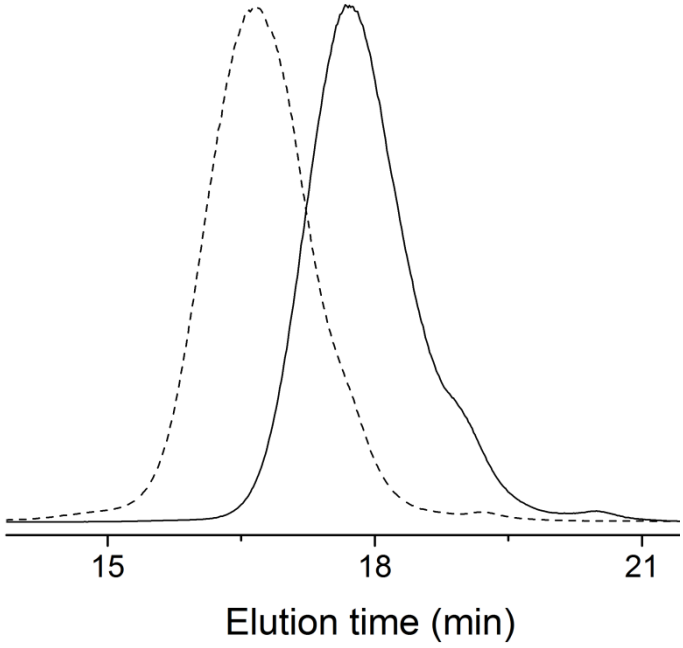

Fig. **S9**. SEC chromatograms in THF of $MPEO_{44}$-*b*-PCL_{17} diblock copolymer (—) (1, in Table 2) and $MPEO_{44}$-*b*-PCL_{44} diblock copolymer (---) (2, in Table 2).

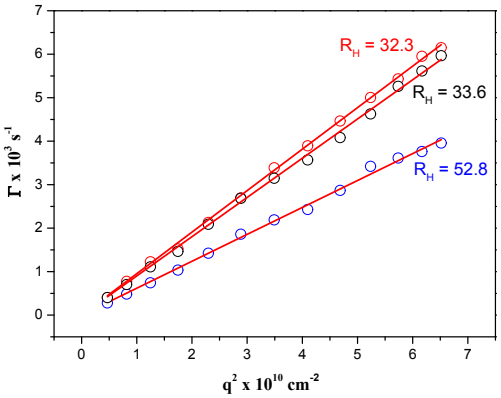

Fig. **S10**. Angular variation of the frequency $\Gamma = 1/\tau$ as a function of q^2 at 37 ºC for: (○) $MPEO_{44}$-*b*-PCL_{17} micelles in PBS (pH ~ 7.4) and 0h, (○) in PBS (pH ~ 7.4) and 24h and (○) in acetate buffer (pH ~ 5) after 24 hours.

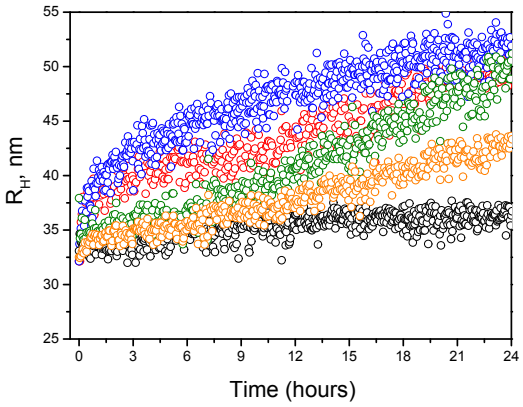

Fig. **S11**. Temporal dependence on R_H distribution of $MPEO_{44}$-*b*-PCL_{17} micelles in (○) PBS (pH ~ 7.4) and in acetate buffer (○) pH ~ 6.5, (○) pH ~ 6.0, (○) pH ~ 5.5 and (○) pH ~ 5.0 at 37 °C.

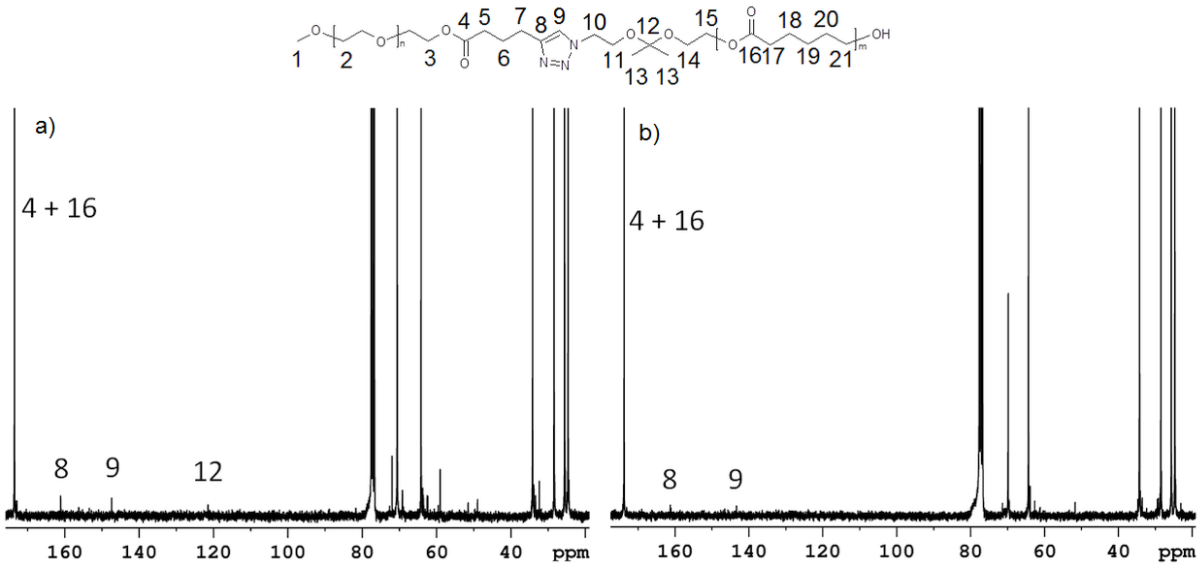

Fig. **S12**. ^{13}C NMR spectra of $MPEO_{44}$-*b*-PCL_{17} diblock copolymer (a) before degradation and (b) after degradation.

Publication 10

E. Jäger, A. Höcherl, O. Janoušková, A. Jäger, M. Hruby, **R. Konefał**, M. Netopilik, J. Panek, M. Slouf, K. Ulbrich, P. Stepanek

Fluorescent boronate-based polymer nanoparticles with reactive oxygen species (ROS)-triggered cargo release for drug-delivery applications.

Nanoscale, **2016**, 8, 6958-6963.

Nanoscale

COMMUNICATION

View Article Online
View Journal | View Issue

Cite this: *Nanoscale*, 2016, **8**, 6958

Received 28th January 2016,
Accepted 23rd February 2016

DOI: 10.1039/c6nr00791k

www.rsc.org/nanoscale

Fluorescent boronate-based polymer nanoparticles with reactive oxygen species (ROS)-triggered cargo release for drug-delivery applications†

Eliézer Jäger,* Anita Höcherl,* Olga Janoušková, Alessandro Jäger, Martin Hrubý, Rafał Konefał, Miloš Netopilik, Jiří Pánek, Miroslav Šlouf, Karel Ulbrich and Petr Štěpánek

A new drug-delivery system of polymer nanoparticles (NPs) bearing pinacol-type boronic ester and alkyne moieties displaying triggered self-immolative polymer degradation in the presence of reactive oxygen species (ROS) with the capability of cellular imaging is presented. The NPs specifically release their drug cargo under concentrations of ROS that are commonly found in the intracellular environment of certain tumors and of inflamed tissues and exhibit significant cytotoxicity to cancer cells compared to their non-ROS-responsive counterparts.

The incorporation of selectively chemically degradable linkages into polymer-based nanoparticles (NPs) and microparticulate drug-delivery systems allows one to achieve external stimulus-triggered polymer degradation and triggered release.[1–3] This is a very useful feature both to release the therapeutic cargo and to eliminate the biomaterial from the body after the cargo is released and the carrier is no longer needed. Such a stimulus may be an enzymatic removal of protecting groups, a pH change, light or more recently, the presence of reactive oxygen species (ROS) in the surrounding environment.[4–6] The ROS plays a crucial role in human physiological and pathophysiological processes. An increasing amount of data indicates that ROS such as H_2O_2 are a component of cell signaling pathways that are necessary for the growth, development, and fitness of living organisms.[7] On the other hand, imbalances in H_2O_2 production lead to oxidative stress and inflammation events, which damages the tissue and organ systems and are correlated with the onset and advancement of various diseases, including cancer, diabetes, cardiovascular and neurodegenerative diseases.[8–11] Among the ROS species, H_2O_2 is the most expressed in tumors and at higher concentrations when compared to other ROS species, as well as, when compared with normal cells where intracellular concentration levels may span four orders of magnitude from 10^{-8} M in proliferation to 10^{-4} M in apoptosis.[12,13] In line with this, several studies have detected elevated rates of ROS in almost all human cancer cells compared to their normal counterparts.[14–18] Therefore, H_2O_2 has become a common marker for oxidative stress playing important roles in carcinogenesis and is also linked to apoptosis, cell proliferation and DNA mutations.[19–21] Thus the involvement of ROS in cellular signaling and disease states has motivated the construction of clever chemical tools such as ROS-responsive micro- and NPs as drug carriers.[22–24]

The ability to generate a triggered NP carrier response (*e.g.*, release of cargo or polymer degradation) in a ROS rich microenvironment is of particular interest, *e.g.*, for the targeted drug delivery to tumors and sites of inflammation.[4,5,23–26]

Herein, a biocompatible and biodegradable ROS-sensitive polymer backbone with the capability of cellular imaging in a ROS-rich environment was synthesized by step-growth polymerization from monomers bearing a ROS-degradable pinacol-type boronic ester and an alkyne moiety suitable for click chemistry-based attachment of the active cargo (see Scheme 1).

It is important to highlight that the pinacol-type boronic ester groups have been shown to be the most ROS selective and sensitive probes to detect H_2O_2 at physiological concentrations with high specificity.[12,23,27,28]

Initially, monomer **1** was synthesized according to the previously reported procedure[23] (see the ESI† for the synthetic route). Monomer **2** (Scheme 1) was synthesized by the protection of 2,6-bis-(hydroxymethyl)-*p*-cresol with *tert*-butyldimethylsilyl chloride generating compound **2** that was then reacted with propargyl bromide to provide the protected alkyne compound **3** (Fig. S1, see the ESI† for the synthetic route). Monomer **2** (Scheme 1) was obtained in high yield (94%) after the removal of the protecting groups from com-

Institute of Macromolecular Chemistry v.v.i., Academy of Sciences of the Czech Republic, Heyrovsky Sq. 2, 162 06 Prague 6, Czech Republic.
E-mail: jager@imc.cas.cz, hocherl@imc.cas.cz

†Electronic supplementary information (ESI) available. See DOI: 10.1039/c6nr00791k

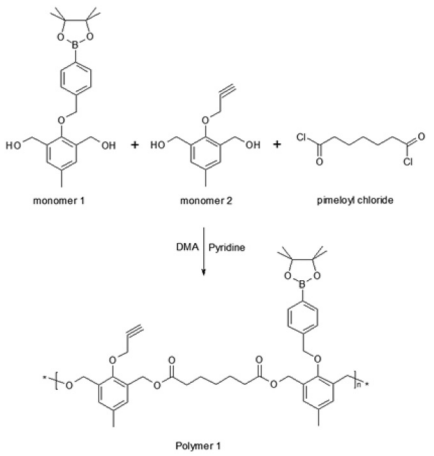

Scheme 1 Synthetic route of the ROS-responsive polymer 1 (**P1**) bearing the alkyne group-containing monomeric unit **2** suitable for the click reaction.

pound **3** (ESI Fig. S2†). The synthesized monomers **1** and **2** were further successfully copolymerized with pimeloyl chloride generating the ROS-responsive polymer 1 (**P1**) (Scheme 1 and the ESI†).

Successful polymer synthesis was confirmed by ^{1}H NMR (Fig. 1) and by size exclusion chromatography (SEC) analysis (Fig. 2a). Weight-average molecular weight (M_w) of polymer **P1** was 21.5 kDa with a reasonable polydispersity index PDI = M_w/M_n = 1.49 (where M_n is the number-average molecular weight) as determined by SEC (Fig. 2a – black line). The ^{1}H NMR spectrum of **P1** shows characteristic signals for protons belonging to the repeating units of the monomers. The signals from the protons in monomer **1** and monomer **2** aromatic rings were detected at δ = 7.68 ppm (1 – see Fig. 1 for signal-structure assignment), δ = 7.41 ppm (2), and δ = 7.16 ppm (3). The methylene protons (4) of monomers **1** and **2** from the main chain of **P1** were observed in the same position at δ = 5.08 ppm, whereas the signals attributed to the methylene groups of side chains of monomers **1** (5) and **2** (6) appear at

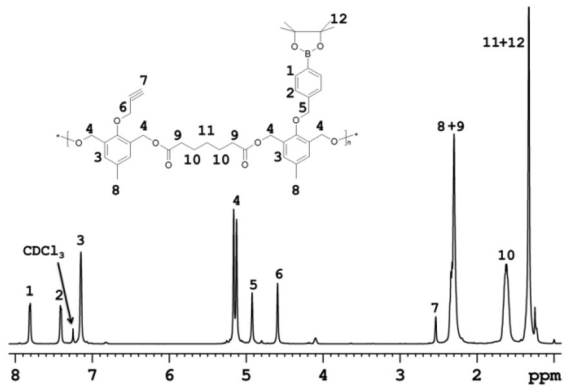

Fig. 1 ^{1}H NMR spectra of the synthesized ROS-responsive polymer (**P1**) containing the monomer **2** units enabling the polymer modification by the click reaction.

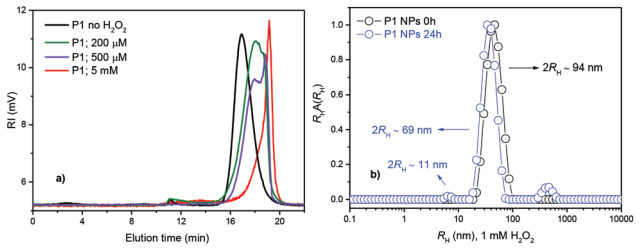

Fig. 2 SEC chromatograms of **P1** prior to the addition of H_2O_2 (black line) and after degradation in 20% PBS/DMF solutions containing 200 μM and 500 μM (physiologically relevant levels) or 5 mM H_2O_2, respectively (incubation at 37 °C for 1 day) (a), and (b) intensity-weighted distributions of R_H for **P1** (○) prior to the H_2O_2 addition and (○) after 24 h of incubation in 1 mM H_2O_2.

δ = 4.88 and 4.57 ppm, respectively (Fig. 1). The signal of the proton of the terminal alkyne group (7) is at δ = 2.51 ppm (spectrum of **P1** in d_6-DMSO is also given, see ESI Fig. S3†). Furthermore, the spectrum displayed signals of methylene groups (10) from the pimeloyl chloride monomeric repeating unit at δ = 1.48 ppm, and the peaks of the methyl with methylene groups (8 + 9, 12 + 11) with chemical shifts at δ = 2.25 and 1.26 ppm, respectively. A ROS-insensitive counterpart to the **P1** polymer (polymer 2; **P2**) was also synthesized to investigate the ROS response to the intracellular drug release efficiency.

Spectra of the ROS-insensitive counterpart polymer 2 in $CDCl_3$ showed the characteristic peaks (Fig. S4, ESI†), which also indicated successful polymer synthesis.

The degradation of the **P1** polymer in the presence of H_2O_2 was characterized by SEC analysis and ^{1}H NMR following a modified methodology.[23] Under exposure to H_2O_2 the aryl boronic ester groups are oxidized and subsequently hydrolyzed to display a phenol. The latter undergoes a quinone methide rearrangement to degrade the polymer in conformation with Scheme S1 (see the ESI†).

In a typical experiment, **P1** was incubated in a 20% PBS/DMF (v/v) solution containing different H_2O_2 concentrations and at predetermined time intervals aliquots were examined by SEC (see the ESI† for methods).

The SEC chromatogram (Fig. 2) shows that **P1** degraded into small molecules and oligomers in a time- and H_2O_2-dependent manner. Polymer degradation proceeds more extensively with an increasing incubation time and H_2O_2 concentration. **P1** was shown to be responsive to physiologically relevant levels of H_2O_2 ($\lesssim$1 mM)[12,13,23,27,28] after 1 day of incubation (Fig. 2a) while the non-ROS-responsive counterpart polymer (**P2**) showed no degradation during the same time and under the same conditions (data not shown). When degradation of both the polymers was compared at higher H_2O_2 concentrations and for a longer time (5 mM, 4 days), the degradation of the **P2** polymer was only partial (Fig. S5†). The degradation of polymer **P1** evaluated with ^{1}H NMR was complete after 5 days of incubation (see ESI Fig. S6†) as broad peaks in ^{1}H NMR related to the polymer are replaced by sharp peaks of the low-molecular-weight degradation products

(monomers) confirming the depolymerisation of **P1** triggered by H_2O_2 (ESI, Fig. S6†).

The NPs from the **P1** and **P2** polymers were prepared by a nanoprecipitation protocol (see the ESI†) and their behavior under different ROS concentrations was evaluated in detail by dynamic light scattering (DLS), static light scattering (SLS), transmission electron microscopy (TEM) and by *in vitro* drug model release experiments.

Note that the NPs were prepared with a hydrodynamic radius ($2R_H = D_H \sim 94$ nm), *e.g.*, within a range known to be ideal for efficient tumor accumulation due to the enhanced permeability and retention (EPR) effect.[29]

The ROS-responsiveness capability of the **P1** NPs was tested by DLS after 24 h of incubation with 1 mM of H_2O_2. Fig. 2b shows the distribution of R_H for **P1** NPs before and after 24 h of incubation as measured by DLS. The distribution of R_H for **P1** NPs appears as only one single distribution of R_H relative to the presence of the single spherical polymer NP in PBS solution with an average diameter of $2R_H \sim 94$ nm (Fig. 2b, black circles). Furthermore, the polydispersity of the NPs is very low as estimated through the cumulant analysis ($\mu/\Gamma^2 = 0.08 \pm 0.007$) (ESI†). This is important for the homogeneous biological behavior of such NPs. However, after 24 h of H_2O_2 incubation, a trimodal distribution of R_H was observed. In addition to the NP peak, the presence of molecularly dissolved copolymer chains as well as a peak of large aggregates could be noticed in the aqueous solution at 1 mM H_2O_2. Three well-defined peaks highlighting the three populations of the scattering polymer with average diameters of $D_H \sim 11$ nm, 69 nm and 1.9 μm were identified (Fig. 2b, blue circles). They can be attributed to free chains and their fragments, surface-eroded nanoparticles (decrease in D_H of ~25 nm) and polymer aggregates, respectively.[3,30] The NP degradation can be clearly visualized in the volume-weighted distribution of R_H (see Fig. S7, ESI†). Further the polymer degradation-triggered cargo release was studied using the release of the fluorescent model drug Nile Red (NR). Incorporation of the fluorescent marker also provided the means to study the cellular uptake of the NPs by microscopy and flow cytometry (FC). The NR-loaded ROS-responsive (from polymer **P1**) and non-ROS-responsive (from polymer **P2**) NPs were examined with fluorescence spectroscopy measurements over 24 h of incubation with 1 mM of H_2O_2 (Fig. S8–S10, ESI†). After 24 h the NR release from the ROS-responsive NPs was almost ~6 times faster than the NR release from their non-ROS-responsive counterparts, thus confirming the potential of the **P1** polymer NPs to release the model drug specifically in simulated ROS-rich microenvironments (Fig. S10, ESI†). The NP degradation was also investigated by TEM microscopy (Fig. 3). The TEM microscopy showed the particle size qualitatively comparable to that determined by DLS (Fig. 2b). Prior to incubation with H_2O_2, compact NPs of spherical morphology and narrow size distribution ($D_H \leq 85$ nm) were observed (Fig. 3a).

After incubation with 1 mM H_2O_2, the NPs showed diffused irregular shapes and a very broad size distribution, with the smallest NPs well below 10 nm and the largest NPs above

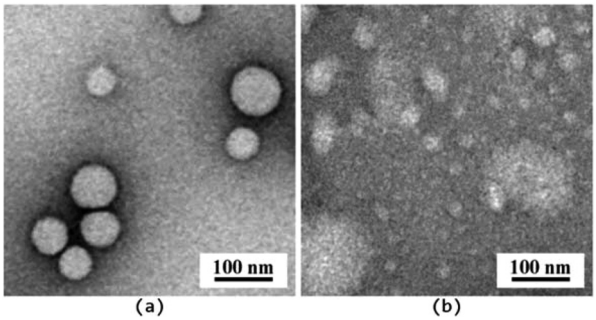

Fig. 3 TEM micrographs of polymer NPs from polymer **P1** prior to incubation with H_2O_2 (a) and after 2 days of incubation with 1 mM of H_2O_2 (b).

~100 nm (Fig. 3b). This suggested that H_2O_2 caused decomposition of the NPs, and the decomposed parts were probably re-agglomerated due to their hydrophobicity. SLS data support the findings that the NPs underwent surface degradation as well as core decomposition, as the particles' D_H decreased (by 25 nm, see Fig. 2b) as well as the overall scattering intensity (Fig. S11a†) followed by the increase in particles R_G (gyration radius), a characteristic of core hydration and swelling of the scattering particles in solution (Fig. S11b†).[31–33] The decomposition was also in agreement with the observed low contrast for the incubated NPs (Fig. 3b). Compact NPs exhibited sharp edges and high contrast, whereas decomposed NPs, NP fragments and their agglomerates showed only a vague interface.

The cellular uptake of **P1** and **P2** NPs loaded with NR (dye loading ~0.2 wt%, see ESI Fig. S8 and S9†) and the intracellular NR release were followed *in vitro* in human prostate cancer (PC-3) cells (see the ESI† for methods). The latter are known to produce high ROS levels.[34] While NR is highly fluorescent when incorporated inside the NPs, after ROS-triggered NP degradation in the cells the dye is released and quenched outside the NPs (due to polarity changes in the micro-surrounding). After a short incubation of 4 h both the NPs displayed comparable fluorescence intensity in the cells under the microscope, however, after 20 h the fluorescence of **P1** was much lower compared to **P2** NPs (see Fig. S12†). This indicated a faster ROS-triggered degradation of **P1** NPs after a prolonged exposure in ROS-producing cells. Based on a similar uptake rate of the NPs (as also confirmed by FC, see Fig. S13†), the ROS-mediated fluorescence decay and cargo release of **P1** NPs was further pursued *via* fluorescence lifetime microscopy (FLIM) and FC. In a quantitative study *via* FC the NR quenching of the NPs was evaluated in PC-3 and human fibroblast (HF) cells (see the ESI† for methods). The latter is known for their low levels of ROS production contrary to PC-3.[34–37] The cells were loaded with **P1** NPs, washed and incubated for 4 h, thus exposing the internalized NPs to intracellular ROS insofar as present in the cells. After incubation the NR fluorescence was significantly reduced in PC-3 cells compared to the HF cells (Fig. 4).

By the same experimental setup the Nile Red quenching of **P1** and **P2** NPs in PC-3 cells was compared. In line with the

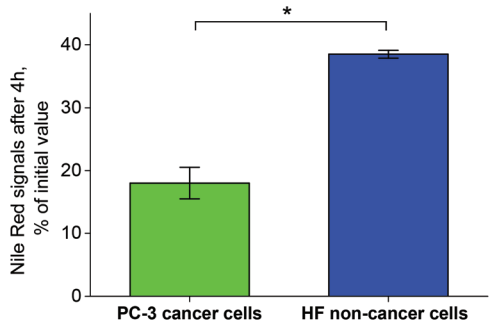

Fig. 4 Nile Red fluorescence signals from NR-loaded **P1** NPs in PC-3 and HF cells after 4 h of incubation. At t_0 prior to incubation, the cells have been loaded with **P1** NPs by a 2 h pre-incubation step, further the NPs were washed off (see the ESI† for methods). *0.01 level (ANOVA One-way).

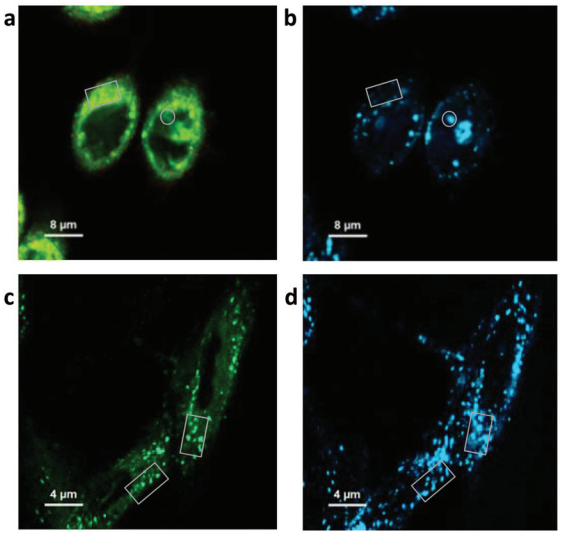

Fig. 5 FLIM microscopy of dual-marked **P1** NPs in PC-3 (a, b) and HF (c, d) cells after 8 h incubation, visualizing (released) NR and polymer-bound Alx647. Fluorescence was detected after separate excitation at 485 nm (NR, in a, c) and 640 nm (Alx647, in b, d). In a, b locations with high polymer content but little co-localizing NR are pointed out (circle), and *vice-versa* (square). In c, d the fluorescence patterns predominantly co-localize (squares).

previous imaging data a lowered NR fluorescence of **P1**, factor 0.7, compared to **P2** was observed. The NR release from the **P1** and **P2** NPs in PC-3 cells and in the presence of catalase (H_2O_2 scavenger agent) was also performed (see the ESI† for methods). A similar NR release from **P2** NPs (non-responsive) was observed *i.e.*, independent of catalase (Fig. S14b†), however, from the responsive **P1** NPs the NR release is prevented in the presence of catalase (Fig. S14a†) demonstrating the specificity of the **P1** NPs to release the drug in the presence of H_2O_2 (Fig. S14a and c†). In conclusion, the FC data acquired in PC-3 cancer cells (with and without catalase) and non-cancer HF cells indicated a ROS-induced degradation of **P1**, and demonstrated the polymer's potential to specifically trigger the cargo release in an ROS-rich intracellular environment. As the released NR inside the cells can interact with hydrophobic cell structures and partially recover fluorescence, released NR is never fully quenched and some residual fluorescence can be visualized by microscopy.

To show the NR release *via* co-localization in FLIM microscopy, a second dye Alexa Fluor® 647 (Alx647) azide was covalently bound to the clickable alkyne linker of **P1** *via* the click reaction (see ESI Fig. S15 and S16†). NR was physically entrapped into the Alx647-labeled NPs as described previously. With two fluorophores the intracellular fate of the cargo (NR) and the polymer (stained covalently with Alx647) could be tracked independently. The two dyes were visualized after separate excitation at 485 nm (NR) and 640 nm (Alx647). The co-localization of **P1** NPs and the NR cargo after 8 h incubation in PC-3 (Fig. 5a and b) and HF cells (Fig. 5c and d) was compared.

Analysis of the lifetime τ (see the ESI† for method) clearly differentiated the free NR (τ 4.2 ± 0.3 ns, exc. at 485 nm) from the NPs marked with Alx647 (τ 2.2 ± 0.1 ns, exc. at 640 nm).

After 1 h incubation of PC-3 cells with dual-marked **P1** NPs, both NPs and NR were highly co-localizing and hardly any release of NR was observed (see ESI Fig. S17†). But after incubation in PC-3 cells for 8 hours, the cytoplasm was more homogeneously colored with the released NR (Fig. 5a), while the polymer was clustered up in few locations (Fig. 5b). Oppositely in HF cells only a little homogeneous NR fluorescence was visible outside the NPs after 8 h incubation (Fig. 5c), and the NR co-localized with the polymer to a high extent (Fig. 5d). However, after 8 h even in ROS-producing PC-3 cells the NPs likely were not fully degraded and the cells still contained NP-loaded NR as well (see the ESI†). In line with the findings after separate excitation, after simultaneous excitation at 485 nm and 640 nm the spread fluorescence of released NR was visible in PC-3 but barely in HF cells, and the co-localization of not-yet released NR with the particles was visible in HF but not in PC-3 cells (Fig. 6a and b).

This indicates that the **P1** polymer NPs can be used for selective cargo release to PC-3 cancer cells, with the release

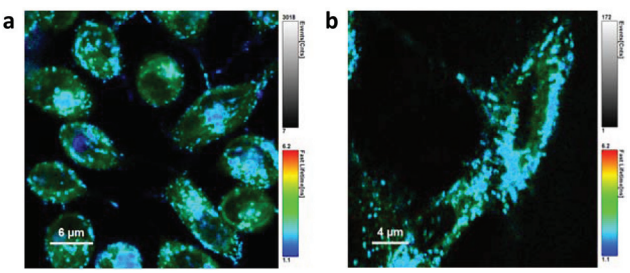

Fig. 6 FLIM images of PC-3 (a) and HF (b) cells after 8 h incubation with dual-marked **P1** NPs, color-coded by the averaged obtained lifetime per pixel. The localization of the polymer (covalently bound Alx647, tau *ca.* 2 ns, shown in blue) and of released Nile Red (spread throughout the cell, tau *ca.* 4 ns, shown in green), and local overlap of lifetimes (turquoise tones) was visualized after simultaneous excitation at 485 nm and 640 nm.

rate in non-cancer HF cells being lower than that in the cancer cells with higher ROS levels.

Finally, to investigate the inhibitory effect on tumor cells, the ROS-responsive (**P1**) and non-responsive counterpart (**P2**) NPs were loaded with the antitumor drug paclitaxel (PTX) with an overall cargo content of ~2.2 wt% and a loading efficiency of 94% (see the ESI†). Firstly, because stimuli-responsive NPs have been shown to have environment-dependent PTX release behavior,[38,39] the *in vitro* PTX release from **P1** and **P2** NPs was evaluated in the presence of H_2O_2 (1 mM) and in PBS (pH 7.4) (see the ESI† for methods). The PTX release from the NPs was similar to the NR release (Fig. S10†) where after 24 h the PTX release from the ROS-responsive NPs was ~2.5 times faster than the PTX release from their non-ROS-responsive counterparts (Fig. S19†).

Further, the alamarBlue® viability assay was used to evaluate the cytotoxicity of the PTX-loaded **P1** and **P2** NPs in cancer cell lines and in HF cells.

For this study various cancer cell lines, which are known for increased ROS production, such as human cervix carcinoma (HeLa),[37] colorectal adenocarcinoma (DLD1)[40] and prostate cancer (PC-3)[34] cells were used and the NP cytotoxicity was compared with that found for the HF fibroblast cells as low ROS controls (see the ESI† for methods). The drug-loaded NPs were incubated with the ROS-producing cells and with HF cells for 24 up to 72 h. Both NPs were at all times more toxic than the free drug (Fig. S20 and S22, ESI†), which is generally attributed to the fact that the vast majority of the freely administered drug molecules are bound to serum proteins.[41] Incubation of PC-3 and HF cells for 48 h showed a comparable toxic effect of the PTX-loaded **P1** and **P2** NPs (Fig. S20†). Note that the polymer material itself had no relevant effect on cell viability (Fig. S21, ESI†). As another test in HeLa cells had confirmed that NP toxicity steeply increases with the incubation time (raised from 12 h to 96 h in HeLa cells, see Fig. S22, ESI†), the difference in toxicity of **P1** and **P2** NPs could become more significant after longer incubation times (under conditions of extensive ROS-triggered NP degradation). Indeed after incubation for 72 h the higher toxicity of the PTX-loaded **P1** NPs compared to **P2** NPs was visible. The superior toxicity of the ROS-responsive NPs may be expected to be more prominent after a longer incubation time, because a longer incubation will increase the amount of internalized NPs, the timespan for ROS-triggered drug release and the exposure of cells to the drug. PC-3, HeLa and DLD1 cancer cells were incubated for 72 h with the NPs under standard cell culture conditions and in a second test under conditions of a low serum content of 2% in the medium (Fig. 7). Cell viability was not affected by the reduced serum content (data not shown). However, low serum content is known to enhance the overall uptake rate of the NPs,[42] which in return might further enhance the superior toxicity of **P1** NPs for cancer cells.

In all three cancer cell lines including the experiments in medium with 2% and with 10% serum content, the toxicity of the ROS-responsive **P1** NPs was higher than that of non-responsive **P2** NPs. The viability testing demonstrated herein

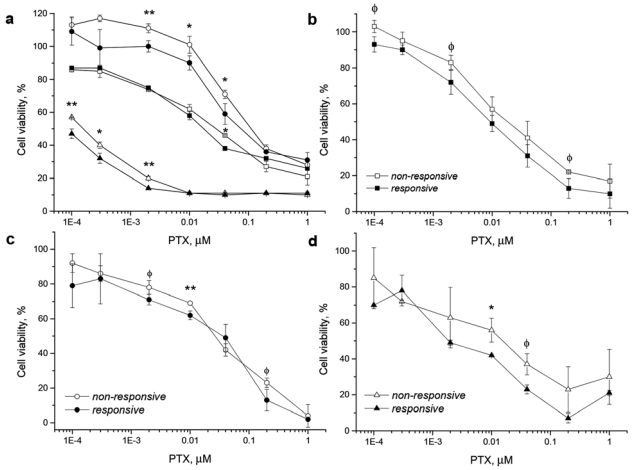

Fig. 7 Incubation of PTX-loaded ROS-responsive **P1** (filled marker) and non-responsive **P2** (hollow marker) particles with DLD1 (circle), PC-3 (square), and HeLa (triangle) cells for 72 h in medium with 10% serum (a). Similar testing was done in medium with only 2% of serum, comparing again the cell lines PC-3 (b), DLD1 (c) and HeLa (d) cells after 72 h incubation. Significant differences: **<0.05; *<0.1; $^{\phi}$<0.2 (ANOVA).

that under the studied conditions the PTX-loaded ROS-responsive NPs appear more cytotoxic in tumor cells than their non-responsive counterpart NPs (Fig. 7).

To summarize, we have shown evidence that fluorescent polymer NPs, bearing pinacol-type boronic ester linkers trigger self-immolative polymer degradation and subsequently release the cargo drug in the presence of ROS concentrations typically present in an intracellular environment of certain tumor cells. Co-localization studies evidenced that the **P1** polymer NPs can be used for selective cargo release to PC-3 cancer cells, with the release rate in non-cancer HF cells being lower. Finally the drug-loaded ROS-responsive NPs were shown to be more cytotoxic to tumor cells compared to their non-responsive counterparts making the presented polymer a promising candidate for applications as the delivery system and the imaging agent (theranostics) aimed at inflamed microenvironments and cancer tissue.

Acknowledgements

Financial support from Norwegian Grants (grant # 7F14009), the Ministry of Industry and Trade of the Czech Republic (grant # FR-TI4/625) and the Ministry of Education, Youth and sports (grant # LH14292; grant POLYMAT # LO1507) is gratefully appreciated. The electron microscopy at the Institute of Macromolecular Chemistry was supported through the Technology Agency of the Czech Republic (grant #TE01020118).

Notes and references

1 Y. Wu, D. Zhou, Y. Qi, Z. Xie, X. Chen, X. Jing and Y. Huang, *RSC Adv.*, 2015, **5**, 3523.

2 H. Cho, J. Bae, V. K. Garripelli, J. M. Anderson, H.-W. Jun and S. Jo, *Chem. Commun.*, 2012, **48**, 6043.
3 S. Petrova, E. Jäger, R. Konefal, A. Jäger, C. G. Venturini, J. Špěváček, E. Pavlova and P. Štěpánek, *Polym. Chem.*, 2014, **5**, 3884.
4 H. Chen, W. He and Z. Guo, *Chem. Commun.*, 2014, **50**, 9714.
5 H.-L. Pu, W.-L. Chiang, B. Maiti, Z.-X. Liao, Y.-X. Ho, M. S. Shim, E. Y. Chuang, Y. Xia and H.-W. Sung, *ACS Nano*, 2014, **8**, 1213.
6 D. Lee, S. Khaja, J. C. Velasquez-Castano, M. Dasari, C. Sun, J. Petros, W. R. Taylor and N. Murphy, *Nat. Mater.*, 2007, **10**, 765.
7 B. D'Autréaux and M. B. Toledano, *Nat. Rev. Mol. Cell Biol.*, 2007, **8**, 813.
8 A. Mantovani, P. Allavena, A. Sica and F. Balkwill, *Nature*, 2008, **454**, 436.
9 S. Reuter, S. C. Gupta, M. M. Chaturvedi and B. B. Aggarwal, *Free Radicals Biol. Med.*, 2010, **49**, 1603.
10 N. Houstis, E. D. Rosen and E. S. Lander, *Nature*, 2006, **440**, 944.
11 B. Uttara, A. V. Singh, P. Zamboni and R. T. Mahajan, *Curr. Neuropharmacol.*, 2009, **7**, 65.
12 W. Zhao, *Angew. Chem., Int. Ed.*, 2009, **48**, 3022.
13 M. Giorgio, M. Trinei, E. Migliaccio and P. G. Pelicci, *Nat. Rev. Mol. Cell Biol.*, 2007, **8**, 722.
14 S. Toyokuni, K. Okamoto, J. Yodoi and H. Hiai, *FEBS Lett.*, 1995, **358**, 1.
15 T. P. Szatrowski and C. F. Nathan, *Cancer Res.*, 1991, **51**, 794.
16 G.-Y. Liou and P. Storz, *Free Radical Res.*, 2010, **44**, 479.
17 G. Waris and H. Ahsan, *J. Carcinog.*, 2006, **5**, 14.
18 P. T. Schumacker, *Cancer Cell*, 2006, **10**, 175.
19 M. López-Lázaro, *Cancer Lett.*, 2007, **252**, 1.
20 W. Dröge, *Physiol. Rev.*, 2002, **82**, 47.
21 B. Kumar, S. Koul, L. Khandrika, R. B. Meacham and H. K. Koul, *Cancer Res.*, 2008, **68**, 1777.
22 E. Lallana and N. Tirelli, *Macromol. Chem. Phys.*, 2013, **214**, 143.
23 C. de G. Lux, S. Joshi-Barr, T. Nguyen, E. Mahmoud, E. Schopf, N. Fomina and A. Almutairi, *J. Am. Chem. Soc.*, 2012, **134**, 15758.
24 M. S. Shim and Y. Xia, *Angew. Chem., Int. Ed.*, 2013, **52**, 6926.
25 E. A. Mahmoud, J. Sankaranarayanan, J. M. Morachis, G. Kim and A. Almutairi, *Bioconjugate Chem.*, 2011, **22**, 1416.
26 D. Jeanmaire, J. Laliturai, A. Almalik, P. Carampin, R. D'Arcy, E. Lallana, R. Evans, R. E. P. Winpeny and N. Tirelli, *Polym. Chem.*, 2015, **5**, 1393.
27 A. Savina, A. Peres, I. Cebrian, N. Carmo, C. Moita, N. Hacohen, L. F. Moita and S. Amigorena, *Immunity*, 2009, **30**, 544.
28 B. C. Dickinson and C. J. Chang, *J. Am. Chem. Soc.*, 2008, **130**, 9638.
29 E. Jäger and F. C. Giacomelli, *Curr. Top. Med. Chem.*, 2015, **15**, 328.
30 F. C. Giacomelli, P. Štěpánek, C. Giacomelli, V. Schmidt, E. Jäger, A. Jäger and K. Ulbrich, *Soft Matter*, 2011, **7**, 9316.
31 A. Jäger, D. Gromadzki, E. Jäger, F. C. Giacomelli, A. Kozlowska, L. Kobera, J. Brus, B. Říhová, M. El Fray, K. Ulbrich and P. Štěpánek, *Soft Matter*, 2012, **8**, 4343.
32 T. Hu and C. Wu, *Phys. Rev. Lett.*, 1996, **83**, 4105.
33 J. Fu and C. Wu, *J. Polym. Sci., Part B: Polym. Phys.*, 2001, **39**, 703.
34 B. Kumar, S. Koul, L. Khandrika, R. B. Meacham and H. K. Koul, *Cancer Res.*, 2008, **68**, 1777.
35 U. E. Martinez-Outschoorn, R. M. Balliet, Z. Lin, D. Whitaker-Menezes, A. Howell, F. Sotgia and M. P. Lisanti, *Cell Cycle*, 2012, **11**, 4152.
36 M. P. Lisanti, U. E. Martinez-Outschoorn, Z. Lin, S. Pavlides, D. Whitaker-Menezes, R. G. Pestell, A. Howell and F. Sotgia, *Cell Cycle*, 2011, **10**, 2440.
37 R. S. Bhimani, W. Troll, D. Grunberger and K. Frenkel, *Cancer Res.*, 1993, **53**, 4528.
38 Y. Shi, C. F. van Nostrum and W. E. Hennink, *ACS Biomater. Sci. Eng.*, 2015, **1**, 393.
39 W. Chen, F. Meng, R. Cheng and Z. Zhong, *J. Controlled Release*, 2010, **142**, 40.
40 J. M. Lluis, F. Buricchi, P. Chiarugi, A. Morales and J. C. Fernandez-Checa, *Cancer Res.*, 2007, **67**, 7368.
41 D. A. Smith, L. Di and E. H. Kerns, *Nat. Rev. Drug Discovery*, 2010, **9**, 929.
42 G. Baier, C. Costa, A. Zeller, D. Baumann, C. Sayer and P. H. Araujo, *Macromol. Biosci.*, 2011, **11**, 628.

Nanoscale

Electronic Supporting Information for

Fluorescent boronate-based polymer nanoparticles with reactive oxygen species (ROS)-triggered cargo release for drug-delivery applications

Eliezer Jäger,[a,*] Anita Höcherl,[a,*] Olga Janoušková,[a] Alessandro Jäger,[a] Martin Hrubý,[a] Rafal Konefal,[a] Miloš Netopilik,[a] Jiří Pánek,[a] Miroslav Šlouf,[a] Karel Ulbrich[a] and Petr Štěpánek[a]

[a.] *Institute of Macromolecular Chemistry v.v.i., Academy of Sciences of the Czech Republic, Heyrovsky Sq. 2, 162 06 Prague 6, Czech Republic.*

Email: jager@imc.cas.cz; höcherl@imc.cas.cz

Tel: +420 296 809 322;

Materials:

Propargyl bromide solution (~ 80% in toluene), 2,6-bis-(hydroxymethyl)-*p*-cresol (95 %), imidazole (≥ 99.5 %), tert-butyldimethylsilyl chloride (97 %), anhydrous pyridine anhydrous (99.8 %), triethylamine (≥ 99.5 %) Nile Red (microscopy grade), 2,7-dichlorodihydrofluorescein diacetate and copper (I) iodide (99.999 %) were obtained from Sigma-Aldrich (Czech Republic, CZ) and were used without further purification. Pimeloyl chloride 98 % (Sigma-Aldrich/CZ) was distilled under reduced pressure right before use. Alexa Fluor® 647 was purchased from Life Technologies (Czech Republic, CZ). Paclitaxel was purchased from Aurisco (China). All solvents, unless otherwise stated, were used without further purification. PC-3, HeLa, HF and DLD1 cells were obtained from American Type Cell Culture (ATCC) and cultured according ATCC guidelines.

^{1}H NMR and ^{13}C NMR Instruments

^{1}H NMR and ^{13}C NMR spectra of the monomers (300 and 600 MHz, respectively) were obtained using a Bruker Avance DPX 300 MHz NMR spectrometer or Bruker 600 MHz NMR spectrometer with $CDCl_3$ or d_6-DMSO as solvents at 25 °C and at 37 °C for polymer degradation studies. The chemical shifts are relative to TMS using hexamethyldisiloxane (HMDSO, 0.05 and 2.0 ppm from TMS in ^{1}H NMR and ^{13}C NMR spectra, respectively) as internal standard. Chemical shifts as, δ, in units of parts per million (ppm).

^{1}H NMR and ^{13}C NMR measurements of the polymer degradation

15 mg of the polymer P-1 were added into 600 µL of d_6-DMSO followed by the addition of 160 µL of deuterated PBS (pH 7.4) buffer solution. The solution was transferred to a NMR tube and incubated at 37 °C. To the solution, 40 µL of H_2O_2 (30 % *w*/*w* solution in H_2O; Sigma-Aldrich - CZ) was added to make a 50 mM solution (in analogy to Almuatiri *et al*., 2012).[1]

Size exclusion chromatography (SEC) analysis

The weight-average molecular weight (M_w), number-average molecular weight (M_n) and the respective polydispersity I = (M_w/M_n) were obtained by size exclusion chromatography (SEC) analysis. The SEC of the isolated polymers was performed at 25 °C with two PLgel MIXED-C columns (300 × 7.5 mm, SDV gel with particle size 5 µm;

Polymer Laboratories, USA) and with UV (UVD 305; Watrex, Czech Republic) and RI (RI-101; Shodex, Japan) detectors. *N*,*N*-Dimethylformamide (Sigma-Aldrich, Czech Republic) with LiBr (0.01 % *v*/*v*) was used as a mobile phase at a flow rate of 1 mL·min^{-1}. The molecular weight values were calculated using Clarity software (Dataapex, Czech Republic). Calibration with PMMA standards was used.

SEC analysis of polymer degradation.

P-1 and P-2 polymers solutions were prepared by dissolving 6 mg of the polymers in a mixture of 1.625 mL of DMF-PBS (pH 7.4, 80/20 *v*/*v*). The aqueous H_2O_2 (30 % *w*/*w* solution in H_2O) was added to reach the final hydrogen peroxide concentration of 200 µM, 500 µM, 1 mM and 5 mM, respectively. Aliquots of 250 µL were taken after 24 h, 1 day, 3 days and 4 days, respectively and evaporated to dryness. The DMF (350 µL, containing 0.01 % LiBr) was added and the filtered solutions (0.22 µM PVDF, Millipore® – Czech Republic) were injected (20 µL) into the SEC instrument. No hydrolysis in the absence of H_2O_2 of the tested polymers over 4 days was observed.

Scattering techniques

The dynamic light scattering (DLS) measurements were performed using an ALV CGE laser goniometer consisting of a 22 mW HeNe linear polarized laser operating at a wavelength (λ = 632.8 nm), an ALV 6010 correlator, and a pair of avalanche photodiodes operating in the pseudo cross-correlation mode. The samples were loaded into 10 mm diameter glass cells and maintained at 25 $\pm$ 1 °C. The data were collected using the ALV Correlator Control software and the counting time was 30 s. The measured intensity correlation functions $g_2(t)$ were analysed using the algorithm REPES[2] resulting in the distributions of relaxation times shown in equal area representation as τ A(τ). The mean relaxation time or relaxation frequency ($\Gamma = \tau^{-1}$) is related to the diffusion coefficient (D) of the nanoparticles as $D = \frac{\Gamma}{q^2}$ where $q = \frac{4\pi n \sin\frac{\theta}{2}}{\lambda}$ is the scattering vector with n the refractive index of the solvent and θ the scattering angle. The hydrodynamic radius (R_H) or the distributions of R_H were calculated by using the well-known Stokes-Einstein relation:

$$R_H = \frac{k_B T}{6\pi\eta D} \quad \text{(eq. S1)}$$

with k_B the Boltzmann constant, T the absolute temperature and η the viscosity of the solvent.

The polydispersity of the nanoparticles was accessed by using the cumulant analysis[2] of the correlation functions measured at 90 ° as:

$$\ln g_1(t) = \ln C - \Gamma t + \frac{\mu_2}{2} t^2 .... \quad \text{(Eq. S2)}$$

wherein C is the amplitude of the correlation function and Γ is the relaxation time (τ^{-1}). The parameter μ_2 is known as the second-order cumulant and it was used to compute the polydispersity index of the samples (PDI = μ_2/Γ^2).

In the static light scattering (SLS), the scattering angle was varied from 30 to 150° with a 10° stepwise increase. The absolute light scattering is related to weight-average molar mass (M_w(NP)) and to the radius of gyration (R_G) of the nanoparticles by the Zimm formalism represented as:

$$\frac{K_c}{R_\theta} = \frac{1}{M_{w(NP)}}\left(1 + \frac{R_{Gq}^2}{3}\right) \quad \text{(eq. S3)}$$

where K is the optical constant which includes the square of the refractive index increment (dn/dc), R_θ is the excess normalized scattered intensity (toluene was applied as standard solvent) and c is the polymer concentration given in mg·mL^{-1}. The refractive index increment (dn/dc) of the P-1 NPs in PBS (0.148 mL·g^{-1}) was determined using a Brice-Phoenix differential refractometer operating at λ = 632.8 nm.

Transmission electron microscopy (TEM)

The TEM observations were carried out on a Tecnai G2 Spirit Twin 120kV (FEI, Czech Republic). Two microliters of P-1 NPs (1 mg·mL; 1 mM of H_2O_2 for the P-1 after 48 h incubation) were dropped onto a copper TEM grid (300 mesh), which was coated with thin, electron-transparent carbon film. After 1 min the solution was sucked out by touching the bottom of the grid with filtering paper. This fast removal of the solution was performed in order to minimize oversaturation during the drying process; this step was found necessary to preserve the structure of nanoparticles. The NPs were negatively stained with uranyl acetate (2 µL of 1 wt.% solution dropped onto the dried nanoparticles and sucked out after 1 min, using the same way that was described above). The sample was left to dry completely at ambient temperature and then observed in the TEM microscope using bright field imaging. Under these conditions, the micrographs display dark, negatively stained background with bright spots, which correspond to the investigated nanoparticles.

Synthesis of the polymer precursors and monomers

Synthesis of the monomer 1

The monomer 1 and its precursors were synthesized according previously published methodology of Almutairi *et. al*., 2012.[1]

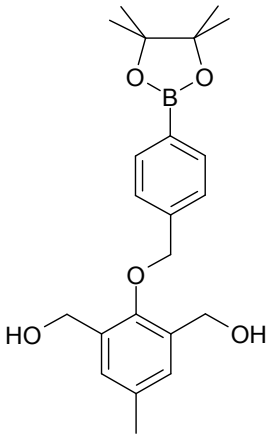

^{1}H NMR ($CDCl_3$): δ 7.89 (*d*, 2H), 7.49 (*d*, 2H), 7.22 (*s*, 2H), 5.03 (*s*, 2H), 4.73 (*s*, 4H), 2.39 (*s*, 3H), 1.74 (*s*, 2H), 1.42 (*s*, 12H). ^{13}C NMR ($CDCl_3$): δ 152.86, 140.01, 135.32, 134.65, 134.03, 129.83, 127.34, 84.05, 76.73, 61.31, 25.02, 20.99.

Synthesis of the monomer 2

Synthesis of the precursor 1: 2,6-Bis-(hydroxymethyl)-*p*-cresol (10 g, 57.7 mmol) and imidazole (8.90 g, 130.7 mmol) were dissolved in 40 mL of dry DMF and cooled to 0°C. tert-Butyldimethylsilyl chloride (TBDMSCl) (19.72 g, 126.9 mmol) dissolved in 30 mL of dry DMF was added dropwise. The reaction mixture was stirred for 2 h at room temperature and monitored by TLC by using hexane-ethyl acetate (95:5) v/v as a mobile phase. After completion, the reaction mixture was diluted with Et_2O and the organic layer was washed 3 times with water. The organic layer was separated, dried over Na_2SO_4 and evaporated under reduced pressure. The crude product was purified by flash-chromatography on silica gel using hexane-ethyl acetate (95:5) v/v as a mobile phase to give **compound 1** (21.65 g, 95 %) as a colorless oil.

^{1}H NMR ($CDCl_3$): δ 7.89 (*d*, 2H), 7.49 (*d*, 2H), 7.22 (*s*, 2H), 5.03 (*s*, 2H), 4.73 (*s*, 4H), 2.39 (*s*, 3H), 1.74 (*s*, 2H), 1.42 (*s*, 12H). ^{13}C NMR ($CDCl_3$): δ 152.86, 140.01, 135.32, 134.65, 134.03, 129.83, 127.34, 84.05, 76.73, 61.31, 25.02, 20.99.

Synthesis of the precursor 2: To a stirred suspension of the precursor 1 (5.59 g, 14.1 mmol) and potassium carbonate (5.0 g, 36.2 mmol) in DMF (20 mL) was added propargyl bromide (1.9 mL, 16 mmol, 80% solution in toluene) and the reaction mixture was stirred for 12 h at room temperature. The reaction mixture was quenched with H_2O (200 mL) and extracted with Et_2O (3 x 50 mL). Combined extracts were washed with aqueous NaCl solution (10 wt.%, 2 x 50 mL), dried over $MgSO_4$, and solvent was removed under vacuum. The residue was purified by flash column chromatography (gradient elution 20:1 → 15:1 hexanes:ethyl acetate) to afford precursor 2 (5.86 g, quantitative) as a yellow liquid.

^{1}H NMR (300 MHz, CDCl3): δ 6.93 (*d*, J = 8.8 Hz, 2H), 6.85 (*d*, J = 8.8 Hz, 2H), 4.64 (*d*, J = 2.2 Hz, 2H), 3.77 (*s*, 3H), 2.51 (*t*, J = 2.4 Hz, 1H); ^{13}C NMR (300 MHz, $CDCl_3$) δ 154.5, 151.7, 116.1, 114.6, 78.9, 75.3, 56.6, 55.7.

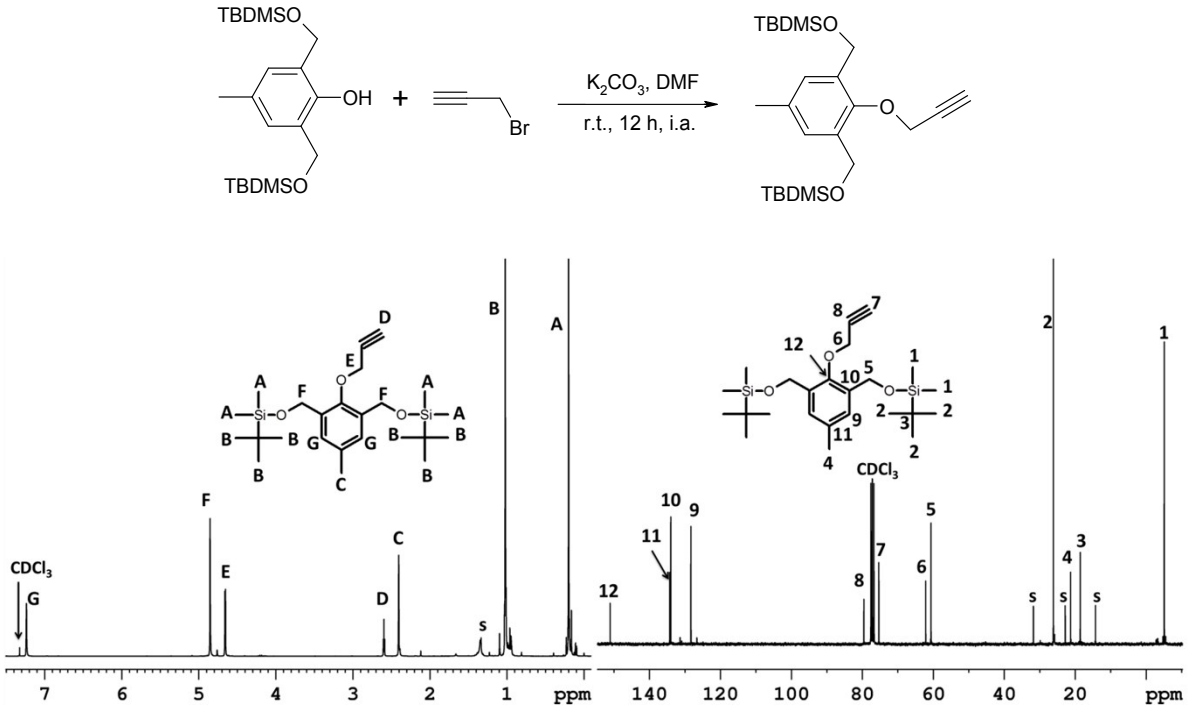

Fig. S1.: ^{1}H NMR (left) and ^{13}C NMR (right) of the synthesized precursor 2.

Removal of the protecting group of the precursor 2

Precursor 2 (2.5 g, 5.75 mmol) was dissolved in 10 mL of methanol. Catalytic amount of pTsOH was added. The reaction mixture was stirred at room temperature overnight and monitored by TLC (Hex/EtOAc 1:1). After completion of the conversion, the solvent was removed under reduced pressure. The product was purified by chromatography on silica gel (hexane-ethyl acetate 1:1 v/v) to give monomer 2 (1.12 g, 94 %) as a white solid.

^{1}H NMR (DMSO): δ 7.18 (*s*, 2H), 5.08 (*s*, 2H), 4.61 (*d*, 2H), 4.57 (*s*, 4H), 3.59 (*t*, 1H), 2.32 (*s*, 3H). ^{13}C NMR (DMSO): δ 151.07, 135.41, 133.53, 128.28, 80.51, 78.64, 62.01, 58.64, 21.32.

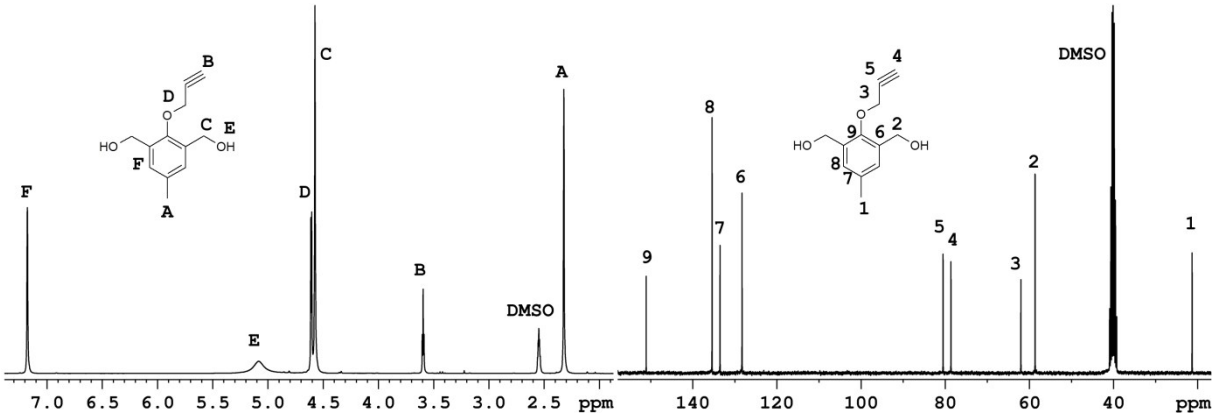

Fig. S2.: ^{1}H NMR (left) and ^{13}C NMR (right) of the synthesized monomer 2.

Synthesis of the polymer 1

To a *N*,*N*-dimethylacetaide (DMA) solution of the synthesized monomer 1 (576 mg, 1.5 mmol), monomer 2 (288.32 mg, 1.5 mmol) and pyridine (3.0 mL, 37 mmol), pimeloyl chloride (591.2 mg, 3 mmol) in DMA (25 mL) was added dropwise over 10 minutes at room temperature. The reaction was stirred at room temperature for 24 h. The slurry was them dialyzed (Spectra/Por dialysis membrane, 6-8 kD MWCO) for 72h in water (water changed after every 12h). The precipitate was further purified by dissolution in dichloromethane (DCM) and precipitation into cold

EtOH. The polymer was recovered and dried under vacuum (48 h) (1.25 g, 72 %) being obtained as a yellow solid. Weight-average molecular weight (M_w), number-average molecular weight (M_n) and polydispersity index (PDI) of the synthesized polymer was determined to be 21 500 Da (M_w), 14 300 Da (M_n) and 1.49 (PDI), respectively, by SEC measurements using polystyrene standards (discussed hereafter).

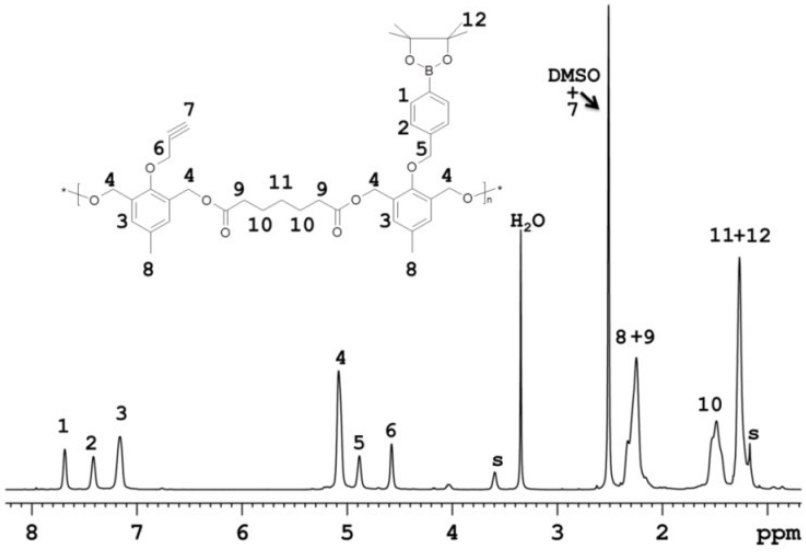

Fig. S3.: ^{1}H NMR of the synthesized polymer 1 (P1) in d_6-DMSO.

Synthesis of the polymer 2

To a DMA solution of the synthesized monomer 2 (288.32 mg, 1.5 mmol) and pyridine (2.0 mL, 24.7 mmol), pimeloyl chloride (295.6 mg, 1.5 mmol) was added dropwise over 10 minutes at room temperature. The reaction was stirred at room temperature for 24 h. The slurry was them dialyzed (Spectra/Por dialysis membrane, 6-8 kD MWCO) for 72h in water (water changed after every 12h). The precipitate was further purified by dissolution in DCM and precipitation into cold EtOH. The polymer was recovered and dried under vacuum (48 h) (396.5 mg, 68 %) being obtained as a yellow solid. Weight-average molecular weight (M_w), number-average molecular weight (M_n) and polydispersity index (PDI) of the synthesized polymer was determined to be 21 200 Da (M_w), 12 900 Da (M_n) and 1.64, respectively, by SEC measurements using polystyrene standards (Fig. S5, black lines).

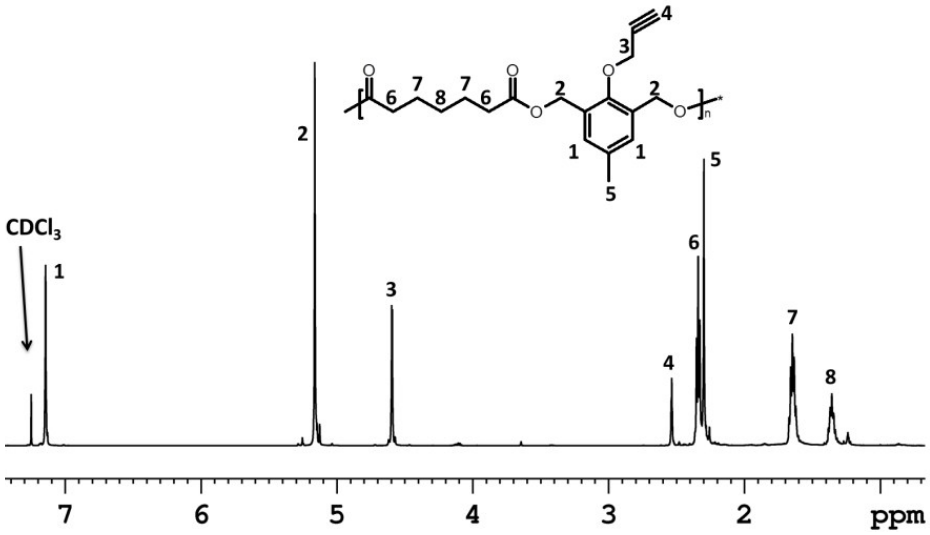

Fig. S4.: ^{1}H NMR of the synthesized counterpart polymer 2 (P2) in $CDCl_3$.

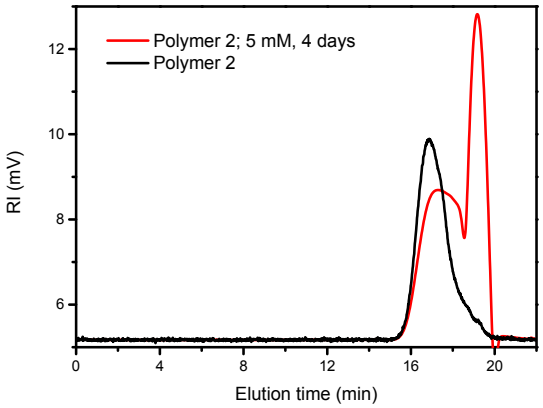

Fig. S5.: SEC chromatograms of P2 prior to the addition of H_2O_2 (black line) and after degradation in 20% PBS/DMF solutions containing 5 mM of H_2O_2 incubated at 37 °C for 4 days (red line).

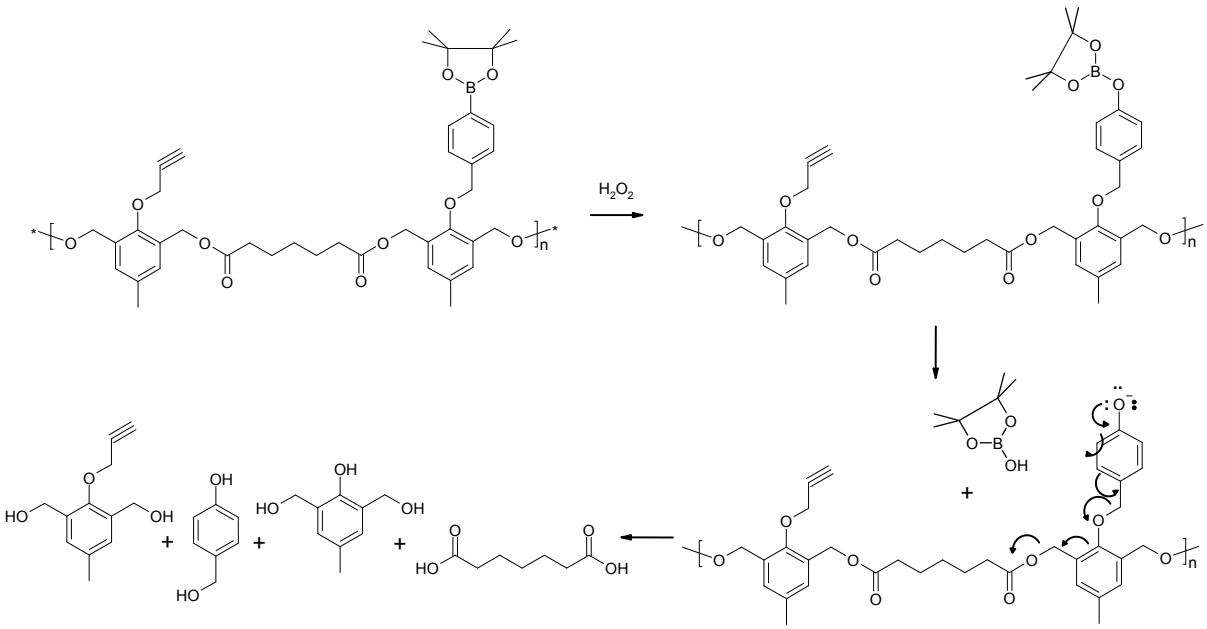

Scheme S1.: Mechanism of P1 polymer degradation triggered by H_2O_2.

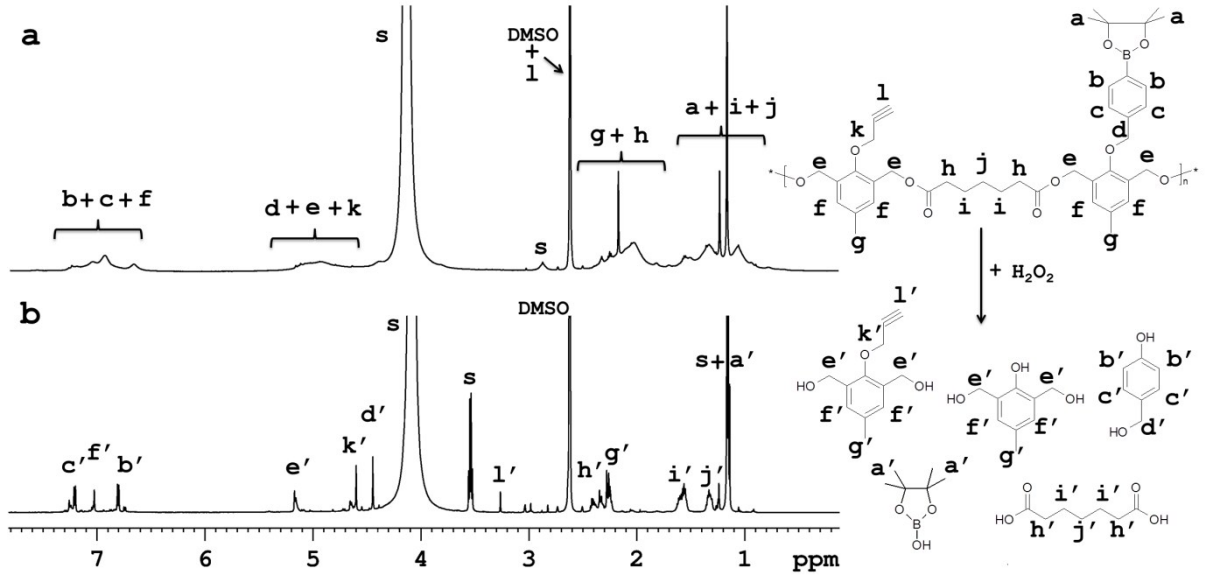

Fig. S6.: ^{1}H NMR spectra of polymer 1 in d_6-DMSO, deuterium PBS (a) without H_2O_2 and (b) incubated with 50 mM H_2O_2 after 5 days at 37 °C. “s” refers to solvent peaks (HDO in D_2O and ethanol).

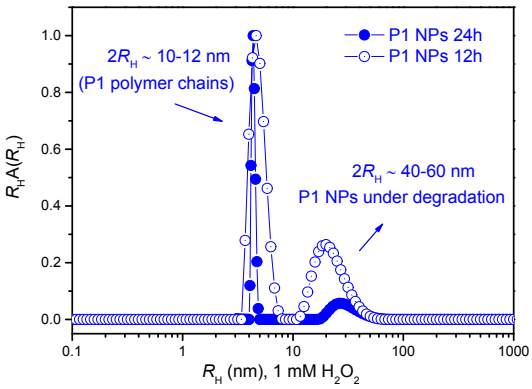

Fig. S7.: Volume-weighted distributions of R_H for P1 after 12h (○) and 24 h (●) of incubation in 1 mM of H_2O_2.

Nile Red assays

Nile Red calibration curves

The amount of Nile Red in the P-1 and P-2 polymers was quantified by fluorescence spectroscopy (JASCO spectroscopy, Model FP-6200 Spectrofluorometer) as described below.

Nanoparticles preparation: Blank and Nile-Red (NR) loaded NPs (NR-NPs)

To 5 mL of a solution of P-1 or P-2 (20 mg) and Nile Red (50 µg) in acetone, 10 mL of PBS (containing 0.01 % tween 80) were added as precipitant. The remaining acetone was removed by evaporation and the final volume of the NPs was concentrated to 5 mg·mL^{-1}. Afterwards the NPs solution was washed twice with PBS by using centrifugation/filtration (Amicon 10 kDa – MilliPore, Czech Republic). The final NR content on the NPs was adjusted to 8.05 µg·mL^{-1} of NR in PBS (0.2 wt % polymers). Blank NPs were prepared by the same procedure, however, with no NR addition (Fig. 2b).

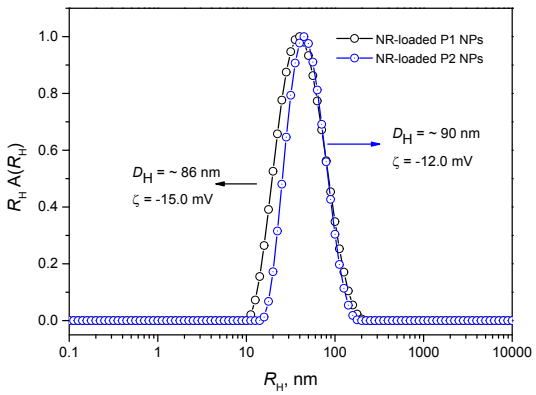

Fig. S8.: Distributions of R_H and ζ-potential values for P1 (○) and P2 (○) NR-loaded NPs.

EE determined by Nile red fluorescence.

P-1 and/or P-2 NPs encapsulating Nile red were dissolved in a mixture of acetone:H_2O (95 : 5) to release Nile red into the solution. Nile red fluorescence intensity was measured (excitation at 530 nm, emission at 605 nm) and the amount of dye encapsulated was determined according to the calibration curve presented in Fig. S8. All calibration curves were obtained by measuring fluorescence of various concentrations of Nile red in acetone. Linear regression of peak area *versus* concentration yielded the curve.

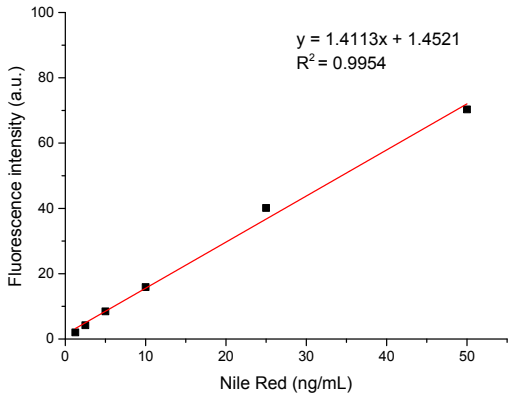

Fig. S9. Calibration curve for Nile Red fluorescence.

Nile-Red release experiments

To 5 mL vials the P-1 or P-2-loaded NR-NPs (250 µg of polymer – 0.5 µg NR) in PBS (pH ~ 7.4) were added and dissolved to 5 mL with PBS aqueous buffer (pH ~ 7.4). Afterwards H_2O_2 was added to reach the concentration of 1 mM and the vials were incubated at dark at 37 °C along 24 h. Aliquots were removed and directly quantified as described above. The release experiments were performed in 3 replicates at various time points. The neglected fluorescence interaction between NR and H_2O_2 was previously demonstrated by Almutari *et al*., 2012.[1]

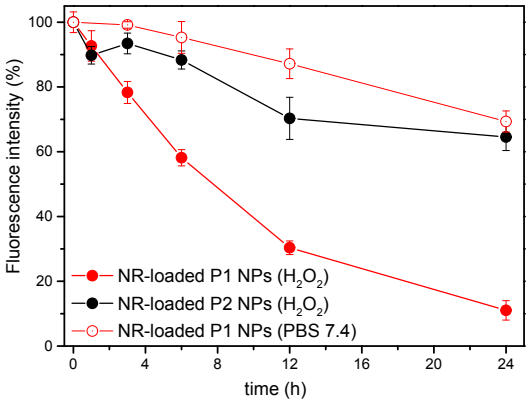

Fig. S10.: Nile Red (NR) release from the ROS-responsive P1 NPs (red filled circles) and from the ROS-non-responsive counterpart P2 NPs (black filled circles) along 24 h incubation in 1 mM H_2O_2 at 37 °C. (Open circles shows the NR release from the responsive P1 NPs in phosphate buffer saline (PBS) pH 7.4 at 37 °C along 24h).

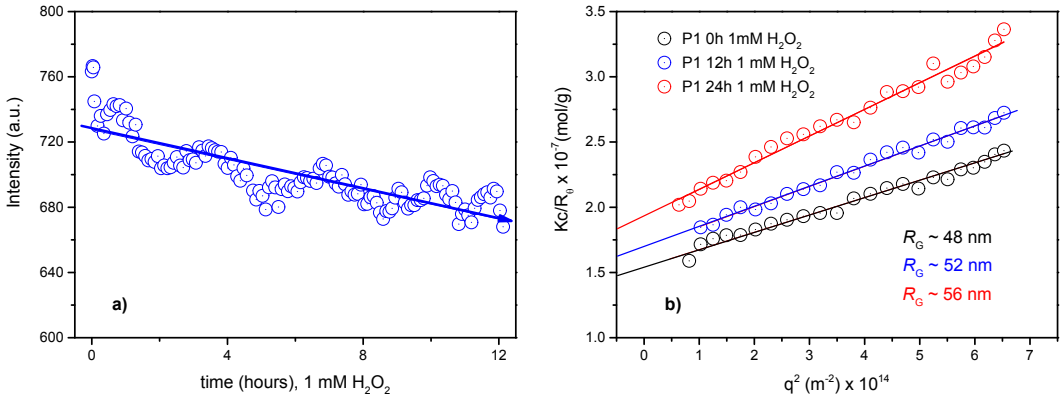

Fig. S11. Overall scattering intensity (a) and (b) static light scattering measurement (Kc/R_θ *vs.* q^2) for P1 NPs (1.0 mg·mL^{-1}) in PBS (pH ~ 7.4) under incubation with 1 mM of H_2O_2.

Confocal Laser Scanning Microscopy (cLSM) Studies of P1 and P2 NPs internalization in cells

Microscopy data was acquired at a confocal laser scanning microscope FV10-ASV (Olympus Europe, Czech Republic) equipped with a FLIM module (PicoQuant, Germany), on a 60x oil objective. The software FV10-ASW and SymphoTime64 from Olympus and PicoQuant, respectively, was used for acquisition and analysis. 10·10^{-3} PC-3 cells per well were seeded in coated Ibidi® 8 well µ-slides (Ibidi, Germany) and left to adhere at least overnight.

The cells were incubated with 200 µg·mL^{-1} of Nile Red-loaded (~ 0.2 % wt) P1 or P2 polymer NPs for 4 h or 20 h. All cells were washed after incubation and topped with PBS for visualization, containing if required 0.5 µg·mL^{-1} of Hoechst 33342 dye. The Hoechst dye (exc. 405 nm, emission in BP425/50), Nile Red (exc. 546 nm, emission in BP610/50) and transmission were visualized. After only 4 h incubation, the ROS-triggered NR release out of P1 particles could not have progressed far, with the majority of NR still entrapped inside the NPs. After 4 h incubation P1 and P2 NPs displayed, as was expected owed to the near identical nature of the particle and material, similar uptake efficiency (*see* Fig. S13). Therefore, the observed difference in NR fluorescence after 20 h incubation (when P1 signals were weaker than P2 signals, *see* Fig. S12b and S12d), the NR quenching is attributed to ROS-mediated P1 degradation and release of NR.

a **b**

c **d**

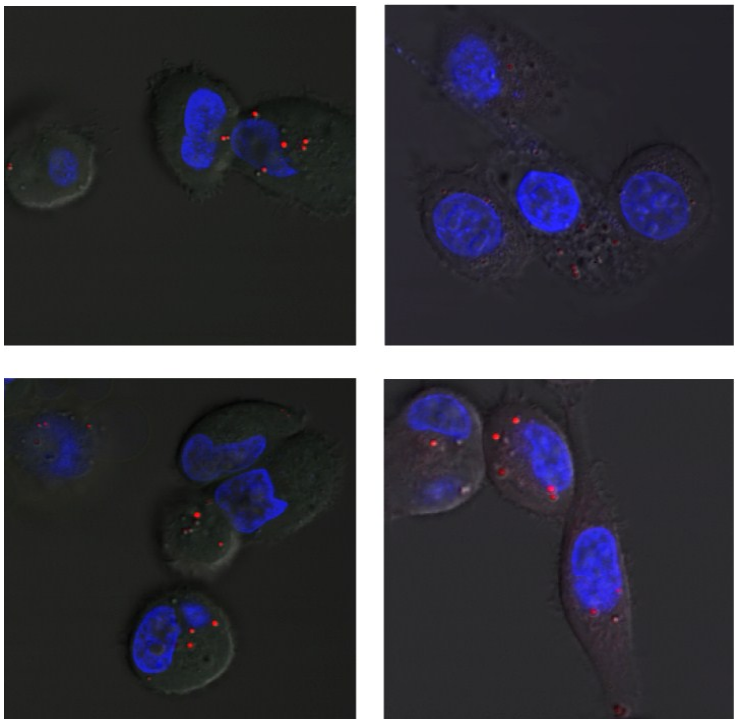

Fig. S12 Confocal microscopy images of Nile Red-loaded P1 NPs (a,b) and P2 NPs (c,d) in PC3 cells after incubation for 4 h (a,c) and 20 h (b,d) at 200 µg·mL^{-1} polymer concentration. Blue the Hoechst-stained nucleus; red the NR.

Flow Cytometry (FC) analysis: In vitro release of Nile Red from internalized NPs

The FC studies were done at a BD FACSverse machine and software FlowJo (FlowJo, Oregon, US) for data analysis. The PC-3 cells were seeded in triplicate in 24 well plates, cell density 50·10^{-3} per well, and left to adhere at least overnight before adding the NPs. HF cells were seeded at a density of 30·10^{-3} per well. After particle incubation cells were washed, trypsinized, and prepared for analysis in PBS supplied with 0.5 µg·mL^{-1} of Hoechst 33342. Hoechst was excited at 405 nm and detected in the UV channel (BP448/45), Nile Red was excited at 488 nm and detected in the PerCP-Cy5.5 channel (BP700/54). At least 10·10^{-3} cells were acquired. In data analysis, after pre-gating in a fluorescence-vs-time graph (to exclude potential flow disturbances), cells were gated subsequently *via* forward scatter area-*vs*-height (singlet duplet distinction), and forward scatters *vs* UV channel (gating on live cells).

HF and PC-3 cells were incubated for 2 h with 200 µg·mL^{-1} of Nile Red-loaded P1 polymer NPs and in a similar setup, PC-3 cells were loaded with NR-loaded P1 or P2 NPs. After washing with buffer, one half of the cell samples was topped with fresh incubation medium (without particles) and returned to the incubator for another 4 hours (samples 't=4h'). The other half of

samples was trypsinized immediately and proceeded to FC analysis (samples 't=0h'). Keeping the second incubation time at 4 h reduces inaccuracy potentially introduced by *e.g.*, cell division and exocytosis of the NPs.[3]

The NR fluorescence of P1 NPs before and after 4 h incubation was compared in HF and in PC-3 cells to track down cancer cell-specific NR quenching caused by ROS-mediated P1 degradation (*see* Fig. 4). Indeed the NR fluorescence in PC-3 cells was quenched more than in the low-ROS HF cells, indicating the triggering of specific cargo release.

Moreover a comparison of the NR fluorescence P1 and P2 NPs in PC3 cells confirmed that both NPs have the same cellular uptake efficiency (*see* Fig. S13). This provided the base for the toxicity studies, where the ROS-triggered release of PTX and the subsequent cell kill efficiency of drug-loaded P1 was compared to the non-responsive P2 NPs system.

The remaining fluorescence in P2 NPs was x 1.3 higher than the remaining NR fluorescence in P1 NPs after incubation in PC-3 cells. Therefore these findings also demonstrated that the P1 NPs can selectively release their cargo in the presence of ROS *e.g.*, to a higher extent than the non-responsive P2 NPs.

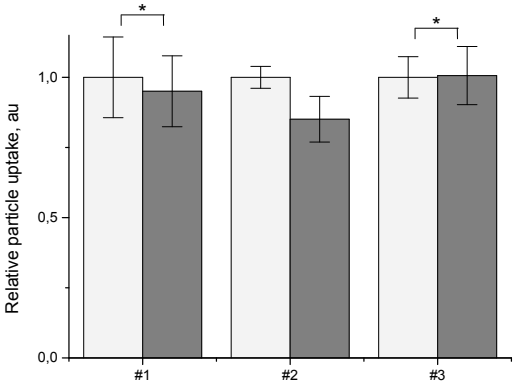

Fig. S13 Comparison of the cellular uptake of responsive P1 (grey) and non-responsive P2 (white) NPs in PC3 cells after 2 h incubation at 200 µg·mL^{-1}. *Equal under < 0.01 conditions in Student's t-Test.

In vitro release of Nile Red (NR) from NPs in PC-3 cells in presence of catalase (ROS-scavenger)

Catalase scavenges the hydrogen peroxide and will thus prevent the peroxide-induced degradation of P1 NPs in cancer cells. In order to test the effect of a ROS scavenger on the release of NR from the ROS-responsive P1 NPs in cells, PC-3 cells were pre-incubated with catalase prior to particle addition (bovine liver catalase, Sigma Aldrich). The PC-3 cells were seeded as described and after 30h they were pre-incubated with 1 mg·mL^{-1} of catalase enzyme for 16 h prior to particle addition. Then the catalase content was reduced 1/5 and 200 ug·mL^{-1} of NR loaded P1 or P2 NPs were added. After 8h incubation the fluorescence of NR in the cells was analysed *via* flow cytometry. An average of at least 10000 cells was detected and NR

fluorescence in the PE channel (excitation 488 nm, emission BP 586/42) was read out. The displayed data represents 5 experiments (n=5) done in triplicate well setup (Fig. S14).

Catalase scavenges the hydrogen peroxide which prevents the peroxide-induced degradation of P1 NPs in PC-3 cells. Therefore the P1 samples with catalase showed less NR release and subsequently less quenching of NR fluorescence. In the presence of the ROS scavenger, a significantly higher fluorescence of NR remained than in the P1 samples without the scavenger. Moreover, the fluorescence level in cells incubated with the non-responsive P2 NPs was not significantly altered by the presence of catalase.

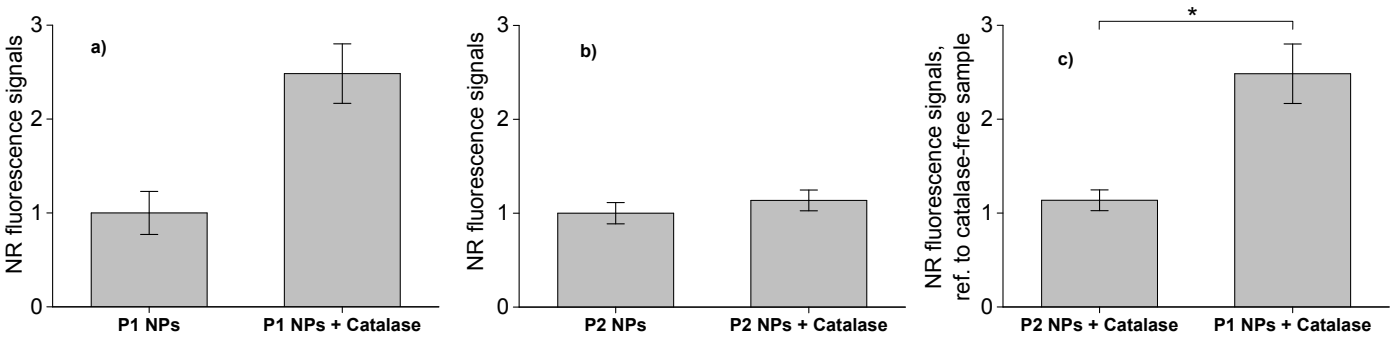

Fig. S14. Nile Red (NR) release from NR-loaded P1 and P2 NPs in presence of catalase. PC-3 cells were incubated for 8h with NR-loaded P1 (a) and P2 (b) NPs, demonstrating the effect of the ROS scavenger catalase (16 h pre-treated) on the NR signals in the cells. Figure (c) demonstrates that catalase-induce increase of NR fluorescence of P1 NPs, as opposed to the unchanged NR fluorescence in the samples with the non-responsive P2 NPs. Catalase scavenges the hydrogen peroxide which prevents the peroxide-induced degradation of P1 NPs in PC-3 cells. Therefore the P1 samples with catalase showed less NR release and subsequently less quenching of NR fluorescence. Note that the columns in (c) both represent the relative NR signal as compared to the respective samples of catalase-free incubation (shown in a, b).* Significant at < 0,01 (ANOVA One-Way Tukey).

Synthesis of the polymer P-1-with conjugated Alexa Fluor® 647

To a 5 mL vial equipped with a magnetic stirrer and containing dry DMF (2.5 mL) was charged polymer P1 (40 mg, 0.05 mmol terminal alkyne groups), Alexa Fluor® 647 azide dye (0.5 mg, 0.000588 mmol) and triethylamine (10 µL, 0.05 mmol). Under argon, rapid stirring was initiated, after which copper (I) iodide (0.2 mg, 0.001 mmol) was added and the vessel was quickly sealed with a crimp teflon cap. The mixture was stirred for 5 min at room-temperature then placed on a pre-heated carousel plate and vigorously stirred at 40 °C for 6h. The reaction was cooled and filtered to aluminium column to remove cooper

catalyst. The blurry mixture was then dialyzed for 48h at dark. Afterwards the P1 polymer-Alexa Fluor® 647 conjugate was recovered by lyophilisation (31.2 mg, 78 %) being obtained as a light blue solid.

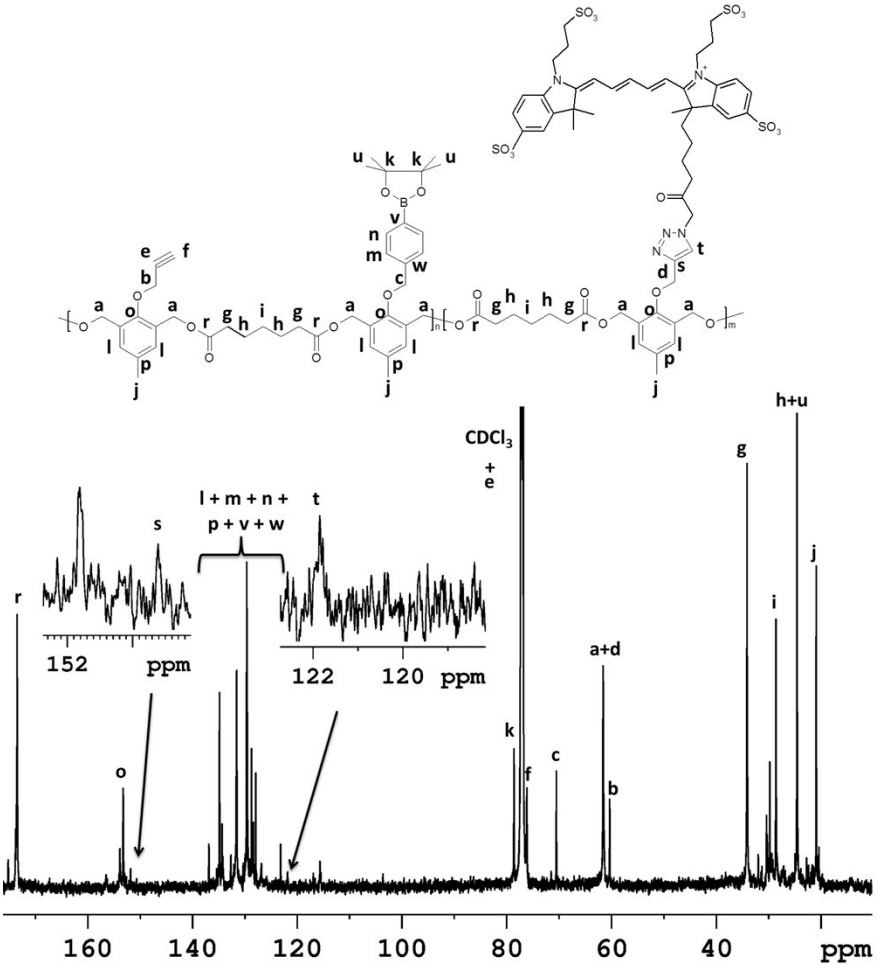

Fig. S15. ^{13}C NMR spectra of the P1 NPs covalently bonded to Alexa Fluor® 647 in $CDCl_3$. The peaks corresponding to the 1,2,3-triazole ring of the linker are more them 3 times signal of background noise (proof of presence).

Preparation of NR-loaded- and Alexa Fluor® 647-bonded NPs

To 2.5 mL of a solution containing 1mg of P1 bonded Alexa Fluor + 9 mg of P1 and Nile Red (25 µg) in acetone, 5 mL of PBS (containing 0.01 % tween 80) were added as precipitant. The remaining acetone was removed by evaporation and the final volume of the NPs was concentrated to 2.5 mg·mL^{-1}. Afterwards the NPs solution was washed twice with PBS by using centrifugation/filtration (Amicon 10 kDa – MilliPore, Czech Republic). The final NR content on the NPs was adjusted to 3.75 µg·mL^{-1} of NR (Fig. S9) in PBS containing 0.082 µg·mL^{-1} of Alexa Fluor® 647 (Fig. S16).

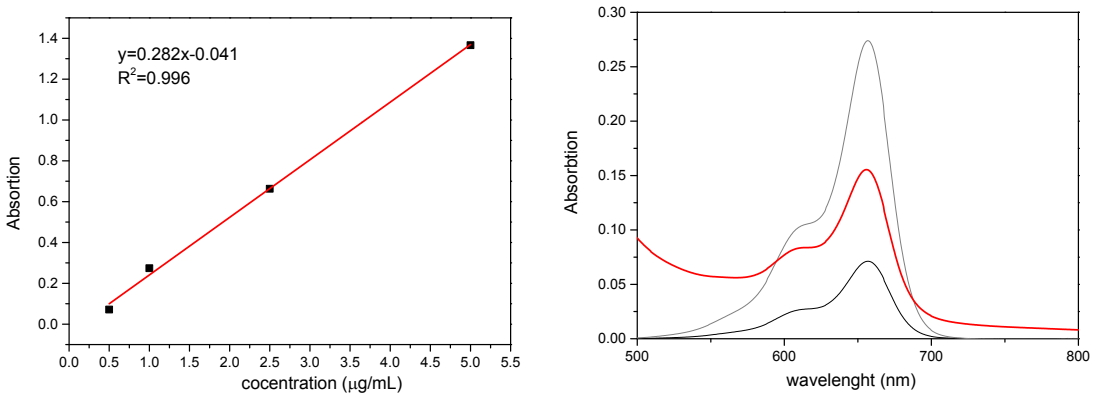

Fig. S16. Calibration curve for Alexa Fluor® 647 (left) and quantification of polymer P1 with conjugated Alexa Fluor® 647 (right – red lines) by UV-Vis spectrometer in DMF (black line corresponds to 0.25 µg·mL^{-1} and grey line corresponds to 1.0 µg·mL^{-1}).

Microscopy: Fluorescence Lifetime Imaging (FLIM) analysis of P-1 Nile Red release in PC-3 and HF cells

As described above, microscopy studies were done using an Olympus FV10-ASV upgraded with a PicoQuant FLIM module (PicoQuant, Germany), on a 60x oil objective. The software FV10-ASW and SymphoTime64 from Olympus and PicoQuant, respectively, was used for acquisition and analysis. 10·10^{-3} PC-3 cells per well were seeded in coated Ibidi® 8 well µ-slides (Ibidi, Germany) and left to adhere at least overnight. Otherwise 30·10^{-3} cells HF per well were seeded in Poly(L-lysin)-coated 4-chamber glass bottom dishes (Cellvis, California, US).

Alexa Fluor® 647 dye was chosen for its high photostability and more even for its insensitivity to self-quenching, to changes in hydrophobicity or pH as described by the manufacturer. The short lifetime of 2.2 ns should therefore be rather constant under different conditions, providing reliable identification of Alx647 from the 2nd used dye, Nile Red. Nile Red fluorescence is most intense in hydrophobic surroundings (as *e.g.*; inside the NPs), and most quenched in hydrophilic surroundings (as *e.g.*; in cell cytoplasm). Just as the spectrum and intensity of NR fluorescence vary with external factors, the NR lifetime is equally affected. A lifetime of roughly 4.2 ns is most common for Nile Red, however its lifetime may vary between 3 and 5 ns in specific surroundings.[4-6] Note that despite these variations NR in particular the NR released in the cell volume has at all times a lifetime that is easily distinguished from that of Alx647 in FLIM.

PC-3 and HF cells were incubated for 1h and 8h with 200 µg·mL^{-1} of dual-stained (physically entrapped NR and covalently bound Alx647) P1 NPs. Cells were washed and visualized without further staining. Pretesting, data not shown here, had

identified the most suitable settings and had also ensured that under these settings, minimal cross-bleeding of the dyes and no false-positive signals (from the respective other dye, or from cell autofluorescence) occurred. Nile Red was excited with a pulsed 485 nm laser and Alx647 with a pulsed 640 nm laser, and both dyes were visualized in the red channel (Ch2 at 650/50 nm).

The dyes were first measured separately to visualize P1 NPs in PC-3 and HF cells (Fig. 5), excluding any false-positive signals from the respective other dye. Note that contributions of NR excited at 640 nm are very low and not relevant. For a better display of the co-localization (*e.g.*; colour-coded display in one image), the dyes were also measured with simultaneous excitation by both lasers – thus acquiring an image of colour-coded co-localization of the dyes in PC-3 and HF cells (Fig. 6). Areas containing predominantly one dye yield an average lifetime in each pixel that is near identical to that dye's lifetime ($\tau_{(NR)}$ or $\tau_{(Alx647)}$). In areas where both dyes are present, photons from both dyes and therefore values of $\tau_{(NR)}$ and $\tau_{(Alx647)}$ are detected. The lifetimes of all photons per one pixel are averaged, and as a result an averaged lifetime is assigned to the pixel. The degree of dye co-localization is therefore colour-coded by averaged lifetime per pixel. A differentiation between released Nile Red ($\tau_{(NR)}$ *ca*. 4ns, displayed as green), predominantly Alexa 647 ($\tau_{(Alx647)}$ *ca*. 2 ns, displayed as blue) and co-localization of both dyes (lifetime between 2-3 ns, displayed as green-blue) is therefore possible. It was observed that in pixels depicting internalized nanoparticles the average lifetime was close to 2, but that however two decay processes (at *ca*. 1 ns and 2 ns lifetime) were present, that correspond to Alx647 and Nile Red, respectively. As described by Jee *et al*., in 2009,[5] Nile Red lifetime in polymer materials is distinctly shorter than 3 ns, therefore Nile Red inside the P1 NPs has a different lifetime than the released Nile Red displaying τ of higher 4 ns. Owing to the overlapping emission spectra, such precise distinction of the different dyes and dye status would be impossible by regular microscopy based on excitation and emission wavelength.

This study showed that P1 NPs inside PC-3 cells release relatively more NR than the same particles inside HF cells, after 8 h incubation (Fig. 6). It also visible that after only 1 h incubation, the NR release from P1 NPs is low even in PC-3 cells (Fig. S17). Lifetime imaging therefore demonstrated that P1 NPs can release their cargo in a cell type- and time-dependent manner.

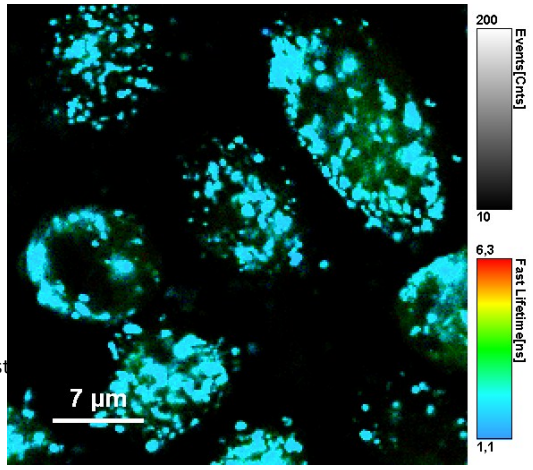

Fig. S17. FLIM images of PC-3 cells after 1 h incubation with dual-marked P1 NPs, color-coded by the averaged obtained life-time per pixel. The localization of polymer (covalently bound Alx647, tau 2 ns, shown in blue) and of Nile Red (originally physically entrapped in the NPs, tau 4 ns, shown in green), and local overlap of both (turquoise tones) was visualized in the red fluorescence channel *via* FLIM microscopy after simultaneous excitation at 485 nm and 640 nm.

Paclitaxel assays

Preparation of the nanoparticles

To a solution of P1 or P2, respectively (in acetone, 5 mL, 10 mg·mL^{-1}) containing paclitaxel (250 µg·mL^{-1}), PBS (10.0 mL, containing 0.01 % tween 80) were added as precipitant. The increase in polarity of the solvent led to the aggregation of the polymer chains forming the NPs. The remaining acetone was removed by evaporation and the final volume of the NPs was concentrated to 2.5 mL. Afterwards the NPs solution was washed twice with PBS by using centrifugation/filtration (Amicon 10 kDa – MilliPore, Czech Republic). The final PTX concentration was adjusted to 220 µg·mL^{-1} of PTX (P1) (~ 94 % E.E, HPLC; Fig. S18) and 202 µg·mL^{-1} of PTX (P2) (~ 92 % E.E, HPLC. Fig. S18). The drug-free NPs were prepared by the same way without adding paclitaxel.

Paclitaxel (PTX) drug loading and loading efficiency

The total amount of the chemotherapeutic PTX loaded into the nanoparticles was measured by high performance liquid chromatograpy (HPLC, Shimadzu, Japan) using a reverse-phase column Chromolith Performance RP-18e (100 x 4.6 mm), eluent water-acetonitrile with acetonitrile gradient 0-100 vol%, flow rate = 1.0 mL·min^{-1}, as described previously.[7-9] The aliquote (100 µL) of drug-loaded NPs was collected from the bulk sample and diluted to 900 µL with acetonitrile. Afterwards, 20 µL of the final sample was injected through a sample loop. PTX was detected at 230 nm using ultraviolet (UV) detection. The retention time of PTX was 12.0 min under such experimental conditions. An analytical curve with linear response in the range 0.5 – 100 µg·mL^{-1} was obtained and used to determine PTX contents (Fig. S10). The drug-free was separated from the drug-loaded NPs by ultrafiltration-centrifugation (Ultrafree-MC 10,000 MW, Millipore) as detailed elsewhere.[10] The samples were centrifuged at 6000 rpm for 30 min. The free PTX amount was measured in the filtrated after the dissolution of NPs by using acetonitrile as described earlier. The drug-loading content (LC) and the drug-loading efficiency (LE) were calculated by using the following equations:

$$LC(\%) = \frac{drug\ ammount\ in\ NPs}{mass\ of\ NPs}\ x\ 100 \quad \text{(eq. S4)}$$

$$LE(\%) = \frac{drug\ ammount\ in\ Nps}{drug\ feeding}\ x\ 100 \quad \text{(eq. S5)}$$

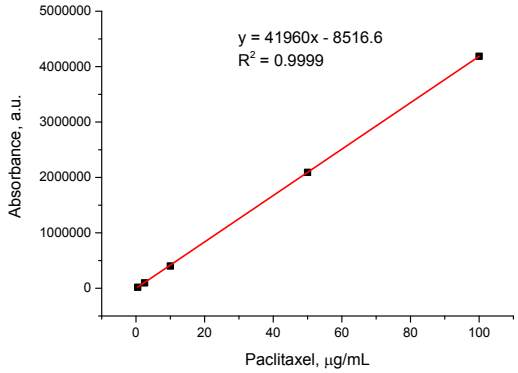

Fig. S18. Calibration curve for paclitaxel.

Paclitaxel release Experiments

The release experiments were carried out at 37 °C in pH-adjusted release media (pH 7.4 and 1 mM of H_2O_2). Aliquots (500 µL) of PTX-NPs were loaded into 36 Slide-A-Lyzer MINI dialysis microtubes with MWCO 10 kDa (Pierce, Rockford, IL). These microtubes were dialyzed against 4 L of PBS (pH 7.4 and 1mM of H_2O_2). The release media was changed periodically to reduce the possibility of drug-diffusion equilibrium (every 12h). The drug release experiments were done in triplicate. At each sampling time, three microtubes were removed from the dialysis system and 0.1 mL from each microtube was diluted to 900 µL with acetonitrile and the sample was ultracentrifuge (18 000 x *g*, 20 min). Afterwards, 20 µL of the final sample was injected through a sample loop. PTX was detected at 230 nm using ultraviolet (UV) detection using the aforementioned methodologies (Fig. S18). The reported data are expressed as the amount of released PTX relative to the total PTX content in the PTX-NPs.

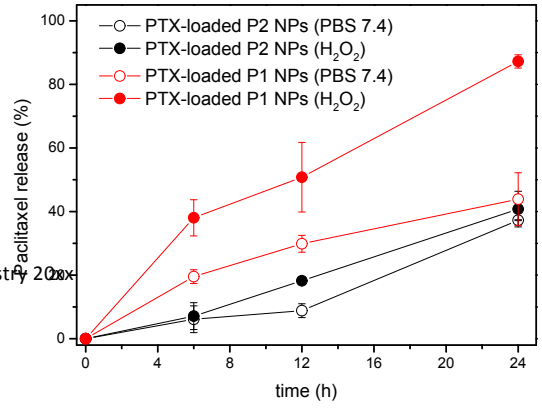

Fig. S19. Paclitaxel (PTX) release from responsive P1 and non-responsive P2 NPs in presence of 1mM of H_2O_2 (filled circles) and in presence of phosphate buffer saline (PBS pH 7.4) (open circles) along 24h incubation at 37 °C.

Cytotoxicity assays

For the cytotoxicity assay, 5000 cells per well (HeLa, DLD1), 7000 (HF) or 10.000 (PC-3), were seeded in duplicates in 96 well plates in 100 µL of media at least one day (2 days for PC-3) before adding the NPs. For adding of the particles the volume was calibrated to 80 µL, and 20 µL of the 5-times concentrated dilution of PTX or particle dispersion were added per well to a final PTX concentration ranging from 10^{-5} to 1 µg·mL^{-1}. All dilutions were made in full incubation medium under thorough mixing of each dilution step. The sample concentrations of the PTX-loaded NPs were adjusted to contain the same total amount of PTX as the samples with free PTX. The cells were incubated with free drug or NPs for 24 h, 48 h (Fig. S20) or 72 h (Fig. 7). In a similar manner, HeLa cells were also incubated for 72 similar to the setup described above, but the cells were incubated medium that contained only 2% serum (Fig. 7). A second control of cells incubated in full medium containing 10% serum proved that the reduced serum content had no toxic side effect on the cells (data not shown). Moreover a test with HeLa cells screening the toxicity after 12h, 24h, 48h, 72h and 96h incubation was done (*see* Fig. S22). After incubation, in all samples 10 µL of alamarBlue® cell viability reagent (Life Technologies, Czech Republic) were added per well and incubated at least 3 h at 37 °C. The fluorescence of the reduced marker dye was read with a Synergy H1 plate reader (BioTek Instruments, US) at excitation 570 and emission 600 nm. Samples of untreated cell and of cells killed with peroxide were used as samples of 100% and 0% viability, respectively. The shown cell assays data is in average of at least 2 measurements, and was obtained in triplicate well setup. PTX-dilutions in incubation medium were made from a PTX stock solution of 200 µg·mL^{-1} in PBS/DMSO (96.5 : 3.5 *v*/*v*).[11] Precipitation of the hydrophobic PTX out of the cell culture medium can therefore be excluded because the PTX was previously fully dissolved and subsequently diluted in the serum-supplied medium under thorough mixing. The final DMSO concentration in the incubation medium was never above 0.4% and therefore of no consequence.[12]

The non-toxic character of the blank particles without drug was shown by incubation of cells with the blank NPs at the same polymer concentrations as were used for the toxicity tests with PTX-loaded NPs (*see* Fig. S21, below). This ensured that no toxic effect of the polymer material itself interfered with the viability assay. Non-cancer cells HF as well as one representative cancer cell line, PC-3, were incubated for up to 48h with the applied concentrations of P1 and P2 polymer NPs (drug-free), and with diluted DMSO (without drug).

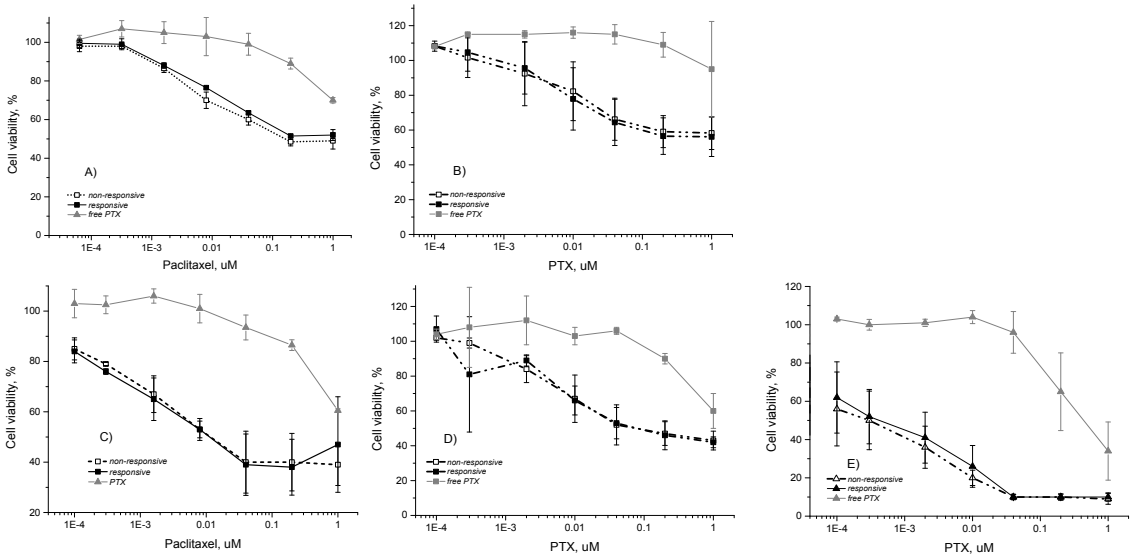

Fig. S20 Incubation of PTX-loaded P1 and P2 NPs with HF (a, c), PC-3 (b, d) and HeLa (e) for 24 h (a, b) and 48 h (c, e). The graphs compare samples with P1 NPs (black, solid symbols), P2 NPs (black, hollow symbols) and free PTX (grey).

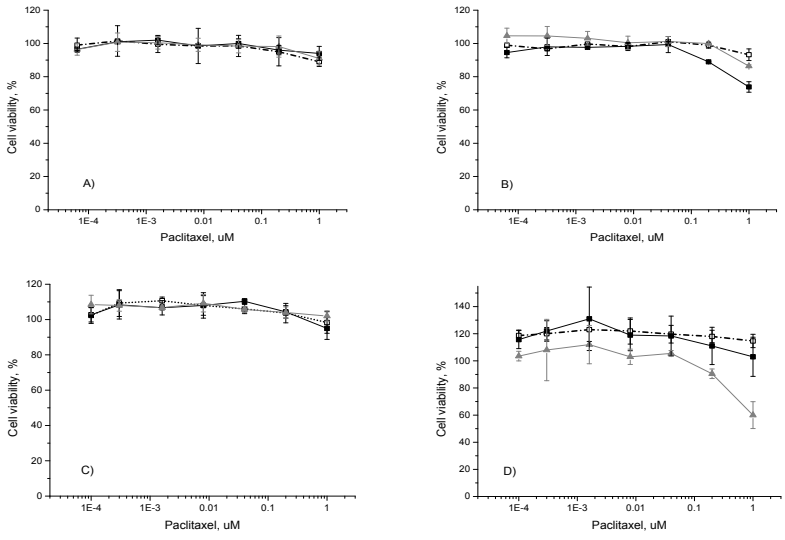

Fig. S21 Control study of the PTX-free NPs in HF (a, b) and PC-3 (c, d) cells. Viability was measured after 24 h (a, c) and 48 h (b, d) of incubation with different concentrations of P2 NPs (open square), ROS-responsive P1 NPs (closed square) and DMSO

(triangle). A maximum concentration of 0.5 (P1 polymer) and 0.6 mg·mL^{-1} (P2 polymer), and maximal content of 0.4 % DMSO were applied. As these concentrations of DMSO and polymer correspond precisely to those present in the studies with PTX, all graphs are displayed as functions of PTX for convenient comparison.

After 48h incubation at the maximum concentration, minor toxicity of the ROS-responsive polymer NPs (P1) was observed in HF cells, but the effect was also observed in the cancer cells. However, this can be neglected when opposed to the high cell mortality caused by the drug in the respective samples (maximal polymer concentration also corresponds to 1 µM of PTX, which is mortal to both HeLa and HF cells). In another test using HeLa cells, the incubation-dependent toxicity of PTX-loaded NPs was screened and cell viability was measured after 12 h up to 96 h.

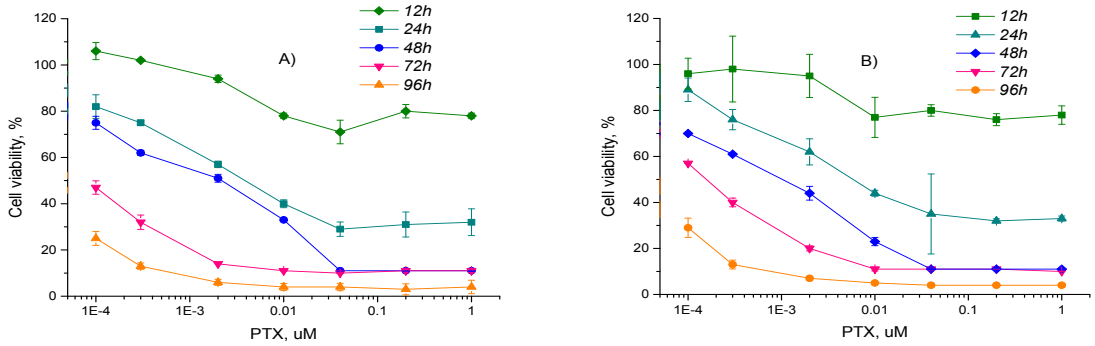

Fig. S22 Incubation of PTX-loaded P1 (a) and P2 (b) NPs with HeLa cells for (from top to bottom) 12h (green), 24h (turquoise), 48h (blue), 72h (pink) and 96h (orange).

The test showed that the PTX-loaded NPs reduced cell viability beneath 50% after 24h incubation time; first toxic effects were even visible after 12 h. The toxicity of the drug-loaded ROS-sensitive NPs (P1) increased steeply when incubation time was raised up to 96 h. At all times the particle toxicity was significantly above that of the free drug (data not shown). The non-responsive NPs (P2) showed similar efficient killing of the cells as the P1 NPs responsive NPs. However, especially at longer incubation > 48 h, the test indicated a higher efficiency of the ROS-responsive system (P1 NPs). With HeLa cells as an aggressive cancer cell line comparable to PC-3 this test indicated a selective, ROS-induced cargo release from P1 NPs in the cells.

References

[1] C. de G. Lux, S. Joshi-Barr, T. Nguyen, E. Mahmoud, E. Schopf, N. Fomina and A. Almutairi, *J. Am. Chem. Soc.*, 2012, **134**, 15758.

[2] P. Štěpánek, In Dynamic light scattering: The Method and Some Applications; Brown, W., Ed.; Oxford Science Publications: Oxford, 1993.

[3] J. Panyam and V. Labhasetwar, *Pharm. Res.*, 2003, **2**, 20.

[4] A. Cser, K. Nagy and L. Biczók, *Chem. Phys. Lett.*, 2002, **360**, 473.

[5] A.-Y. Jee, S. Park, H. Kwon and M. Lee, *Chem. Phys. Lett.*, 2009, **477**, 112.

[6] A.K. Dutta, K. Kamada and K. Ohta, *J. Photochem. Photobiol. A Chem.*, 1996, **93**, 57.

[7] F.C. Giacomelli, P. Štěpánek, C. Giacomelli, V. Schmidt, E. Jäger, A. Jäger and K. Ulbrich, *Soft Matter* 2011, **7**, 9316.

[8] A. Jäger., D. Gromadzki, E. Jäger, F.C. Giacomelli, A. Kozlowska, L. Kobera, J. Brus, B. Říhová, M. El Fray, K. Ulbrich, P. Štěpánek, *Soft Matter* 2012, **8**, 4343.

[9] A. Jäger., E. Jäger, F. Surman, A. Höcherl, A. Angelov, K Ulbrich, M. Dreschler, V.M. Garamus, C. Rodriguez-Emmenegger, F. Nallet, P. Štěpánek, *Polym. Chem.*, 2015, **8**, 4343.

[10] E. Penott-Chang, A. Walther, P. Millard, A. Jäger, E. Jäger, A.H.E. Müller, S.S. Guterres, A.R. Pohlmann, *J. Biomed. Nanotechnol.*, 2012, **8**, 272.

[11] E.A. Dubikovskaya, S.H. Thorne, T.H. Pillow, C.H. Contag and P.A. Wender. *Proc. Natl. Acad. Sci. U.S.A* 2008, **105**, 12128.

[12] A. B. Trivedi, N. Kitabatake, E. Do. *Agr. Biol. Chem.*, 1990, **54**, 2961.

Publication 11

A. Höcherl, E. Jäger, A. Jäger, M. Hruby, **R. Konefał**, O. Janoušková, J. Spevacek, Y. Jiang, P. W. Schmidt, T. P. Lodge, P. Stepanek

One-pot synthesis of reactive oxygen species (ROS)-self-immolative polyoxalate prodrug nanoparticles for hormone dependent cancer therapy with minimized side effects.

Polymer Chemistry, **2017**, 8, 1999-2004.

Polymer Chemistry

COMMUNICATION

View Article Online
View Journal | View Issue

Cite this: *Polym. Chem.*, 2017, **8**, 1999

Received 16th February 2017,
Accepted 2nd March 2017

DOI: 10.1039/c7py00270j

rsc.li/polymers

One-pot synthesis of reactive oxygen species (ROS)-self-immolative polyoxalate prodrug nanoparticles for hormone dependent cancer therapy with minimized side effects†

Anita Höcherl,*[a] Eliézer Jäger,*[a] Alessandro Jäger,[a] Martin Hrubý,[a] Rafał Konefał,[a] Olga Janoušková,[a] Jiří Spěváček,[a] Yaming Jiang,[b] Peter W. Schmidt,[b] Timothy P. Lodge[b] and Petr Štěpánek[a]

A new reactive oxygen species (ROS)-sensitive, self-immolative biodegradable polyoxalate prodrug based on the anticancer chemotherapeutic hormone analog diethylstilbestrol was synthesized *via* one-pot step-growth polymerization. The nanoparticles prepared from this prodrug undergo self-immolative degradation releasing the chemotherapeutic drug in ROS-rich environments, *e.g.*, in cancer cells. This new ROS self-immolative polyprodrug backbone eliminates the need for a linker between polymer chain and drug, resulting in a more specific drug release and minimized toxic side effects to non-ROS-producing cells as proven by *in vitro* experiments. The strategy enables re-utilization of a successful chemotherapeutic agent that has been clinically under-utilized due to dose-related side effects.

Introduction

Cancer is a leading cause of mortality worldwide, accounting for 8.2 million deaths in 2012, and it is expected that annual cancer cases will rise from 14 million in 2012 to 22 million within the next two decades.[1] In men, one of the five most common causes of death is due to cancers of the prostate.[1] Diethylstilbestrol (DEB, synthetic non-steroidal estrogen) has been a standard approach to the treatment of advanced prostate cancer for 50 years.[2] DEB is highly effective in prostate cancer treatment, with studies reporting that DEB has a similar efficacy to orchiectomy, at a daily dosage from 1 mg (low dose regime) to 3 mg.[2a–d] DEB was also successfully employed in estrogen additive therapy for women with estrogen receptor (ER)-positive metastatic breast cancer,[3] with studies showing that the survival of patients treated with daily 5 mg DEB was significantly higher than with Tamoxifen.[2d] However, DEB was eventually withdrawn from the clinical repertoire due to persistent severe dose-related toxicities, mainly cardiotoxicity.[2,3]

In recent years, the re-utilization of neglected and/or toxic drugs becomes possible by virtue of the encapsulation of drugs into lipid- or polymer-based nanoparticles (NPs) as *e.g.*, Doxorubicin encapsulated in liposomes (Doxil®) or through the synthesis of polymer–drug(protein) conjugates, *e.g.*, PEGaspargase (Oncaspar®).[4] Both approaches have proven clinically efficient in the treatment of several diseases. Despite this good efficiency, encapsulation can lead to drug leakage from the NPs during storage and blood circulation,[4] and most of the polymer–drug(protein) conjugates require the use of specific linkers and long synthetic pathways, *e.g.*, through acetal,[5] ester[6] or hydrazone[7] bonds. Consequently, polymer systems gain much more relevance in biomedical applications if they are tailored to be degradable in response to a stimulus, *e.g.*, light, pH change, or more recently, the elevated presence of ROS in cancer tissues.[8] The increased H_2O_2 production of cancer cells causes locally high peroxide concentrations, which can even exceed the oxidative burst of activated macrophages.[8d] This is due to imbalances in the ROS production (especially H_2O_2), and it leads to oxidative stress and activation of inflammation events, which can damage tissues and organs.[9]

Oxidation-responsive polymers and their relevant NPs including poly(propylene sulfide)s,[10] ferrocene-based,[11] boronic ester-based,[12] thioketal-based,[13] or polyoxalate-based[14] polymers have been prepared and studied for their potential in biomedical applications. Among these, the preparation of polymer systems sensitive to H_2O_2 through the cleavage of oxalate bonds is a particularly straightforward approach. Polymers containing oxalate bonds have been recently tested in murine models demonstrating interesting properties as antioxidants,[14a,b] as antioxidant-theranostic

[a]*Institute of Macromolecular Chemistry v.v.i., Academy of Sciences of the Czech Republic, Heyrovsky Sq. 2, 162 06 Prague 6, Czech Republic*
[b]*Department of Chemistry, University of Minnesota, 207 Pleasant Street SE, Minneapolis, MN, USA. E-mail: hocherl@imc.cas.cz, jager@imc.cas.cz*
†Electronic supplementary information (ESI) available. See DOI: 10.1039/c7py00270j

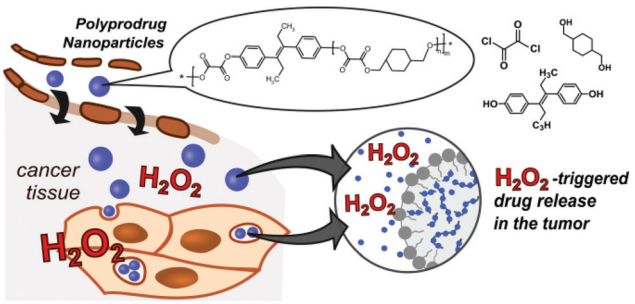

Scheme 1 Polyoxalate prodrug NPs (PDEB NPs) with self-immolative polymer degradation and DEB release in H_2O_2-rich tumor microenvironments.

agents,[14c] ischemia/reperfusion-targeted nanotherapeutics,[14d] and as nanoreactor systems for *in vivo* imaging of H_2O_2.[14c,d] Further attractive properties of the oxalate based polymers NPs include their degradation-induced luminescence (discussed hereafter) with tunable emission by the encapsulation of selected dyes, excellent specificity to H_2O_2 over other ROS species, deep-tissue imaging capabilities, and continuous detection of *in situ* produced H_2O_2 for long times.[14]

However no application for the treatment of cancer cells with this promising system has been reported yet. Herein, we describe a one-pot synthesis route to a novel self-immolative H_2O_2-sensitive polyprodrug material that provides biocompatibile and biodegradable nanoparticles with triggered degradation and chemotherapeutic drug release in ROS-rich environments (Scheme 1). The concept of polyprodrugs avoids the use of chemically specific linkers for drug release, by integrating the drug molecules into the polymer carrier backbone with stimuli-responsive bond and hyper-fast chain-breakage capabilities.[15]

Results and discussion

Polymers PDEB1, PDEB2, PDEB3

The three ROS self-immolative polyprodrug backbones with varied DEB amounts were synthesized by a one-pot step-growth polymerization. The reaction conditions were optimized and fine-tuned according to the molar ratio of the diols and the oxalyl chloride, in accordance with the reaction pathway detailed in the ESI† (see ESI† for methods). Briefly, diethylstilbestrol and 1,4-cyclohexanedimethanol (CHD) were dissolved in tetrahydrofuran (THF), and triethylamine was added dropwise at 4 °C. Afterwards oxalyl chloride dissolved in THF was added dropwise, and the polymerization reaction was continued for 6 hours at room temperature under nitrogen atmosphere. The resulting polyprodrugs were obtained by extraction using DCM and precipitation in cold hexane. Polyprodrugs with varied amounts of DEB (PDEB1 ~2.3 wt%; PDEB2 ~7.5 wt% and PDEB3 ~13.0 wt% of DEB) were obtained by varying the DEB, oxalyl chloride and CHD ratio (see Fig. S3 and ESI† for methods). The PDEBs were obtained as yellowish solids and the chemical structure was identified with ^{1}H NMR spectroscopy (Fig. 1A top and Fig. S1, ESI†). Successful polymer synthesis was confirmed by ^{1}H NMR (Fig. 1A top) and by size exclusion chromatography (SEC) analysis (Fig. S2, ESI†). The weight-average molecular weight (M_w) of polymer PDEB1 was 11.8 kDa with reasonable dispersity $M_w/M_n \approx 1.4$ as determined by SEC (Fig. S2, ESI†). No important differences in M_w were observed for PDEB2 and PDEB3 (Fig. S2, ESI†). The ^{1}H NMR spectrum of PDEB1 (Fig. 1A top, see ESI† for methods) shows the characteristic signals for protons belonging to the repeat units (see ESI† for peak assignments). Significantly lower mobility was revealed for aromatic protons of DEB units (signals a, b in Fig. 1A) in DMF-d_7 solutions of PDEB polyprodrugs in comparison with solution of the neat DEB from ^{1}H spin–spin relaxation times T_2 (see ESI† for measurements details), which in polyprodrugs (T_2 = 0.76 s) were twice shorter in comparison with the neat DEB (T_2 = 1.42 s). This fact together with the disappearance of the signal of DEB OH protons at 9.5 ppm in the spectra of the polyprodrugs (see ESI, Fig. S1B†) indicate that DEB units are covalently incorporated in the polymer chain. The degradation of PDEB1 as evaluated by ^{1}H NMR spectroscopy was complete after 3 days of incubation (Fig. 1A middle after 24 h and bottom after 72 h) as the broad peaks in ^{1}H NMR related to the polyprodrug are replaced by sharp peaks of the low-molecular-weight degradation products (monomers), confirming the self-immolative depolymerization triggered by H_2O_2.

Nanoparticles

With the aim to reduce the required dose, to minimize toxic side effects and to increase the specificity of DEB for cancer tissue, Tween-stabilized NPs based on the ROS self-immolative polyprodrug backbone PDEB1 were prepared (see ESI† for methods). Due to the incorporated oxalate linkers in the polyprodrug backbone, in an ROS-rich environment the polyprodrug will be self-immolatively degraded and the chemotherapeutic DEB released. We recently developed a NP drug-delivery system with H_2O_2-sensitive groups, which was able to deliver its drug cargo selectively to cancer cells (exploiting the higher level of peroxide in cancer cells compared to non-cancer cells).[12a] This approach is here refined with the insertion of the peroxide-sensitive oxalates as cleavable breakpoints integrated into the backbone as self-immolative polyprodrugs for selective drug release.

PDEB1 was chosen for *in vitro* evaluation (PDEB1 ~2.3 wt% of DEB, Fig. S3 and eqn (S3), ESI†) due to the superior stability of the PDEB1 NPs (see ESI† for methods). Dynamic light scattering (DLS) demonstrated NP stability in simulated physiological conditions and proved their peroxide-triggered degradation (Fig. 1B), and the degradation-triggered DEB release (Fig. S4, ESI†) specifically in simulated ROS-rich environments (H_2O_2). Note that the NPs were prepared to an average size of *ca.* 72 nm in diameter (hydrodynamic radius, $2R_H = D_H \approx$ 72 nm), *e.g.*, within a range known to be ideal for efficient tumor accumulation due to the EPR effect.[4,7]

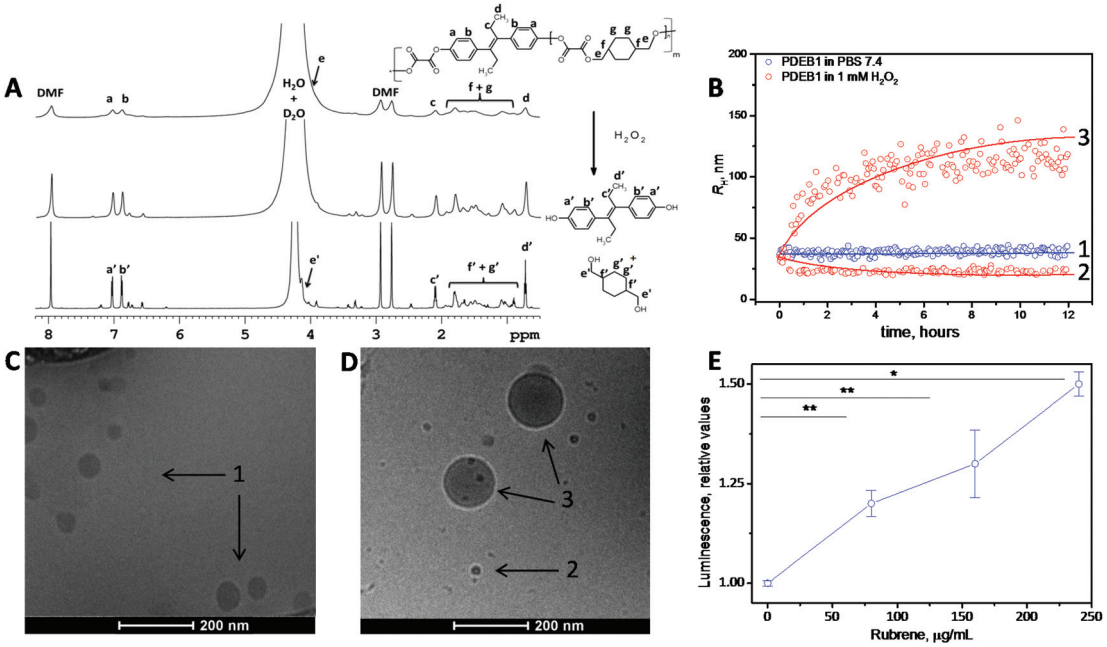

Fig. 1 (A) ^{1}H NMR spectra of the synthesized ROS self-immolative PDEB1 polyprodrug (before H_2O_2 addition in PBS/DMF-d_7) (top) and the degradation upon incubation with 1 mM of H_2O_2 after 24 h (middle) and 72 h (bottom). (B) Average R_H for PDEB1 polyprodrug NPs (blue – 1) with no H_2O_2 addition and after 12 h of incubation (red – 2 and 3) in 1 mM of H_2O_2 at 37 °C in PBS. (C) Cryo-TEM of the PDEB1 polyprodrug NPs before incubation with H_2O_2 and (D) after incubation with 1 mM H_2O_2 for 24 h. (E) Luminescence in MCF7 cancer cells after 2 h incubation with rubrene-loaded PDEB1 NPs, indicating the ROS-triggered cleavage of the oxalate groups in the polymer backbone. Sample '0 μg·mL^{-1} rubrene' corresponds to the NP-free control sample (*p < 0.01; **p < 0.03). The arrows in (C) and (D) correspond to the average R_H from the DLS in (B).

H_2O_2-Triggered polymer degradation

Under exposure to physiologically relevant levels of H_2O_2 [8a,12a] (250 μM, Fig. S4, ESI†) the oxalate groups of PDEB1 are oxidized and subsequently hydrolyzed triggering a self-immolative polymer backbone degradation releasing the chemotherapeutic DEB (see Scheme 1, Fig. 1B, S3 and S4, ESI†). The degradation of PDEB1 in the presence of H_2O_2 was also probed by cryo-TEM (Fig. 1C and D). Applying several different techniques, ^{1}H NMR spectra, DLS and the cryo-TEM images we showed that PDEB1 polyprodrug NPs degraded into small molecules and oligomers in a time- and H_2O_2-dependent manner. The larger objects observed in DLS and cryo-TEM during degradation (DLS in red Fig. 1B and cryo-TEM in Fig. 1D) most probably are related to the hydrophobicity of the polymer fragments that re-aggregate in solution due to the presence of the stabilizing agent and/or to NPs swollen due to the H_2O_2 attack.[16] Polymer degradation proceeds more extensively with increasing incubation time and H_2O_2 concentration (Fig. 1B and C and S5, ESI†). It is well established that the degradation of polyoxalate-based polymers induces chemiluminescence in peroxide-rich environments.[14,17] In this way the polymer degradation in cancer cells was demonstrated using PDEB1 polyprodrug NPs loaded with the dye rubrene (Fig. 1E), where the ROS-triggered cleavage of oxalate bounds induced rubrene luminescence (see Scheme S1, ESI† for proposed mechanism). The chemiluminescence was observed in MCF7 cancer cells (Fig. 1E) as well as in macrophages (see Fig. S6, ESI†), and the intensity of rubrene chemiluminescence correlated with the particle concentration, making the PDEB1 polyprodrug NPs useful for theranostics as well.[14c,17]

Cell viability testing

Taking into account previous works reporting the significantly higher cell viability for particles prepared from polyoxalates lacking DEB,[18] herein the cell viability experiments were performed with PDEB NPs. *In vitro* evaluation of the self-immolative PDEB1 polyprodrug NPs was performed in selected cell lines (see Fig. 2). Cell model systems for hormone therapy-treatable (LNCaP) and therapy-resistant (PC3) prostate cancer were used to evaluate the potential of PDEB1 in prostate cancer

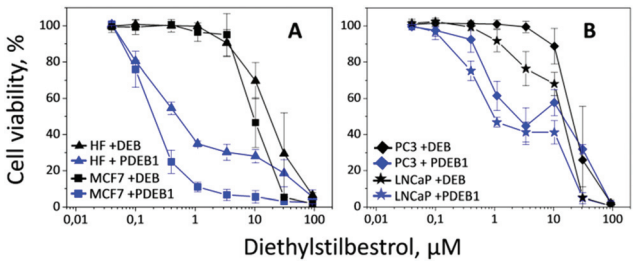

Fig. 2 Cell viability after 5 days incubation with the free drug DEB (black) and with the polyprodrug PDEB1 NPs (blue). The cell lines of HF (triangle) and MCF7 (square) are shown in (A), and of LNCaP (star) and PC3 (diamond) in (B).

treatment. Like all cancer cells, these cells have higher ROS levels, and PC3 and LNCaP produce up to 3-times more H_2O_2 than non-cancerous cells,[8d] thus being well suited to demonstrate the ROS-sensitive drug release of PDEB1. MCF7 cells were selected as a breast cancer model system, based on recent studies showing satisfactory results of DEB in the treatment of post-menopausal breast cancer.[2d,3] Human fibroblasts (HF) were used as a non-cancerous reference system. Cell viability after 5 days of incubation with PDEB1 polyprodrug NPs was evaluated using the AlamarBlue Assay (Fig. 2, see ESI† for methods and for DEB toxicity mechanism). The lower toxicity of the free, highly hydrophobic, drug compared to the drug-carrier system is a known effect and it is attributed both to the extensive adsorption of the hydrophobic drug molecules onto serum components such as serum albumin, whereas NPs drug carriers transport the drug directly into the cells[19a,b] and to the enhanced endocytotic uptake of polymer NPs when compared with the free drugs.[19c–h] HF cells produce a significantly lower level of ROS compared to the cancer cells,[8] hence the PDEB1 polyprodrug is degraded. However, as clearly visible in Fig. 2A, the ROS-sensitive polyprodrug NPs exerted a much higher toxicity on the cancer cells, MCF7, than on HF, while the free drug was equally toxic to cancer and non-cancer cells. Note that PDEB1 is specifically efficient *versus* the cancer cells in the low micromolar range, *i.e.*, at a concentration approximating the DEB blood plasma level in breast cancer therapy.[2d] Also for prostate cancer cells (Fig. 2B) LNCaP and even for the hormone-resistant PC3, PDEB1 polyprodrug NPs significantly lowered the required dose compared to the free drug. Similarly, the improved toxicity of PDEB1 was observed with cancer cell lines.[2c] PDEB1 also showed superior toxicity over the free drug.

Microscopy studies

Light microscopy revealed initial morphological changes and M-phase cell cycle arrest after 24 h incubation (and significant nuclear aneuploidy at >72 h) with PDEB1 polyprodrug NPs, while the free drug had no visible effect (data not shown). For the evaluation of morphological changes the cells were further studied after 24 h incubation with free DEB and PDEB1 NPs using confocal laser scanning microscopy (CLSM) (Fig. 3 and S7, ESI†). CLSM images in Fig. 3 show that the non-cancer cells (HF) were the least affected by PDEB1 polyprodrug NPs. HF displayed only an altered, less fibrous cell morphology and occasional nuclear fragmentation. Compared to that, cancer cell lines showed significant morphological changes such as nuclear fragmentation (indicating mitotic arrest) and aneuploidy (indicating G2/M arrest) in a high number of cells after incubation with PDEB1. The free drug did not have any visible toxic effects. Specifically LNCaP cells were strongly affected by PDEB1 in that most cells were detached, forming clusters (see Fig. S8†). This indicates a specific sensitivity of LNCaP to PDEB1 polyprodrug that results in disrupted cell adhesion, thereby promising additional cytotoxic effects in long-term, which adds to the attractiveness of PDEB1 polyprodrug for application in prostate cancer therapy. For further details on the microscopy studies, see ESI and Fig. S9.†

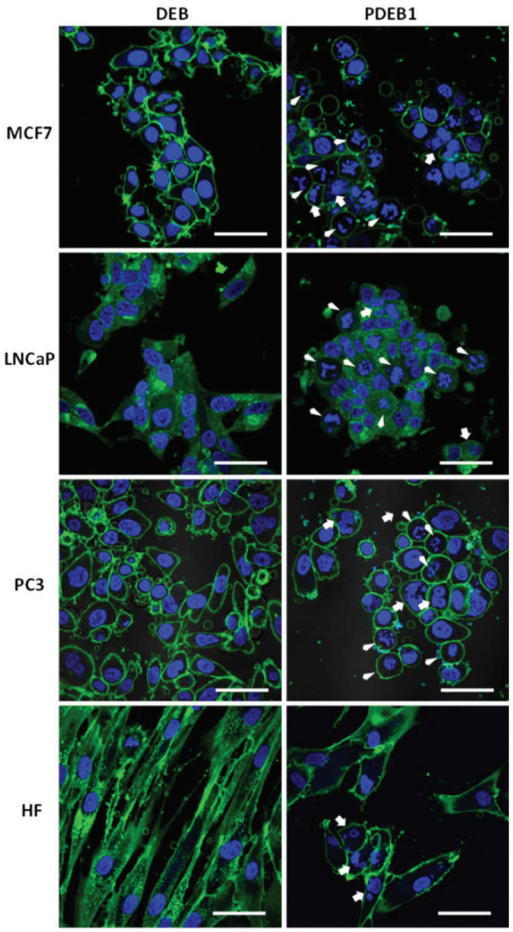

Fig. 3 Cells were incubated for 24 h with free DEB or PDEB1 NPs, at a total concentration of 3.4 μM DEB, to visualize nuclear fragmentation (arrow) and cells in mitotic arrest (arrowhead); nuclei were stained using Hoechst 33342 (blue) and the cytoplasmic membrane was labelled with CellMask™ (green). Scale bar = 50 μm.

Conclusions

The CLSM data correlates with the viability analysis, demonstrating again the enhanced toxicity of the PDEB1 prodrug against cancer cells. Note that the cytotoxicity of the PDEB1 polyprodrug NPs to HF cells was comparable to the toxicity of NPs prepared with the FDA-approved polymer polylactic acid PLA (Fig. S10, see ESI† for methods). The presented system shows great promise to achieve drug release specifically into tumors and lower the required drug dose in estrogen-dependent hormone therapy. In summary, for the first time a one-pot synthetic pathway to synthesize a new ROS self-immolative polyprodrug backbone based on the chemotherapeutic hormone analogue DEB is presented. The prepared NPs demonstrate higher activity against prostate and breast cancer cells *in vitro*, with lower activity in non-cancer cells due to the

selectivity to ROS-rich environments. Particle degradation in ROS-rich environments can be followed by chemiluminescence, opening the possibility for usage as theranostics. Finally the strategy presented here eliminates the need for a biodegradable linker. The NPs make it possible to reduce the side-effects of a highly effective and successful therapeutic molecule that was utilized for the treatment of hormone-dependent cancers, through a simple and efficient strategy.

Acknowledgements

The financial support of the Ministry of Education, Youth and Sports (grants # LH14079, POLYMAT #LO1507), the Czech Science Foundation (grant # 16-02870S, 15-13853S and 17-09998S), and the National Science Foundation through the University of Minnesota MRSEC, Award DMR-1420013 is gratefully appreciated.

Notes and references

1 World Health Organization (WHO), http://www.who.int/mediacentre/factsheets/fs297/en/ (July, 2016).
2 (*a*) S. B. Malkowicz, *Urology*, 2001, **58**, 108; (*b*) E. D. Crawford, *Rev. Urol.*, 2004, **6**, S3; (*c*) R. Turo, M. Smolski, R. Esler, M. L. Kujawa, S. J. Bromage, N. Oakley, A. Adeyoju, S. C. W. Brown, R. Brough, A. Sinclair and G. N. Collins, *Scand. J. Urol.*, 2014, **48**, 4; (*d*) P. P. Peethambaram, J. N. Ingle, V. J. Suman, L. C. Hartmann and C. L. Loprinzi, *Breast Cancer Res. Treat.*, 1999, **54**, 117; (*e*) H. A. Kemp, G. F. Read, D. Riad-Fahmy, A. W. Pike, S. J. Gaskell, K. Queen, M. E. Harper and K. Griffiths, *Cancer Res.*, 1981, **41**, 4693.
3 (*a*) R. Twombly, *J. Natl. Cancer Inst.*, 2011, **103**, 920; (*b*) J. N. Ingle, D. L. Ahmann, S. J. Green, J. H. Edmonson, H. F. Bisel, L. K. Kvols, W. C. Nichols, E. T. Creaan, R. G. Hahn, J. Rubin and S. Fryak, *N. Engl. J. Med.*, 1981, **304**, 16.
4 (*a*) T. Sun, Y. S. Zhang, B. Pang, D. C. Hyun, M. Yang and Y. Xia, *Angew. Chem., Int. Ed.*, 2014, **53**, 12320; (*b*) E. Jäger and F. C. Giacomelli, *Curr. Top. Med. Chem.*, 2015, **15**, 328.
5 J. Zou, G. Jafr, E. Themistou, Y. Yap, Z. A. P. Wintrob, P. Alexandridis, A. C. Ceacareanu and C. Cheng, *Chem. Commun.*, 2011, **47**, 4493.
6 A. G. Cheetham, Y.-C. Ou, P. Zhang and H. Cui, *Chem. Commun.*, 2014, **50**, 6039.
7 (*a*) K. Ulbrich, K. Holá, V. Šubr, A. Bakandritsos, J. Tuček and R. Zbořil, *Chem. Rev.*, 2016, **116**, 5338; (*b*) E. Jäger, A. Jäger, P. Chytil, T. Etrych, B. Říhová, F. C. Giacomelli, P. Štěpánek and K. Ulbrich, *J. Controlled Release*, 2013, **165**, 153.
8 (*a*) M. Giorgio, M. Trinei, E. Migliaccio and P. G. Pelicci, *Nat. Rev. Mol. Cell Biol.*, 2007, **8**, 722; (*b*) S. Toyokuni, K. Okamoto, J. Yodoi and H. Hiai, *FEBS Lett.*, 1995, **358**, 1; (*c*) T. P. Szatrowski and C. F. Nathan, *Cancer Res.*, 1991, **51**, 794; (*d*) B. Kumar, S. koul, L. Khandrika, R. B. Meacham and H. K. Koul, *Cancer Res.*, 2008, **68**, 177.
9 (*a*) A. Mantovani, P. Allavena, A. Sica and F. Balkwill, *Nature*, 2008, **454**, 436; (*b*) S. Reuter, S. C. Gupta, M. M. Chaturvedi and B. B. Aggarwal, *Free Radicals Biol. Med.*, 2010, **49**, 1603; (*c*) N. Houstis, E. D. Rosen and E. S. Lander, *Nature*, 2006, **440**, 944.
10 B. L. Allen, J. D. Johnson and J. P. Walker, *ACS Nano*, 2011, **5**, 5263.
11 (*a*) M. Hmyene, A. Yassar, M. Escorne, A. Percheron-Guegan and F. Garnier, *Adv. Mater.*, 1994, **6**, 564; (*b*) J. Tian, J. Chen, C. Ge, X. Liu, J. He, P. Ni and Y. Pan, *Bioconjugate Chem.*, 2016, **27**, 1518.
12 (*a*) E. Jäger, A. Höcherl, O. Janoušková, A. Jäger, M. Hrubý, R. Konefal, M. Netopilík, J. Pánek, M. Šlouf, K. Ulbrich and P. Štěpánek, *Nanoscale*, 2016, **8**, 6958; (*b*) C. de G. Lux, S. Joshi-Barr, T. Nguyen, E. Mahmoud, E. Schopf, N. Fomina and A. Almutairi, *J. Am. Chem. Soc.*, 2012, **134**, 15758.
13 (*a*) G. Saravanakumar, J. Kim and W. J. Kim, *Adv. Sci.*, 2016, 1600124; (*b*) D. S. Wilson, G. Dalmasso, L. Wang, S. V. Sitaraman, D. Merlin and N. Murthy, *Nat. Mater.*, 2010, **9**, 923.
14 (*a*) D. Jeong, C. Kang, E. Jung, D. Yoo, D. Wu and D. Lee, *J. Controlled Release*, 2016, **233**, 72; (*b*) S. Kim, H. Park, Y. Song, D. Hong, O. Kim, E. Jo, G. Khang and D. Lee, *Biomaterials*, 2011, **32**, 3021; (*c*) C. Kang, W. Cho, M. Park, J. Kim, S. Park, D. Shin, C. Song and D. Lee, *Biomaterials*, 2016, **85**, 195–203; (*d*) D. Lee, S. Park, S. Bae, D. Jeong, M. Park, C. Kang, W. Yoo, M. A. Samad, Q. Ke, G. Khang and P. M. Kang, *Sci. Rep.*, 2015, **5**, 16592.
15 (*a*) X. Hu, G. Liu, Y. Li, X. Wang and S. Liu, *J. Am. Chem. Soc.*, 2015, **137**, 362; (*b*) X. Hu, J. Hu, J. Tian, Z. Ge, K. Luo and S. Liu, *J. Am. Chem. Soc.*, 2013, **135**, 17617.
16 (*a*) A. Jäger, E. Jäger, F. Surman, A. Höcherl, B. Angelov, K. Ulbrich, M. Drechsler, V. M. Garamus, C. Rodriguez-Emmenegger, F. Nallet and P. Štěpánek, *Polym. Chem.*, 2015, **6**, 4946; (*b*) S. Petrova, E. Jäger, R. Konefał, A. Jäger, C. G. Venturini, J. Spěváček, E. Pavlova and P. Štěpánek, *Polym. Chem.*, 2014, **5**, 3884; (*c*) F. C. Giacomelli, P. Štěpánek, V. Schmidt, E. Jäger, A. Jäger and C. Giacomelli, *Nanoscale*, 2012, **4**, 4504.
17 (*a*) D. Lee, S. Khaja, J. C. Velasquez-Castano, M. Dasari, C. Sun, J. Petros, W. R. Taylor and N. Murthy, *Nat. Mater.*, 2007, **6**, 765; (*b*) D. Hong, B. Song, H. Kim, J. Know, G. Khang and D. Lee, *Ther. Delivery*, 2011, **2**, 1407.
18 (*a*) S. Cho, O. Hwang, I. Lee, G. Lee, D. Yoo, G. Khang, P. M. Kang and D. Lee, *Adv. Funct. Mater.*, 2012, **22**, 4038; (*b*) S. Kim, K. Seong, O. Kim, H. Seo, M. Lee, G. Khang and D. Lee, *Biomacromolecules*, 2010, **11**, 555; (*c*) H. Park, S. Kim, S. Kim, Y. Song, K. Seung, D. Hong, G. Khang and D. Lee, *Biomacromolecules*, 2010, **11**, 2103.
19 (*a*) D. A. Smith, L. Di and E. H. Kerns, *Nat. Rev. Drug Discovery*, 2010, **9**, 929; (*b*) A. I. Minchinton and I. F. Tannock, *Nat. Rev. Cancer*, 2006, **6**, 583; (*c*) G. Gaucher, R. H. Marchessault and J.-C. Leroux, *J. Controlled Release*,

2010, **143**, 2; (*d*) D. Li, Y. Zhang, S. Jin, J. Guo, H. Gao and C. Wang, *J. Mater. Chem. B*, 2014, **2**, 5187; (*e*) F. Danhier, N. Lecouturier, B. Vroman, C. Jérôme, J. Marchand-Brynaert, O. Feron and V. Préat, *J. Controlled Release*, 2009, **133**, 11; (*f*) H. S. Yoo, E. A. Lee and T. G. Park, *J. Controlled Release*, 2002, **82**, 17; (*g*) M. J. Vicent, R. Tomlinson, S. Brocchini and R. Duncan, *J. Drug Targeting*, 2004, **12**, 491; (*h*) V. Giménez, C. James, A. Armiñán, R. Schweins, A. Paul and M. J. Vicent, *J. Controlled Release*, 2012, **159**, 290.

Electronic Supplementary Material (ESI) for Polymer Chemistry.

One-pot synthesis of reactive-oxygen species (ROS)-self-immolative polyoxalate prodrug nanoparticles for hormone dependent cancer therapy with minimized side effects

Anita Höcherl,[a*] Eliézer Jäger,[a*] Alessandro Jäger,[a] Martin Hrubý,[a] Rafał Konefał,[a] Olga Janoušková,[a] Jiří Spěváček,[a] Yaming Jiang,[b] Peter W. Schmidt,[b] Timothy P. Lodge[b] and Petr Štěpánek[a]

[a] *Institute of Macromolecular Chemistry v.v.i., Academy of Sciences of the Czech Republic, Heyrovsky Sq. 2, 162 06 Prague 6, Czech Republic.*
[b] *Department of Chemistry, University of Minnesota, 207 Pleasant Street SE, Minneapolis, MN, United States.*

Email: jager@imc.cas.cz;hocherl@imc.cas.cz;

Tel:+420 296 809 322;

Supporting Information

Materials and Methods

Materials and characterization

1,4-Cyclohexanedimethanol, diethylstilbestrol, oxalyl chloride, triethylamine, rubrene, molecular sieves 3Å and Polysorbate 80 (Tween 80®) were purchased from Sigma Aldrich (Czech Republic) and used as received. Tetrahydrofuran (THF), dichloromethane (DCM), *N*,*N*-dimethylformamide (DMF) and hexane were purchased from Lach·ner (Czech Republic). All solvents, unless otherwise stated, were used without further purification. PC3, HF, LNCaP, RAW and MCF7 cells lines were obtained from American Type Cell Culture (ATCC) and cultured according ATCC guidelines.

^{1}H NMR spectroscopy

^{1}H NMR spectra of the polyprodrugs were obtained using a Bruker Avance III 600 MHz NMR spectrometer with DMF-$_{d7}$ as solvent at 25 °C and at 37 °C for polymer degradation studies. The chemical shifts are relative to TMS using hexamethyldisiloxane (HMDSO, 0.05 ppm from TMS in ^{1}H NMR) as an internal standard. Chemical shifts, δ, are in units of parts per million (ppm). ^{1}H spin-spin relaxation times T_2 were measured at 25 °C on degassed DMF-d_7 solutions (c = 3.3 wt%) using the CPMG pulse sequence 90°_x-(t_d-180°_y-t_d)$_n$-acquisition.[1] NMR tubes were sealed under nitrogen. The relaxation delay between scans was 100 s, acquisition time 2.84 s, 4 scans. All obtained T_2 relaxation curves were monoexponential. The relative error for T_2 values did not exceed ±5%.

^{1}H NMR measurements of the polyoxalate prodrug degradation

To 10.0 mg of the polymer, 0.6 mL of DMF-$_{d7}$ was added and the NMR tube was incubated at 37 °C. Afterwards, deuterated PBS buffer solution (pH 7.4, 160 µL) was added (Figure 1A, top). Finally, 40 µL of H_2O_2 was added to make a 1 mM solution, and the experiments proceeded for 24 up to 72 h (Figure 1A middle and bottom). For the ^{1}H NMR measurements of the polymer incubated for longer times (*e.g.*, 72h) the incubation was performed outside of the magnet (NMR tube Heat&Mix Apparatus, Labio a.s., CZ).

Size exclusion chromatography (SEC) analysis

The weight-average molecular weight (M_w), number-average molecular weight (M_n), and the respective dispersity $Đ$ = (M_w/M_n) were obtained by size exclusion chromatography (SEC) analysis. The SEC of the isolated polyprodrugs was performed at 25 °C with two PLgel MIXED-C columns (300 × 7.5 mm, SDV gel with particle

size 5 µm; Polymer Laboratories, USA) and with UV (UVD 305; Watrex, Czech Republic) and RI (RI-101; Shodex, Japan) detectors. *N*,*N*-Dimethylformamide (Sigma-Aldrich, Czech Republic) with LiBr (0.01 % v/v) was used as a mobile phase at a flow rate of 1 mL·min^{-1}. The molecular weight values were calculated using Clarity software (Dataapex, Czech Republic). Calibration with PMMA standards was used.

Scattering techniques

The dynamic light scattering (DLS) measurements were performed using an ALV CGE laser goniometer consisting of a 22 mW HeNe linear polarized laser operating at a wavelength λ = 632.8 nm, an ALV 6010 correlator, and a pair of avalanche photodiodes operating in the pseudo cross-correlation mode. The samples were loaded into 10 mm diameter glass cells and maintained at 25 ± 1 °C. The data were collected using the ALV Correlator Control software and the counting time was 30 s. The measured intensity correlation functions $g_2(t)$ were analyzed using the algorithm REPES[1] resulting in the distributions of relaxation times shown in equal area representation as $\tau A(\tau)$. The mean relaxation time or relaxation frequency $(\Gamma = \tau^{-1})$ is related to the diffusion coefficient (D) of the nanoparticles as $= \frac{\Gamma}{q^2}$, where $q = \frac{4\pi n \sin\frac{\theta}{2}}{\lambda}$ is the scattering vector with *n* the refractive index of the solvent and θ the scattering angle. The hydrodynamic radius (R_H) or the distributions of (R_H) were calculated by using the well-known Stokes-Einstein relation:

$$R_H = \frac{k_B T}{6\pi\eta D} \qquad \text{(S1)}$$

with k_B the Boltzmann constant, T the absolute temperature and η the viscosity of the solvent. The dispersity of the nanoparticles was accessed by using cumulant analysis[2] of the correlation functions measured at 90° as:

$$ln\, g_1(t) = lnC - \Gamma t + \frac{\mu_2}{2}t^2 \qquad \text{(S2)}$$

where C is the amplitude of the correlation function. The parameter μ_2 is known as the second cumulant and it was used to compute the dispersity of the samples (μ/Γ^2).

Cryogenic transmission electron microscopy (cryo-TEM)

The cryo-TEM observations were carried out using a FEI Tecnai G2 Spirit BioTWIN quipped with an Eagle 4 megapixel CCD camera. For each specimen, 3.5 – 4 µL of polyoxalate prodrug PDEB1 NPs solution (before and

after H_2O_2 incubation) was loaded onto a carbon-coated and lacey film-supported copper TEM grid (NetMEsh, Ted Pella Company) in the climate chamber of a FEI Vitrobot Mark III vitrification robot. The climate chamber was kept at 26 °C with saturated water vapor. The grid loaded with solution was blotted for 5 s and rested for 1 s before it was plunged into liquid ethane, which was kept around its freezing point by liquid N_2. Vitrified samples were kept under liquid N_2 before imaging. The microscope was operated at 120 kV, and the specimen was held by a Gatan-626 single tilt cryo-transfer holder. Images were taken at an underfocus for adequate phase contrast.

Synthesis of the polyprodrugs:

The polyprodrugs PDEB1, PDEB2 and PDEB3 were obtained by synthesis as follows: 1,4-cyclohexanedimethanol (PDEB1: 26.352 mmol – 3.800g ; PDEB2: 24.705 mmol – 3.563g; PDEB3: 21.96 mmol – 3.166g) and diethylstilbestrol (PDEB1: 1.098 mmol – 0.29464g; PDEB2: 2.745 mmol – 0.7366g; PDEB3: 5.49 mmol – 1.4732g) were dissolved in 10 mL of dry tetrahydrofuran (THF), under nitrogen, to which 60 mmol (6.069g) of triethylamine was added dropwise at 4 °C. Then 27.45 mmol (3.4843g) oxalyl chloride in 20 mL of dry THF was added to the mixture dropwise at 4 °C. The polymerization reaction was continued for 6 h at room temperature under nitrogen atmosphere. The resulting polymers were obtained through extraction using DCM and precipitation in cold hexane. The polymers were obtained as yellowish solids (yield ~ 60 %) and their chemical structure was identified with ^{1}H NMR spectroscopy (600 or 300 MHz spectrometer).

PDEB1: ^{1}H NMR (600 MHz, DMF, δ): 7.02 ppm (s, Ar, 4H), 6.87 ppm (s, Ar, 4H), 4.15 ppm (d, O-**CH_2**, 4H), 2.11 ppm (s, **CH_2**-CH_3, 4H), 1.91-0.88 ppm (m, **CH-CH_2**, 10H), 0.73 ppm (s, CH_2-**CH_3**, 6H). PDEB2: ^{1}H NMR (600 MHz, DMF, δ): 7.02 ppm (s, Ar, 4H), 6.87 ppm (s, Ar, 4H), 4.15 ppm (d, O-**CH_2**, 4H), 2.11 ppm (s, **CH_2**-CH_3, 4H), 1.91-0.88 ppm (m, **CH-CH_2**, 10H), 0.73 ppm (s, CH_2-**CH_3**, 6H). PDEB3: ^{1}H NMR (600 MHz, DMF, δ): 7.03 ppm (dd, Ar, 4H), 6.88 ppm (dd, Ar, 4H), 4.15 ppm (dd, O-**CH_2**, 4H), 2.12 ppm (m, **CH_2**-CH_3, 4H), 1.91-0.84 ppm (m, **CH-CH_2**, 10H), 0.74 ppm (m, CH_2-**CH_3**, 6H).

Preparation of the polyoxalate prodrug nanoparticles

A predetermined amount of PDEB1 polyprodrug (12.5 mg) was dissolved in acetonitrile (10 mL) and precipitated into a water solution (20 mL) containing 2 times the amount of Tween-80® (FDA-approved) stabilizing agent (25 mg). The solvent was evaporated and the polyprodrug NPs were concentrated to the desired volume (5 mL). In the case of rubrene loaded NPs, rubrene 2.5 *w*t% (per polymer *w*t) was added and dissolved in acetonitrile. PLA NPs (control) were prepared as PDEB1 aforementioned.

Diethylstilbestrol (DEB) amount in the polyoxalate prodrugs

The total amount of the chemotherapeutic DEB in the polyprodrug backbone was measured by high performance liquid chromatography (HPLC, Shimadzu, Japan) with a reverse-phase column Chromolith Performance RP-18e (100 x 4.6 mm), eluent water-acetonitrile with acetonitrile gradient 0–100 vol%, flow rate = 4.0 mL·min^{-1}. The aliquot (100 µg) of polyprodrug NPs was weighed and diluted to 1000 µL with a mixture of acetonitrile/H_2O_2 solution (70/30 *v*/*v*) (H_2O_2 30 % volume in H_2O, Sigma-Aldrich). The aliquot was further ultrasonicated (5 min) and then ultracentrifuged (18 000 x g, 20 min). Afterwards, 20 µL of the final sample (supernatant) was injected through a sample loop. DEB was detected at 280 nm using ultraviolet (UV) detection. The retention time of DEB was 1.74 min under such experimental conditions. An analytical curve with linear response in the range 0.5 – 100 µg·mL^{-1} was obtained and used to determine DEB content (Figure S3). The drug-loading content (LC) was calculated based on the following equation:

$$LC(\%) = \frac{drug\ ammount\ in\ NPs}{mass\ of\ NPs}\ x\ 100 \qquad \text{(S3)}$$

***In vitro* diethylstilbestrol release experiments**

The release experiments were carried out at 37 °C in pH-adjusted release media (pH 7.4 and 1 mM of H_2O_2). Aliquots (500 µL) of the polyprodrug PDEB1 NPs were loaded into 36 Slide-A-Lyzer MINI dialysis microtubes with MWCO 10 kDa (Pierce, Rockford, IL). These microtubes were dialyzed against 4 L of PBS (pH 7.4 and 1 mM of H_2O_2). The release media was changed periodically to reduce the possibility of drug-diffusion equilibrium (every 12h). The drug release experiments were done in triplicate. At each sampling time, three microtubes were removed from the dialysis system and 0.1 mL from each microtube was diluted to 0.9 mL with a mixture of acetonitrile/H_2O_2 solution (70/30 *v*/*v*) (H_2O_2 30 % volume in H_2O, Sigma-Aldrich). The aliquot was further ultrasonicated (5 min) and then ultracentrifuged (18 000 x g, 20 min). Afterwards, 20 µL of the final sample was injected through a sample loop. DEB released was detected at 280 nm using ultraviolet (UV) detection using the aforementioned methodologies (Figure S3). The reported data are expressed as the amount of released DEB relative to the total DEB content in the PDEB1 polyprodrug NPs.

In vitro biological studies

Viability assays

Cells were seeded in triplicate in 96 well plates at a density of 3000 (HF), 2500 (MCF7), 4000 (PC3) and 5000 (LNCaP) cells per well and left to adhere at least overnight. Cells were then topped with 80 µL of fresh medium, and 20 µL of 5x concentrated dilution of DEB or particle dispersion were added for a final concentration ranging from 0.13 – 280 µM DEB. For this purpose a dilution row in full incubation medium with a starting concentration of 5x 280 µM DEB was made under thorough mixing in order to ensure that all samples were fully homogenous. In a similar manner, dilutions of a 1.88 $mg \cdot mL^{-1}$ DEB stock in Tween 80-supplied 3.5 % DMSO were added in the samples for evaluation of the toxicity of free DEB. The highest concentration sample contained 280 µM DEB and 140 µM Tween 80; after 2nd dilution (*i.e.,* in the 3rd highest concentrated sample), the Tween 80 concentration was below toxic levels (20 $\mu g \cdot mL^{-1}$) (Sigma Aldrich, product data sheet). The reference samples with free DEB were supplied with the similar amount of Tween 80 as was contained in the PDEB1 samples in order to take into account potential toxic effects of Tween 80 at the two maximum sample concentrations. The final content of DMSO (0.14% at maximum) was below the toxicity threshold. Cells left untreated and cells killed with hydrogen peroxide provided control points of maximal and minimal viability. After incubation for 5 days the cells were supplied with 10 µL of AlamarBlue® reagent (Life Technologies) and returned to the incubator for 3-6 hours. The fluorescence of the viability marker resorufin was evaluated using a Synergy H1 plate reader (BioTek Instruments, US) at 600 nm (excitation 570 nm). All experiments were done in triplicate (n = 3).

Microscopy studies

Cells were seeded in polylactide-coated 4-chamber glass bottom dishes of 35 mm and left to adhere for at least one day. The number of cells seeded per chamber was 10^4 (HF), $20 \cdot 10^3$ (PC3), $20 \cdot 10^3$ (LNCaP) and $15 \cdot 10^3$ (MCF7). The cells were incubated for 24 h with 3.4 µM or for 72 h with 1.13 µM of diethylstilbestrol, applied as free drug DEB or in the form of PDEB1 NPs; for longer incubation of 3 days the drug dose was reduced slightly to avoid excessive cell death. For imaging, cells were rinsed carefully with PBS, topped with the staining solution and kept in the incubator for 10 min, after which the solution was exchanged for 200 µL of 3.5% paraformaldehyde and left for 10 min. Then the samples were topped with 200 µL PBS and imaged. As staining solution a 1:10 dilution of serum-supplied incubation medium, supplied with 1 $\mu g \cdot ml^{-1}$ Hoechst 33342 and CellMask™ Green at 1x working concentration according to the manufacturer's instruction (all Invitrogen, USA) was used. For live-dead labeling, propidium iodide (PI) 4 $\mu g \cdot mL^{-1}$ was added to the staining solution. Data were acquired on an Olympus FV 10-ASV confocal laser scanning microscope with a 60x oil objective. Fluorescence

was detected in Channel 1 (Hoechst exc. 405 nm, em. 450/50 nm), Channel 2 (CellMask™ Green exc. 488 nm, em. 515/30 nm) and Channel 3 (PI exc. 543, em. 610/100).

Toxicity mechanism

DEB gets oxidized to a DEB-quihinone which binds covalently to the DNA, which is a DNA damaging mechanism that occurs in any cell type without distinction,[3] and is held responsible for the carcenogenicity of long-term DEB exposure. On a shorter timescale of up to 24 h in *in vitro* studies in a concentration range of 20-50 µM, DEB toxicity for non-cancer cells, *e.g.,* fibroblasts, has been reported by Ochi, et al.. Here DEB interferes with the mitotic process by causing multi-polar spindles, which leads to G2/M cell cycle arrest and unregulated multipolar cell division. These changes can results in the observed aneuploidy and eventually trigger apoptosis. In a concentration-dependent manner, after 24h incubation DEB caused changes in the chromosomal number (at 20 µM), disturbed the microtubuli network (at 50 µM) and raised toxicity (100 µM).[4] In all tested cell lines in this study, the PDEB1 polyprodrug NPs caused, next to the specific toxic effects described below, a general decrease in cell viability and growth (see Figure S7).

Prostate cancer cells

The PDEB1 polyprodrug was tested in two model cell lines for hormone therapy-resistant (PC3) and therapy-responsive (LNCaP) prostate cancer. The DEB-induced M-phase arrest, aneuploidy and apoptosis induction in a concentration range of 30 µM in PC3 cells, which was described by Robertson, et al.[5] They further reported that DEB equally triggered cell cycle arrest and apoptotic death in LNCaP and PC3 cells, *via* an estrogen receptor-independent mechanism. The microscopy studies of PC3 showed that, despite being resistant to hormone therapy, they were notably affected by the PDEB1 polyprodrug NPs. The cycle arrest and nuclear fragmentation occurred as described in the literature.[5,6,7] Similar effects were observed for the LNCaP cells, except that LNCaP, unlike PC3, also displayed an impairment of the cytoskeleton because the cells detached in vast numbers and forming lose clumps. This was demonstrated using a light microscope, where LNCaP cells were visualized without washing to avoid losing detached cells. Note that these samples (see Figure S7) contained Tween 80 and DMSO at maximal 5.3 µM resp. 0.01% concentration, *i.e.,* the concentrations of both chemicals were below the toxicity threshold. Moreover, the overall concentration of Tween 80 was identical in the free DEB and the PDEB1 NPs samples, which effectively excludes Tween 80 as the reason for detachment. This cell detachment is therefore an impairment that will add to the long-term toxicity of PDEB1 NPs for LNCaP. Beyond the detachment, PDEB1-treated LNCaP also showed the same toxic effects as PC3, *i.e*., significant M-phase arrest

(Figure S7). It is important to note that the cell death by mitotic arrest-induced apoptosis has a timeframe of several days.[5] Fluorescence imaging of the clustered detached LNCaP cells confirmed that after 3 days incubation with PDEB1 NPs, the detached LNCaP were still viable (propidium iodide staining negative, see Figure S8). Due to restrictions concerning cell density, the AlamarBlue™ assay was not incubated for longer than 5 days. But it is expected that, due to the slow nature of apoptosis induction *via* cell cycle arrest, the final toxicity of PDEB1 NPs on LNCaP and PC3 cells is even higher than what we were able to document in the range of 5 days.

Breast cancer cells

The apoptosis induction through estrogen-receptors (specifically ERα type I) is described as major mechanism of DEB apoptosis induction in breast cancer cells.[6] But it is generally acknowledged that DEB acts *via* several pathways to induce toxicity, and the DEB binding to other estrogen-related receptors in breast cancer cells is under discussion.[7] The fact that ERα type I acts in a genomic pathway and triggers apoptosis swiftly, after 24 h and not *via* cell cycle arrest, likely contributed to the high efficiency of PDEB1 versus MCF7.[6] On the other hand, the high numbers of G2/M arrested cells suggests the involvement of at least one more pathway – that induces apoptosis more slowly, in the range of several days. The MCF7 cells from all tested cell lines showed the most severe toxicity, where the vast majority of cells were damaged, accumulated in the mitotic phase or displaying nuclear aneuploidy (see Figure S7). Similar to the prostate cancer cells, the slow nature of cell cycle arrest-induced cell death indicates that the final toxicity of PDEB1 on MCF7 may be higher than can be measured after 5 days. In MCF7 the difference between DEB toxicity and polyprodrug toxicity was striking, and higher than in any of the other tested cell lines. The MCF7 cells were highly sensitive to the polyprodrug PDEB1 NPs.

Non-cancerous cells

In stark contrast to the MCF7 cells, in the non-cancerous HF cells the toxicity of PDEB1 was mostly visible in the decreased cell numbers, morphology change into a less elongated shape and fragmentation aneuploidy of the nucleus in several cells (DEB-induced aneuploidy in fibroblasts as reported by Ochi.[4] The general cell death (number of dead cells) was less excessive than in MCF7 and an increase of the G2/M cell population like in the cancer cell samples was not observed in the fibroblast samples exposed to PDEB1.

We can conclude that HF fibroblasts were in general less affected by the PDEB1 polyprodrug NPs in comparison with the used cancer cells. HF cells displayed decreased cell growth, shape changes and nuclear aneuploidy and fragmentation. The cancer cells displayed all this as well, but in addition also significant G2/M arrest,

detachment (LNCaP) and general higher cell damage. PDEB1 lowered the required dose in LNCaP and also in therapy-resistant PC3 cells, and it was particularly effective in the MCF7 breast cancer model system. Finally, while being highly efficient against cancer cells, towards non-cancerous cells the polyprodrug NPs was barely more toxic than the gold standard of biocompatible polymers polylactide, PLA (see Figure S10).

Chemiluminescence of rubrene in PDEB1 polyoxalate prodrug NPs in cells

The oxalate bonds are oxidized by H_2O_2 to produce 1,2-dioxetanedione (or other high-energy intermediates which interact with an appropriate fluorophore to form an activated complex, the mechanism still not fully elucidated). After decomposition of the complex along with CO_2 release, the excited fluorophore decays to the ground state with fluorescent emission (Scheme S1). The MCF7 cells were selected to demonstrate the degradation of PDEB1 by chemiluminescence. The H_2O_2-triggered cleavage of the oxalate groups in the prodrug backbone includes an intermediate step, which in the presence of rubrene will cause a proportionate chemiluminescence emission of the dye molecule (see Scheme S1). The appearance of rubrene luminescence is therefore a direct sign that the degradation of PDEB1 NPs is taking place.

MCF7 cells were seeded in duplicate at a density of $8 \cdot 10^3$ cells per well in 96 well plates and left overnight to adhere. The cells were then given 350 µL of PDEB1-supplied fresh medium containing up to 240 $\mu g \cdot mL^{-1}$ rubrene (PDEB1 NPs with 2.5 %wt rubrene) and the cells were incubated for 2h. Chemiluminescence of the rubrene, as caused by the ROS produced by MCF7, was read out with a Synergy H1 plate reader (BioTek Instruments, US) at 10 s integration time and each well (duplicates) was measured 4 times. Statistical significance was calculated based on ANOVA ONE-WAY and Tukey test, using the Origin 9.0 software (Originlab, US). A NPs-concentration dependent luminescence was observed (see Figure 1E).

A similar experiment was done in RAW macrophages with the aim to reproduce the effect in a different cell type (Figure S6). RAW macrophages were seeded at a density of $115 \cdot 10^3$ cells per well in 96 well plates in duplicates and left to adhere. Then the cells were incubated for 16h with rubrene-loaded PDEB1 NPs (final rubrene concentration 56 $\mu g \cdot mL^{-1}$).

The initiation of chemiluminescence in the cells after incubation with rubrene-loaded PDEB1 NPs demonstrated that these cells produced sufficient ROS species to initialize degradation of PDEB1. The cleavage of the oxalate groups in the prodrug backbone includes a dioxoborolone intermediate step, which in the presence of rubrene will cause a proportionate chemiluminescence of rubrene (see Scheme S1).

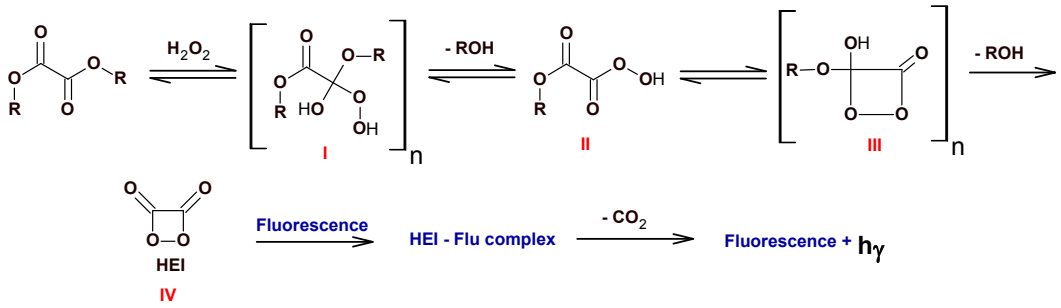

Scheme S1. Proposed mechanism for fluorescence from oxalate based polymers.[,8,9]

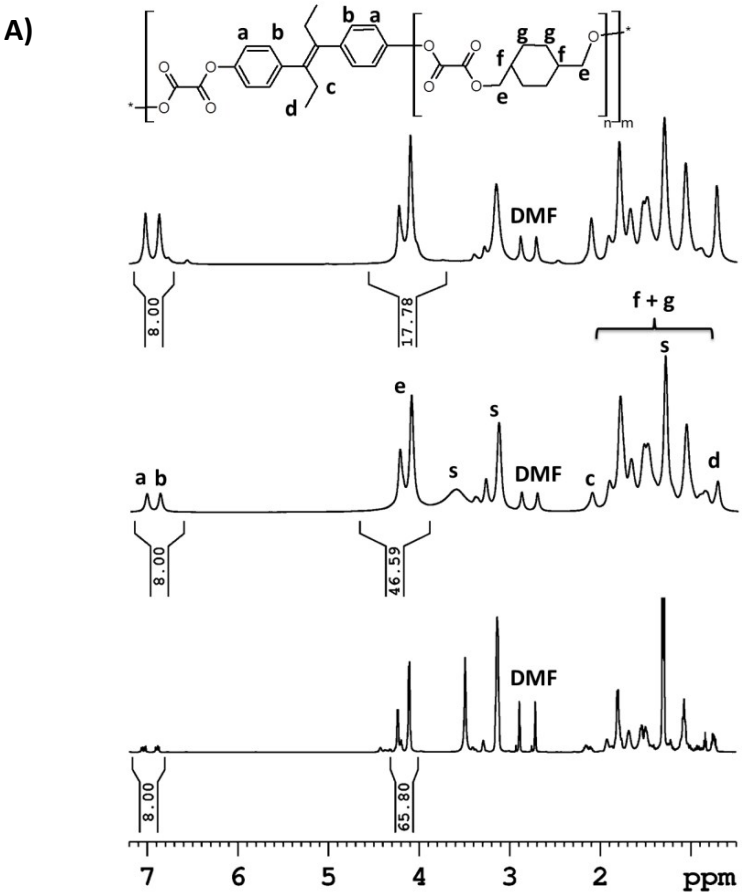

Figure S1. A) ^{1}H NMR of the synthesized polyprodrugs with different DEB moles ratio PDEB3 1~4 (top), PDEB2 1~12 (middle) and PDEB1 1 ~ 16 (bottom) in deuterated DMF, „s“ is related to solvents impurities. The spectra depict the observed characteristic signals for protons belonging to the repeating units of monomers. Peaks assignments of the various proton types are shown in the spectrum and chemical structure of the polymer is shown in the same figure. The signals from protons of the DEB aromatic rings were detected at δ = 7.02 ppm (a) and δ = 6.87 ppm (b). The methylene (c) and methyl (d) protons of DEB where observed at δ = 2.09 and δ= 0.72 ppm respectively, whereas the signals attributed to the methylene group (e) of 1,4-Cyclohexanedimethanol monomer units are at δ = 4.00-4.30 ppm. The signals of the protons of the aliphatic cycle (f, g) are in the range between δ = 0.88-1.91 ppm. B) Top - the ^{1}H NMR spectrum of the Diethylstilbestrol in deuterated DMF and showing the small change of the chemical shift in the aromatic region. Bottom - the disappearance of the signal related to the –OH group of the Diethylstilbestrol at 9.5 ppm in the spectrum of PDEB3 in DMF-d_7 solution.

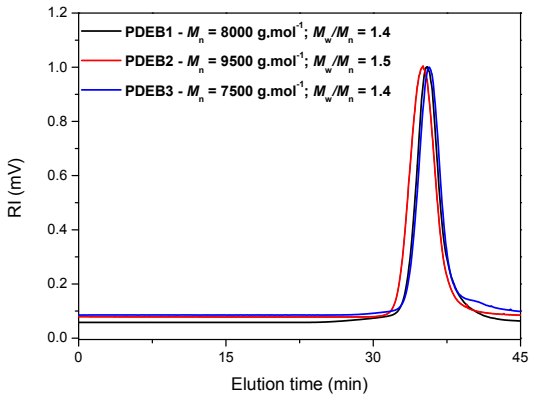

Figure S2. SEC chromatograms in DMF of the synthesized polyprodrugs PDEB1 (black), PDEB2 (red) and PDEB3 (blue).

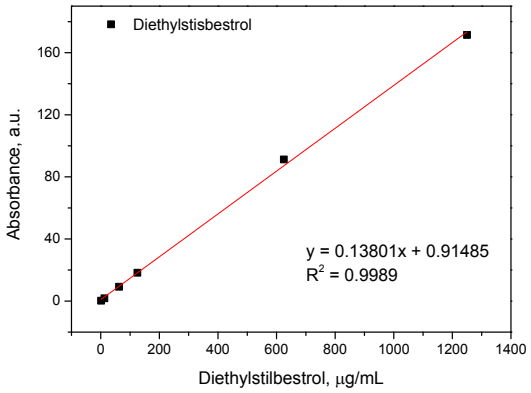

Figure S3. Calibration curve for diethylstilbestrol.

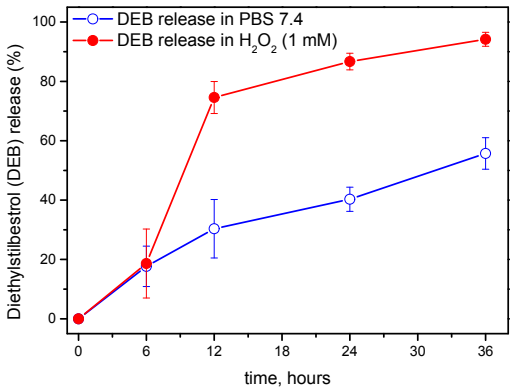

Figure S4. DEB release from PDEB1 polyprodrug NPs at pH 7.4 (blue lines) and in the presence of 1 mM of H_2O_2 (red lines) along 36h of incubation at 37 °C.

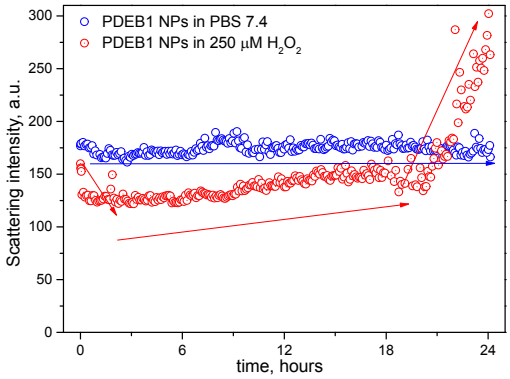

Figure S5. Overall scattering intensity from the NPs under incubation with physiologically relevant levels of H_2O_2 (250 μM, right).

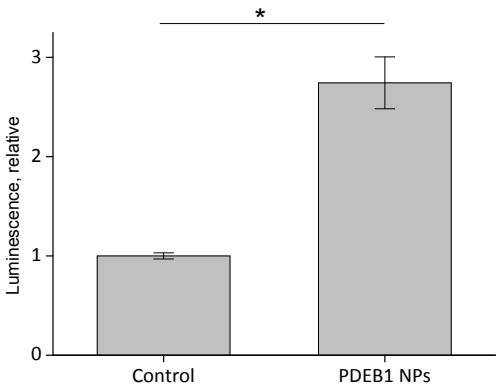

Figure S6. Luminescence in RAW cells after 16h incubation with rubrene-loaded PDEB1 NPs indicating the degradation of the polyoxalate prodrug NPs. * $p < 0.02$.

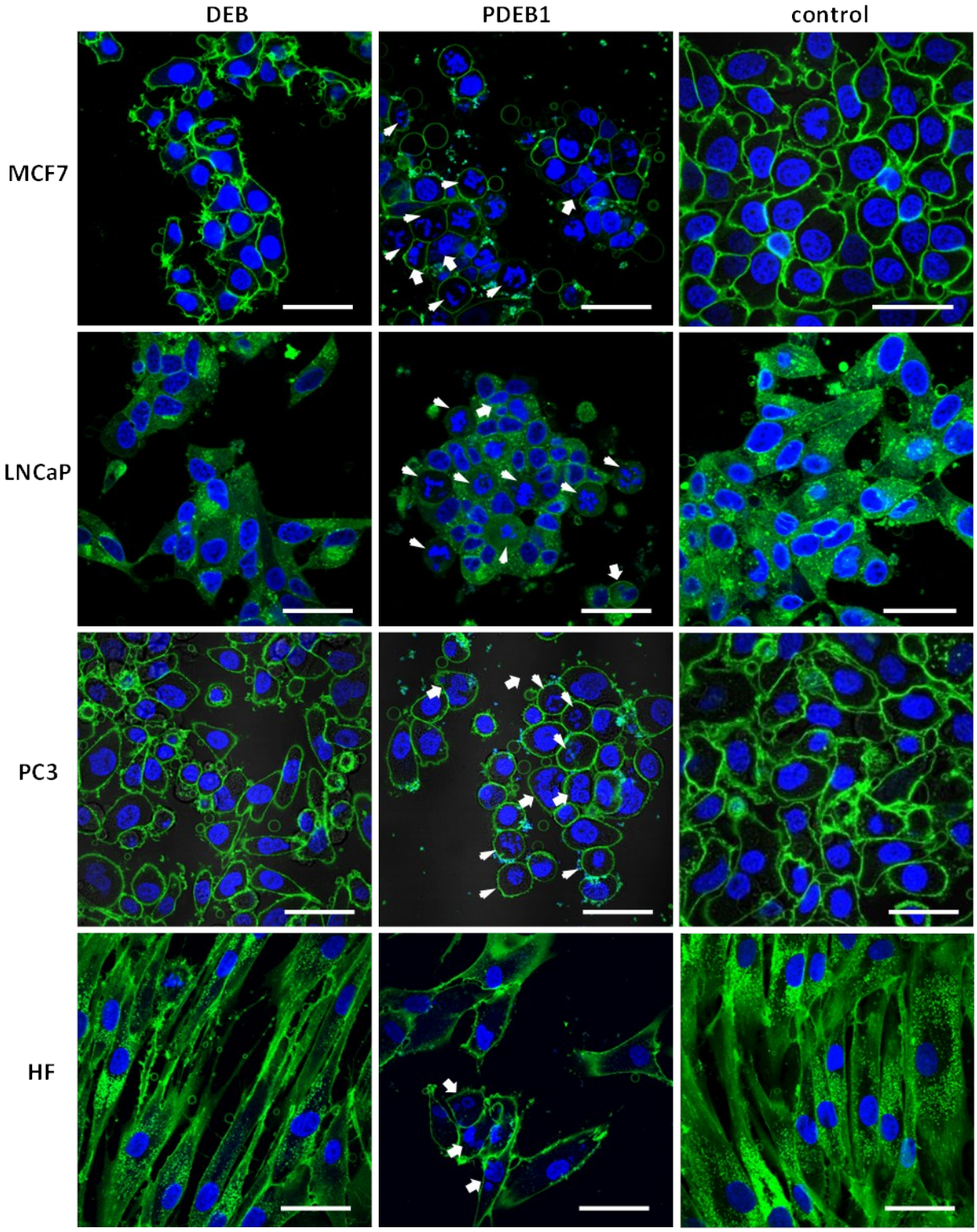

Figure S7. Cells were incubated for 24 h with 3.4 μM DEB (related to DEB amount) to visualize nuclear fragmentation (arrow) and G2/M cell cycle arrest (arrowhead); stained nuclei (Hoechst 33342) in blue, the cytoplasmic membrane (CellMask™ Green) in green. (Scale bar = 50 μM).

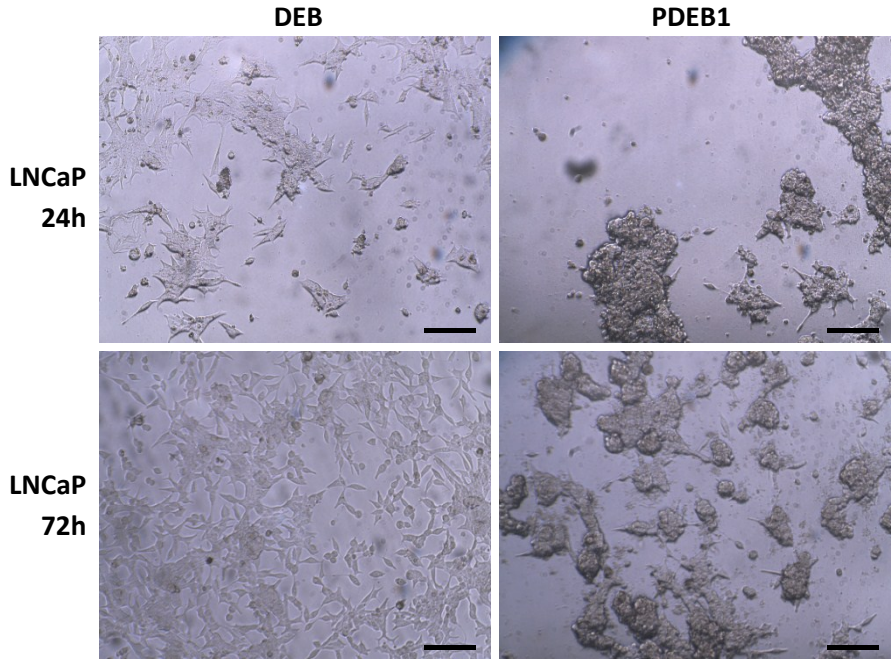

Figure S8. LNCaP cells after 24 h (3.4 μM DEB) and 72 h (1.1 μM DEB) incubation with PDEB1 polyoxalate prodrug. The pictures documented a selective sensitivity of LNCaP to the polymer prodrug by detaching of the cells and forming clumps. (Scale bar = 100 μM).

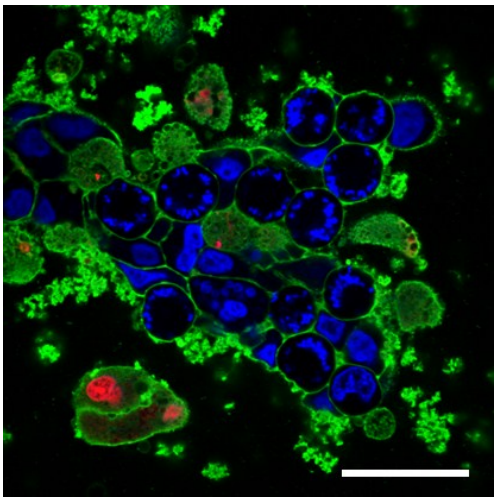

***Figure S9*.** A cluster of detached LNCaP cells after 72h incubation with PDEB1 (1.13 μM DEB) were stained with the cell death marker propidium iodide (PI) for live-dead differentiation (PI in red). Nuclei were stained using Hoechst 33342 (blue) the cytoplasmic membrane was labeled with CellMaskTM (green). (Scale bar = 50 μM)

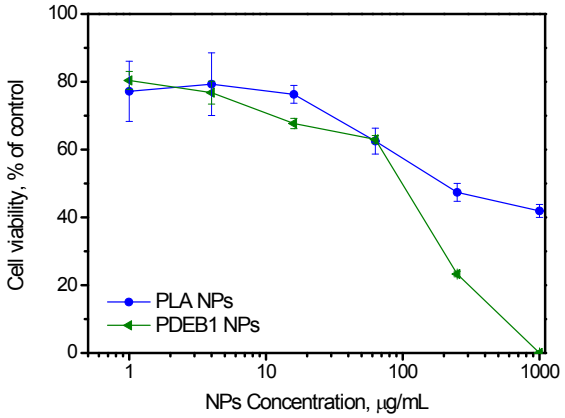

Figure S10. Cytotoxicity of the PDEB1 polyoxalate prodrug NPs in human fibroblast (HF) cells in comparison with the NPs prepared from the FDA-approved polymer, polylactic acid (PLA) after 48h incubation.

References:

[1] T. C. Farrar, E. D. Becker, Pulse and Fourier Transform NMR. Academic Press: New York, 1971, pp. 27-29.

[2] P. Štěpánek, In Dynamic light scattering: The method and Some Applications; Brown, W., Ed. Oxford Science Publications: Oxford, 1993.

[3[B. Hinrichs, M. Zahid, M. Saeed, M. F. Ali, E. L. Cavalieri, E. G. Rogan, *J. Steroid Biochem. Mol. Biol.*, **2011**, *127*, 276–281.

[4] T. Ochi, *Mutat Res - Fundam Mol Mech Mutagen* **1999**, *431*, 105–121.

[5] C. N. Robertson, K. M. Roberson, G. M. Padilla, E. T. O'Brien, J. M. Cook, C. S. Kim, R. L. Fine, *J. Natl. Cancer Inst.*, **1996**, *88*, 908–917.

[6] I. E. Obiorah, V. C. Jordan, *Br. J. Pharmacol.*, **2014**, *171*, 4062–4072.

[7] K. Nam, P. Marshall, R. M. Wolf, W. Cornell, *Biopolymers* **2003**, *68*, 130–8.

[8] D. Lee, S. Khaja, J.C. Velasquez-Castano, M. Dasari, C. Sun, J. Petros, W.R. Taylor, N. Murthy, *Nat. Mater.*, **2007**, *6*, 765-769.

[9] C.-C. Song, F.-S.Du, Z.-C. Li, *J. Mater. Chem. B*, **2014**, *2*, 3413-3426.